2015

Terahertz spectroscopy of magnetic metal oxides

Evan Constable
University of Wollongong
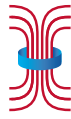
UNIVERSITY OF WOLLONGONG

DOCTORAL THESIS

Terahertz spectroscopy of magnetic metal oxides

Author:

Evan CONSTABLE

Supervisors:

Prof. Roger A. LEWIS

A/Prof. Joseph HORVAT

A thesis submitted in fulfilment of the requirements

for the degree of Doctor of Philosophy

in the

Institute for Superconducting and Electronic Materials

School of Physics

March 2015

Declaration of Authorship

I, Evan CONSTABLE, declare that this thesis titled, 'Terahertz spectroscopy of magnetic metal oxides' and the work presented in it are my own. I confirm that:

- This work was done wholly or mainly while in candidature for a research degree at this University.

- Where any part of this thesis has previously been submitted for a degree or any other qualification at this University or any other institution, this has been clearly stated.

- Where I have consulted the published work of others, this is always clearly attributed.

- Where I have quoted from the work of others, the source is always given. With the exception of such quotations, this thesis is entirely my own work.

- I have acknowledged all main sources of help.

- Where the thesis is based on work done by myself jointly with others, I have made clear exactly what was done by others and what I have contributed myself.

Signed:

_____

Date: 24/11/2014

_____

Abstract

Doctor of Philosophy

Terahertz spectroscopy of magnetic metal oxides

by Evan CONSTABLE

The optical excitation and control of spins in magnetic materials promises new avenues for devices that couple photonic and spintronic functionality, with the prospects of a new paradigm in information processing. An understanding of the behaviour of the magnetic interactions in candidate materials is essential to the design of devices that exhibit these desirable properties. Terahertz radiation presents an ideal medium for the study of spin dynamics in magnetic materials. Its low energy in the meV range is equivalent to the many weak magnetic coupling mechanisms present. Terahertz radiation is therefore also complementary to established methods that probe these mechanisms such as inelastic neutron scattering and magnetometry. The electromagnetic nature of terahertz radiation means that the magnetic field component can couple directly to the ordered spin moments. Furthermore, the electric field component may interact with lattice coupled magneto-electric excitations. The metal oxides, which combine magnetic super-exchange, strongly correlated electrons and low symmetry crystalline environments, are good candidates for technological applications invoking these interactions. This is because they often feature exploitable properties such as antiferromagnetism, ferroelectricity, semiconducting behaviour and magneto-electric coupling. They are also typically insulating allowing for terahertz transmission investigations. In this thesis terahertz transmission spectroscopy is performed on a number of magnetic metal oxides as well as a non-magnetic semiconductor. Specifically, a non-magnetic semiconductor (ZnTe); a geometrically frustrated metamagnet ($Cu_3Bi(SeO_3)_2O_2Cl$); a canted antiferromagnet ($NdFeO_3$) and a quantum spin ladder system ($Sr_{14}Cu_{24}O_{41}$) are investigated. Collectively, the work establishes terahertz radiation as an effective probe of material properties. The results reveal a diverse range of magnetic excitations, characterising their temperature and external magnetic field dynamics. The physical interactions probed are commented on regarding their relevance to the emerging field of spintronics.

Acknowledgements

Publications

Papers and proceedings directly related to this thesis:

- E. Constable, D. L. Cortie, J. Horvat, R. A. Lewis, Z. Cheng, G. Deng, S. Cao, S. Yuan, and G. Ma. Complementary terahertz absorption and inelastic neutron study of the dynamic anisotropy contribution to zone-center spin waves in a canted antiferromagnet NdFeO$_3$. *Physical Review B*, 90:054413, 2014.

- E. Constable, G. Deng, J. Horvat, and R. A. Lewis. THz absorption bands in Sr$_{14}$Cu$_{24}$O$_{41}$ by synchrotron radiation. In *International Conference on Infrared, Millimeter, and Terahertz Waves (IRMMW-THz)*, Tucson, USA, 2014. doi: 10.1109/IRMMW-THz.2014.6956359.

- E. Constable, J. Horvat, D. L. Cortie, Z. Cheng, S. Yuan, S. Cao, and R. A. Lewis. High temperature anisotropy of NdFeO$_3$ determined using time-domain THz spectroscopy. In *International Conference on Infrared, Millimeter, and Terahertz Waves (IRMMW-THz)*, Mainz, Germany, 2013. doi: 10.1109/IRMMW-THz.2013.6665932.

- E. Constable and R. A. Lewis. Optical parameters of ZnTe determined using continuous-wave terahertz radiation. *Journal of Applied Physics*, 112:063104, 2012.

- K. H. Miller, P. W. Stephens, C. Martin, E. Constable, R. A. Lewis, H. Berger, G. L. Carr, and D. B. Tanner. Infrared phonon anomaly and magnetic excitations in single-crystal Cu$_3$Bi(SeO$_3$)$_2$O$_2$Cl. *Physical Review B*, 86:174104, 2012.

- K. H. Miller, E. Constable, H. Berger, D. B. Tanner, and R. A. Lewis. Complementary techniques for probing terahertz magnetic excitations in Cu$_3$Bi(SeO$_3$)$_2$O$_2$Cl. In *International Conference on Infrared, Millimeter, and Terahertz Waves (IRMMW-THz)*, Wollongong, Australia, 2012. doi: 10.1109/IRMMW-THz.2012.6380234.

- E. Constable and R. A. Lewis. Characterising zinc telluride wafers using continuous-wave terahertz spectroscopy. In *International Conference on Infrared, Millimeter, and Terahertz Waves (IRMMW-THz)*, Houston, USA, 2011. doi: 10.1109/irmmw-THz.2011.6104849.

Other publications:

- R. A. Lewis, A. Bruno-Alfonso, G. V. B. de Souza, R. E. M. Vickers, J. A. Colla, and E. Constable. Spherical, cylindrical and tetrahedral symmetries; hydrogenic states at high magnetic field in Si:P. *Scientific Reports*, 3:3488, 2013.

- G. Seniutinas, G. Gervinskas, E. Constable, A. Krotkus, G. Molis, G. Valusis R. A. Lewis, and S. Juodkazis. THz photomixer with a 40-nm-wide nanoelectrode gap on low-temperature grown GaAs. In *SPIE: Micro/Nano Materials, Devices, and Systems*, Melbourne, Australia, 2013. doi: 10.1117/12.2033746.

- C. Weickhmann, R. Jakoby, E. Constable, and R. A. Lewis. Time-domain spectroscopy of novel nematic liquid crystals in the terahertz range. In *International Conference on Infrared, Millimeter, and Terahertz Waves (IRMMW-THz)*, Mainz, Germany, 2013. doi: 10.1109/IRMMW-THz.2013.6665423.

- E. Constable, and R. A. Lewis. Continuous-wave terahertz spectroscopy as a non-contact, non-destructive method for characterising semiconductors In *35th Annual Condensed Matter and Materials Meeting*, Wagga Wagga, Australia, 2011. URL: http://www.aip.org.au/info/sites/default/files/cmm/2011/p7.pdf.

- A. Tuniz, R. Lwin, A. Argyros, S. C. Fleming, E. M. Pogson, E. Constable, R. A. Lewis, and B. T. Kuhlmey. Stacked-and-drawn metamaterials with magnetic resonances in the terahertz range. *Optics Express*, 19:16480–16490, 2011.

- A. Tuniz, R. Lwin, A. Argyros, S. C. Fleming, E. M. Pogson, E. Constable, R. A. Lewis, and B. T. Kuhlmey. Direct-drawn metamaterial fibers with magnetic response in the 100GHz range. In *International Quantum Electronics Conference (IQEC) and Conference on Lasers and Electro-Optics (CLEO) Pacific Rim*, Sydney, Australia, 2011. URL: http://www.opticsinfobase.org/abstract.cfm?URI=CLEOPR-2011-C676.

- E. Constable, J. Horvat, and R. A. Lewis. Mechanisms of x-ray emission from peeling adhesive tape. *Applied Physics Letters*, 97:131502, 2010.

- E. Constable, Y. Hu, J. Horvat, and R. A. Lewis. The emission of visible radiation by peeling adhesive tape. In *33rd Annual Condensed Matter and Materials Meeting*, Wagga Wagga, Australia, 2009. URL: http://www.aip.org.au/info/sites/default/files/cmm/2009/p22.pdf.

Contents

List of Figures

List of Tables

Abbreviations

ANSTO	**A**ustralian **N**uclear **S**cience and **T**echnology **O**rganisation
CBSCl	$\mathbf{Cu_3Bi(SeO_3)_2O_2Cl}$
CBSBr	$\mathbf{Cu_3Bi(SeO_3)_2O_2Br}$
CDW	**C**harge-**D**ensity **W**ave
DM	**D**zyaloshinsky **M**oriya (interaction)
EDS	**E**nergy **D**ispersive (x-ray) **S**pectroscopy
EM	**E**lectro**m**agnetic
FTIR	**F**ourier **T**ransform **I**nfra**R**ed (spectroscopy)
HTS	**H**igh-**T**emperature **S**uperconductivity
INS	**I**nelastic **N**eutron **S**cattering
LIA	**L**ock-**I**n **A**mplifier
LTG	**L**ow **T**emperature **G**rown
ME	**M**agneto-**E**lectric
NMR	**N**uclear **M**agnetic **R**esonance
SEM	**S**canning **E**lectron Microscope
SR	**S**pin **R**eorientation
TDS	**T**ime-**D**omain **S**pectroscopy
THz	**T**erahertz $(10^{12}\,\mathrm{s}^{-1})$
VTI	**V**ariable **T**emperature **I**nsert
XRD	**X**-**r**ay **D**iffraction
ZPD	**Z**ero **P**ath **D**ifference

Symbols

$\mathbf{B}_{\mathrm{ext}}$ externally applied magnetic field vector

$\mathbf{B}_{\mathrm{int}}$ internal magnetic field vector in a material due to atomic interactions

$B_S(X)$ Brillouin function

c speed of light

d sample thickness

d_{hkl} d-spacing between lattice planes in direction given by $[hkl]$

D_{ij} anisotropic (DM) exchange constant between atom i and atom j

$\mathbf{E}$ electric field vector

E energy or electric field scalar

e charge of an electron

$\mathbf{H}$ magnetic field vector

H Hamiltonian

I radiation intensity

J exchange constant based on exchange integral for magnetic coupling of electrons

J_{s} spin current

K magnetic anisotropy energy

$\mathbf{k}$ wave vector indicating direction of wave propagation

k_{B} Boltzmann constant

g the dimensionless gyromagnetic ratio

n carrier concentration or order integer

U internal energy

$\hbar$ Planck's constant

M magnetisation

m	mass
p	momentum
$\mathbf{q}$	scattering vector between incoming and outgoing wave vector
$\mathbf{Q}$	scattering vector perpendicular to scattering plane
R	reflectance
S_i^z	z component of spin moment of atom i
T	transmittance or temperature
T_{N}	Néel temperature
P	power
Z	atomic number
ϵ	dielectric constant
η	real refractive index
κ	imaginary refractive index (absorption)
λ	wavelength
μ	magnetic moment dipole
μ_{B}	Bohr magneton (unit of electron magnetic moment)
ν	normal frequency
χ	magnetic susceptibility
ω	angular frequency

Chapter 1

Introduction

"...the component parts of natural Bodies may be conjectured by their Colours."

Sir Isaac Newton, 1704, Opticks [1]

1.1 Background

Like other natural phenomena, the rainbow of colours visible when light falls upon a prism was known to the philosophers of classical antiquity [2]. In 1666, Newton established that the white light produced by the sun was a composite of many colours [3]. The rainbow formed by a prism was indeed the separated components of white light and Newton referred to this image as the *Spectrum* [3]. The study of the spectrum and how it interacts with matter is known as spectroscopy and throughout humankind's history has proven invaluable in assisting our understanding of the universe and for developing new and world changing technologies [2, 4]. Today this scientific technique has become routine in all frontiers of scientific discovery. Indeed, the subject of this thesis is terahertz spectroscopy of magnetic materials, the convergence of two fields of science which represent frontiers in both spectroscopy [5–7] and the next generation of information technology [8–10]. But how can the study of the colours of light reveal so much to us about the universe? The answer to this becomes apparent with an appreciation of the historical context of the nature of light and its spectroscopic application.

1

1.1.1 The nature of light and the terahertz spectrum

Standing on the shoulders of Newton, the scientists of the early 19th century understood that light was made up of different colours. However, they would soon discover that the 'rainbow' of colours in the spectrum extended far beyond what was visible. In 1800, upon measuring the temperature of the colours in the spectrum, Herschel discovered that the portion of the spectrum that produced the most heat was in fact an invisible band beyond the red [11]. One year later, Ritter discovered that chemical reactions in silver chloride occurred at a faster rate when positioned above the violet portion of the spectrum [12]. These invisible rays, that could affect matter, would later be known as the infrared and ultraviolet bands of light and mark the first instance of the notion of a broader continuous spectrum.

During this period, the double slit experiments of Young supported by further work on the interference of light by Fresnel, laid the foundations for the modern wave theory of light [2, 13]. By 1865, following the tremendous achievements in understanding electricity and magnetism by Faraday and Ampère, Maxwell combined these phenomena into a single dynamic theory of electromagnetism [14]. The solutions to the equations of electromagnetism established that electromagnetic waves propagated as transverse undulations of orthogonal electric and magnetic fields as shown in Figure 1.1. The waves are generated by the acceleration of charge and the propagation speed of these waves was found to match that of light. Therefore, it was established that visible light was indeed only a small portion of a continuous spectrum of electromagnetic radiation spanning from very low frequency (low energy) radio waves through to high frequency (high energy) gamma rays. The colour of light was defined by its frequency (or wavelength) referring to the number of oscillations in the electromagnetic field in one second. This unit of frequency is referred to as hertz or Hz. The intensity of the light is defined by the wave's amplitude.

While this interpretation allows for an impressive amount of understanding and application, the current understanding of light naturally involves a quantum mechanical model. The important theoretical insight for this came from Planck when he introduced a quantised packet of light, later to be known as the photon. This was introduced to account for the spectral distribution of blackbody radiation that could not be explained by the
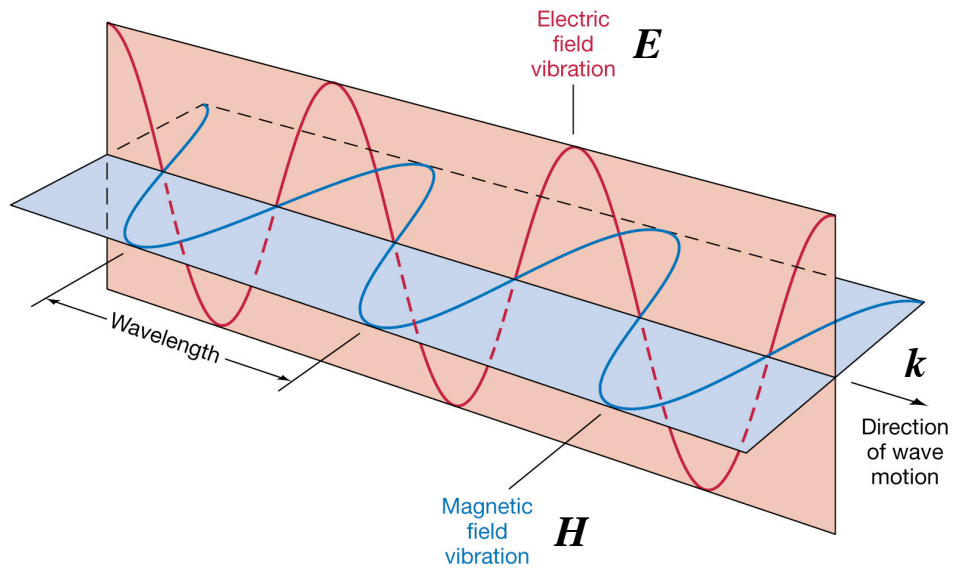
FIGURE 1.1: Diagram of the wave-like nature of electromagnetic radiation sourced from Reference [18]. Waves propagate along the wave vector (**k**) with oscillations of the orthogonal electric (**E**) and magnetic (**H**) fields.

classical wave theory of Maxwell and won him the 1918 Nobel prize in physics [15]. Later, Einstein's description of the photoelectric effect using Planck's quantised light packets gave strong support to a particle nature of light for which he was also awarded a Nobel prize in 1921 [16]. The work of de Broglie in establishing the quantum mechanical wave-particle duality interpretation of matter showed that the photon could act as both a particle and a wave. This also won de Broglie a Nobel prize in 1929 [17] and subsequently the understanding of light has been one of both waves and particles. For the purposes of this thesis, however, it will suffice mostly to consider the electromagnetic radiation as a wave in the form of Figure 1.1.

Even after Maxwell established the notion of a continuous electromagnetic spectrum, it would take further scientific discovery by the likes of Hertz (discoverer of radio waves, 1887) and Röntgen (discoverer of x-rays, 1895) to detect the existence of the entire spectrum. However, by the 21$^{\text{st}}$ century we now have an understanding and spectroscopic techniques to access its entirety.

A portion of the electromagnetic spectrum that until recently has long been inaccessible is the *terahertz* (or simply THz) frequency band. Generally considered to span the frequency

range of 0.1–10×10^{12} Hz (0.1–10 THz, 2998–29.98 μm, 3.336–333.6 cm^{-1}, 0.414–41.4 meV), THz radiation is situated between the traditional bands of microwave and infrared frequencies (Figure 1.2). The word terahertz is a compound of the order of magnitude prefix *tera* (10^{12}) and the frequency unit *hertz* that defines its frequency band. While THz radiation has always existed, only in recent years, in light of important technological advances such as the laser, has it been possible to generate and detect these frequencies to a sufficient level for experimentation [6, 7].

The reason for this lies in the fundamental limitations of how radiation is generated. As established by Maxwell, electromagnetic radiation is generated by the acceleration of charge, typically in the form of electrons. At the low end of the THz spectrum, traditional electronic systems generate radio and microwaves by oscillating conduction band electrons in a metal or a semiconductor material at range of frequencies. An example includes mobile phone telecommunications. The higher those frequencies are the more difficult it becomes to oscillate the electrons at high amplitude. As the frequency is increased, electron collisions with the material's lattice generate heat and the efficiency of radiation production rolls off. Of course this is a very simplistic description but the principle remains, at high frequencies such as in the THz band no usable signal is obtained. At the high end of the THz spectrum, traditional optical systems such as fibre optic telecommunications, generate photons of light by discrete atomic transitions between the electron valence and conduction bands in semiconductor materials. The energies of these discrete transitions are fixed by specific material properties. While these properties are often tuned to produce a range of transition energies, they are still much higher than those of THz energies. Terahertz radiation therefore represents a fundamental gap between traditional electronic and optical systems.

Naturally, this makes THz waves very useful for studying the physics at the boundaries of such systems and the realm of THz science has flourished over the last three decades. Its unique properties have made it useful in the application of security scanning [19], medical diagnostics [20] and secure high-bandwidth communications [21]. As a result, in 2013 the THz industry was valued at $50 million dollars and is set approach $1 billion over the next decade [22]. The continued research of THz science therefore has considerable benefits
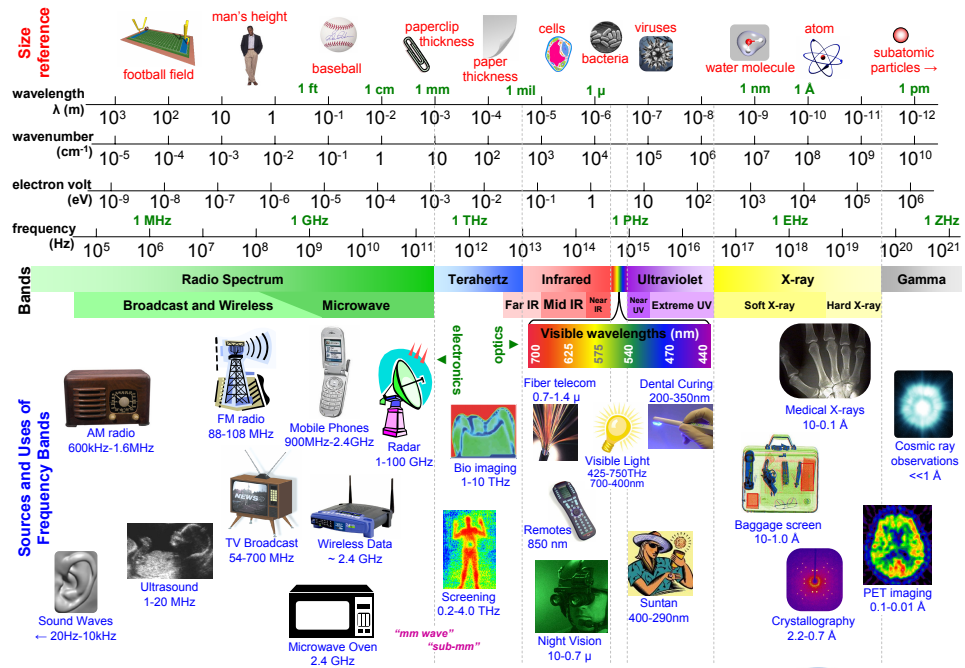
FIGURE 1.2: Representation of the electromagnetic spectrum spanning from radio waves (far left) to gamma rays (far right). The terahertz (THz) spectrum is positioned in the centre at the boundaries of electronic and optical technologies. Image obtained from Reference [23].

for both society at large as well as investing bodies and unsurprisingly many unexplored applications of its use still exist.

1.1.2 The investigation of matter by spectroscopy

As the study into the nature of light progressed in the 19th century, in parallel and very much interwoven with this effort, was the study of how it emanated from and interacted with matter. Newton himself in his *Treatise on Opticks* had speculated on what the colour of objects could tell us about their internal properties [1]. The spectral emission from the flames of alcohol and various salts were routinely examined through a prism later in the 18th century [2]. The accounts of these experiments noted the appearance of lines at definite positions within the colour spectrum but did not draw any conclusion as to the link between certain lines and different elements.

It was not until Fraunhofer in 1814 that the foundations of a quantitative method of spectroscopy were formulated by his development of an accurate spectrometer and the

implementation of defined diffraction gratings [2]. Training his spectrometer on the sun, Fraunhofer observed a series of dark lines overlaid on the colour spectrum (Figure 1.3). Some of these lines were indeed consistent with lines observed in the flame experiments. Furthermore, when the spectra of other stars was viewed, both differences and similarities in the lines was observed. While the mechanisms behind this phenomenon were still not clear, Fraunhofer could reason that some of the properties of the sun were similar to that of flames (they contained similar elements). This also revealed that properties of the sun must have both similarities and differences to many of the stars. As it would come to be discovered such measurements revealed that elements in the sun's atmosphere were absorbing certain frequencies of light. Those same elements could be found on earth and were observed in emission from flames. The stars were made up of the same elements as that of the sun but in many cases the star also contained different species of elements. Essentially, this established that spectroscopy could reveal information about the make up and mechanics of matter.

As improvements in spectroscopic techniques developed hand-in-hand with atomic theory, the ability for spectroscopy to inform on the chemical properties of matter improved. Great progress was achieved with the development of electromagnetic wave theory by Maxwell, which postulated that light radiation is an effect of the acceleration of electric charge. Such a theory was essential for the ground work in discovering the electron [24] and the notion that the spectral features observed by Fraunhofer were due to electronic transitions in atoms [2].

Progress came to an impasse however, when the current theories could not explain observation. Famously, the Rutherford model of the atom, which featured an electron orbiting like a planet around a positive charge [25], could not explain why the electron did not radiate all of its energy as it accelerated in its orbit [26, 27]. This model was rectified by the development of quantum mechanics [28]. One could therefore acknowledge that spectroscopy's defining achievement is that it was the technique responsible for the insights that led to the development of quantum mechanics.

Hand in hand, the development of quantum mechanics was also responsible for improving the understanding of the physics that was being probed by spectroscopy. The essential

principles of spectroscopy are that light interacts with charges in matter. At specific frequencies (f_0) resonance conditions are met and light is absorbed (or emitted) as in Figure 1.3 (c). The spectra observed by Fraunhofer were the absorption spectra of atoms where an electron in the atom is promoted to a higher energy level when the resonance condition is met. Many other forms of resonance may also be observed in this way, such as collective atomic vibrations in crystals (phonons), collective charge oscillations in metals (plamons), vibrational and rotational oscillations in molecular gases and even collective magnetic resonance in magnetic materials (magnons) [29].

The development of spectroscopy and a firm understanding of the interactions it probes, has lead to a paradigm shift in our understanding of the universe with profound impacts on society at large. A classic example is the *age of silicon*. The insights made available by quantum mechanics in the 20th century led to rapid uptake in the study of condensed matter [29, 30]. The development of the solid state transistor by Shockley, Bardeen and Brattain in 1947 [31] required an understanding of the quantum mechanical band structure of the electronic states in semiconductors. Spectroscopic measurements once again proved invaluable in further development of the improved Metal Oxide Semiconductor Field Effect Transistor (MOSFET) with infrared transmission measurements refining values of the electronic band structure [32, 33]. The field effect transistor along with other silicon based devices such as the integrated circuit are keystone technologies in the consumer based electronics world of today [30]. Interestingly, in a return to the early applications of spectroscopy, condensed matter spectroscopy has even been able to inform on cutting edge astro-spectroscopic studies, with magnetic field effects on impurity states in silicon being used to model the far stronger magnetic fields in stars and their effects on hydrogen states [34, 35]. Spectroscopy has therefore always been a pivotal tool for developing and improving fundamental theories and important technologies.

1.1.3 New frontiers in spectroscopy and materials science

As the THz 'gap' closes, with the improvement of technologies that can access this spectral region, opportunities for spectroscopic studies have increased. This is further supported by the interesting physics that exists at these energies. Terahertz frequencies are associated
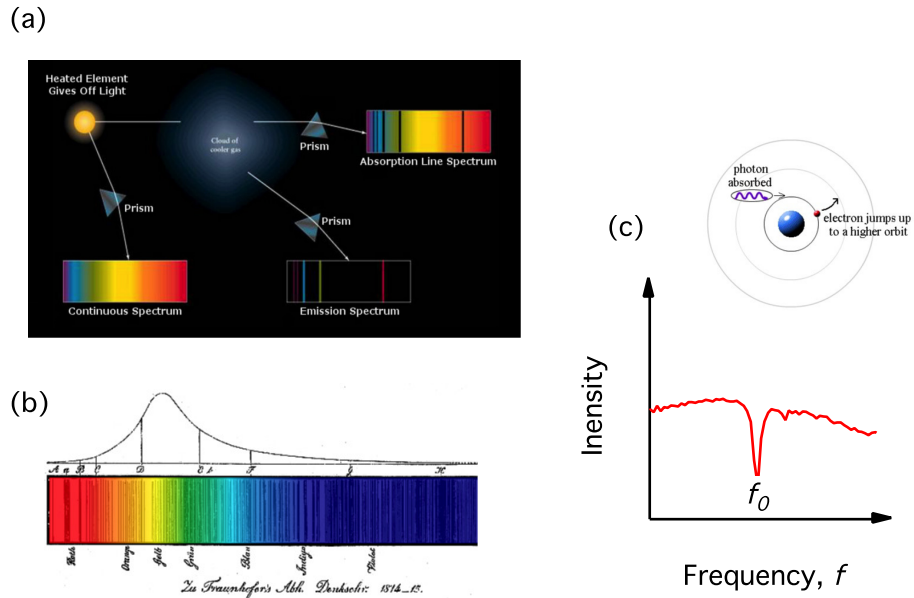
FIGURE 1.3: (a) Demonstration of spectroscopic measurements of the sun by absorption and emission [36]. (b) Fraunhofer's observations of absorption lines in the sun's spectrum. The lines would become to be known as Fraunhofer lines [37]. (c) Principle behind atomic absorption, showing change in intensity of light when resonance condition is met.

with a range of elementary interactions and excitations including phonon vibrations in crystals [38], molecular and protein vibrations in biological samples [39], and spin-wave excitations in magnetic materials [40].

The interaction of THz radiation with magnetic materials is particularly appealing as it offers the possibility of monitoring ultrafast magnetisation processes in the time domain [41], inducing magnetisation switching [42, 43], and to serve as a powerful experimental probe of spin wave behaviour [44]. Furthermore, the THz energy-range is comparable with the low-energy magnetic interactions that define magnetic ordering, providing a route to probe these directly.

Such prospects are important in the development of materials suitable for the next generation of electronics which aims to invoke magnetic interactions [45, 46]. The measurement of weak magnetic properties is typically challenging for other experimental techniques such as inelastic neutron scattering [47, 48], and even for computational methods such as density functional theory [49]. The optical excitation and control of magnetisation using THz radiation therefore promises new avenues for devices that couple optical, electrical

and magnetic functionality. This type of functionality lends itself to a new paradigm in information processing which is commonly referred to as *spintronics* [50].

Spintronics derives its name from a contraction of spin transport electronics [8]. The spin of an electron refers to its intrinsic magnetic moment. Spin is a quantum mechanical state and can either be up or down as in Figure 1.4 (a). Standard electronic-based information processing neglects the spin property, performing operations based only on the electron's charge. In analogy to the spin a cricket bowler can impart onto a bowled ball, the electron spin can increase the information density available in an electronic operation. For instance, as in Figure 1.4 (b), a bowled cricket ball incorporating spin can be either present or not but also break left or right. Thus, the information available has increased two fold.

As traditional electronics reaches the physical limitations of processing speeds in standard electronic materials, new frontiers in both material science and electrical engineering are being met with the development of spintronic based devices. The use of spin to perform operations not only has increased information density but also has the benefits of operating at faster switching speeds and requiring much less energy to manipulate [8, 9].

An understanding of the behaviour of the magnetic interactions in candidate materials is essential to the design of spintronic based devices. Spectroscopy at THz frequencies presents a promising method to characterise candidate materials for such applications. The work covered in this thesis demonstrates the use of THz spectroscopy in the study of novel metal oxide magnetic materials including a layered geometrically frustrated metamagnet ($Cu_3Bi(SeO_3)_2O_2Cl$), a canted antiferromagnet ($NdFeO_3$), and a low-dimensional spin ladder system ($Sr_{14}Cu_{24}O_{41}$).

1.2 Statement of research

1.2.1 Research aims

This thesis aims to develop the technique of THz spectroscopy as tool for characterising magnetic materials. Experimental results are presented on a range of materials including a non-magnetic semicondutor (ZnTe), a candidate multiferroic metamagnetic material
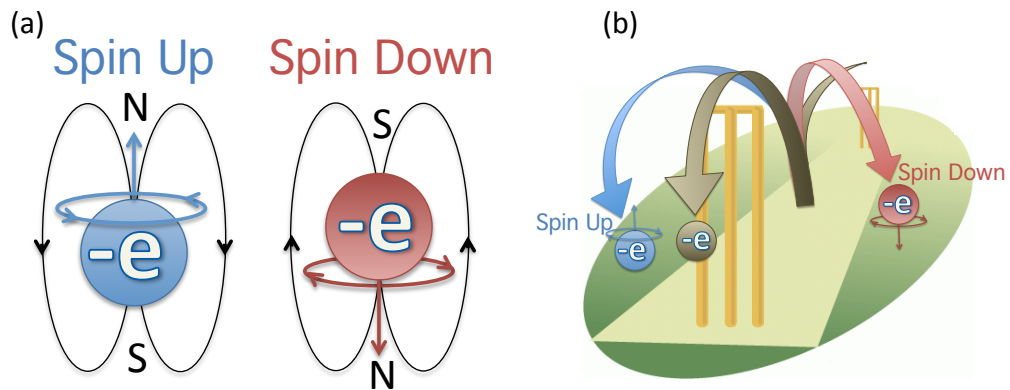
FIGURE 1.4: (a) Representation of electrons with charge $-e$ and spin states up ($\uparrow$) and down ($\downarrow$). Black curves represent the intrinsic magnetic dipole. (b) Analogy of electron spin polarisation to bowled cricket ball. A bowled ball with spin can break left or right depending on the orientation of spin.

$(Cu_3Bi(SeO_3)_2O_2Cl)$, a canted antiferromagnet $(NdFeO_3)$ and a low-dimensional spin-ladder system $(Sr_{14}Cu_{24}O_{41})$. Collectively the work addresses the following problems:

- What species of excitation exist and which component ($\mathbf{E}$ or $\mathbf{H}$) of the electromagnetic field do they couple to?

- What are the temperature and magnetic field dependent properties of the excitations?

- Can the presence of excitations and their properties be used to characterise underlying physical processes?

- Are these physical processes relevant to the emerging field of spintronics?

1.2.2 Original contributions of thesis

As a result of this study, the work presented in this thesis makes a number of original contributions to the fields of terahertz spectroscopy and condensed matter physics. The principal contributions include:

- The development of a statistical analysis method known as the *bootstrap method* for determining accurate uncertainties when fitting spectral data of semiconductor wafers (Chapter 5).

- The identification and characterisation of two weak THz frequency spin-wave modes in $Cu_3Bi(SeO_3)_2O_2Cl$ (Chapter 6).

  - The magnetic field dependence of the spin-wave frequencies indicates the two modes result from different copper sites.

- The identification and characterisation of two orthogonal THz frequency spin-waves in $NdFeO_3$ (Chapter 7).

  - Terahertz spectroscopy is used to probe the magnetic susceptibility in the xy plane and along the z magnetic axis revealing large magnetic anisotropy.

  - The temperature dependence of the spin-wave frequencies and polarisation reveals a spin-reorientation transition from 110–$170\,K$.

  - A fine splitting of the lower frequency spin-wave mode is observed over a small temperature span around $15\,K$.

- A complementary analysis of the spin-waves in $NdFeO_3$ by inelastic neutron scattering (Chapter 8).

  - A spin gap in the spin-wave dispersion is linked to the high-frequency spin-wave mode observed by THz spectroscopy.

  - An analysis of the spin-wave frequencies is used to extract the quantitative temperature dependence of the magnetic anisotropies.

  - A model of the spin reorientation resulting from competing anisotropic magnetic forces is proposed.

- The identification and temperature characterisation of a number of anisotropic absorption bands in $Sr_{14}Cu_{24}O_{41}$ across the 1–$3\,THz$ frequency range (Chapter 9).

1.2.3 Structure of thesis

Proceeding this introductory chapter, Chapter 2 provides a brief review of the literature surrounding THz science, magnetism, spintronics and recent developments in THz studies of magnetic excitations. More detailed reviews of the literature surrounding each material

examined is provided in each experimental chapter. Chapter 3 outlines the experimental instruments used throughout the thesis. Chapter 4 develops some of the background theory on elementary crystal and magnetic excitations. An overview on the theory of microscopic magnetic interactions is also given. More detailed theories are presented as they are required in each experimental chapter. Brief descriptions of the main analysis techniques used are also provided here. Chapter 5 begins the experimental analysis with a series of transmission measurements on ZnTe crystals of different thicknesses. The chapter is used to introduce transmission-geometry THz spectroscopy on a non-magnetic material. The results are used to determine the optical properties of ZnTe, an important semiconductor in THz science. Chapter 6 presents magnetic field-dependent THz spectroscopy on a candidate multiferroic material $Cu_3Bi(SeO_3)_2O_2Cl$. A number of magnetic excitations are identified and characterised. Chapter 7 and 8 are the centrepiece of the thesis. Chapter 7 presents THz spectroscopy on a canted antiferromagnet, $NdFeO_3$, identifying two orthogonal magnetic excitations and characterising a temperature dependent spin reorientation. Chapter 8 complements this work with inelastic neutron scattering measurements of the same material. The neutron scattering and THz results are combined to determine the temperature dependent anisotropy energies. The two chapters together, establish the strong complementary nature of THz spectroscopy and inelastic neutron scattering. Chapter 9 presents temperature dependent THz spectroscopy using synchrotron radiation on a novel low-dimensional magnetic system, the quantum spin ladder $Sr_{14}Cu_{24}O_{41}$. The results establish a diverse range of anisotropic excitations and strong temperature dependence of transmission. Chapter 10 concludes the thesis highlighting the major findings and proposes a future outlook for the research covered. Two appendices follow the conclusion. Appendix A presents source code for a unique statistical fitting analysis performed in Chapter 5. Appendix B presents the crystallographic information files used to generate the three-dimensional visualisations of the crystal lattices studied.

Chapter 2

Literature review

2.1 Overview

This chapter provides a brief review of the broad topics covered in this thesis. Section 2.2 outlines the development of THz science and technology with an overview of the many ways THz radiation is generated and detected. The spectroscopic applications of THz radiation are also covered. Section 2.3 then goes over some background on magnetism and the general types of magnetic materials encountered in the thesis. A brief introduction into multiferroics and spintronics, their development and applications is also provided here. Section 2.4 brings these two fields together with a look into recent and exciting developments in the study of magnetism and spin excitation using THz radiation. Further background and details on the specific materials studied in each chapter are given in the introductory sections of the experimental chapters.

2.2 Terahertz science and spectroscopy

As mentioned in Chapter 1, the THz frequency band has long been considered as a gap between electronics and optics. In the past, owing to a lack of efficient sources and detectors, the THz band has only been of interest to a limited number of scientists and engineers [7]. Often referred to as the far-infrared region, measurements in this energy

range employed weak thermal sources implementing interference and dispersion based spectroscopic techniques [51, 52]. In recent years, developments in ultrafast electronics have pushed microwave technologies into the THz domain [53]. At the other end of the gap, optical sources have been approaching lower and lower frequencies [54]. However, it was the developments of photoconductive switches [55, 56] and the femtosecond self-mode-locked Ti:sapphire laser [57] over the last four decades that has helped to advance the scope of research into THz radiation dramatically.

A new field of research known as THz optoelectronics with applications in information processing and telecommunications has developed as a result [7]. The early work of Grischkowsky *et al.* in developing THz optoelectronics for spectroscopic application, laid the ground work for modern applications of THz science [58–60]. As a result, the publication output in the field of THz science for has grown exponentially since 1975, with over 3000 publications in 2013 containing *terahertz* in the abstract, title or keyword field [61]. Naturally, in the early years much of this research was focused on THz generation and detection but as sources and detectors, as well as full spectroscopic systems, became more available, the applications for THz waves have become more prominent. Today a large amount of research is focused on practical applications such as high-speed communication [21], medical and biological studies [62], and security imaging [63]. Terahertz scientists are benefiting from increased funding opportunities and today the THz global market, valued at over \$50 million in 2013, is growing rapidly each year [22].

2.2.1 Terahertz sources and detectors

Essential to the study of THz radiation, particularly in spectroscopic applications, is its generation and detection. There are a number of techniques to generate THz radiation, ranging from the radiant heat of blackbodies [64], ultrafast transient currents in semi-conductors [7] and even relativistic radiation blasts from synchrotron accelerators [65]. A description and some background on the various types of THz sources and detectors encountered in this thesis follows.

2.2.1.1 Thermal sources

Thermal sources of THz radiation operate on the principle of blackbody radiation. A blackbody is a theoretical construct that absorbs all frequencies of electromagnetic radiation [66]. At a constant temperature a blackbody also emits a broadband spectrum of radiation defined only by the body's temperature according to Planck's law [66]. A small fraction of that radiation exists at THz frequencies. Our solar system's sun is a good example of a blackbody THz emitter and in fact the environment around us, heated by the sun, will also emit some radiation at THz frequencies. Real-world materials, however, deviate from perfect theoretical blackbody emission and only radiate a fraction of the ideal amount but the principle is the same. In the laboratory, typical thermal sources which operate at temperatures in the $1000\,\mathrm{K}$ range include mercury discharge lamps [67] and globars which are electrically heated rods of silicon carbide (SiC) [64]. These sources are generally used in conventional far-infrared spectrometers such as Fourier transform interferometers and diffraction grating dispersion spectrometers [51].

2.2.1.2 Pulsed laser sources

Perhaps the most common sources in a modern THz laboratory are those produced by femtosecond-pulse ($10^{-15}\,\mathrm{s}$) laser excitation. Pulsed laser sources fall into the realm of optoelectronics and are characterised by a short time scale broadband (typically from 0.2–3.0 THz) THz pulse. The **E** field of the THz pulse can also be detected coherently at precise time delays. The entire time dependent wave-form is then built up from a train of the THz pulses. These sources are therefore primarily used in THz time-domain spectroscopy (TDS) systems. Pulsed laser THz sources may be further defined by the mechanism of THz generation:

Photoconductive switches – Fist developed by the work of Auston [55] and Lee [56] in the late 1970s (also known as Auston switches) these are among the most common THz sources in pulsed systems. An antenna is fabricated on a semiconductor surface. The laser pulse (with photon energy above the semiconductor bandgap) excites electron-hole pairs. A bias across the antenna separates the electrons and holes forming a radiating dipole which couples to the antenna and into free space (see Figure 2.1 (a)). The semiconductor

material should have a short carrier lifetime, high mobility and high breakdown voltage so that the dipole can be created and decay within a picosecond (10^{-12} s), the period of a THz wave [7]. Typical semiconductors used include low-temperature grown (LTG) gallium arsenide (GaAs) [68], ion-implanted indium phosphide (InP) [69] and amorphous silicon (Si) [7]. Depending on the antenna design and laser pump power, THz power in the range of $\sim 10\,\mu$W are achievable with band widths of ~ 0.1–3 THz [7].

Surface depletion field transient currents – The surface of a material is characterised by a break in the symmetry of the lattice with unoccupied or 'dangling' atomic bonds. In semiconductors with a wide bandgap, Fermi-level pinning occurs leading to band bending and the formation of a depletion layer at the surface [70]. The depletion layer sets up an intrinsic electric field normal to the surface (see Figure 2.1 (b)). When the femtosecond laser pulse excites electron-hole pairs, the surface field accelerates them in opposite directions normal to the surface, forming a transient dipole that radiates at THz frequencies [71]. Powers up to $10\,\mu$W with band widths above 3 THz may be achieved [7].

The **photo-Dember effect** – Similar to the surface field effect, THz radiation from the photo-Dember effect occurs by transient currents. However, in this case the dipole originates from the different diffusion rates of the electrons and holes (see Figure 2.1 (c)). When the electron-hole pairs are generated, the higher mobility of the electrons allows them to diffuse deeper into the semiconductor than the holes. This creates the transient dipole necessary for THz generation. Recent measurements have shown that this effect can be enhanced in InAs by the application of magnetic fields [72, 73]. With the magnetic field oriented normal to the diffusion direction, the Lorentz force acts to further accelerate the electrons improving the dipole amplitude. Other methods for improving the photo-Dember effect are by shadowing a portion of the pump laser beam profile. The non-symmetrical beam profile acts to increase diffusion normal to the beam propagation direction in a mechanism known as the lateral photo-Dember effect [74]. Powers similar to that of the surface field effect are expected.

Optical rectification– Rather different to the previous mechanisms based on the second-order non-linear effects of transient currents, optical rectification is a second-order non-linear effect based on transient polarisability. When the strong electric field of a femtosecond laser-pulse interacts with the atomic electrons in a non-centrosymmetic (optically active) material such as ZnTe, GeSe or $LiNbO_3$ [75], the electrons bound to atoms oscillate. The oscillations occur both in a linear manner, at the same frequency as the laser photons, and non-linearly, at higher and lower orders of this fundamental frequency. This non-linear polarisability is the foundation of optical rectification and occurs both as a surface and bulk effect [61]. As the laser pulse passes through the optically active material (see Figure 2.1 (d)) the nonlinear polarisation replicates the optical pulse envelope. This time varying polarisation on the order of 1 picosecond is the source of THz radiation. Optical rectification is characterised by its high modulation when rotating laser polarisation relative to crystal orientation [76]. While THz power output is lower in comparison to photoconductive switches, emission by optical rectification is attractive for its higher bandwidth (up to $\sim$100 THz for GeSe [77]) simplicity of use and lack of saturation with high pump power [7, 61]. Recent developments in organic nonlinear optical materials have been attractive for this form of THz generation. The organic material 4-N,N-dimethylamino-4'-N'-methyl-stilbazolium tosylate, or simply DAST, possesses an extremely large nonlinear response with strong anisotropy that enables phase matching over a large frequency range. Using this material, THz generation by optical rectification has achieved ultra-broadband responses above 200 THz [78].

Air plasma generation – One of the more recently developed pulsed laser THz sources, air plasma THz generation offers some of the highest powers and broadest bandwidths available [79]. The effect was first demonstrated by Cook *et al.* in 2000 by mixing a laser's fundamental and second harmonic fields in air [80]. While it was originally suggested that the mechanism involved a four-wave difference frequency mixing parametric process in the ionised air plasma [80–82], a recent study has suggested a transient photocurrent model [79]. This model suggests that optical field ionisation and subsequent electron motion in a symmetry-broken laser field are the key mechanisms for producing a quasi-DC electron current and simultaneous THz pulse radiation (see Figure 2.1 (a)). THz emission with bandwidths up to 60 THz are routinely achieved [79].
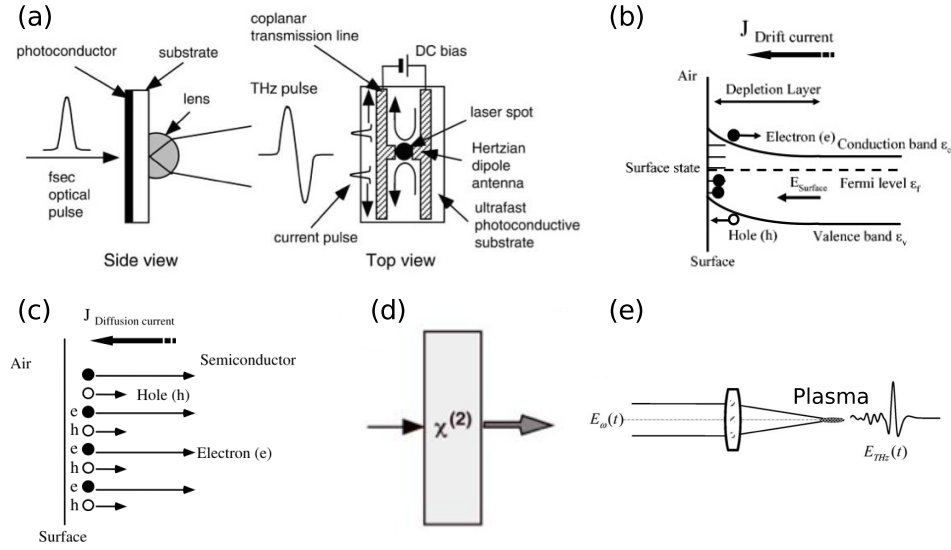
FIGURE 2.1: Mechanisms of pulsed laser THz sources. (a) Photoconductive switch. (b) Surface depletion field effect. (c) Photo-Dember effect. (d) Optical rectification. (e) Air plasma. (a)-(d) are adapted from Reference [7], (e) is from Reference [82].

Other less common sources of THz radiation by pulsed laser excitation include semiconductor quantum well structures [83], coherent phonon excitation [84], high-temperature superconducting bridges [85] and magnetic dipoles [86]. It should also be noted that a typical pulsed laser source based on a semiconductor material will often feature a combination of these mechanisms. The mechanisms evident in a particular emitter are routinely characterised by polarisation dependent measurement [61, 76] and external magnetic field application [61].

2.2.1.3 Continuous-wave laser pumped sources

Continuous-wave lasers, rather than pulsed lasers, can also be used to generate THz radiation by optoelectronic techniques. In a process known as photomixing, optical heterodyne or difference frequency mixing, THz radiation is produced when the laser fields of two continuous lasers (ν_1 and ν_2) are mixed and used to excite photocarriers in a semiconductor material [87]. The two lasers are typically tuned to have a frequency difference in the order of $1\,\text{THz}$ ($|\nu_1 - \nu_2| = \nu_3 \approx 1\,\text{THz}$). This introduces a beat modulation of the mixed field at THz frequencies that oscillates the excited electrons and holes in the semiconductor. The oscillating dipole then radiates as a quasi-monochromatic source equal to the difference

frequency of the two lasers (see Figure 2.2). Typically, the laser's fundamental frequencies are tunable over a relatively short range (∼0.5% of the laser's wavelength) but this can achieve frequency differences from 10 MHz to 1–2 THz [88]. The early work on photomixer technology was primarily done by Brown *et al.* in the early 1990's [89]. Initial experiments used Ti:Al$_2$O$_3$ lasers operating near 780 nm or distributed-Bragg-reflector lasers operating near 850 nm to pump LTG-GaAs photomixers [90].

The most important characteristic of the photomixer material is the electron-hole photo-carrier lifetime [89]. One of the more common photomixing emitters that has emerged in recent years is LTG GaAs, which has the advantage of a short photoconductive lifetime and a high electrical breakdown field [89, 91]. Most applications of this material as a photomixer involve the fabrication of LTG-GaAs wafers with interdigitated electrodes by electron-beam lithography [88–92]. The electrodes are connected to a broadband antenna array allowing a useful output frequency range. The type of antenna design used greatly affects the power output and tunable frequency range and is therefore an area of constant development [93–95]. Early antenna designs involve three-turn self-complementary spirals [89, 92, 93, 96] and bow-tie arrangements [91]. A more recent antenna design proving to be quite effective is the logarithmic-periodic design which reduces the influence of the finite antenna dimensions on the antenna impedance and radiation pattern by shorting out the currents beyond the resonant tooth. This gives a linearly polarised single-lobed emission pattern which is more desirable than the double-lobed pattern of the bow-tie design [91].

While GaAs is the most common material used for photomixing it is by no means the only one. It has been shown that LTG GaAsSb can have an increase in power output of about 2.5 when compared to normal LTG GaAs [91]. However, the maximum allowable bias across the photomixer is 8 volts as compared to 20 volts for LTG GaAs, making it much more delicate which is an undesirable property when considering commercial applications. Other competing photomixers include indium antimonide (InSb) [97] and organic crystalline salts which posses very high non-linear susceptibilities and electro-optic coefficients, making them one of the best non-linear materials for THz generation and detection to date [98]. Optical fibre coupling to the semiconductor substrate greatly improves the efficiency of the device's operation. This also allows for safer operation as the chance of scattered laser light is reduced as well as convenient placing of the photomixer
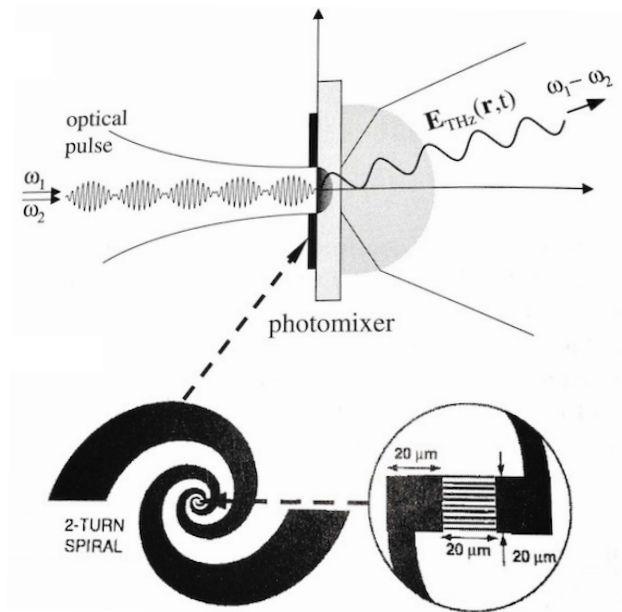
FIGURE 2.2: Mechanism of continuous wave THz generation by a photomixer source
(adapted from Reference [6]).

to interface with instruments that might be situated some distance from the pump laser
setup, if a considerably long fibre is used [99]. Further improvements have also been made
by implementing telecommunication wavelengths as the pump laser source [100].

2.2.1.4 Free electron sources

Free electron sources are so named because unlike the previously discussed sources, where
the electrons are confined in a medium such as a semiconductor, in these sources the
electrons are freely moving in a vacuum. Essentially, they work on the principle that
an electron moving in a vacuum, undergoing an acceleration, will radiate electromagnetic
radiation. The acceleration can be tuned using electric and magnetic fields so that the ra-
diation frequency falls in the THz domain. Such sources include klystrons [101], gyrotrons
[102] and backward wave oscillators [103]. These free electron sources constitute 'bench
top' style instruments that contained within a normal laboratory environment. A detailed
review on the operation and applications of these systems can be found in Reference [104].

Another class of free electron sources are known as accelerator based sources. These sources are contained in large facilities where beam time must be requested via proposal and review based processes. The two main accelerator type sources are:

Free electron lasers – which operate by accelerating high speed electron packets through a periodic magnetic structure (see Figure 2.3 (a)). They are the highest powered THz sources available [105]. An average power of up to 500 W is achievable [105].

Synchrotrons – while not as powerful as the free electron laser, are more widely accessible around the world. They operate by containing relativistic electrons in a large (order of 100 m circumference) storage ring [106]. The electrons are first accelerated to close to the speed of light by large electric fields in a linear accelerator. The electrons then pass into a booster ring that increases the electron speed further using synchronously ramped magnetic and electric fields. The electrons are then injected into the large storage ring where they travel around at close to the speed of light, stabilised by precise magnetic fields [106]. As the electrons approach certain sections of the ring where strong dipolar bending magnets are placed, they experience a large acceleration force as their direction is change to continue around the ring (see Figure 2.3 (b)). This acceleration emits electromagnetic radiation [5]. Because the electrons are relativistic, all the frequencies of the radiation build up into a broad spectrum blast, similar to the sound waves of a sonic boom when a jet plane breaks the sound barrier. The synchrotron electromagnetic pulse produces frequencies from the THz domain up to x-rays [107]. Recent developments in the operation of synchrotron facilities has allowed for improved power in the THz region. In normal operation the electrons are bunched into long stretched out packets. To improve THz output the packets are compressed so that the radiation emitted becomes coherent [65]. This process is known as coherent synchrotron radiation (CSR) and may provide powers at THz frequencies of up to 20 W [108].

2.2.1.5 Other terahertz sources

The above review of THz sources covers the main types of sources encountered in a standard THz laboratory or facility. The broad classes of pulsed laser, continuous wave and accelerator based sources are implemented in this thesis and this is why attention has
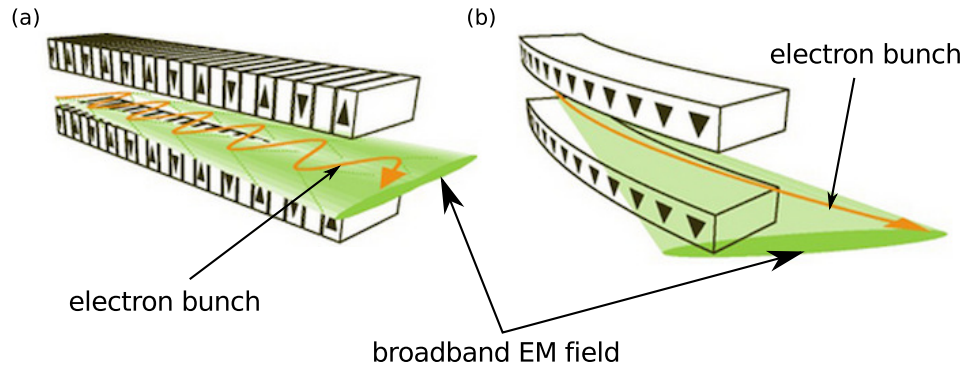
FIGURE 2.3: Emission of electromagnetic radiation from accelerator based sources. (a) Free electron lasers modulate electron bunches by a periodic magnetic structure. (b) Synchrotrons produce broad-spectrum radiation blasts by bending relativistic electrons through a curved path. Images adapted from Reference [107].

been given to them. However, there are many other sources of THz radiation including quantum cascade lasers [54], pumped molecular-resonance gas lasers [109], Gunn diodes [110], Josephen junctions in superconductors [111] and even from peeling adhesive tape [112]. A review of the many sources of THz radiation can be found in References [101] and [61].

2.2.1.6 Terahertz detectors

To utilise THz radiation, not only is it important to have good sources but also detectors that can measure it. The detection of THz radiation experiences the same technical difficulties as THz generation. Essentially, the response of standard electronic based detectors are too slow and the energy of THz waves too small to excite charge carries in semiconductor based optical detectors. As a result, a considerable amount of research has also gone into the development of detectors and a wide range of technologies exist [113]. Broadly speaking THz detectors can be grouped into two categories, *incoherent* and *coherent* techniques.

Incoherent detectors measure only the intensity of the THz radiation and constitute the earliest forms of THz detection [114]. Typically, incoherent detectors are thermal sensors such as bolometers, Golay cells and pyroelectric devices [6] but microwave detection techniques have also improved and solid state Schottky diode detectors are also available

[115]. In general, thermal detectors feature a radiation absorber coupled to a heat sink, the subtle change in temperature when THz radiation is incident on the absorber is detected.

In bolometers, the absorber is a heavily doped semiconductor crystal such as silicon. The change in temperature is measured as a change in the resistance across the semiconductor. Operating at cryogenic temperatures, bolometers are very sensitive. Pyroelectric detectors operate with a pyroelectric material as the absorber. The change in temperature gives rise to a spontaneous electric polarisation which produces a detectable current. Pyroelectric detectors are convenient as they can be operated at room temperature. The Golay cell transfers the heat of the absorber to a small volume of gas. The gas experiences a change in volume as it heats up. This mechanical change is measured by optical reflection using a laser. Each of these detectors operates over a broad spectral range and can be rather sensitive. However, because the absorber must reach thermal equilibrium for the measurement, detection response is slow compared to conventional photonic detectors [6].

Coherent detectors are characterised by their ability to measure both the amplitude and phase of the incident THz radiation. Coherent detection techniques work on similar mechanisms as optoelectronic THz sources. They are therefore often only implemented in those systems since they must use the same optical pump source that operates the THz source but in an opposite fashion. For pulsed optoelectronic techniques, coherent detection operates by either electrooptical sampling [116] or photoconductive switches [117] as seen in Figures 2.4 (a) and (b) respectively.

Electrooptical sampling works by measuring the THz electrical field in the time domain through the Pockels effect related to optical rectification [6]. Essentially, the THz field induces birefringence in a non-linear optical crystal such as ZnTe. The degree of birefringence is proportional to the THz field amplitude and this is measured by analysing the polarisation difference of an optical pulse (split from the initial pumping pulse) as it passes through the non-linear crystal. This is achieved by splitting the two polarisation components using a Wollaston polariser and two photodiodes set up for differential measurement. By sampling at different relative time delays to the THz pulse, the **E** field in the time domain is determined (lower inset of Figure 2.4 (b)). A Fourier transform of the detected **E** field gives a broadband spectrum (upper inset of Figure 2.4 (b)). Limitations

of this technique involve the dispersive properties of the non-linear crystal and its thickness [7]. A thicker crystal gives a larger birefringence effect improving on the noise limit of detection. However, because there is always some dispersion of the THz field through the crystal, a longer optical path will reduce the bandwidth of the detected signal. Thin crystals of ZnTe or GeSe are considered to be the best materials for this detection method with bandwidths in excess of 100 THz observed [77].

Detection by photocondutive switches uses a similar setup, however the mechanism is different (Figure 2.4 (b)). In this case, the incident THz field induces a weak photocurrent in the photoconductive switch when photocarriers are excited by the optical pulse. Modulating the relative delay time between the optical pulse and THz wave maps out the time dependent **E** field [117]. The ability to bias photoconductive switches allows for a higher gain in signal detection. However, the photoconductive switch typically has a low detection bandwidth when compared to electrooptical sampling [7].

Coherent detection may also be implemented in continuous wave techniques. Using the optoelectronic photomixer source described in Section 2.2.1.3, the THz wave can be coherently detected by means of reverse operation [118]. The optical beam that is used to pump the source is split and directed onto the detector mixer. The photocarriers excited by the optical beam are modulated by the incoming THz radiation and a photocurrent is detected across the antenna. The phase of the THz wave relative to the beat frequency of the optical pump is detected by the direction of the current. Limitations for this detection technique are that the optical path of the laser pumping the detector mixer must be modulated relative to the source mixer to account for the phase difference. This has been addressed by a number of methods including modulating the THz beam path [119], and using fibre stretchers on the optical lines [120].

One of the more promising developments in continuous-wave coherent detection at THz frequencies is the prospects of 'lab on a chip' devices [121]. The ease of fibre coupling with photomixer devices and the identical design of transmitter and receiver allows for both the source and detector to be integrated onto the same chip. Such a design could lead to much better signal for measurements of small samples particularly for biological materials that could be deposited directly on the chip. Furthermore, the development of
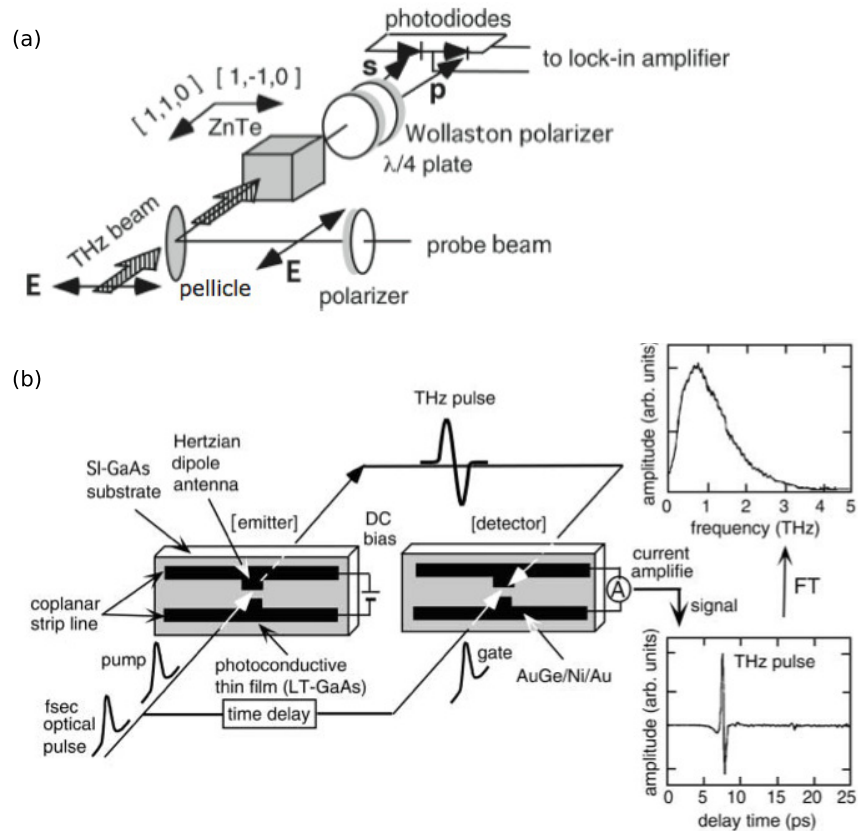
FIGURE 2.4: Pulsed wave THz detection techniques. (a) Electrooptical sampling with non-linear crystal. (b) Electric field sampling by photoconductive switch. The sampled time dependent **E** field and subsequent Fourier transformed spectrum is shown in the inset of (b). Both figures are adapted from Reference [7].

photomixers that can operate with telecommunication wavelength pump lasers, can exploit the established availability of powerful and stable laser sources [122].

2.2.2 Terahertz spectroscopy

Spectroscopy at THz frequencies is not a particularly new area of research, although it has increased substantially in recent years due to the work on sources and detectors described above. Even in the early days of THz or far-infrared spectroscopy, experiments covering a wide range of phenomena such as molecular and phonon excitations, dielectric characterisation and free carrier dynamics in semiconductors were achieved [51]. Such measurements were primarily performed using interferometer or diffraction grating techniques employing thermal sources. The development of optoelectronic sources has considerably improved

the signals available at these frequencies and increased the set of tools available to the THz scientist in general. There are now many more THz spectroscopic techniques. A detailed discussion on the spectroscopic systems of two-colour photomixing, TDS and Fourier transform interferometry is left for the chapter on experimental methods (Chapter 3). A brief discussion on two dominant fields of THz spectroscopy follows.

2.2.2.1 Atomic and molecular spectroscopy

Molecular spectroscopy at THz frequencies has been a fruitful area of study both in the past and presently. High resolution spectroscopy on vibrational and rotational modes have allowed the study of the microscopic mechanisms of molecular collisions [123–125]. Understanding the types of normal modes in this region has been important for studying the composition of distant galaxies and nebulae [126]. The Herschel space observatory, for example, is equipped with many state of the art THz based detectors for studying the early stages of galaxy and star system formation [6]. Back on earth, molecular spectroscopy of cigarette smoke in the THz region has shown potential as a method of remote sensing for atmospheric toxins [127, 128].

The vibrational motion in biological molecules is also often characterised on the picosecond time scale and is therefore sensitive to THz radiation [6]. The stretching, bending and torsional vibrations in large biological molecules are of interest to biological scientists as they can help them understand the mechanics of biological processes [62]. Hydrogen bonds, characterised by attractive intermolecular interactions between two electronegative atoms through a hydrogen atom, are common amongst many biological molecules. The collective nature of intermolecular hydrogen-bond vibrations is evident in the THz response of crystalline nucleotides (adenine, cytosine, guanine and thymine), the bases that make up the DNA polymer molecule [129].

Proteins, the very large macromolecules that perform a vast array of essential functions within living organisms present difficulty in their chemical study due to their shear complexity. Protein structural dynamics such as flexibility, which affects enzymatic reaction rates and sensory transduction cycling times, have been studied using THz time-domain spectroscopy [130]. Underdamped delocalised modes at THz frequencies in proteins have
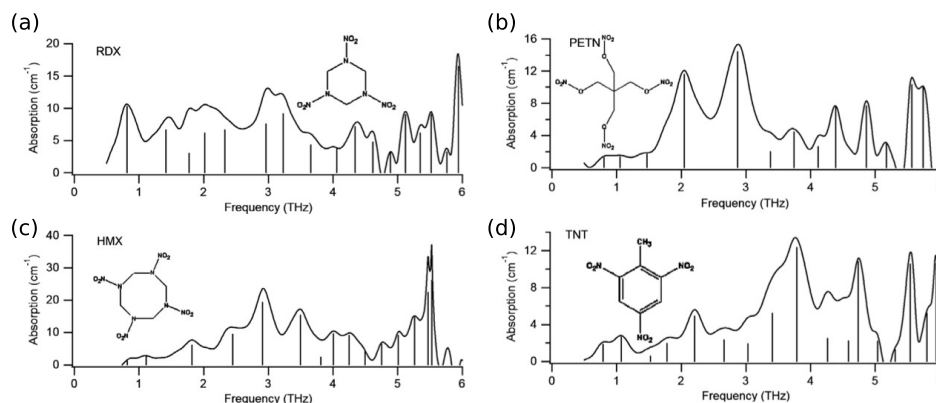
FIGURE 2.5: Representative THz spectral signatures of common explosive materials adapted from Reference [131]. The spectral absorption lines are characteristic of the intra and intermolecular vibrational modes of each material.

also revealed information on the efficiency of ligand binding and protein–molecule interactions [39].

Related to the spectroscopy of organic molecules is the detection of concealed drugs and explosive materials for application in security checks. Common energetic explosives such as RDX, HMX, TNT and PETN are characterised by their unique spectral signatures in the THz region [131]. Examples of these distinct features are shown in Figure 2.5.

2.2.2.2 Condensed matter spectroscopy

Condensed matter spectroscopy is the study of solids using electromagnetic radiation. Solids consist of large collections of atoms ($N \sim 10^{22}\,\mathrm{at/cm^3}$) and may feature a single (elemental or monatomic), two (binary or diatomic), three (ternary or triatomic) or more (polyatomic) types of atoms. They may form into regular crystal lattices or amorphous structures. Since solids are important as structural (metals, ceramics, polymers) and functional (semiconductors, magnets, pyro and piezoelectrics) materials, the spectroscopy of solids as a method for better understanding their properties is an important fundamental science [4].

In the condensed phase, interactions of THz radiation with matter are diverse. Spectral phenomena include lattice vibrations in crystals, intraband transitions in semiconductors,

electron spin and collective modes in strongly correlated electron systems [6, 7]. Transmission measurements on single crystals such as semiconductors have allowed the determination of optical parameters such as, low and high frequency dielectric constants and carrier concentration [132]. The optical parameters of solids are important in contrast imaging. Such techniques were famously applied to the imaging of defects in insulating ceramic foams used for the NASA space shuttle program as a response to the Columbia shuttle disaster of 2003 [133].

In traditional semiconductors, the bandgap energy is in the range of 1–10 eV ($\sim$200–2000 THz). Terahertz excitations ($\sim$1–10 meV) in semiconductors therefore involve transitions *within* an energy band. The study of such intraband carrier dynamics are of great interest not only because of the fascinating fundamental physical processes associated with many body interactions and Coulomb correlations, but also because they have broad applications in ultra-highspeed optoelectronic devices beyond the signal switching rates of 100 GB/s [6]. One of the more interesting developments in recent condensed matter THz research is time resolved spectroscopy [134]. Time resolved THz spectroscopy involves the observation of the THz response of a material at discrete time intervals during and after it has been excited by an optical pulse. This technique is therefore ideally suited for TDS methods and the study of semiconductor charge carrier dynamics. Using this technique the transient photo-currents in GaAs were characterised [135]. The results revealed the influence of phonon dynamics on intraband free-carrier absorption, an important finding for further GaAs based technologies. The carrier dynamics of intraband electron transitions in the Nobel prize winning material graphene [136] as well as physically related topological insulators [137], have also been investigated by THz spectroscopy.

Finally, the exchange and dipolar interactions between spins in magnetic materials is also equivalent to the energies of THz waves [138]. Terahertz radiation is therefore particularly suited for spectroscopic studies of magnetic materials and spintronic applications [40]. A more detailed discussion of this research area follows.

2.3   Magnetism and magnetic materials

Just as the philosophers of classical antiquity observed the spectral properties of light, so did they observe the magnetic effects of the *lodestone*. The lodestone is a naturally occurring magnetic material now know as magnetite (Fe_3O_4) that would attract iron when brought near it [139]. In fact the word magnet, which has its basis in Greek, is thought to arise from lodestones found around Magnesia, Anatolia [140]. As with the understanding of the nature of light, magnetic theory was slowly developed through history. Notable developments came from Gilbert (1540–1603) who pioneered the idea of a magnetic field and established that the earth too was a giant magnet [141] and Oersted (1777–1851) who observed that flowing electrical current produced a magnetic field [140]. Later, Ampère established the time dependent nature of the current induced magnetic fields and observed that loops of current would produce a constant magnetic dipole [140]. Finally, the work of Faraday and Maxwell would tie the two phenomena of electricity and magnetism together, indicating that magnetism was a result of moving electric charge [14]. With the discovery of the electron in 1896 [24] and development of quantum mechanics at the beginning of the 20th century [28], the foundations for an atomic theory of magnetism in solids was formed.

Today we understand the properties of magnetic materials to arise from the net effects of atomic magnetic moments. These moments are largely a property of the atom's orbiting electrons but a small contribution from the nucleus also occurs. In the classical model of the atom, where the electron orbits around the nucleus, the circular path of the electron acts as a current loop and, as established by Ampère, produces a magnetic dipole. This magnetic moment is dependent on the angular momentum of the electron and is therefore termed the orbital moment [28]. A remarkable discovery of quantum mechanics was that a free electron at rest has an intrinsic magnetic moment. A classical interpretation of this is that if the electron was a charged spinning sphere it would produce the magnetic dipole as observed. Thus, this intrinsic magnetic property of the electron was called its spin (although, in the reality of quantum mechanics, the electron is not a charged sphere and does not physically spin). In a brilliant unification of quantum theory and relativity, Dirac established that spin was an automatic property of the relativistic nature of electrons

[142]. As it turns out, many other fundamental particles such as the proton and neutron also possess spin. However, it is the magnetic properties of the electrons and their orbits that are the dominating sources of magnetism in magnetic materials. The numerous ways these magnetic moments interact with external magnetic fields and their alignment with each other gives rise the different classes of magnetic materials. A graphical depiction of the different magnetic classes, also known as magnetic ordering, is shown in Figure 2.6. A brief description follows.

Para- and diamagnetic – In a paramagnetic material the magnetic moments are randomly oriented. In equilibrium they will therefore average out and feature no spontaneous magnetisation (Figure 2.6 (a)). The application of an external magnetic field will act to align the moments producing a net magnetic moment. A diamagnetic material is similar, however, the magnetic moments will anti-align with the external magnetic field [29]. These effects were first explored in detail by Faraday [140]. Examples of paramagnets include many metals such as aluminium and tungsten. Diamagnetism is evident to some extent in all materials, notable cases include glass and some metals such as bismuth.

Ferromagnetic – In a ferromagnetic material the magnetic moments are mutually aligned. The material therefore features a strong spontaneous magnetisation (Figure 2.6)(b)). The application of an external field parallel to that alignment will generally increase the magnetic moment slightly to a saturation point where all the moments are effectively aligned [29]. Ferromagnetism had been known since ancient times but it took the development of quantum mechanics and the work of Dirac and Heisenberg to develop a microscopic theory [142, 143]. Notable examples include transition metals such as Co and Fe with the term ferromagnetism coming from the Latin *ferrum* meaning iron.

Antiferromagnetic – An antiferromagnetic material is much like a ferromagnet only with two ferromagnetic sublattices that align in opposite directions [29]. Although this form of alignment features strong internal fields, the opposing moments cancel each other out and no spontaneous magnetisation occurs (Figure 2.6 (c)). The application of an external magnetic field can induce canting that produces a weak magnetic moment. At very high magnetic fields one of the sublattices may flip producing a ferromagnetic state. The

early work on understanding this class of material was undertaken by Néel [144]. Examples include transition-metal oxide ceramics such as NiO. In some cases natural internal interaction will induce a canted antiferromagnetic order. These systems feature weak ferromagnetic moments. Examples include hematite (Fe_2O_3) and rare earth orthoferrites such as $NdFeO_3$ and $ErFeO_3$.

Ferrimagnetic – A ferrimagnetic material is very similar to an antiferromagnetic material. Two magnetic sublattices are aligned in opposite directions. However, in the case of the ferrimagnet, one of the sublattices has a weaker magnetic moment and a spontaneous magnetisation still occurs as in a ferromagnet (Figure 2.6)(d)). The discovery of this class of material was also a result of Néel's work on magnetic ordering [144]. A famous example of such a material is the lodestone (or magnetite) mentioned at the beginning of this section. While originally classed as a ferromagnet, following the work of Néel, it was discovered to be ferrimagnetic.

Naturally, the interactions of the atomic magnetic moments are governed by the thermodynamics of the material. These properties are therefore highly temperature dependent. In general a material that is ferromagnetic at low temperatures will become paramagnetic at high temperatures as the thermal energy overcomes the energy associated with the magnetic ordering [139]. These temperatures are known as magnetic transition temperatures. The transition temperature between paramagnetic and ferromagnetic states is called the Curie temperature (T_c) and the transition between paramagnetic and antiferromagnetic states is called the Néel temperature (T_N), named after the scientists who first characterised them [29]. The study of the temperature dependent magnetic properties is therefore a very useful way of understanding the inner microscopic magnetic forces at play.

The microscopic mechanism responsible for ferromagnetic ordering was developed simultaneously by Dirac [142] and Heisenberg [143] in 1926. Essentially, the quantum mechanical properties of spin and the Pauli exclusion principle (that no two electrons (fermions) can occupy the same state) act together through an exchange interaction when the wavefunctions of magnetic ions overlap as in Figure 2.7 (a). The exchange interaction simulates an effective internal magnetic field (also called the molecular or Weiss field) that aligns the
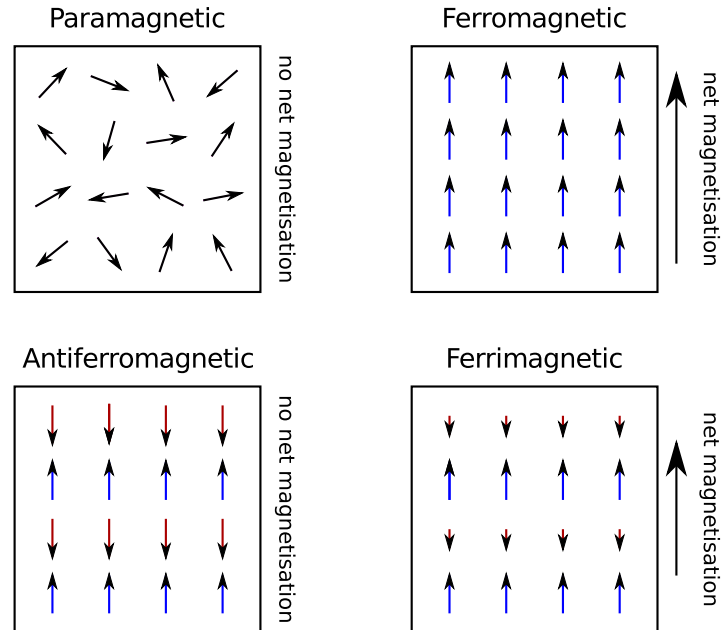
FIGURE 2.6: Types of magnetic ordering in typical magnetic materials. Arrows represent direction of atomic magnetic moments.

microscopic magnetic moments. It is important to understand that the exchange interaction is not actually a magnetic field (it is not present in Maxwell's equations) but rather a quantum mechanical condition. However, it is convenient to consider it as a magnetic field with an equivalent force orders of magnitude larger than the effective dipolar interactions of the neighbouring magnetic moments. A more detailed discussion on this topic is covered in the chapter on theory (Chapter 4).

After the theory of magnetic exchange was established, in the 1930's, Néel postulated that a new type of magnetic order could exist [145]. If the exchange interaction between neighbouring spins was negative, this would lead to antiparralel alignment, essentially forming two magnetic sublattices in opposite directions. Such ordering refers to antiferromagnetism. In 1947, Néel further predicted the occurrence of ferrimagnetism [144]. Since no spontaneous magnetisation exists in an antiferromagnetic material, and a ferrimagnet may behave macroscopically similar to a ferromagnet, it took years before Néel's theories could be proven. In fact, it would take the pioneering work on neutron diffraction by Schull to verify their existence and refine the theory. The work of both Néel and Schull was later celebrated with the awarding of the 1970 and 1994 Nobel prizes in physics respectively [146, 147].
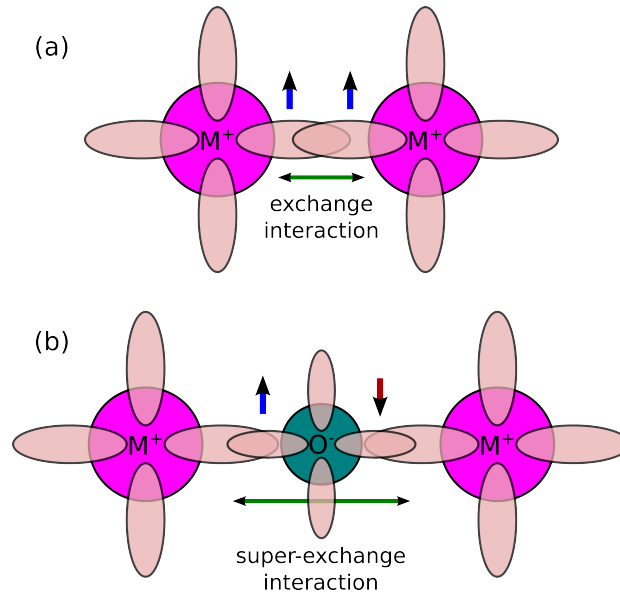
FIGURE 2.7: Overlapping wave functions of nearest-neighbour magnetic ions (M^+) couple spins via the exchange interaction. (a) Shows ferromagnetic coupling by this mechanism. In metal oxides the spins of magnetic ions may couple by a super-exchange across the overlapping bonds with an intermediate oxygen ion (O^-) . (b) Shows antiferromagnetic coupling by this mechanism.

2.3.1 Transition-metal oxides

Transition-metal oxides are materials made up of compounds between metals in the 'd-block' of the periodic table (elements with partially filled d-shells) and oxygen [148]. Notable examples include simple compounds such as NiO, CoO and Fe_2O_3 to more complex systems such as $Sr_{14}Cu_{24}O_{41}$ and $YBa_2Cu_3O_{7-x}$. Due to the unique nature of the outer d electrons, the metal-oxygen bonding can vary anywhere from ionic to metallic, producing a wide variety of structures, properties and phenomena [149]. These can include electrical properties such as conduction, insulation, charge order and ferroelectricity, as well as magnetic properties like ferromagnetism and antiferromagnetism and even more exotic states such as multiferroicity and superconductivity [149].

The magnetic ordering in these materials is particularly intriguing because of the relatively large distance between the magnetic ions. For instance, there is almost no cation orbital overlap for the standard exchange interaction to take effect through. In 1934, Kramers proposed an exchange model between two magnetic ions that acted through the bonds of an intermediate non-magnetic ion [150]. Following new data made available by the

neutron diffraction work of Schull, this theory was later refined in 1950 by Anderson [151]. Referred to as a super-exchange, the oxygen anion acts as a bridge between the two magnetic cations as seen in Figure 2.7 (b). The donated electrons from each cation couple to the spins in the anion and experience an exchange interaction with their next-nearest–neighbour cation. The interaction is empirically explained by the Goodenough-Kanamori rules and predominately favours antiferromagnetism [152–154]. The magnetic coupling by super-exchange can be quite strong resulting rather high magnetic transition temperatures ($T_N = 523\,\mathrm{K}$ for NiO) [149].

This, along with their robust ceramic properties [149], correlated electronic states [46], strong magnetocrystalline anisotropy [155] and intrinsic semiconducting behaviour [156] make transition-metal oxides well suited for technological applications in spintronic and multiferroic based devices. However, its is only recently that research has began to focus seriously on the prospect of using transition-metal oxides for such applications [46, 149]. The study of the intriguing properties of the transition-metal oxides is still a novel enterprise. In particular, the insulating and magnetic properties make them particularly suited for THz spectroscopic studies [40]. Transition-metal oxides are thus encountered predominantly in this thesis.

2.3.2 Multiferroics

Multiferroics refers to a class of materials that simultaneously feature at least two primary ferroic properties, such as ferroelectricity, ferromagnetism, ferrotoroidicity or ferroelasticity in one single homogeneous phase [157]. Of particular interest are those materials which exhibit both ferroelectricity and ferromagnetism (or antiferromagnetism). Ferroelectricity is the spontaneous electric polarisation in a material and is named in analogy to ferromagnetism i.e. the existence of a permanent magnetic moment [29]. These materials are of interest because they promise control of electric properties by magnetic fields and the control of magnetic properties by electric fields [157]. Such magnetoelectric (ME) coupling has strong implications in device applications [46].

However, the occurrence of materials that exhibit these simultaneous states are rare because typical ferroelectricity results from an off-centring of the cations, best achieved in

ions with empty d-shells [158]. The orbits of d-shell electrons are essential for the exchange interactions described above, therefore standard ferroelectricity contradicts the formation of magnetic order. Recent developments in fabrication techniques has facilitated the discovery of new transition-metal oxides such as rare earth manganites ($RMnO_3$, RMn_2O_5, etc. where R is a rare earth ion), that feature strong spin frustration due to competing exchange interactions [159, 160]. The spin frustration leads to complex non-collinear spin order, which can break inversion symmetry inducing ferroelectricity [157].

Even though the phenomenological aspects of multiferroic materials can be explained, the precise microscopic mechanisms of the ME effects are only now beginning to be understood [161]. Fundamental to understanding such interactions is the study of associated elementary excitations which can be investigated using spectroscopic methods [162]. In 2006, Pimenov *et al.* identified the electromagnon, the elementary excitation of the ME interaction, in multiferroic $GdMnO_3$ and $TbMnO_3$ [163]. Distinct from traditional magnetic resonance, the electromagnon is characterised by a spin resonance that is excited by the **E** field of an electromagnetic wave at THz frequencies [162, 163]. Following the discovery by Pimenov *et al.*, electromagnons have been confirmed in other multiferroic materials by spectroscopic [164] and inelastic neutron scattering [165] techniques. Further study of the electromagnon is expected to give insights on the dynamics of the ME interaction and improve prospects for technological applications [162].

Currently, the technological applications of multiferroics are limited by the low transition temperatures of the multiferroic phase in many candidate materials [46]. One material that has recently attracted attention is the multiferroic transition-metal oxide, bismuth iron oxide ($BiFeO_3$). Found to be ferroelectric up to $1100 \, K$ with antiferromagnetic order just above room temperature [166], $BiFeO_3$ is quickly becoming the material of choice for potential multiferroic device applications [46].

2.3.3 Spintronics and magnonics

The term 'spintronics', has appeared a number of times so far. Briefly described in the introduction as a new paradigm in information processing, spintronics refers to electronics based devices and applications that exploit the electron's magnetic spin properties as well
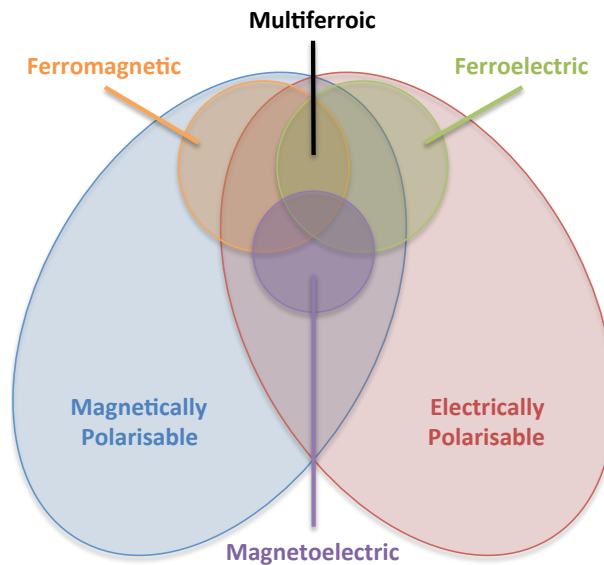
FIGURE 2.8: Venn diagram of different material classes showing multiferroicity as a state simultaneously featuring multiple ferroic orders.

as its charge. As the material limitations of traditional electronics are pushed further and further and demand for increased computational power and data storage grows, there is a need for new technologies that overcome these limitations. Because of the strong coupling effects through the exchange interaction, spin based technologies offer appealing prospects such as nonvolatility, increased data processing speed, decreased electric power consumption, and increased information densities compared with conventional semiconductor devices [8, 9]. The general focus of spintronic research is the generation, control, manipulation and detection of spin currents (J_s, a flow of spin polarised information) in solid state materials using both magnetic and electric fields [9]. It is therefore also inherently linked to the study of multiferroics [46]. Strictly speaking, there is a distinction between spin-current technology based on time dependent spin precession or spin waves (magnonics) [167] and that based on spin-dependent electron transport phenomena (spintronics) [8].

The field of magnonics is primarily concerned with the wave propagation of magnetism in magnetic materials (spin waves or magnons). This is aimed at better understanding the behaviour of the magnetisation on very small (sub-micrometre) length scales and very fast (sub-nanosecond) timescales, prerequisites for developing powerful 'magnonic logic' technologies. Spin-wave quantisation, localisation and interference effects have all recently been

observed [168–170]. These recent discoveries present the possibility of tailoring 'magnonic' bandgaps in candidate materials analogous to semiconductor charge bandgaps which could usher in magnonic-semiconductor integration [167, 171].

The field of spintronics involves active control and manipulation of spin degrees of freedom in solid state systems, including carrier spin polarisation, spin dynamics, and spin-polarised transport [9]. The origins of modern spintronics lie in the discovery of spin-polarised electron injection from a ferromagnetic metal to a normal metal by Johnson and Silsbee in 1985 [172]. This was followed by the discovery of giant magnetoresistance, the phenomenon responsible for large capacity data storage in modern hard disc drives, by Fert *et al.* [173] and Grünberg *et al.* [174] in 1988. The pair were subsequently awarded the 2007 Nobel prize in physics for this achievement [175]. Recent mappings of persistent spin helices in synchronised electrons show promise of usable spin-dynamics for logic operations [176]. Devices such as spin filters, spin diodes and spin transistors are currently under investigation [9].

The increased and perhaps over usage of the term spintronics has lead to its definition to encompass any form of spin manipulation in multiferroic materials [9, 177]. For this reason the term spintronics is often used to describe both spintronic and magnonic properties, a trend that is also used throughout this thesis. A graphical depiction of the different types of spin current that is prevalent in magnonic and spintronic research is shown in Figure 2.9.

2.4 Terahertz spectroscopy of magnetic materials

Separately, the fields of THz science and magnetism have shown enormous potential both in fundamental research and for technological applications. Together, they present new opportunities to improve fundamental understanding of microscopic magnetic interactions at picosecond time scales, leading towards THz frequency spintronic operational devices. The first experimentation between light and magnetism was performed by Faraday, discovering the effect that bears his name (the Faraday effect or Faraday rotation) in 1845 [178]. Faraday rotation, a magneto-optical phenomenon where the polarisation of light

(a) Spin transport spin current

(b) Spin wave spin current
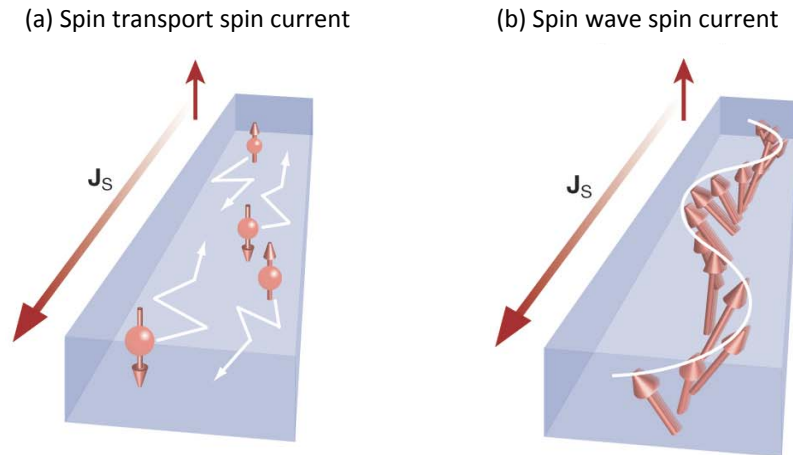
FIGURE 2.9: Distinction between two types of spin current (J_s). (a) Spin transport spin currents are defined by a spin polarised electron current. It is typical of spintronic applications. (b) Spin wave spin currents are defined by a propagating spin precession. It is typical of magnonic applications. Image from Reference [177].

passing through a magnetised material will experience a rotation, is an extensively used phenomenon in the modern age. Applications include fundamental research on magnetism [179] and in optical isolators that are essential to modern optical fibre-based telecommunications [180].

The principles of the magneto-optical phenomenon lie in the fact that the magnetic component of electromagnetic radiation couples to the magnetic moments in a magnetised material. Faraday rotation is a result of different electromagnetic propagation speeds for right and left hand circularly polarised components of the wave due to this magnetic interaction. At lower frequencies on the electromagnetic spectrum, resonance conditions of the magnetic moments can be achieved. A notable example includes nuclear magnetic resonance (NMR) and subsequent magnetic resonance imaging (MRI) techniques that occur at radio frequencies (MHz) [29]. The development of this method for recording the magnetic properties of atomic nuclei won Rabi the 1944 Nobel prize in physics [181].

Moving into higher frequencies, the 1950s brought on microwave magneto-optics of semiconductors [182]. The measurement of microwave cyclotron resonance in semiconductors (electrons moving under influence of the Lorentz force) became a standard technique for determining electron effective mass, an important semiconductor property [183]. The coherent resonance of the aligned spins in a ferromagnet (ferromagnetic resonance) also

occurs at microwave frequencies when a weak external field is applied [184]. Such measurements are a good way of determining ferromagnetic parameters such as the exchange integral [185].

In 1952, Keffer and Kittel established the theory for antiferromagnetic resonance and determined that in typical aniferromagnetic materials with no external fields, the resonance would occur at THz frequencies [138, 186]. Therefore, THz radiation is ideally suited for the study of antiferromagnetism. Early THz frequency measurements on antiferromagnetic crystals such as NiO, NiF, MnO, MnF_2, $CoCl_2$, $FeCl_2$ were extensive. Key work by Foner [187], Sievers *et al.* [188, 189], Richards [190–192] and Jacobs *et al.* [193] established the techniques of temperature and magnetic field dependent antiferromagnetic resonance. The measurements were limited by the weak thermal sources and bolometer detection available at the time. Generally, the results were used to complement other magnetometry and neutron scattering measurements showing the temperature dependence of magnetisation and magnetic anisotropic effects. Such application was helpful in the early development of magnetic bubble memory [194]. However, with the success of the semiconductor industry, interest within condensed matter physics shifted to semiconductor research and magnetic resonance at THz frequencies became less active.

By the 1980s, improvements in laser technology and optical detection techniques facilitated the development of high quality Raman spectroscopy systems [195]. Raman spectroscopy proved very effective at measuring magnetic resonance at THz frequencies [196–200]. Its reliance on polarisation dependence made it effective at tracking spin reorientation in rare earth orthoferrites [197, 200]. However, its reliance on strong spin-orbital coupling limits its ability to probe low spin moment systems with little orbital coupling.

Recently there has been renewed interest in THz spectroscopy of magnetic materials. Partly owing to the drastic improvements in THz sources and detectors but also due to the emerging fields of THz multiferroics and spintronics. The ability to perform pulsed time dependent measurements and record phase information by coherent detection has made THz spectroscopy a standard tool for time dependent magnetic studies [201, 202]. The discovery of the electromagnon by Pimenov *et al.* in 2006 was followed by extensive studies on multiferroics at THz frequencies [162]

The work of Kida *et al.* on THz magnetochromism established the importance of conical spin order to produce magnetically controllable electromagnons and laid the foundations for the use of TDS measurements in the study of multiferroics [203–206]. Such electromagnon sensitivity is said to provide unique opportunities to determine the ME phase diagram and that electromagnon resonance may emerge irrespective of the presence of ferroelectricity [205]. In 2005, Kimel *et al.* showed the ultrafast control of magnetisation in $DyFeO_3$ by pulsed laser excitation in a pump/probe TDS setup [207]. The phenomenon was later explained by inertia driven spin switching at THz frequencies [42]. Analogous to the inertial motion of massive bodies, the exchange interaction between neighbouring spins allows the magnetisation to climb over a potential barrier only during the action of a magnetic-field pulse. The phenomenon has the potential for ultrafast recording and processing of magnetically stored information [42]. Following this work, experiments using THz TDS have shown characteristic signals which were interpreted as the pumping and probing of antiferromagnetic magnetic spin-wave modes on femtosecond time scales [41, 208–210]. New mechanisms such as induced precession and free-induction decay have been proposed which, if accurate, promise new avenues to optically address specific spins and control spin diffusion.

Lastly, THz spectroscopy has emerged as an important complementary technique to inelastic neutron scattering measurements [40]. Inelastic neutron scattering is the standard technique for measuring the spin-wave dispersion across the entire Brillouin zone. Due to the electromagnetic nature of THz waves, it is difficult to differentiate a magnetic excitation from an electrical one based solely on the optical spectrum, since the time-dependent electrical field may also couple to dipolar electric moments within the material [163]. Inelastic neutron scattering may identify magnetic excitations through its unique ability to collect scattered spectra at specific locations in the reciprocal space of the magnetic lattice [48]. Careful monitoring of the form and structure factor of excitations can confirm their magnetic origin. Thus, neutron scattering and THz spectroscopy are strong complementary techniques. Recently, the sensitivity of polarised neutrons to chiral symmetry in spin lattice ordering has assisted THz investigations in identifying novel excitations associated with atomic vibrations, that are both electrically and magnetically active [211]. An example of this complementary measurement is shown in Figure 2.10. Polarised THz
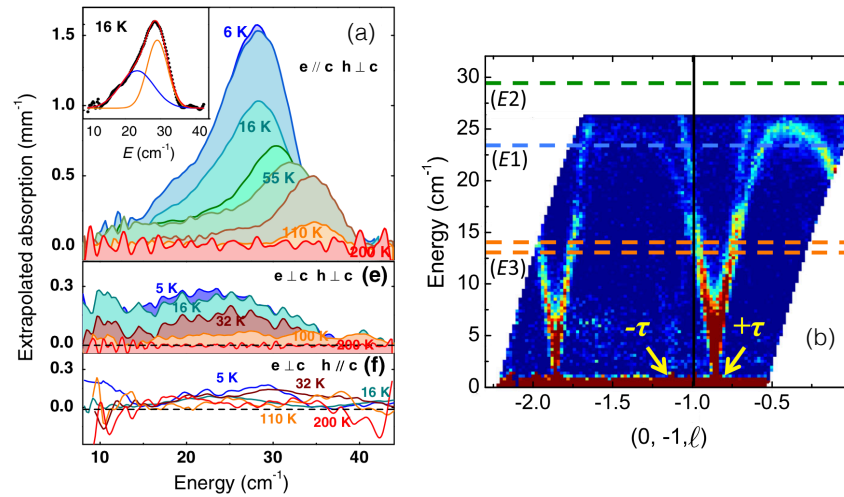
FIGURE 2.10: Complementary THz spectroscopy (a) and inelastic neutron scattering (b) measurements in the analysis of electro- and magneto-active spin waves in $Ba_3NbFe_3Si_2O_{14}$, adapted from Reference [211].

spectroscopy is used to identify electrically and magnetically active excitations based on the orientation of the THz field relative to the crystallographic axes (Figure 2.10 (a)). The dispersion of the excitations is measured by complementary inelastic neutron scattering, suggesting hybridised electrical and magnetic origin. The same complementary techniques are proving valuable in the investigation of spin-wave dynamics in multiferroic materials identifying hybridised states of spin waves and electroactive crystal field transitions [212, 213].

Chapter 3

Experimental techniques

This chapter provides an overview on the experimental apparatus and techniques employed in this thesis. Section 3.1 covers the various THz spectrometers encountered including a two-colour photomixing system, a time-domain system and Fourier transform interferometers featuring thermal and synchrotron sources. Section 3.2 briefly describes some of the complementary apparatus used including, cryogenic sample environments, scanning electron microscopy (SEM), energy-dispersive spectroscopy (EDS), Bragg diffraction using x-rays (XRD) and inelastic neutron scattering (INS).

3.1 Terahertz spectrometers

3.1.1 Two-colour system

The two-colour photomixer system or simply two-colour system, is so named because it operates on the principle of mixing two colours of laser light. Other terms that refer this form of THz generation are difference frequency generation (DFG), beat-frequency generation (BFG), heterodyning, optical heterodyning or optical heterodyning down conversion [5]. The photomixer source (and its use as a detector) was briefly covered in the review on THz sources and detectors in Section 2.2.1. Essentially, two tunable near-infrared diode lasers with a difference frequency in the order of 1 THz are focused onto a photomixer
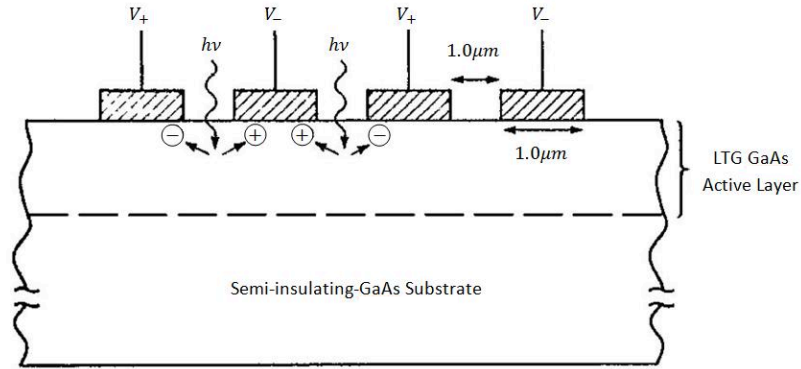
FIGURE 3.1: Cross-section of photomixer with interdigitated electrode fingers. The bias across the electrodes accelerates electrons and holes towards the corresponding electrode generating a photocurrent at the difference frequency between the two incident laser beams [215].

consisting of a LTG GaAs wafer fabricated with a pattern of interdigitated electrode fingers supported by a GaAs substrate. The finger electrodes, constructed by electron-beam lithography, are of the order of $1\,\mu$m wide, $10\,\mu$m long and separated by a $1\,\mu$m gap [214]. The instantaneous optical power on the photomixer due to the pump lasers with individual powers P_1 and P_2 at frequencies ν_1 and ν_2 is given by,

$$P = P_0 + 2\sqrt{mP_1P_2}[\cos 2\pi(\nu_2 - \nu_1)t + \cos 2\pi(\nu_2 + \nu_1)t] \,, \tag{3.1}$$

where $P_0 = P_1 + P_2$ is the averaged total incident power, and m represents an efficiency prefactor that is dependent on the spatial overlap of the two pump laser beams [215]. Electron-hole pairs generated in the LTG GaAs by photon absorption are accelerated towards the electrodes which have a voltage bias across them in the manner seen in Figure 3.1 [215].

Due to the desirable properties of LTG GaAs (high charge carrier mobility with sub picosecond recombination time), conduction band bending at the metal-semiconductor interface is negligible, meaning the electrical properties of the photomixer may mostly be represented by a photoconductance that is a function of the absorbed optical power, shown in Equation 3.1 [215]. Thus, the dominant photocurrents in the photomixer are generated at the sum and difference frequencies of the pump lasers. By coupling the photocurrent to an appropriate resonant load, the difference frequency is selected out and coupled into free space producing the continuous wave THz radiation. To improve free-space coupling the photomixer chip is positioned behind a hemispherical lens made from
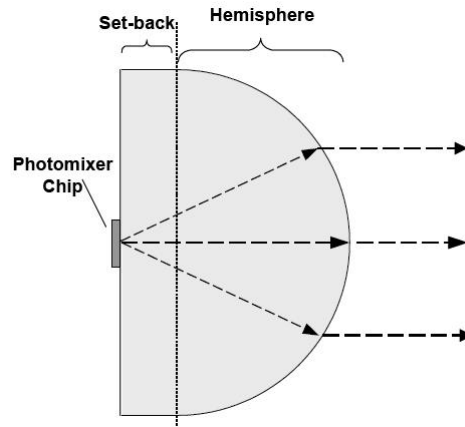
FIGURE 3.2: Cross-section of hyperhemispherical silicon lens used to collimate THz emission from log-periodic antenna [97].

silicon [97]. Figure 3.2 shows how the high refractive index of silicon refracts the diverging THz radiation from the photomixer producing a semi-collimated beam. Due to the large solid angle of radiation produced by the planar antenna, in order to achieve the best collimation the photomixer is positioned behind the centre of curvature of the hemisphere in what is known as a hyperhemispherical lens [97].

A diagram of the two-colour system's general operation is shown in Figure 3.3. The two pump lasers consist of Toptica DL-100 distributed-feedback laser-diodes [119]. The lasers operate at frequencies around $351\,\mathrm{THz}$ ($853\,\mathrm{nm}$) and can be tuned from $350\,\mathrm{THz}$ ($855\,\mathrm{nm}$) to $352\,\mathrm{THz}$ ($851\,\mathrm{nm}$) by means of adjusting the temperature of a diffraction grating incorporated into the semiconductor chip which selects out a single longitudinal mode determining the lasing frequency. The lasers operate at powers of $\sim30\,\mathrm{mW}$. Each laser beam is coupled into a single mode, polarisation-maintaining optical fibre, and the two beams are mixed in a fibre combiner. The power of the lasers' output from the fibres is considerably reduced to the order of $\sim10-20\,\mathrm{mW}$ per beam upon coupling to the fibre.

The fibre output is split into two signals of the mixed beams which are then sent to an Advantest Q8384 optical spectrum analyser (OSA) and the photomixer. The OSA consists of a monochromator with $10\,\mathrm{pm}$ resolution from $600\,\mathrm{nm}$ to $1700\,\mathrm{nm}$ and produces a spectrum of the mixed signal containing information about the power and frequency of each laser signal. This information is then analysed in the control module and used to calculate the frequency of the emitted THz radiation. The details of this control program

are discussed in detail in Reference [216]. The second mixed signal output is sent to the photomixer. The splitting of the laser signal for use with the OSA further reduces the optical power available at the photomixer. This is compensated for by the addition of a Toptica tapered laser amplifier before the photomixer, which can provide powers up to 150 mW. After the amplifier, the mixed laser signal is focused onto the LTG GaAs photomixing chip via an optic fibre fixed directly onto the back of the chip. The all-fibre coupling of the pump lasers to the OSA and photomixer, allows for improved power stability as well as increased flexibility of the setup. Because the pump laser beams are never transmitted through free space, the setup is also much safer with a reduced chance of eye damage from the powerful pump laser beams than if the setup was all free space as in many other cases [90, 92, 119].

The THz signal emitted from the photomixer is electronically modulated by alternating the bias across the photomixer's electrodes between 0 and 20 V depending on the photomixer being used. The modulated signal is then typically collimated by an Edmund optics gold-plated aluminium 90 degree off-axis paraboloidal mirror and focused through a standard THz optics setup depending on the experiment. The transmitted THz signal is then re-collimated by another paraboloidal mirror and focused onto a detector. While a two-colour system is capable of coherent detection, only incoherent detection is employed for the experiments in this thesis.

Three detector types are used. The ACST Schottky diode detector is a room temperature semiconductor detector which is sensitive across the spectral range of 0.05 to 1.5 THz. The Tydex Golay cell is a room temperature thermal detector, sensitive from 0.05 THz and optically filtered to cut off frequencies above 3 THz. The liquid-helium–cooled silicon bolometer is a cryogenic thermal detector, which is sensitive from 0.1 THz and optically filtered to cut off frequencies above 3 THz. The Schottky diode detector offers the quickest response time but lowest sensitivity. It is used when signal is large and fast measurements are desired. The bolometer detector offers the best sensitivity but has a slower response time. It is used when signal is low and long measurements can be taken. The Golay cell has both a lower response time and less sensitivity to the Bolometer but can operate without cryogenics. It is generally used for preliminary measurements before a bolometer
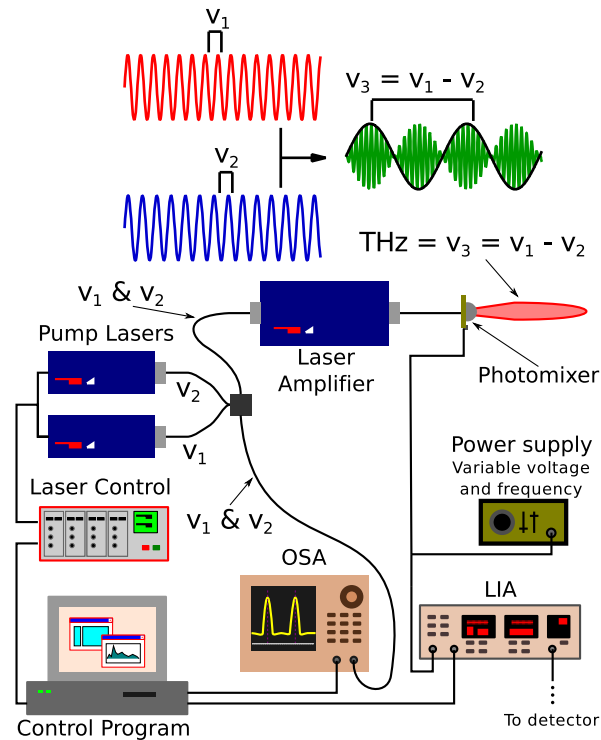
FIGURE 3.3: Diagram of two-colour system operation. The THz signal is a continuous wave generation of the difference between two laser frequencies.

is required. The detected signal is measured using a Stanford SR830 DSP lock-in amplifier (LIA) set up to amplify signals at the frequency of the oscillating photomixer bias.

By systematically stepping through difference frequencies of the pump lasers and recording the transmitted signal, a THz spectrum is constructed directly in the frequency domain. Resolution is controlled by defining the step size between successive changes in laser frequency difference. Resolution down to 70 MHz is achievable, however typical measurements are taken at a resolution of 1 GHz. Bandwidth is controlled by setting a maximum frequency difference. Spectra are usually taken from 0.1–1.0 THz. A typical spectrum of air is shown in Figure 3.4. Resonance lines due to water vapour absorption appear at frequencies of 0.55 THz, 0.75 THz, 0.99 THz. They are noted here as they occur in the spectral region where many of the experiments are undertaken and must be considered when assessing features in sample spectra. Photographs of the setup are shown in Figure 3.5.
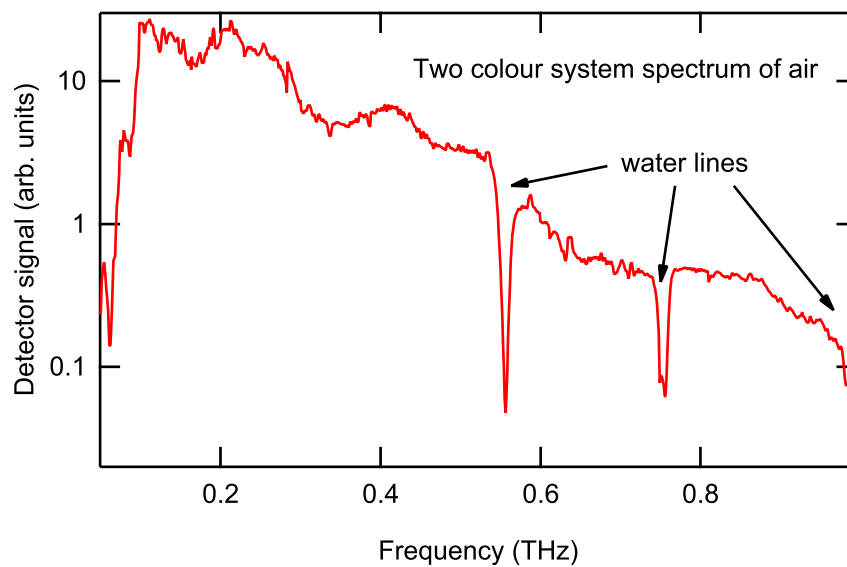
FIGURE 3.4: Sample spectrum of laboratory air using two-colour system. The resolution is 1 GHz and detection was performed using the Schottky diode detector.
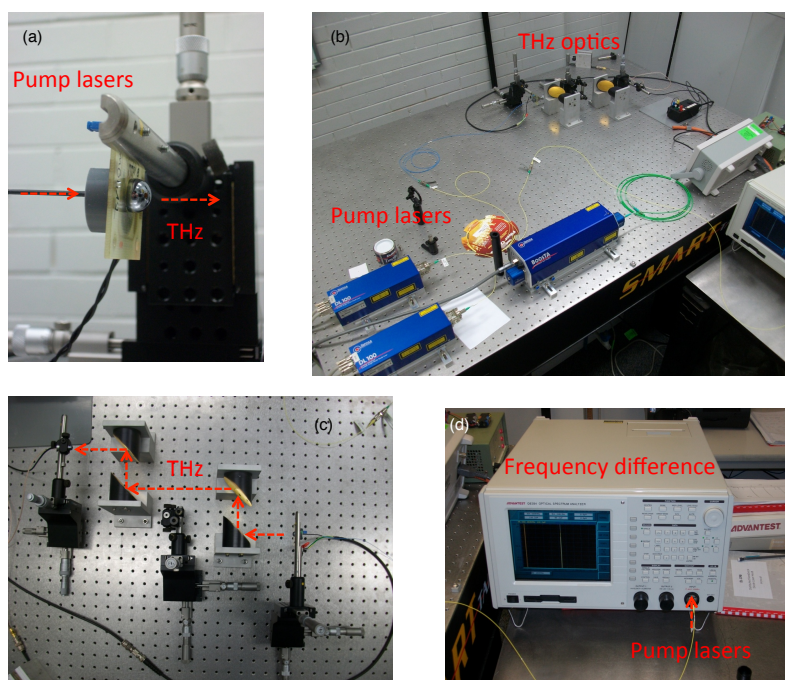
FIGURE 3.5: Photographs of two-colour system. (a) Photomixer unit. (b) View of pump lasers and amplifier. (c) THz optical path. (d) OSA for measuring laser frequency difference.
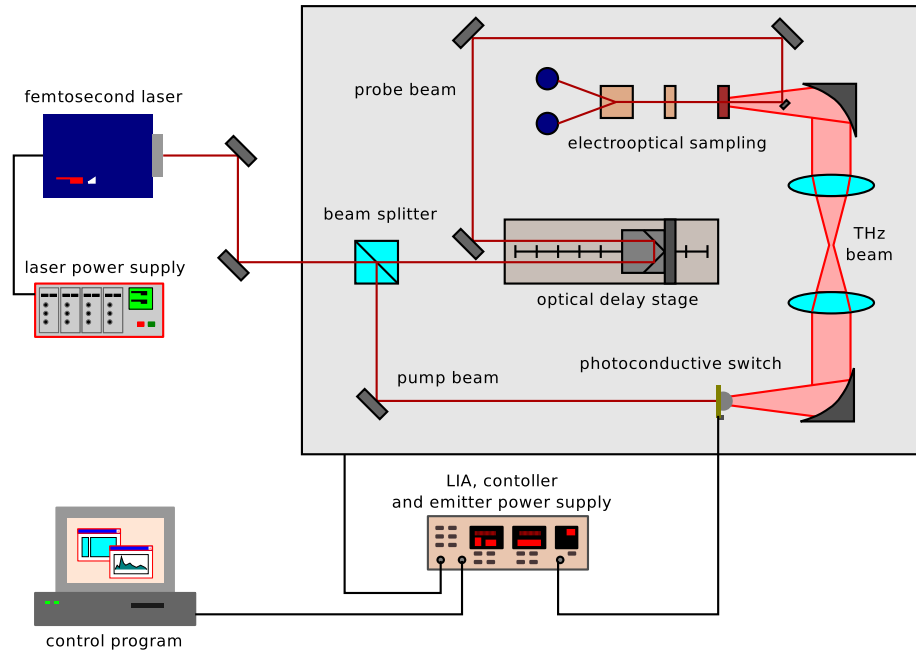
FIGURE 3.6: Diagram of Zomega TDS system. The grey box indicates the enclosed compartment which can be purged with dry air or nitrogen.

3.1.2 Time-domain system

The THz time-domain spectrometer used in this thesis is a commercial 'turnkey' system manufactured by Zomega. It operates as a coherent emission and detection system that emits single-cycle THz pulses and detects them at a repetition rate of 80 MHz. The signal is detected in the form of an **E** field as a function of time and the Fourier transform of the pulse signal provides the intensity and phase as a function of frequency. Pulsed laser THz emission and detection was briefly reviewed in Section 2.2.1. A simple diagram of the system is shown in Figure 3.6.

The pump laser is a dual mode FemtoFibre Pro Toptica femtosecond laser. It can operate with a 193 THz (1550 nm) / 323 mW / 76 fs mode or a 384 THz (780 nm) / 166 mW / 87 fs mode with a pulse repetition rate of 80 MHz. The Zomega system utilises the 384 THz (780 nm) mode. An indium tin oxide coated mirror splits the optical beam into a pump and probe beam line. The pump beam is directed onto a photoconductive switch THz emitter operating with a 100 V bias. The design of the photoconductive switch is similar to the two-colour system photomixer, featuring a silicon collimating lens and a lithography constructed antenna. The emitted THz beam is horizontally polarised and focused onto a

sample position using polymer (TPX) lenses. The collected THz beam is then focused onto a ZnTe crystal and detected by electrooptical sampling. The probe beam is also directed onto the ZnTe crystal. The birefringence of the ZnTe crystal is modulated by the intensity of the THz beam. The two polarisation components of the probe beam are separated by a combination of a quarter wave plate and a Wollaston prism. The two components are then differentially detected using two photodiodes. The entire system, except for the femtosecond pump laser, is housed in an enclosed compartment which can be purged with gases such as dry air or nitrogen. The dry atmospheres help to reduce the humidity in the THz beam path and lower the effects of water absorption.

A representative time-domain **E**-field measurement is shown in Figure 3.7 (a). The initial peak at ∼5 ps represents the pulsed **E** field. A series of high frequency oscillations are observed at time delays greater than ∼5 ps. These are attributed to water vapour absorption in the laboratory air. At ∼27 ps a small localised pulse is also evident. This is attributed to a delayed portion of the initial THz pulse. The silicon lens attached to the THz emitter will feature internal reflections which have time delayed properties. The first reflection, which is the strongest, appears at ∼27 ps. The resultant intensity and phase frequency spectra are shown in Figures 3.7 (b) and (c). Many water lines are seen in the spectrum, particularly above 1 THz. These appear as localised shifts in the phase spectrum. The Fabry-Perot fringes from the reflected pulse of the silicon lens appear throughout the intensity spectrum with a period of ∼4.5 GHz. Resolution can be improved by increasing time delay length. The bandwidth is dependent on the density of time-domain measurement points. The TDS system has a larger bandwidth (0.1–3 THz) than the two-colour system but generally operates at a lower resolution (∼10 GHz). A photograph of the setup is shown in Figure 3.8.

3.1.3 Fourier transform interferometer

The interferometer shares many aspects with the time-domain spectrometer. An initial single beam of light is split into two beams, a time or path delay is applied to one beam, the beams are then recombined and the interference is measured. A Fourier transform of the interference spectrum provides the frequency intensity spectrum. Resolution is increased
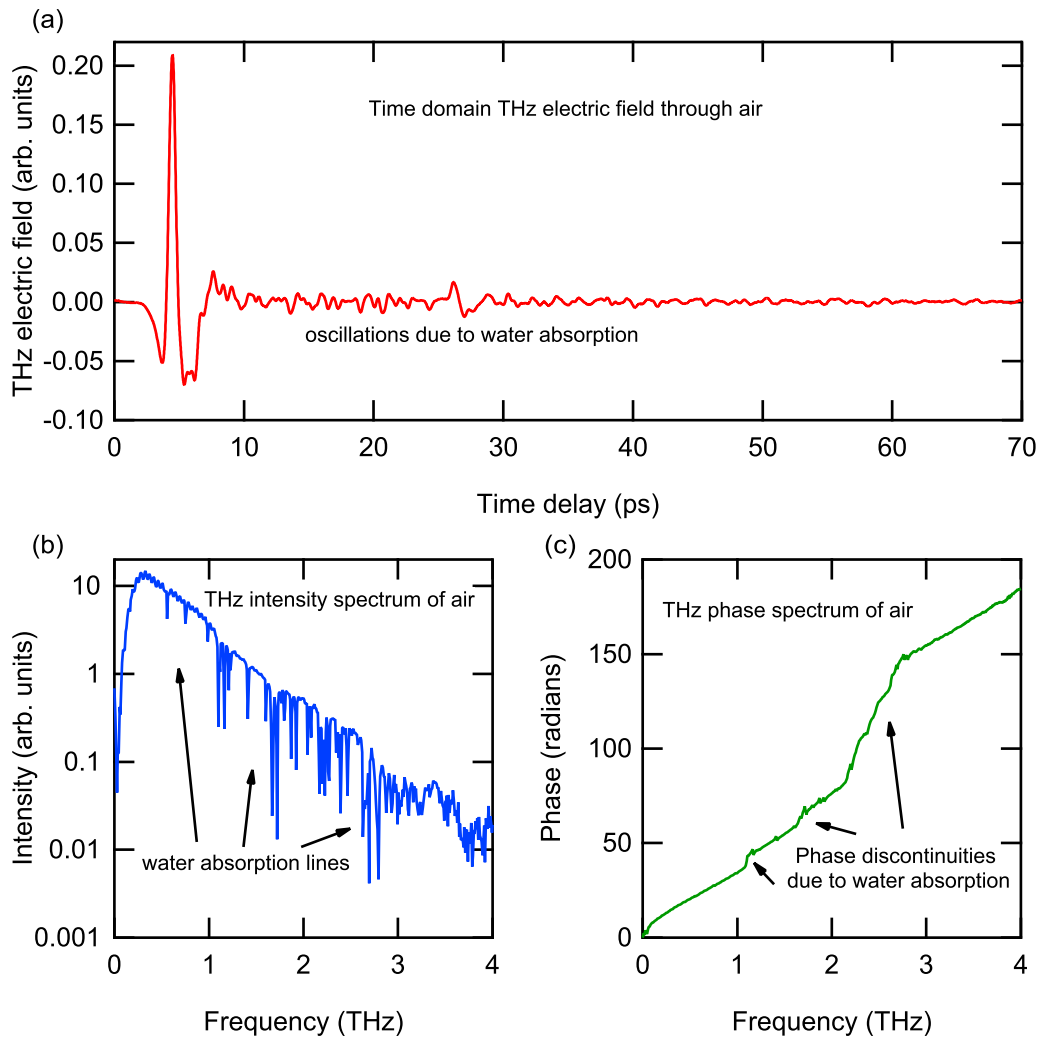
FIGURE 3.7: Representative spectrum of laboratory air using Zomega TDS system. (a) Electric field time-domain waveform extending to 70 ps time delay. (b) Frequency Fourier transform gives intensity spectrum with a resolution of ~7 GHz. (b) Phase Fourier transform gives phase spectrum.

by increasing time delay or optical path difference. The bandwidth is dependent on the density of data points.

The principle element of a Fourier transform interferometer is the Michelson interferometer. A simple diagram demonstrates its operation in Figure 3.9. The Michelson interferometer utilises a beamsplitter (BS) to separate equal amounts of the initial radiation towards mirrors M1 (fixed) and M2 (movable). The movable mirror scans back and forth through the zero path difference (ZPD) position and the light is recombined at the beamsplitter.

FIGURE 3.8: Photograph of enclosed Zomega TDS system. The femtosecond pump laser is positioned to the top of the photograph.

A portion of the recombined light travels towards the detector. As in Figure 3.9 the ZPD position occurs when both mirrors are at an equal distance of d away from the beamsplitter.

To simplify things, the mathematical principles of an interferometer are best developed by considering a monochromatic source with a frequency ν (in wavenumbers) and optical path difference x. The intensity at the detector is then given by [51],

$$I_{\text{det}}(x) = \frac{1}{2}I_{\text{source}}\left[1 + \cos(2\pi\nu x)\right]. \tag{3.2}$$

A maximum occurs when $x = 0$ (the ZPD position) and light from the two arms of the interferometer interfere constructively. As x deviates from zero, the intensity varies sinusoidally, reaching a minimum when the argument of the cosine term is an integer multiple of π. The $1/2$ prefactor stems from the notion that an ideal beamsplitter transmits (and reflects) half of the light incident on it. As the light is recombined, half of the intensity will be directed to the detector while the other half will be directed back to the source and lost. In reality, more losses are incurred by unwanted absorption in the beamsplitter, light reflected from mirrors that do not produce phase shifts equal to π and by the samples being investigated. All of these effects may also be frequency dependent. It is therefore more meaningful to replace the prefactor by a term of lesser value denoted $K(\nu)$. The

interference signal of interest in Fourier transform spectrometry is a result of the dynamics of the interferometer and so only the second term in Equation 3.2 need be considered. The signal at the detector ($S(x)$) then becomes,

$$S(x) = K(\nu)\cos(2\pi\nu x). \tag{3.3}$$

Integrating from zero to infinity extends the formalism to the more practical broadband case.

$$S(x) = \int_0^\infty K(\nu)\cos(2\pi\nu x)d\nu. \tag{3.4}$$

The signal as a function of frequency which gives the frequency intensity spectrum is then given by the inverse Fourier transform,

$$K(\nu) = \int_{-\infty}^\infty S(x)\cos(2\pi\nu x)dx. \tag{3.5}$$

The integration interval is extended over all space to facilitate computation. In practice, displacing the mirror an infinite distance on either side of the ZPD is unachievable. The limits of integration therefore become plus and minus the maximum distance that the mirror moves, denoted as $x_{\max}$. The corresponding optical path difference, which must transverse this distance twice, is then $2x_{\max}$. The optical path difference is therefore inversely proportional to the spacing between data points in the spectrum by the relation $\nu = 1/2x_{\max}$. This gives the resolution limit of the spectrum.

The interferogram is collected by sampling voltages from the detector at discrete intervals of x. Two different sampling techniques are often employed, *step scanning* and *rapid scanning* [5]. The step scanning technique reduces noise by sampling the signal at each discrete x point using lock-in detection over a set integration time. The spectrum can be transformed in real-time and as the path difference increases the resolution will increase. The measurement can be stopped when the desired resolution is reached. However, the signal-to-noise ratio is defined by the lock-in integration time and cannot be changed after initially being set.

The rapid scanning technique reduces noise by averaging over many scans of the interferogram taken in rapid succession. The technique does not require lock-in detection and

therefore no source modulation. The spectrum can be transformed in real-time and as the number of scans increases the signal-to-noise ratio will increase. The scan can be stopped when the desired noise level is reached. However, the resolution must be defined at the start and cannot be improved later. Both methods can take a short or long time to perform scans depending on the noise and resolution requirements. In this thesis, two different interferometers are employed featuring different sources and scanning techniques.

3.1.3.1 Polytec interferometer

The Polytec interferometer is a modified commercial Far-infrared spectrometer system. It operates using the step scan technique with a mechanical chopper providing the source modulation for lock-in detection. The radiation source can be either a globar or mercury arc lamp thermal source. Since thermal radiation is unpolarised, polarisation dependent measurements require a gold-wire-grid polariser to be placed in the beam path before the sample. The polariser is rotatable providing relative polarisation from 0 to 90 degrees. The detector is a liquid helium cooled Si bolometer. A maximum path difference of $10\,\mathrm{cm}$ is achievable producing a maximum resolution of $0.05\,\mathrm{cm}^{-1}$ or $1.5\,\mathrm{GHz}$. The beamsplitter consists of stretched Mylar with a thickness $70\,\mu\mathrm{m}$ or $23\,\mu\mathrm{m}$. The entire setup is contained within a hermetically sealed compartment which can be evacuated to reduce effects of water absorption. A sample interferogram and transformed spectrum under vacuum is shown in Figure 3.10. Because the path difference of the interferometer is usually measured in cm, traditionally the optical frequency is given in wavenumbers with units of reciprocal space (cm^{-1})

3.1.3.2 Australian Synchrotron far-infrared beamline

The far-infrared beamline at the Australian synchrotron implements a Brüker IFS125HR FTIR Michelson interferometer for spectroscopic studies at THz frequencies. The Brüker spectrometer operates using the rapid scan technique. An optical path length of $5\,\mathrm{m}$ is available providing a maximum resolution of $0.001\,\mathrm{cm}^{-1}$ or $30\,\mathrm{MHz}$. A liquid helium cooled Si bolometer is used for detection. The intrinsic polarisation of the synchrotron radiation is horizontal since an accelerating electron radiates energy with the **E** field in
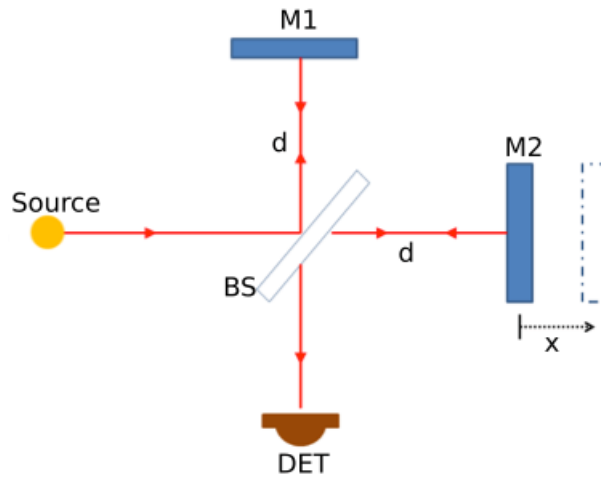
FIGURE 3.9: A schematic of a Michelson interferometer, which constitutes the principal element of a Fourier transform interferometer.
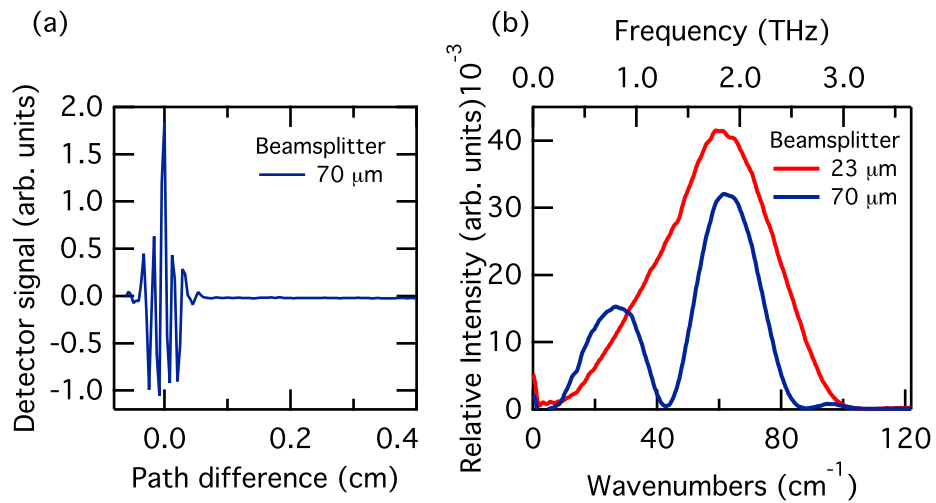
FIGURE 3.10: Representative spectra of vacuum using Polytec interferometer. (a) Sample interferogram of mercury arc lamp source in Polytec interferometer. (b) Frequency spectrum is given as the Fourier transform. Using different beamsplitters allows improved signal in different spectral regions.
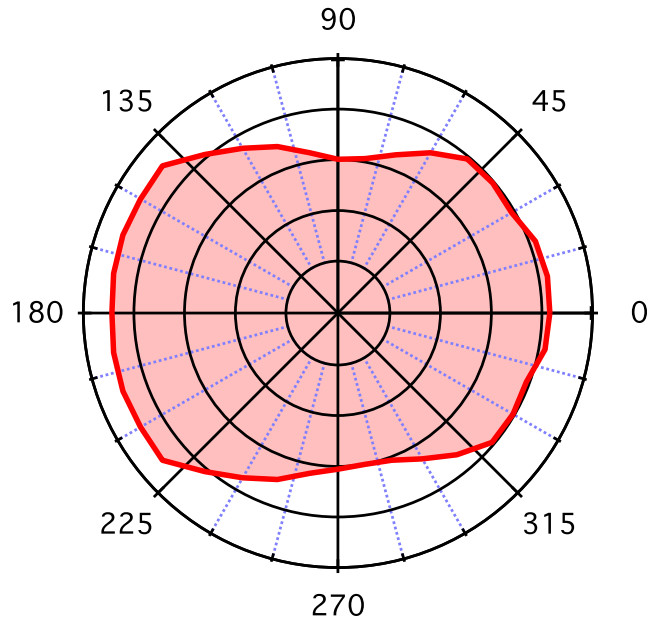
FIGURE 3.11: Polarisation dependence of THz radiation at the far-infrared beamline of the Australian Synchrotron.

the direction of the acceleration. However, from the perspective of an observer away from the horizontal plane of the storage ring, there are also circularly polarised components. The setup at the Australian synchrotron (not being perfectly aligned with the horizontal plane of the storage ring) therefore features circularly polarised components that lead to an elliptical characteristic for the overall polarisation.

The angular dependence of the polarisation has been measured and is depicted in Figure 3.11. As is evident, the major component of the polarisation is in the horizontal plane but there is also a considerable amount of vertical polarisation. To ensure linear polarisation in spectroscopic measurements, a gold-wire-grid polariser is placed in the beam path before the sample. The polariser is fixed in the horizontal orientation taking advantage of the dominant component of the elliptical source radiation. A stretched Mylar beamsplitter of $75 \, \mu$m is used for the measurements in this thesis.

3.2 Complementary apparatus

3.2.1 Cryogenic systems

As briefly discussed in Section 2.3, the magnetic properties of materials are typically very temperature dependent. The use of cryogenic apparatus is therefore essential in studying such temperature dependence. Two types of cryogenic systems have been employed in this thesis. A liquid helium cooled 7 T split-ring superconducting magnet with variable temperature insert (VTI) and a closed-cycle helium cryostat.

3.2.1.1 Superconducting magnet with VTI

The superconducting magnet is an Oxford split-ring magneto-optical spectroscopic magnet. The spit ring setup allows for spectroscopic measurements on a sample while it is cooled to cryogenic temperatures and subjected to strong external magnetic fields. Both Faraday (radiation propagation parallel to external magnetic field) and Voigt (radiation propagation perpendicular to external magnetic field) geometries are achievable by switching detector position and rotating the sample. A photograph of the magnet and schematic of the optical path and field orientation is shown in Figure 3.12.

The superconducting coils are kept at 4.2 K by a bath of liquid helium maintained by a surrounding vacuum sheath and liquid nitrogen cooled radiation shield. Samples are fixed to a sample stick and inserted into the VTI at the centre of the magnet bore. The VTI is cooled by vapours from the helium bath with the vapour flow rate controlled by a manual needle valve. Sample temperature is maintained by balancing the vapour flow rate with a resistive heater element on the sample stick. Temperatures from 300 K down to 4.2 K can be achieved in this manner. For lower temperatures down to 1.6 K, the VTI is allowed to cool to 4.2 K where liquid helium begins to collect. Once a bath of helium has collected in the VTI, the compartment is evacuated using a backing pump. The lower vapour pressure cools the helium bath below its atmospheric liquid temperature of 4.2 K.

The magnet is nominally rated for fields up to 7 T. A previous quench of the magnet at 6.5 T has limited its use to 5.5 T as a conservative measure to reduce the chances of

further quenches. The magnet setup is interfaced to the Polytec interferometer and is typically used in conjunction with Polytec spectroscopic measurements. The two-colour system may also be incorporated into the Polytec's optics and used with the magnet setup. Polyethylene windows provide the THz light path while separating the vacuum chambers from the external environment. The magnet setup is featured in the experiments of Chapters 6 and 7.

3.2.1.2 Closed-cycle cryostat

The closed-cycle cryostat, manufactured by Cryo Industries, operates in a refrigerator cycle. A closed volume of helium vapour is cycled through a thermodynamic process where cold vapour is pumped into a chamber in thermal contact with the cryostat cold head. An external mechanical refrigerator extracts the warmer helium exhaust vapour, which is cooled and recycled. Samples are attached to a sample stick which is placed in a chamber filled with a helium atmosphere. The helium in the sample chamber acts as a heat exchange between the cryostat cold head and the sample, cooling the sample down to a base temperature of $6\,\mathrm{K}$. The sample temperature is regulated with a resistive heater element on the sample stick. Temperatures from $300\,\mathrm{K}$ down to $6\,\mathrm{K}$ can be achieved. The closed-cycle cryostat is interfaced with the interferometer at the Australian Synchrotron. Polyethylene windows separate the cryostat vacuum chamber from the interferometer vacuum. A photograph of the setup is shown in Figure 3.12 (c). The closed-cycle cryostat is featured in the experiments of Chapter 9.

3.2.2 Electron microscopy

Electron microscopy offers a number of techniques for analysing the surfaces of samples. Essentially a beam of accelerated electrons are fired at the sample surface. Special focusing magnets and current carrying coils focus and direct the beam to precise locations on the sample surface. Scattered electrons and photons off the sample may then be analysed depending on what information is of interest. A schematic diagram of this operation is shown in Figure 3.13. Two analysis techniques that are encountered in this thesis are scanning electron microscopy (SEM), which is used to observe an image of the sample
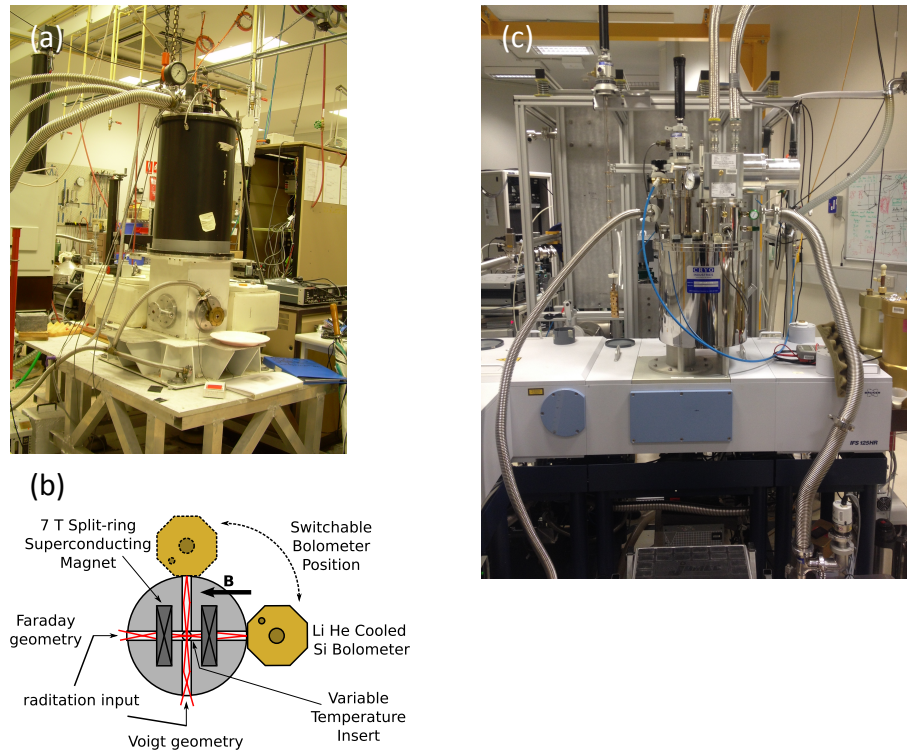
FIGURE 3.12: Cryogenic systems. (a) Photograph of 7 T superconducting magnet with VTI. (b) Schematic of 7 T magnet showing setup for both Faraday and Voigt geometries. (c) Photograph of closed-cycle cryostat in use at the far-infrared beamline of the Australian Synchrotron.

surface and energy-dispersive spectroscopy (EDS), which is used to confirm the elemental make up of a sample.

3.2.2.1 Scanning electron microscopy (SEM)

The scanning electron microscope performs a raster scan of the incident electron beam across the surface of the sample and monitors the electrons re-emitted with detectors placed in a reflection-type geometry. Obtaining a magnified image up to $\times 1000$ is a standard procedure. The SEM measurement detects both reflected (back-scattered) electrons, as well as secondary electrons that are emitted due interactions of the primary electron beam in the sample. The effective electron probe size depends on the interaction volume of the scattered electrons. In this the thesis, a JEOL LV-FEM SEM was used as a rough probe of surface morphology for the sample investigated in Chapters 7 and 8.

3.2.3 Energy-dispersive spectroscopy (EDS)

A modern secondary function of the electron microscope is the ability to perform qualitative chemical analysis by EDS. In EDS, inelastic scattering of the incident electron beam leads to emission of x-ray photons with energies specific to the elements in the sample. There are two processes leading to x-ray emission. In the first case, the Coulombic field of the atoms within the sample will decelerate the incident electrons causing bremsstrahlung x-ray emission. This creates a continuous source of x-ray radiation, since the electrons can lose any amount of energy up to the original maximum energy. The second case refers to characteristic x-ray production that occurs when a high energy electron interacts with a tightly bound inner shell electron in the sample. The incident electron loses energy E_{K}, the binding energy of an electron in the K shell. The inner shell electron is ejected, causing the electronic configuration of the atom to relax. Electrons from the outer shells relax to the inner shell through a set of allowed transitions. As the outer shell electrons drop in energy level, they can either release energy in the form of Auger electrons or x-ray photons. The x-ray spectrum that is generated provides a unique signature of the atomic elements present in the sample.

Mosley's law is the basis for analysis of the emitted spectrum and allows one to predict the characteristic energies for emitted x-rays from an element [66],

$$E = A(Z - C)^2, \tag{3.6}$$

where E is the energy of the peak emission, Z is the atomic number, A is the atomic mass and C is a dimensionless unit ($C = 1.13$ for K series and 7 for L series inner electrons). Performing a raster scan of an area on the sample surface and analysing the emitted x-ray spectrum, the distribution of the elemental make up of the sample can be observed and compared with SEM images and expectations from the material's chemical formula. In this thesis, this technique was used to confirm the chemical phase of the sample studied in Chapters 7 and 8.
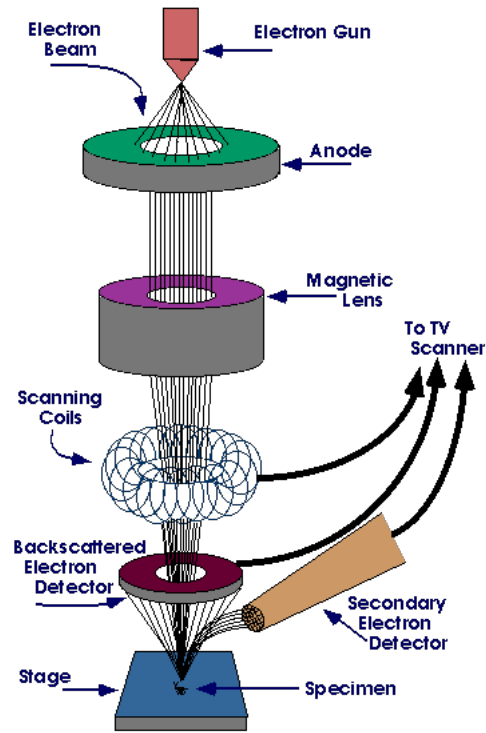
FIGURE 3.13: Schematic diagram of electron microscope operation [217].

3.2.3.1 X-ray diffraction (XRD)

X-ray diffraction techniques are used for the determination of a crystal structure. The energetic photons of x-rays interact with solid crystals to form unusual outgoing patterns, signified by transmitted and reflected beams at specific angles that can be very different from the incident direction, and differ between various crystalline substances. Essentially, the incoming x-ray beam interacts with the electrons around the ordered atoms in a crystal lattice causing each atom to re-radiate a small portion of its intensity as a spherical wave. Since the atoms are arranged symmetrically with a separation d_{hkl}, these spherical waves will be in sync (add constructively) only in directions where their path-length difference $2d \sin \theta$ equals an integer multiple of the wavelength λ [29]. In that case, part of the incoming beam is deflected by an angle 2θ, producing a reflection spot in the diffraction pattern.

This relationship is described by Bragg's law, conceived in 1912 by Australian scientist W. L. Bragg [218],

$$2d_{hkl} \sin \theta = n\lambda. \tag{3.7}$$
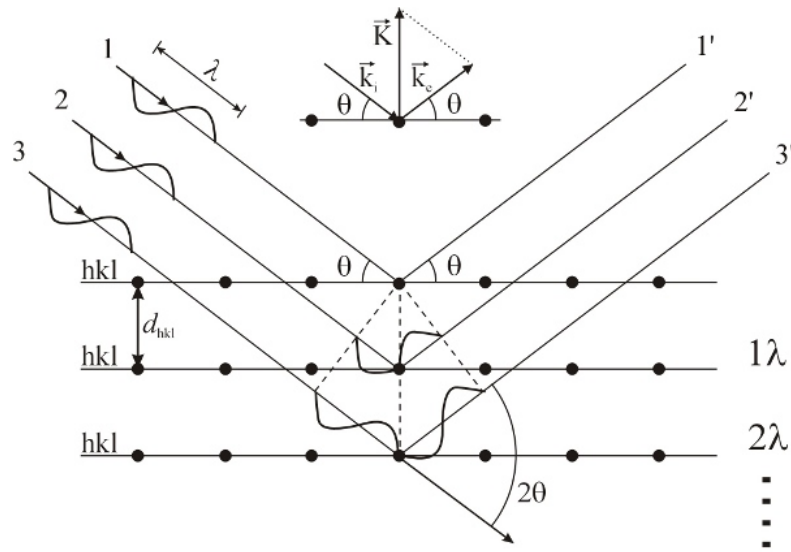
FIGURE 3.14: Bragg diffraction relationship. Planes of atoms (hkl) separated by d_{hkl} scatter x-rays. The scattered rays constructively interfere producing peaks in the reflected signal defined by Bragg's law [219].

A diagram of this relationship is shown in Figure 3.14. The XRD performed in this thesis was done using an X'Pert Panalytical Pro lab x-ray source, operating at a wavelength of 1.54 Å located at the Australian Nuclear Science and Technology Organisation (ANSTO).

3.2.3.2 Neutron scattering

Neutrons are especially well suited to study both the structure and lattice dynamics of solid materials due to their very short wavelengths. Not only does their lack of charge allow them to probe deep into the structure of bulk materials, but their spin 1/2 magnetic moment is extraordinarily useful at providing information on the magnetic structure of crystals containing magnetic ions. Their broad spectrum of momenta also allows for the study of acoustic and optic branches of phonons both near the origin of the Brillouin zone (like photons) and across its entirety, therefore providing a complementary measurement technique to optical spectroscopy [4].

Neutrons are produced in relatively large quantities in nuclear reactors. They are then moderated and brought into equilibrium with a large thermal bath. Typically neutrons are thermalised at room temperature ($T \sim 300$ K) and known as *thermal* neutrons. However,

high flux reactors with specialised facilities are able to produce *cold* neutrons ($T \sim 77\,\mathrm{K}$) and *hot* neutrons ($T \sim 500\,\mathrm{K}$).

Since the method for characterising elementary excitations (phonons, spin waves) involves inelastic scattering processes (absorption of photons, scattered neutrons), it is instructive to compare the wave vector's dependence of on energy for neutrons and for photons, since the energy and momentum are conserved in the scattering processes. The energy of non-relativistic neutrons, such as thermal neutrons is given by,

$$E_{\mathrm{n}} \approx \frac{p^2}{2m} = \left(\frac{\hbar^2}{2m} \right) k^2. \tag{3.8}$$

On the other hand, the energy of the photon is given by

$$E_{\gamma} = cp = (c\hbar)k. \tag{3.9}$$

Evidently, the energy of neutrons goes by k^2 while the photon goes by k.

Naturally, the energy and momentum of a scattered neutron from an elementary excitation is conserved. The energy conservation is therefore,

$$E' - E = \pm \sum_{\mathbf{k},s} \hbar\omega_{\mathbf{k}s}\delta n_{\mathbf{k}s}, \tag{3.10}$$

where E' is the energy of the outgoing neutron and E is that of the incident neutron. The $\pm$ formalism represents emission (+) or absorption (-) of one or more excitations of energy, wave vector and polarisation, given by $\hbar\omega_{\mathbf{k}s}$, $\mathbf{k}$ and s respectively. $\delta n_{\mathbf{k}s} = n'a_{\mathbf{k}s} - a_{\mathbf{k}s}$ is the change in the number of quanta in the mode after the scattering has taken place. Momentum conservation for the same scattering event is given by,

$$\mathbf{p}' - \mathbf{p} = \pm \sum_{\mathbf{k},s} \hbar\mathbf{k}\delta n_{\mathbf{k}s} \pm \hbar\mathbf{K}. \tag{3.11}$$

Since $\omega_{\mathbf{k}s}$ and $\mathbf{k}$ are inversely proportional, the $\pm\hbar\mathbf{K}$ term (where $\mathbf{K}$ is a reciprocal lattice vector) is the only difference between Equations 3.10 and 3.11. The outcome of this reveals that a scattering event that involves a pure reflection of the incident neutron produces only

a change of direction, not a change in energy. Such a scattering event is known as elastic scattering or Bragg reflection. Elastic scattering processes may only take place in specific directions $\pm\mathbf{K}$, being $\mathbf{K}$ the set of reciprocal lattice vectors of the crystal lattice. The conservation equations are given by

$$E' - E = 0 \tag{3.12}$$

and

$$\mathbf{p}' - \mathbf{p} = \pm\hbar\mathbf{K}, \quad \left(\mathbf{q}' - \mathbf{q} = \pm\mathbf{K}\right), \tag{3.13}$$

where $\mathbf{q}'$ and $\mathbf{q}$ are the wave vectors of the scattered and the incident neutrons respectively. $\mathbf{K}$ is the reciprocal lattice vector that defines the set of parallel lattice planes producing the Bragg reflection. Since with elastic scattering $|\mathbf{q}'| = |\mathbf{q}|$, this relation produces the well known Bragg's law encountered above for the XRD technique,

$$2d_{hkl}\sin\theta = n\lambda. \tag{3.14}$$

Thus, elastic neutron scattering or neutron diffraction is analogous to x-ray diffraction providing information on the unit cell symmetry and lattice parameters. Complementary to this, is the neutron's ability to provide the same information about magnetic ordering in magnetised materials due to the neutron's magnetic moment. This property is used to reveal information about ferromagnetic, antiferromagnetic, spiral, commensurate and incommensurate structures.

Inelastic neutron scattering is characterised by a gain or loss of neuron energy in the scattering interaction. For example, energy from the incident neutron may be deposited into the lattice generating an oscillation in the form of an excited phonon. The process can involve one, two and more scattering events. Typically at energies in the THz energy range, only single scattering events occur.

For a single inelastic scattering event, the energy and momentum conservation is given by

$$E' - E = \pm\hbar\omega_s(\mathbf{k}) \tag{3.15}$$

and

$$\mathbf{p}' - \mathbf{p} = \pm \hbar \mathbf{k} \pm \hbar \mathbf{K}, \quad \left(\mathbf{q}' - \mathbf{q} = \pm \mathbf{k} \pm \mathbf{K} \right). \tag{3.16}$$

The periodicity of the lattice ensures that $\omega_s(\mathbf{k} \pm \mathbf{K}) = \omega_s(\mathbf{k})$. Equations 3.16 and 3.15 then imply,

$$\frac{\mathbf{p}'^2}{2m} - \frac{\mathbf{p}^2}{2m} = \pm \hbar \omega_s(\mathbf{k} \pm \mathbf{K}). \tag{3.17}$$

In an INS experiment $\mathbf{p}$ and E are known in advance by selection using specially design monochrometers that operate by Bragg reflection. A neutron detector allows the measurement of the intensity of scattered neutrons for a given direction. By scanning the detector's energy, detecting a peak at energy E' automatically identifies $\mathbf{p}'$ (since $\|\mathbf{p}'\| = (2mE')^{1/2}$). One can then determine $\omega = (E' - E)/\hbar$ and $\mathbf{k} = (\mathbf{p}' - \mathbf{p})/\hbar \pm \mathbf{K}$, which gives a point, $\omega_s(\mathbf{k})$, in the surface of $\mathbf{k}$ space. This corresponds to an excited mode of the material under investigation, with polarisation s, in the reciprocal space direction $\hat{k} = \mathbf{k}/\|\mathbf{k}\|$. The information obtained by INS is the peak intensity (I), related to the scattering cross section of the atoms making up the unit cell. The energy difference ($E' - E$) is analogous to the absorption frequency in THz spectroscopy.

The INS measurements performed in this thesis were undertaken on the thermal triple-axis INS beamline, TAIPAN, at the Open Pool Australian Lightwater (OPAL) reactor. The OPAL reactor is facilitated by the Bragg Institute of ANSTO. The OPAL reactor operates at 20 MW and uses 16 low-enriched plate-type fuel assemblies undergoing controlled fission by neutron bombardment. A steady flow of neutrons is released in the reactor core which are moderated by a 13 m open pool of light water (normal H_2O). Heavy water (D_2O) is used as the neutron reflector. Neutrons are roughly monochromated and collimated by slabs of [115] oriented Germanium crystals. They are then directed by means of slits towards a beam port in the reactor wall.

With the reactor 'on' and the beam port open, a stream of neutrons (2.4×10^7)n/cm^{2}s on TAIPAN beamline) becomes available for scattering at the sample [220]. A shielded high pressure ^{3}He detector properly mounted to scan the $2\theta_s$ scattering angle in a wide range, counts the scattered neutrons which carry the desired information about the energy and momentum of the excitations in the sample.
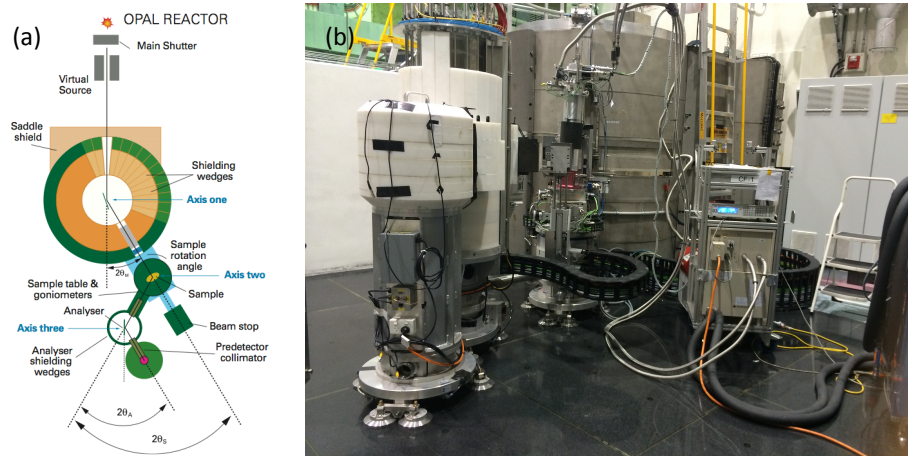
FIGURE 3.15: (a) Schematic diagram of TAIPAN INS beamline at the Bragg Institute, ANSTO. (b) Photograph of TAIPAN.

TAIPAN is able to make either constant $\mathbf{Q}$ (momentum) scans, or constant E (energy) scans to obtain more precise information on the peaks giving the phonon (or spin-wave) dispersion relations, $(\omega(\mathbf{k}))$. The experimental uncertainty depends on the degree of collimation and the quality of monochromatisation, which is always limited by the flux of the neutrons available. A schematic diagram of the TAIPAN spectrometer along side a photograph is shown in Figure 3.15.

Chapter 4

Supporting theory and analysis techniques

This chapter provides some discussion on the supporting theory and mathematical formalism encountered in this thesis. Section 4.1 takes a brief look at the nature of spectroscopic excitations, with particular focus on crystal and magnetic lattice modes. Details about the components that make up the magnetic Hamiltonian are covered in Section 4.2. Finally, Section 4.3 details some of the analysis techniques used to study the spectra obtained in the experiments. More detailed theories and analysis techniques are presented and discussed when required in the experimental chapters.

4.1 Spectroscopic excitations

As reviewed in Section 2.2.2, spectroscopy at THz frequencies presents opportunities to study a broad range of material properties. Many examples of this, such as the dielectric constant and carrier concentration are presented in Chapter 5 which focuses on the semiconductor ZnTe. The rest of the experimental chapters however, focus on the discrete crystal and magnetic excitations prevalent in magnetic materials. The two elementary excitations predominantly encountered are known as phonons and spin waves. A brief discussion of the origin and mathematical derivation of these two excitations follows.

4.1.1 Phonons

Phonons are the elementary excitations or vibrations of the atoms in a solid crystal material. Essentially, a crystallised solid is a lattice of relatively heavy nuclei surrounded by a network of localised and de-localised electrons. At equilibrium temperatures above $0\,\mathrm{K}$, the thermal energy exists in the form of vibrations within the lattice that are distributed according to the partition laws of quantum mechanical statistics. The quantised energy $(\hbar\omega)$ and momenta $(\hbar\mathbf{k})$ are known as phonons which obey Bose-Einstein statistics and Planck's distribution law [4]. That is, for a system in thermal equilibrium at a temperature T, the number of phonons (N) is given by $N = \left(e^{\hbar\omega/k_{\mathrm{B}}T} - 1\right)^{-1}$ where k_{B} is the Boltzmann constant. Phonons can be considered as normal modes of the lattice, which are vibrations characterised by a wave vector $(\mathbf{k})$, a polarisation (s) and a frequency $(\omega_{\mathbf{k}})$. The polarisation can either be longitudinal, $\parallel \mathbf{k}$ or transverse, $\perp \mathbf{k}$. The frequency is related to the wave vector through a propagation velocity $v_s(\hat{k}) = \omega_s(\mathbf{k})|\mathbf{k}|$, which is the sound velocity in the solid [4]. Such modes are called acoustic modes where all atoms move in the same direction along a chain. In a lattice with more than one kind of atom with a different charge, optical modes are also present where neighbouring atoms will move in opposite directions.

4.1.1.1 Phonon dispersion

The dynamics of a phonon and the relationship between its frequency and wave vector are given by the dispersion relation. This relationship is best derived by considering the equations of motion in a one-dimensional monatomic crystal. Figure 4.1 shows a chain of spring coupled masses m, where the pth mass is coupled to the $p-1$ and $p+1$ masses by a spring constant C. The force acting on one side of mass p is defined by Hook's law, $F = C(x_{p+1} - x_p)$. Here $(x_{p+1} - x_p)$ represents the extension of the spring to the right of m_p. Including all nearest-neighbour interactions (spring extensions on both sides of m_p) and equating the force to the rate of change in momentum, gives the equation of motion,

$$m\frac{d^2 x_p}{dt^2} = C(x_{p+1} + x_{p-1} - 2x_p). \tag{4.1}$$

Solutions are sought where the displacements vary sinusoidally in time and position and take the form,

$$x_{p\pm1} = x e^{(ika(p\pm1))} e^{(-i\omega t)}, \tag{4.2}$$

where ω is the angular frequency, a is the spacing between masses and k is the wave vector. Substituting through and cancelling common factors gives,

$$\omega^2 m = -C \left[e^{(ika)} + e^{(-ika)} - 2 \right]. \tag{4.3}$$

The identity $2\cos ka = \exp[ika] + \exp[-ika]$ gives the common form of the dispersion relation $\omega(k)$,

$$\omega^2 = 2\frac{C}{m}(1 - \cos ka) = 4\frac{C}{m}\sin^2\left[\frac{ka}{2}\right]. \tag{4.4}$$

The boundary of the first Brillouin zone lies at $k = \pm\pi/a$.

For a diatomic system with two masses m and M the dispersion relation becomes [29],

$$\omega_\pm^2 = C\left(\frac{1}{m} + \frac{1}{M}\right) \pm C\sqrt{\left(\frac{1}{m} + \frac{1}{M}\right)^2 - \frac{4\sin^2(ka/2)}{mM}}. \tag{4.5}$$

The (+) gives solutions to the optical mode while the (-) to the acoustic mode. The dispersion relation for the diatomic case is shown graphically in Figure 4.2. The **E** field of photons can couple to the oscillating dipole of certain phonons and excite them. In reciprocal space, for all of the optical frequencies (THz up to ultraviolet), the wave vector for electromagnetic radiation in a typical solid is very small in comparison to the reciprocal lattice vectors ($\|\mathbf{k}\| << \pi/a, \pi/b, \pi/c$). The magnitude can therefore be approximated as zero $k \approx 0$ which indicates that optical photons only probe zone-centre excitations. Referring to Figure 4.2, this means that only 'optical' phonons are optically active (hence their name) and this is because they feature changing dipole moments required for coupling to the photon's **E** field while acoustic phonons do not.

4.1.2 Spin waves or magnons

The ordering of magnetic moments in a lattice network, such as in a ferromagnetic material, is analogous to the ordered atomic structure of a crystal lattice and is accompanied by
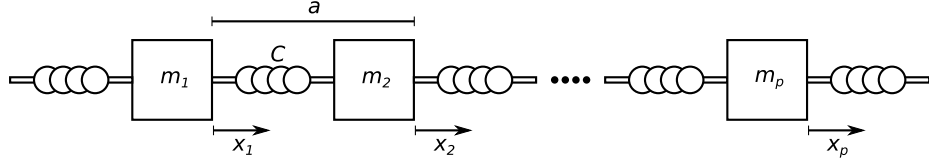
FIGURE 4.1: One-dimensional monatomic model. A chain of masses m, separated by a distance a, are linked by springs with force constant C.
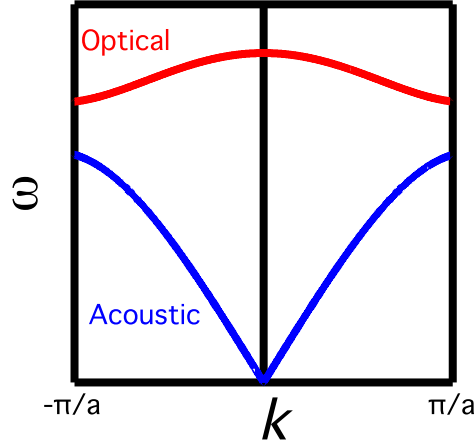
FIGURE 4.2: Phonon dispersion for diatomic model. In the monatomic case only the acoustic mode exists. Optical photons can excite modes at the zone centre ($k = 0$).

elementary excitations similar to phonons. These excitations are referred to as spin-wave or magnon modes and constitute oscillations in the microscopic magnetisation. In the case of a simple one-dimensional ferromagnet shown in Figure 4.3 (a), the ground state is characterised by all spins being in parallel alignment. In analogy to the spring connected masses, the nearest-neighbour interaction of spin moment $\mathbf{S}_p$ to $\mathbf{S}_{p+1}$ is given by the Heisenberg interaction and the net internal energy U, over N spins, is therefore,

$$U = -2J \sum_{p=1}^{N} \mathbf{S}_p \cdot \mathbf{S}_{p+1}. \tag{4.6}$$

Here J is the Heisenberg exchange integral. Treating the spin moments as classical vectors with $\mathbf{S}_p \cdot \mathbf{S}_{p+1} = S^2$, the internal energy becomes $U_0 = -2NJS^2$. A possible excited state is shown in Figure 4.3 (b) by flipping one spin moment. This increases the energy by $8JS^2$, i.e. $U_1 = U_0 + 8JS^2$. There is however, a lower energy state if each spin moment is able to share the effects of the reversal producing a wave like oscillation as in Figure 4.3 (c)

and (d). This is the spin-wave excitation which, like the phonon, is a boson and follows Bose-Einstein statistics with Planck's distribution at a temperature T [29].

4.1.2.1 Spin-wave dispersion

The dispersion relation is determined by the mechanical equivalence of the rate of change of angular momentum and torque. The magnetic moment is written as $\mu_p = -g\mu_B \mathbf{S}_p$ where g is the g-factor and μ_B is the Bohr magneton. Then, from Equation 4.6 the interaction on the pth spin moment is,

$$-2J\mathbf{S}_p \cdot (\mathbf{S}_{p-1} + \mathbf{S}_{p+1}) = -\mu_p \cdot [(-2J/g\mu_B)(\mathbf{S}_{p-1} + \mathbf{S}_{p+1})]. \tag{4.7}$$

Treating the exchange interaction as an effective magnetic field, Equation 4.7 is of the form $-\mu_p \cdot \mathbf{B}_p$ with $\mathbf{B}_p = (-2J/g\mu_B)(\mathbf{S}_{p-1} + \mathbf{S}_{p+1})$. Therefore, equating the rate of change of angular momentum to a torque in the form $\hbar d\mathbf{S}_p/dt = \mu_p \times \mathbf{B}_p$ gives,

$$\hbar \frac{d\mathbf{S}_p}{dt} = \frac{2J}{\hbar} (\mathbf{S}_p \times \mathbf{S}_{p-1} + \mathbf{S}_p \times \mathbf{S}_{p+1}). \tag{4.8}$$

Converting to Cartesian coordinates $\mathbf{S}_p = (S_p^x, S_p^y, S_p^z)$, with $S_p^z = S$ and assuming small oscillations (i.e. $S_p^z, S_p^z \ll S$), Equation 4.8 can be simplified into three linear equations,

$$dS_p^x/dt = (2JS/\hbar)(2S_p^y - S_{p-1}^y - S_{p+1}^y); \tag{4.9}$$

$$dS_p^y/dt = (2JS/\hbar)(2S_p^x - S_{p-1}^x - S_{p+1}^x); \tag{4.10}$$

$$dS_p^z/dt = 0. \tag{4.11}$$

As with the phonon case, solutions are sought where the displacements vary sinusoidally in time and position,

$$S_p^x = ue^{[i(pka - \omega t)]}; \tag{4.12}$$

$$S_p^y = ve^{[i(pka - \omega t)]}, \tag{4.13}$$

where u and v are constants and a is the lattice spacing. Following the process used in the phonon case, substitution and solving the simultaneous equations gives the dispersion

relation for a one dimensional ferromagnet,

$$\hbar\omega = 4JS(1 - \cos ka). \tag{4.14}$$

The antiferromagnetic case is reminiscent of the diatomic phonon case and requires the treatment of two spin sublattices. Following a similar procedure the dispersion relation is given as,

$$(\hbar\omega)^2 = (4JS)^2(1 - \cos^2 ka). \tag{4.15}$$

The square property of the antiferromagnetic case indicates two modes ($\pm$ solutions to the square root) due to the two sublattices. Under normal conditions these modes are degenerate but this degeneracy may be lifted by the application of external fields or by internal anisotropic effects. The dispersion curves for the ferromagnetic and antiferromagnetic cases is shown in Figure 4.3. Because the antiferromagnetic model has two sublattices the effective lattice spacing doubles. This means that the zone boundary occurs at $\pi/2a$ in Figure 4.3.

For distinction, the magnon is usually referred to the quantised state whereas spin wave is the more classical interpretation analysed above, however both are often used intermittently in the literature. The **H** field component of a photon can couple to the spin-wave excitation generating resonance. Since the photons at optical wavelengths are confined to $k \approx 0$ excitations, referring to Figure 4.3, only modes with $\omega = 0$ are expected. The application of an external magnetic field or the presence of strong anisotropic effects can act to raise the energy generating a so called 'spin gap' creating optically active spin waves. Inelastic neutron scattering techniques are however able to access spin waves at higher **k** values. Neutron scattering is therefore the standard technique used to probe the dispersion of both phonons and spin waves across the entire Brillouin zone.

4.2 The magnetic Hamiltonian

As described above, the dynamics of interacting spins in a magnetic material are dependent on the coupling energies of the system. As well as the Heisenberg model described above,
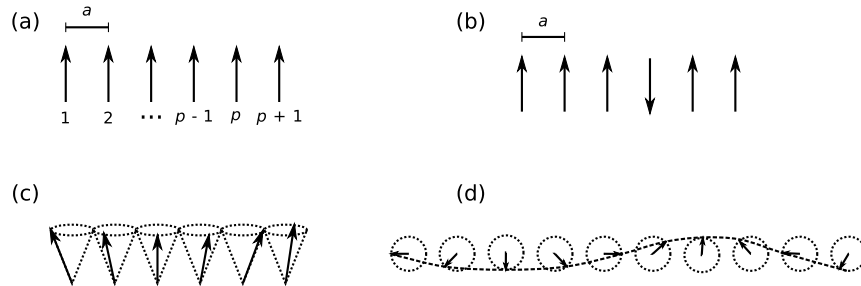
FIGURE 4.3: One-dimensional Heisenberg spin model. (a) Ground state of ferromagnet. (b) Possible excitation state. (c) Lower energy excited state with the spin reversal compensated by a precession of the system. (d) Top down view of spin moment precession forming spin wave.
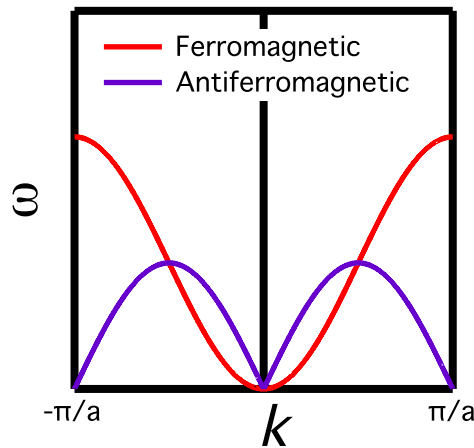
FIGURE 4.4: Spin wave dispersion for one-dimensional ferromagnet and antiferromagnet. The lattice spacing is double for the antiferromagnetic case making the zone boundary appear at $\pi/2a$ here.

there can be a variety of competing interactions between the individual magnetic moments, the crystal lattice and applied external fields. It is the compromise between these various interactions that determines the magnetic structure, macro scale magnetic properties and spin dynamics detectable by spin-wave excitation. The internal energy of a system at rest is given by the Hamiltonian. For a magnetic material which can be simulated as a system of atomic magnetic moments, the magnetic Hamiltonian can be separated into three main sections:

$$H_{\text{magnetic}} = H_{\text{exchange}} + H_{\text{anisotropy}} + H_{\text{Zeeman}}. \tag{4.16}$$

4.2.1 Exchange interaction

The first term refers to the effect of an array of neighbouring atomic moments each coupled to each other by a Heisenberg exchange which was first encountered in Section 4.1.2.1.

$$H_{\text{exchange}} = -J \sum \mathbf{S}_i \cdot \mathbf{S}_j, \tag{4.17}$$

where J is the exchange coupling constant (or exchange integral) and $\mathbf{S}_i$ and $\mathbf{S}_j$ are neighbouring spin moments. As briefly reviewed in Section 2.3, the exchange interaction results from quantum mechanical conditions invoking Coulombic coupling and the Pauli exclusion principle. The coupling acts to lower energy when spins are aligned in specific directions with respect to each other. When J is positive this mechanism is responsible for ferromagnetism. When J is negative antiferromagnetism occurs. The strength of the interaction is dependent on the distance between the two atoms. In a periodic lattice the factor of the atomic separation is combined into the exchange integral producing J. In systems where the magnetic atoms are too far apart to have overlapping orbitals, a super-exchange operating over a shared intervening anion (usually oxygen) can support long-range exchange coupling. The super-exchange can be expressed in identical form to the Heisenberg model above.

However, treating magnetic exchange with a spherically symmetric dot-product is only a good approximation for symmetrical systems. In low symmetry systems, such as metal oxides with rhombahedral structure, there is often some directionality in the bonding process leading to super-exchange. This results from a lack of inversion symmetry across the bond. Such bonding leads to another important exchanging interaction, namely the Dzyaloshinsky-Moriya (DM) interaction. The DM interaction is characterised by spins coupled with a cross-product,

$$H_{\text{DM}} = \mathbf{D}_{ij} \cdot (\mathbf{S}_i \times \mathbf{S}_j), \tag{4.18}$$

where $\mathbf{D}_{ij}$ is the DM coupling constant. Using symmetry arguments as a way to explain the weak ferromagnetism in αFe_2O_3, this interaction was first proposed by Dzyaloshinsky in 1958 [221]. Later, Moriya derived its form from quantum mechanics [222]. Since in the

case of perfectly parallel or antiparallel spins, the cross product vanishes ($\mathbf{S}_i \times \mathbf{S}_j = 0$) the DM interaction is most prevalent in systems with non-collinear spin structure which is a common property of multiferroic materials. The DM interaction is also often responsible for coherent spin canting (weak ferromagnetism) or incommensurate structures.

4.2.2 Anisotropy

While the exchange interaction is responsible for the mutual alignment of the individual spin moments in a magnetic material, it does not necessarily lead to the macroscopic alignment of the net magnetic moment in a physical sample. This stems from the dot product in the exchange interaction which only depends on the relative orientation of spins and not on their absolute directions. Yet when a ferromagnetic sample is examined, the spin moments are seen to favour certain crystallographic directions. The effect of a spin system favouring a long range direction in a physical crystal is termed magnetic anisotropy. Since the spin moments are localised to atomic sites in the crystal lattice there is an inherent spin-lattice coupling which may have a certain symmetry that is not completely spherical. Furthermore, the spins will also interact over long distances with each other by dipolar coupling. Such lowered symmetries influence the preferred directions for spins to point. The magnitude of this anisotropy in terms of energy is actually very small compared to the exchange coupling J. Nevertheless, it serves a crucial role in determining the actual spin structure of the system, along with hysteresis and angular dependent phenomena and is therefore important in technological applications.

Mathematically the form of the anisotropy must depend on the direction of the spin with respect to spacial directions and can be expressed either as some function of the angle between crystal axes, or equivalently as some function of the spin-variables. The simplest type of anisotropy is uniaxial, having only one important direction defined by an anisotropy constant K:

$$H_{\text{ansitropy}} = K S_z^2 \quad \text{(uniaxial case)}. \tag{4.19}$$

4.2.3   Zeeman coupling

The final component of the magnetic Hamiltonian is given by Zeeman coupling, where spin moments couple to an externally applied magnetic field $\mathbf{B}_{\text{ext}}$. This follows from the classical dipole coupling in a magnetic field and is given by,

$$H_{\text{Zeeman}} = -\mathbf{S}_i \cdot \mathbf{B}_{ext}. \tag{4.20}$$

This coupling is what allows an external magnetic field to polarise spins, magnetise and demagnetise permanent magnets. By definition, the magnetisation (M) in a certain direction ($\alpha = x, y, z$) reflects the average of all spins moments in the system along that direction,

$$M_\alpha = g\mu_{\text{B}} \sum_i^{i \leq N} \frac{S_i^\alpha}{N}, \tag{4.21}$$

where N is the total number of spins. Mathematically the relationship between M and B_{ext} is often expressed in terms of susceptibility χ,

$$\mu_0 M = \chi B_{\text{ext}}. \tag{4.22}$$

4.3   Analysis techniques

As described above, the frequency of the excitation modes is dependent on the energies associated with the interacting masses or spins. Analysis of the mode frequency is therefore a useful technique to assist understanding of the internal material properties. When radiation is incident on a sample, a portion of the incident intensity I_0 will be reflected (R) and a portion transmitted (T), as in Figure 4.5. It should also be noted that a portion is usually absorbed by the material requiring another coefficient A. However, in the materials studied in this thesis, this contribution is usually negligible and can be incorporated into the transmittance coefficient. The expression relating incident radiation to reflection and transmission is,

$$I_0 = (R + T)I_0 = I_{\text{R}} + I_{\text{T}}, \tag{4.23}$$
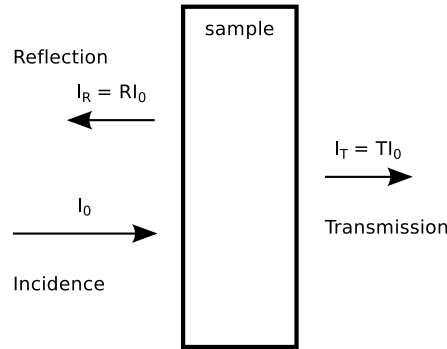
FIGURE 4.5: Relationship between incident radiation on a sample and the reflected and transmitted beams.

where $R, T < 1$. The reflectance and transmittance coefficients are then determined by measuring the reflected and transmitted intensities (I_R and I_T) and dividing them by the incident intensity,

$$R = \frac{I_R}{I_0}; \tag{4.24}$$

$$T = \frac{I_T}{I_0}. \tag{4.25}$$

In the spectroscopic measurements of R and T for materials that feature optically active phonon and spin-wave modes, the excitations will appear as absorption peaks in the R and T data. Typically in reflection, the Reststrahlen effect will cause narrow bands of high reflectivity near a strongly absorbing feature. This is due to a change in refractive index concurrent with the specific absorbance, which inhibits the propagation of the radiation resulting in increased reflectivity. Reflection measurements are further complicated by the difficulty in experimental setup. When measuring in reflectance, it is important that no reflected rays from surfaces other than the sample are detected which may give erroneous data. For this reason it is also often difficult to measure reference reflectance spectra. The angular dependence must also be taken into consideration since normal incidence measurements are not usually feasible.

Contrary to this, transmittance measurements are relatively simple. Normal incidence measurements are routinely achieved by placing the source, sample and detector in the same optical plane with the radiation incident on each component at normal incidence. Placing an opaque aperture around the sample ensures only radiation transmitted through the sample is detected. Transmittance measurements, however, are limited to samples with

low conductivity and density of spectral features to allow a good portion of the radiation to transmit through. This limits the transmission geometry for many interesting material types. Fortunately the oxide materials investigated in this thesis are characterised by low conductivity and therefore transmit a detectable intensity.

The spectral features in transmission typically appear as clear adsorption dips. They are therefore easily fitted with a Lorentzian distribution of the form

$$\frac{A}{(r - r_0)^2 + B} \ . \tag{4.26}$$

The value of r_0 gives the central position of the function's peak. When applied to the absorption dip, this gives the frequency of the excitation. The line width can then be determined from the full width at half maximum of the Lorentzian fit. This is given as,

$$\text{FWHM} = 2\sqrt{B} \ . \tag{4.27}$$

As a way of quantifying the strength of the absorption feature, the area under the Lorentzian distribution is used [223],

$$\text{area} = \frac{\pi A}{\sqrt{B}} \ . \tag{4.28}$$

When the transmitted signal is divided by the background signal the resultant transmission as a function of frequency is dimensionless. Therefore the area under the curve will have units of Hz.

A full treatment of the transmittance properties and formalism of THz radiation through a physical sample is left for the experimental chapter on ZnTe (Chapter 5). However, it is beneficial to briefly discuss the technique of extracting the transmittance response from the magnetic contribution separately from the crystal lattice contribution, as it is used a number of times. The transmittance coefficient, for now, is defined as [224],

$$T = \left[\frac{4\eta}{(\eta + 1)^2 + \kappa^2} \right] e^{-\alpha d}, \tag{4.29}$$

where η is the refractive index, κ is the imaginary refractive index or absorption loss and α is the extinction coefficient. The first factor (contained within the square braces) represents

the percentage of radiation transmitted at the sample interfaces and is considered a purely dielectric response (resulting only from the electrical properties of the crystal lattice). The second term (featuring the exponential) represents the Beer-Lambert absorption as the radiation transmits through the sample of thickness d.

It may seem awkward to have both κ and α in the same expression as if they were independent. In a material with only a dielectric response, α is related to κ by $\alpha = \frac{2\pi\omega}{c}\kappa$, where ω is the angular frequency of the radiation. However, when there is a magnetic response from the spin lattice of a sample, the extinction coefficient contains terms relating to the magnetic susceptibility (explained further in Section 7.4.5). It is therefore convenient to treat α, which contains dielectric and magnetic components, separately from κ, which is only a dielectric property. In this regard, the dielectric response from the crystal lattice (lat) can be separated from the magnetic response (mag) by breaking the extinction coefficient into two terms,

$$\alpha = \alpha_{\text{lat}} + \alpha_{\text{mag}}. \tag{4.30}$$

Substituting back into Equation 4.29 gives the following expression, where the magnetic response is entirely confined to one factor $(\exp\left[-\alpha_{\text{mag}}d\right])$,

$$T = \left[\frac{4\eta}{(\eta+1)^2 + \kappa^2}\right] e^{-\alpha_{\text{lat}}d} e^{-\alpha_{\text{mag}}d}. \tag{4.31}$$

Therefore dividing through by an intensity that is purely a lattice response, the magnetic response is separated out,

$$I_{\text{mag}} = \frac{I_{\text{lat+mag}}}{I_{\text{lat}}} = e^{-\alpha_{\text{mag}}d}. \tag{4.32}$$

The technique is performed by measuring a sample under two (or many) different conditions where the magnetic response has changed but the crystal response has remained constant. This can be achieved for example by changing the sample temperature or applying an external magnetic field. While both of those conditions will indeed affect the crystal lattice, this change will be negligible to the change observed in the magnetic contribution and can therefore generally be neglected. A 'lattice reference' is constructed by taking points with the maximum value at a specific frequency from the two spectra under different magnetic conditions. This has the effect of sampling the spectra without the magnetic
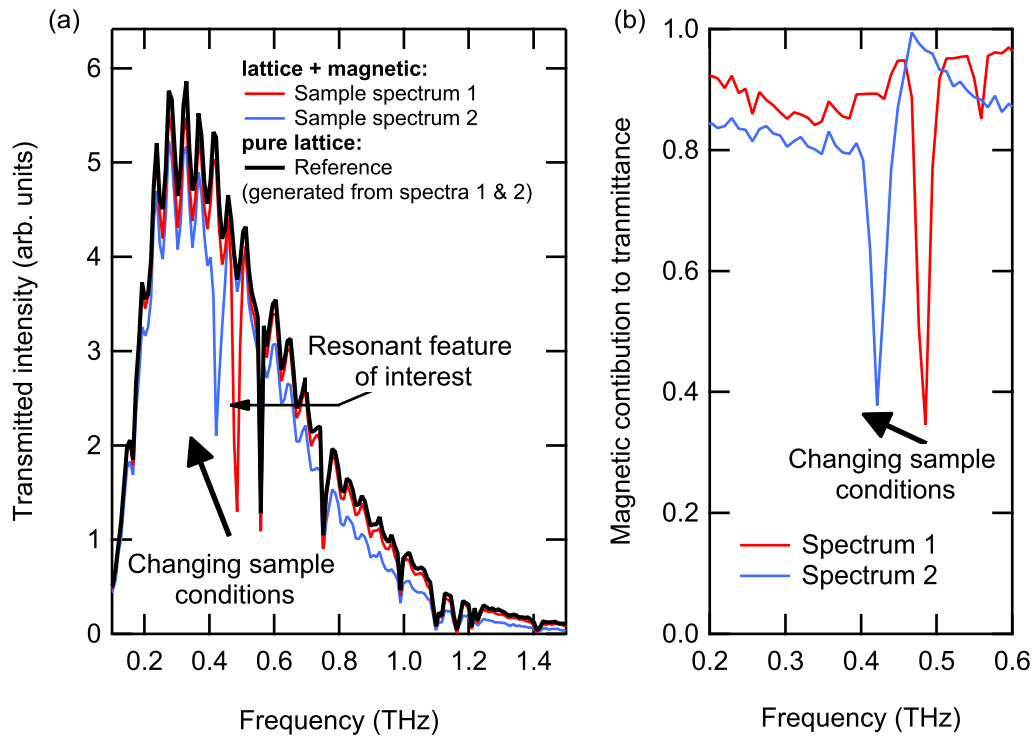
FIGURE 4.6: Procedure for extracting magnetic contribution to transmittance spectrum. (a) Transmission spectra at different magnetic conditions. (b) Spectra divided by constructed lattice spectrum.

spectral features of interest. Dividing the individual spectra by the lattice spectrum gives the a pure magnetic transmittance contribution. The process is shown in Figure 4.6 using sample data from Chapter 7.

4.3.1 A note on frequency, wavenumber and energy units

Radiation is quantified in many ways. In this thesis, frequency is primarily used. The frequency of radiation is measured as cycles per second. This refers to how many oscillations of the **E** field occur in one second. This unit is referred to as hertz (Hz).

$$1 \text{ Hz} = 1 \text{ s}^{-1} = 1 \text{ cycle per second.}$$

Terahertz refers to an order of magnitude of hertz, precisely, 10^{12} Hz or THz. As has already been prevalent in this thesis, the short form THz is often used to denote both a specific frequency, i.e 1 THz, and a short form way of referring to terahertz radiation

i.e. the spectral band of 0.1–10 THz. While this may seem like a confusing notion, when reading, the context should make it easy to follow. In general, when a specific frequency is given, "THz" will always be preceded by a number.

As well as the time between electromagnetic oscillations there is also a spacial separation. Furthermore, radiation also carries energy. Therefore, there are also other units used to quantify radiation such as wavelength, wavenumber and energy. The use of these other units generally depends on the branch of research. Optical physics using laser light in the visible range, for example, tends to use wavelength, i.e metres (m) or the nanometre (nm). High energy physics involving x and gamma rays use energy, i.e the electron volt (eV) as well as kilo (keV) or mega (MeV) electron volts. Infrared physics uses the wavenumber or inverse meters (m^{-1}) and inverse centimetres (cm^{-1}). The hertz is a convenient unit as it is directly proportional to the radiation energy unlike wavelength and scales well across a large spectral range. Therefore, in this thesis the THz unit is used almost exclusively. A table of the conversion from THz into other common spectroscopic units is given in Table 4.1.

However, in interferometer studies, the path length is measured in cm and so the naturally converted radiation unit is the wavenumber (cm^{-1}). In most cases measurements taken in this realm have been converted to THz for consistency with the thesis and other spectrometer systems. Except, there are certain cases where direct comparison with path length and radiation frequency/wavenumber/resolution etc. are made, and therefore the cm^{-1} unit is used. In all of these cases, the THz conversion is also given.

Lastly, for the complementary measurements using inelastic neutron scattering provided in Chapter 8, the energy unit meV or milli electron volt is also frequently used. This is because, while a neutron can be represented as a waveform, conventionally they are considered particles with an energy governed by their kinetics. In this case the meV unit is convenient and, following convention, is used in this thesis when referring to neutron studies presented as results, and from the literature. In all cases the THz conversion is also given.

TABLE 4.1: Common spectroscopic unit conversions to four significant figures.

	THz	cm^{-1}	meV	μm
THz	1	33.36	4.136	299.8
cm^{-1}	0.02998	1	0.1240	10^4
meV	0.2418	8.066	1	1240
μm	299.8	10^4	1240	1

Chapter 5

Introduction to terahertz transmission spectroscopy: Optical properties of ZnTe

5.1 Introduction

Before the magnetic properties of materials are studied by THz radiation, it is beneficial to cover ground on standard dielectric based spectroscopy to establish some of the methods and theory used later. This chapter demonstrates the fundamental techniques of transmission THz spectroscopy in characterising a non magnetic semiconductor material with no distinct absorption features. In particular, transmittance THz spectra of the II-VI semiconductor, ZnTe, are studied.

The rapid development of optoelectronic based devices for use in THz emission and detection was established in Chapter 2. Of particular interest in this field is the II-VI polar semiconductor zinc telluride (ZnTe), which exhibits birefringence at visible frequencies when illuminated with THz radiation [225, 226]. The magnitude of the birefringence is dependent on the incident THz power, which in turn can be monitored using optical sampling, hence forming a THz detector system [227]. Conversely a high-powered optical pulse incident on a ZnTe crystal will experience nonlinear effects, which can produce THz

radiation through optical rectification [225–228]. Recent work has demonstrated marked impoundments in the THz output by optical rectification for ZnTe through unique modifications of the pump pulse shape [229, 230] and by fabrication of ZnTe structures [231]. For device applications such as this, it is important that accurate values of the material's optical parameters are known. While the various properties of ZnTe have been investigated for some time [232–237], there is still considerable discrepancy between the results presented in the literature [116, 238–248]. The results presented within this chapter help to address such discrepancies and borrow heavily from Constable and Lewis [JAP 112, 063104 (2012)], *Optical parameters of ZnTe determined using continuous-wave terahertz radiation.* The optical parameter measurements of ZnTe are presented by analysing transmission geometry measurements with theoretical fits based on a model of the dielectric function. It is established that THz radiation is particularly useful for characterising semiconductor materials due to its strong coupling with the free electrons and phonon interactions of the material [247, 249]. The measurements are performed using the two-colour THz source as a tunable continuous-wave THz spectrometer with the transmittance measured at normal incidence for three ZnTe crystal wafers with different thicknesses. A central finding is that the genuine quality of fit and hence uncertainty in the determined parameters must be calculated by a statistical method known as the bootstrap analysis. The information is presented in summary with results given in the literature and therefore provides a valuable reference for the optical parameters of ZnTe.

The bootstrap analysis technique offers a way of accurately determining the quality of fitted parameters in functions where the higher order differentials, with respect to the parameter, are non zero [250]. Standard least squares fitting procedures used by most graphing software packages determine parameters and their uncertainties by a series of partial differentials, with respect to the fitting parameters. When the higher order differentials of a parameter are non zero, the series must be approximated to converge and therefore calculated errors tend to be underestimated. This is especially prevalent when there is cross-correlation between the fitted parameters. The bootstrap technique is an established statistical analysis method and has had some traction in the chemical and biological sciences with applications in reaction statistics [251]. However, it has gone largely unused in the realm of condensed matter physics as a method for improving the accuracy

of theoretically fitted parameters. Unfortunately, in the age of cheap computer processing power, researchers may often apply the fitting procedures of software packages to their data in blind faith. The assumption that since the experimental data are analysed by a computer, the results must be meaningful and correct is naturally problematic and can lead the researcher to overestimate the significance of their results [252]. The development of a bootstrap analysis of the results presented in this chapter is therefore of considerable importance not only in THz science analysis but in the broader physics community.

The chapter is structured as follows: Section 5.2 establishes the theoretical basis for the transmittance of plane wave THz frequency light normal to a semiconducting wafer. The outcome produces a model for the transmittance as a function of frequency with the optical parameters as fitting parameters. Section 5.3 outlines the experimental and analysis details. This covers the instrument setup, sample details and a detailed explanation of the bootstrap fitting procedure. Section 5.4 presents the results of the experiments and fitting procedure. A discussion of the results is provided with particular attention to the uncertainties introduced by cross-correlation between fitting parameters. The values obtained are compared with previously published results and used to calculate carrier concentration. Section 5.5 provides a summary of the chapter.

5.2 Derivation of terahertz transmittance for plane parallel semiconductor

The transmittance of plane wave THz radiation incident on a plane parallel semiconductor are derived from first principles starting with Maxwell's equations. By treating the sample as an insulator, the dispersion relation inside the crystal for a plane wave in one dimension can be represented as a function of the angular frequency of the incident THz radiation ($\omega = 2\pi\nu$) [182],

$$k^2 = \frac{\omega^2}{c^2}\epsilon(\omega),\qquad(5.1)$$

where both the wave number, k, and the angular frequency-dependent dielectric function, $\epsilon(\omega)$ are complex. In solving Maxwell's equations, when considering the crystal polarisation and current density, it is found that for a polar material containing free charge carriers

such as ZnTe the dielectric function can be modelled using three terms taking the form [247],

$$\epsilon(\omega) = \epsilon(\infty) - \frac{\epsilon(\infty)\omega_{\mathrm{p}}^2}{\omega^2 + i\omega\gamma} + \frac{(\epsilon(0) - \epsilon(\infty))\omega_{\mathrm{TO}}^2}{(\omega_{\mathrm{TO}}^2 - \omega^2) + i\omega\Gamma}, \tag{5.2}$$

where $\epsilon(\infty)$ is the high frequency dielectric constant, also referred to as the optical, lattice, or ac dielectric constant. $\epsilon(0)$ is the low frequency dielectric constant and is also known as the static, or dc dielectric constant. ω_{p} is the angular plasma frequency ($\omega_{\mathrm{p}}^2 = ne^2/m^*\epsilon_0\epsilon(\infty)$), ω_{TO} is the angular transverse optical phonon frequency, γ is the plasma damping constant or collision frequency, and Γ is the phonon damping constant. The first term is referred to as the atomic term since it results from the displacement of the atomic electrons in relation to their effectively stationary ions in the lattice. The second term comes from the Drude model assumption of the motion of free electrons with respect to the lattice. The final term, known as the Lorentz term, represents the oscillation of the positive Zn^{2+} ions relative to the negatively charged neighbouring Te^{2-} ions.

It is convenient, when working with a complex dielectric function, to separate the real and imaginary parts by defining

$$\epsilon \equiv \epsilon_1 + i\epsilon_2, \tag{5.3}$$

where

$$\epsilon_1 = \epsilon(\infty) - \frac{\epsilon(\infty)\omega_{\mathrm{p}}^2}{\omega^2 + \gamma^2} + \frac{(\epsilon(0) - \epsilon(\infty))\left(\omega_{\mathrm{TO}}^2 - \omega^2\right)\omega_{\mathrm{TO}}^2}{\left(\omega_{\mathrm{TO}}^2 - \omega^2\right)^2 + \omega^2\Gamma^2}, \tag{5.4}$$

and

$$\epsilon_2 = \frac{\epsilon(\infty)\omega_{\mathrm{p}}^2\gamma}{\omega^3 + \omega\gamma^2} - \frac{(\epsilon(0) - \epsilon(\infty))\omega\omega_{\mathrm{TO}}^2\Gamma}{\left(\omega_{\mathrm{TO}}^2 - \omega^2\right)^2 + \omega^2\Gamma^2}. \tag{5.5}$$

The same treatment is given to the complex wave number, defining

$$k \equiv \alpha + i\beta = \frac{\omega}{c}N = \frac{\omega}{c}(\eta + i\kappa). \tag{5.6}$$

Here, N is the complex index of refraction, α determines the wavelength ($\lambda \equiv 2\pi/\alpha$) and β determines the attenuation length ($\zeta \equiv 1/\beta$) . Relating this to the dispersion relation (Equation 5.1) gives

$$\alpha = \frac{\omega}{c}\eta = \frac{\omega}{c}\left(\frac{|\epsilon| + \epsilon_1}{2}\right)^{\frac{1}{2}} \tag{5.7}$$
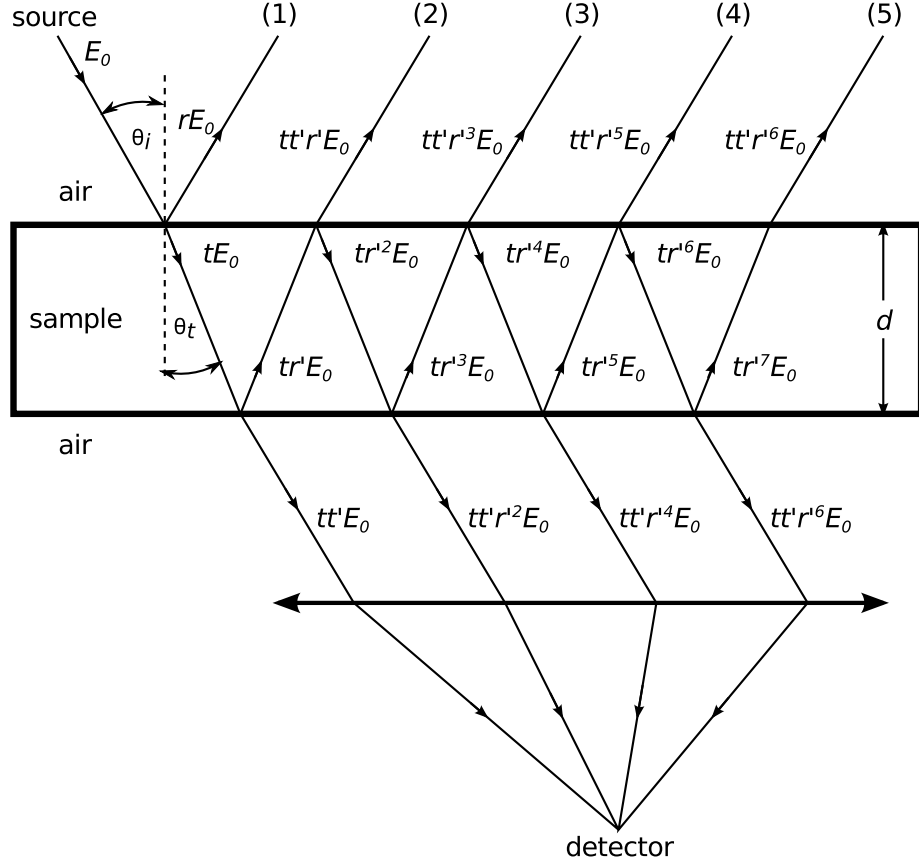
FIGURE 5.1: Multiple ray paths through a plane parallel sample. Constructive and deconstructive interference can occur when path lengths equal integer and half integer multiples of the incident light wavelength.

and

$$\beta = \frac{\omega}{c}\kappa = \frac{\omega}{c}\left(\frac{|\epsilon| - \epsilon_1}{2}\right)^{\frac{1}{2}},$$

(5.8)

where $|\epsilon| \equiv (\epsilon_1^2 + \epsilon_2^2)^{\frac{1}{2}}$.

The propagation of linearly polarised THz radiation through the ZnTe samples at normal incidence is described by standard Fabry-Perot theory. When considering a plane parallel slab such as the ZnTe wafer examined here, one must consider the multiple reflections and transmission that occur as a result of interactions with the two parallel surfaces of the sample (see Figure 5.1). When working through this problem, the total transmission or reflection is calculated by summing all of the individual components due to the multiple reflections from each surface. Interference occurs as a result of phase mismatch due to the different optical path lengths experienced by the different components.

The incident **E** field in scalar form is defined as $E_0 e^{-i\omega_0 t}$. Phase differences due to the differing optical paths are represented by additional factors of $e^{i\delta}$, where δ is the phase difference, $\delta = k\Delta = \left(\frac{2\pi}{\lambda_0}\right)\Delta$. The optical path difference, Δ, is given by $\Delta = 2Nd\cos\theta_t$. Therefore, the common $e^{-i\omega t}$ factors can be neglected. The total electric field transmitted through the slab is defined as $E_t e^{-i\omega_t t}$. So in reference to Figure 5.1, the total (E_t) becomes,

$$E_t = tt'E_0 e^{i\delta} + tt'r'^2 E_0 e^{3i\delta} + tt'r'^4 E_0 e^{5i\delta} + tt'r'^6 E_0 e^{7i\delta} + ...$$
$$= tt'E_0 e^{i\delta}\left[1 + r'^2 e^{2i\delta} + r'^4 e^{4i\delta} + r'^6 e^{6i\delta} + ...\right].$$

The factor enclosed in brackets is a converging geometric series with $r'^2 E_0 e^{2i\delta}$, giving,

$$E_t = tt'E_0 e^{i\delta}\frac{1}{1 - r'^2 E_0 e^{2i\delta}}$$
$$= (1 - r^2)E_0 e^{i\delta}\frac{1}{1 - (-r)^2 E_0 e^{2i\delta}}$$
$$\therefore \quad \frac{E_t}{E_0} = \tau = \frac{(1 - r^2)e^{i\delta}}{1 - r^2 E_0 e^{2i\delta}},$$

where $r = |r|e^{i\phi_r}$ is complex and given by the Fresnel equations for an infinite half-space at normal incidence. The magnitude and phase of the infinite half space reflection coefficient are given by [182],

$$|r| = \left[\frac{(1 - \eta)^2 + \kappa^2}{(1 + \eta)^2 + \kappa^2}\right]^{\frac{1}{2}} \tag{5.9}$$

and

$$\phi_r = \arctan\left[\frac{2\kappa}{1 - \eta^2 - \kappa^2}\right]. \tag{5.10}$$

To find the observable transmittance, $T = \tau\tau^*$ is taken, where $T = \frac{I_\mathrm{T}}{I_0}$ as defined in Section 4.3.

$$
\begin{aligned}
\tau\tau^* &= \frac{\left(1 - |r|^2 e^{2i\phi_r}\right) e^{i\alpha d} e^{-\beta d}}{1 - |r|^2 e^{2i\phi_r} e^{2i\alpha d} e^{-2\beta d}} \frac{\left(1 - |r|^2 e^{-2i\phi_r}\right) e^{-i\alpha d} e^{-\beta d}}{1 - |r|^2 e^{-2i\phi_r} e^{-2i\alpha d} e^{-2\beta d}} \\
&= \frac{e^{-2\beta d} \left(1 - |r|^2 e^{2i\phi_r}\right) \left(1 - |r|^2 e^{-2i\phi_r}\right)}{\left(1 - |r|^2 e^{2i(\phi_r+\alpha d)} e^{-2\beta d}\right) \left(1 - |r|^2 e^{-2i(\phi_r+\alpha d)} e^{-2\beta d}\right)}.
\end{aligned}
$$

Expanding and simplifying through both the numerator and denominator gives

$$
T = \frac{e^{-2\beta d}(1 - |r|^2)^2 + 4|r|^2 \sin^2\left(\phi_r\right)}{\left(1 - |r|^2 e^{-2\beta d}\right)^2 + 4|r|^2 e^{-2\beta d} \sin^2\left(\alpha d + \phi_r\right)}. \tag{5.11}
$$

Substituting back through Equations 5.4, 5.5, 5.7, 5.8, 5.9 and 5.10 gives T as a function of ω, $\epsilon(0)$, $\epsilon(\infty)$, ω_p, ω_TO, γ, Γ, and d. The source code for the fitting function of Equation 5.11 as implemented by the WaveMetrics: Igor Pro software package is given in Appendix A.1

5.3 Experimental methodology

5.3.1 Equipment setup

The transmittance measurements are performed using the continuous-wave two-colour THz spectrometer. The samples are kept at room temperature. The spectrometer is operated as outlined in Section 3.1. In this experiment the laser amplifier was not required. A free-space optical path is implemented for the THz beam to allow transmission measurements of the ZnTe wafers. The modified setup is shown in Figure 5.2. The ZnTe wafers are placed at the focus of the THz beam between two off-axis parabolic mirrors. An 8 mm aperture was placed in front of the wafers to ensure the detected beam was entirely transmitted though the samples. A wire-grid linear polariser was placed in the beam path before the sample to ensure linear polarisation of the incident radiation. The ZnTe samples have a high transmission percentage providing a strong signal at the detector. The Schottky diode detector was implemented for detection. The spectrum is taken by measuring the transmitted intensity as a function of frequency from 0.15–1.0 THz at a resolution of 0.001 THz (1 GHz).
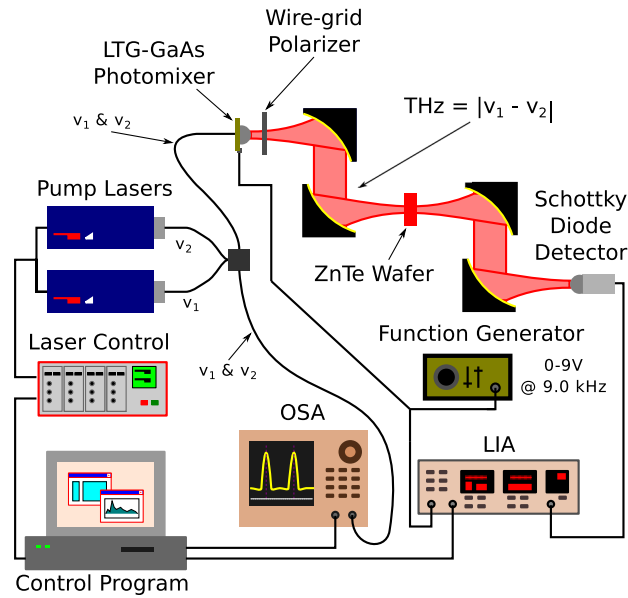
FIGURE 5.2: Two-colour THz spectrometer setup for measuring the ZnTe transmittance.
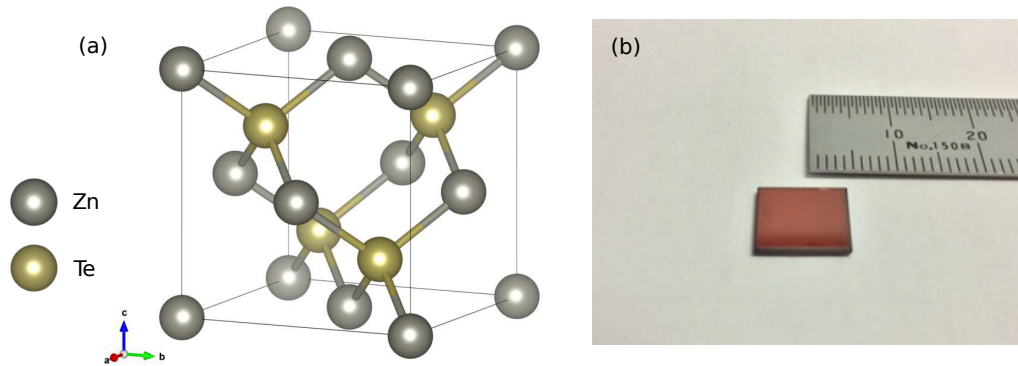
FIGURE 5.3: (a) Cubic zincblend structure of ZnTe (generated using VESTA [253] and information in Appendix B.1). (b) Photograph of ZnTe wafer sample ($10.0 \times 10.0 \times 1.0$ mm)

5.3.2 Sample details

ZnTe is a typical p-type II-VI semiconductor with a band gap of 2.23-2.25 eV [29]. Crystallising in the cubic zincblend crystal structure, it forms ruby-red crystals as seen in Figure 5.3 In this experiment, three separate ZnTe wafers with (110) faces (the standard for optoelectronic detection) are measured. The samples were commercially bought high purity wafers, obtained from Cradley Crystals. The wafers have faces of 10.0×10.0 mm^2 but different thicknesses.

TABLE 5.1: Average values of sample thickness, d, measured by micrometer for 10 different points on sample face.

nominal d (mm)	measured d (mm)
0.3	0.3075±0.0020
0.5	0.4932±0.0006
1.0	0.9908±0.0027

The nominal thickness for the wafers are $d = 0.3$, 0.5 and 1.0 mm. However, since the theoretical transmittance equation depends strongly on the thickness parameter, it is convenient to take the thickness parameter as a known constant. This is because its variability in the fitting procedure can correlate strongly with the variability of the material's optical parameters thus leading to fits where d may be incorrect at the expense of a minimum variance in another parameter. This would also be an incorrect value but still a minimised variance of fit. To ensure optimum accuracy of the fits, the values for d are therefore measured externally using a micrometer. Ten measurements of d were taken at different positions on the surface of the crystals giving an average value with a statistically determined 95% confidence interval uncertainty. Using this approach the values of d are summarised in Table 5.1.

5.3.3 Bootstrap analysis technique

With the thickness of the wafers taken as a known constant, the fitting function for the theoretical model of transmittance therefore consists of six variable parameters: $\epsilon(0)$, $\epsilon(\infty)$, ω_{TO}, Γ, ω_{p}, and γ. The function is fitted to the experimental data using a Marquardt-Levenberg nonlinear least-squares fitting algorithm implemented by a standard graphing application (WaveMetrics: Igor Pro) using the form presented in Appendix A.1.

The Marquardt-Levenberg algorithm (MLA) is essentially a modified Gauss-Newton algorithm (GNA) that interpolates between iterations using a method of gradient descent [250]. It is more robust than the standard GNA but follows the same general procedure.

The procedure essentially approximates each of the i data points as a first-order series expansion of the fitting function expanded about an estimation of the parameter values to

be fit (α_i).

$$\frac{1}{\sigma_i} Y_i \approx \frac{1}{\sigma_i} G(\alpha, X_i) = \frac{1}{\sigma_i} G(\alpha', X_i) + \frac{1}{\sigma_i} \sum_j \left[\frac{\partial G(\alpha', X_i)}{\partial \alpha'_j} \left(\alpha_j - \alpha'_j \right) \right] + \dots \qquad (5.12)$$

Here, Y_i is the dependent variable, X_i is the independent variable, σ_i is the standard error of the mean of Y_i, G is the fitting function, α is the set of parameter values to be determined by the least squares procedure and α' is the guessed set of parameter values [251]. The j subscript refers to a specific fitting parameter and the i subscript refers to a specific data point. Therefore, minimisation procedures that are based on the GNA such as MLA, evaluate a matrix (M) of partial derivatives,

$$M_{jk} = \sum_{i=1}^{n} \left[\frac{1}{\sigma_i} \frac{\partial G(\alpha, X_i)}{\partial \alpha_j} \right] \left[\frac{1}{\sigma_i} \frac{\partial G(\alpha, X_i)}{\partial \alpha_k} \right]. \qquad (5.13)$$

Here, the jk elements of the matrix are the sum over each of the i data points for the products of weighted partial derivatives of the fitting function, with respect to the parameters being estimated.

The inverse of M is used by the GNA minimisation procedure to find the direction and magnitude to change the parameters that decreases the overall weighted sum-of-squared-residuals. This is the 'chi squared' (χ^2) factor,

$$\chi^2 = \sum_{i=1}^{N} \left(\frac{Y(X_i) - G(X_i, \alpha')}{\sigma_i} \right)^2. \qquad (5.14)$$

A function that has no second or higher-order derivatives, with respect to the fitting parameters, is known as a linear type function,

$$\frac{\partial^2 G(X_i, \alpha)}{\partial \alpha_j \partial \alpha_k} = 0. \qquad (5.15)$$

In such functions, the first-order series expansion in Equation 5.12 is exact and will provide accurate answers for the parameters. An exact solution for the precision of these parameter values also exists by calculation of a covariance matrix (V). This is evaluated as the square

root of the jth diagonal element of the inverse of M times the variance-of-fit,

$$V = \sqrt{\chi^2 (M^{-1})_{jj}}. \tag{5.16}$$

For a non-linear model however, such as the transmittance function used in this chapter (Equation 5.11), the higher order derivative with respect to the parameters (Equation 5.15) are not equal to zero. This is because it includes factors where the fitting parameters are arguments of exponential and trigonometric functions, which have cyclic derivatives. Therefore, no exact solution to Equation 5.12 exists and an iterative approach to the series expansion is implemented which can only be approximate. The approximate values determined in one iteration are used as guesses for the next iteration. The algorithm is repeated until the values converge, i.e. the values do not change within a certain tolerance for a determined number of successive iterations. Thus, non-linear least squares algorithms function by successive approximation and there is a possibility of multiple minima for the convergence. Essentially, there can be many sets of parameters that give a relative minimum for the χ^2 factor. The covariance matrix used to determine parameter precision does not take this into account and commonly underestimate the actual uncertainty of the estimated parameters. Therefore, a statistical approach is required where a population of possible solutions are generated and the 'most likely' value is considered from the population distribution with appropriate statistical uncertainty. To execute this approach the bootstrap method is implemented [250, 251, 254].

The procedure of the bootstrap method is presented in Figure 5.4 and the source code for its implementation by the WaveMetrics: Igor Pro software package is given in Appendix A.2. A description of the procedure follows:

1. The built-in MLA fitting procedure of igor Pro and the theoretical transmittance equation (Equation 5.11) is applied to the transmittance data.

    - Initial sensible values for the parameters are input into the fitting program.
    - The value of d is held constant.

2. The parameters determined by a successful fit are then used to generate a theoretical set of data using Equation 5.11.

3. The difference between the measured and theoretically generated transmittance data is then calculated producing an array of residuals.

4. An array of residual noise is created by random sampling with replacement from the array of residuals.

   • Sampling with replacement refers to the notion that once a residual has been selected from the array it is not actually removed from the array. Therefore, in any particular set of residual noise, certain residual data points will be used more than once, while others will not be used at all.

5. A synthetic set of data is then generated by adding the residual noise to the theoretical transmittance.

6. The MLA fitting procedure is then applied to the synthetic data set.

   • If the fit produces physically real solutions to the parameters, then the parameter values are stored in an array. Otherwise the fit is discarded.

   • The physical constrains used were: $\epsilon(0), \epsilon(\infty), \omega_{\text{TO}} > 0$, $\epsilon(\infty) < \epsilon(0)$.

7. The sampling with replacement of the residuals array is then repeated and a new synthetic data set produced.

8. The new synthetic data set is fitted using the parameters from the last successful fit as the initial conditions for the next fit.

   • The process of generating new synthetic data sets and fitting them using the MLA process is repeated until 1000 successful fits have been achieved.

With a bootstrap procedure completed, the $n = 1000$ tables of fitted parameters then represent populations of possible values. The tables can be analysed statistically to produce the most likely value with an appropriate uncertainty. To be sure the optimal parameter values are reliable, the cross-correlation coefficients for each parameter pair are also calculated for every successful bootstrap fit. Statistical analysis of the cross-correlation coefficient populations allow monitoring for any cross-correlations between the parameters that would affect the accuracy of the results. As a rule of thumb, parameters with high
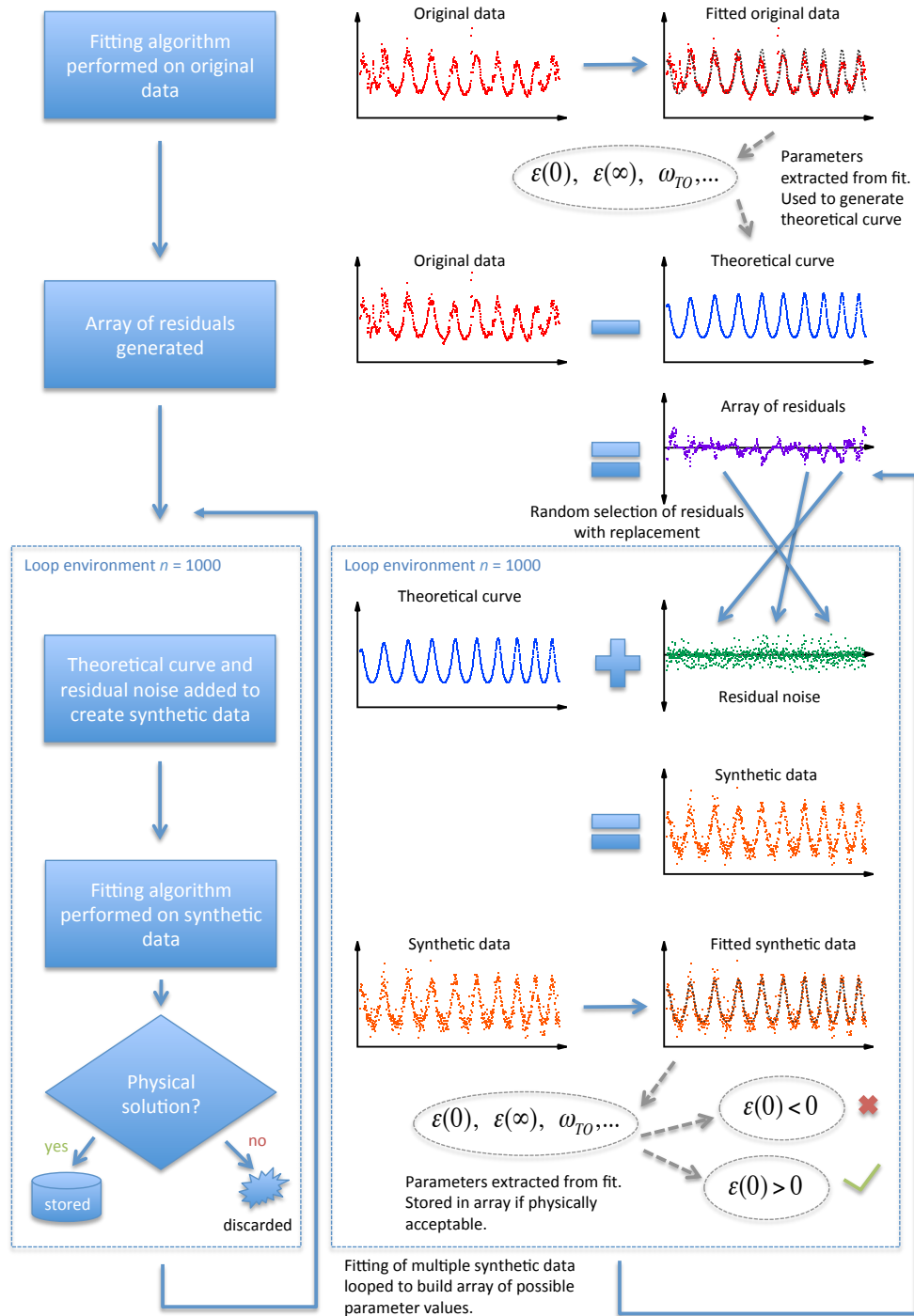
FIGURE 5.4: Flowchart outlining the iterative procedure of the bootstrap analysis method. The source code for the algorithm is presented in Appendix A.

cross-correlation will have cross-correlation coefficients with magnitudes higher than ± 0.97 with ± 1.0 representing complete correlation [250, 251]. The cross-correlations may also be monitored by observing scatter graphs produced by plotting the bootstrap determined parameter values against each other. Cross-correlated parameter pairs will produce a dependent curve when plotted against each other. Uncorrelated parameter pairs will have circular scatter distributions with Gaussian cross-sections [251].

5.4   Results and discussion

In this section the experimental measurements are presented along with the theoretical fits produced using the optimal parameter values obtained through the bootstrap analysis. The results of the analysis are then tabulated with a comprehensive list of other results taken from the literature. While the fitted values are consistent with the previously published values, the table demonstrates the spread in the accepted values and highlights the need for accurate results. Finally, a discussion on each variable is given, with consideration given to the previously published values.

5.4.1   Spectroscopic measurements

The spectrum of the 0.5 mm ZnTe wafer is shown against a reference spectrum in Figure 5.5. The characteristic water vapour absorption lines are observed at 0.55 THz and 0.75 THz. The interference fringes (or Fabry-Perot oscillations) present in the sample spectrum are easily resolved by the spectrometer. Even without detailed analysis, the relatively high resistivity of the sample can be seen in the spectrum. The maxima in the fringes is approximately equal to the reference spectrum, indicating low absorption (high resistivity).

The ratio of the sample spectrum with the reference spectrum gives the transmittance, shown in Figure 5.6 for 0.3 mm, 0.5 mm, and 1.0 mm wafer thicknesses. The Fabry-Perot oscillations now dominate the transmittance data and are used to aid the theoretical fitting. The separation of these fringes is approximately 0.16 THz, 0.10 THz, and 0.05 THz for the 0.3 mm, 0.5 mm, and 1.0 mm samples, respectively. Outlying data points in the
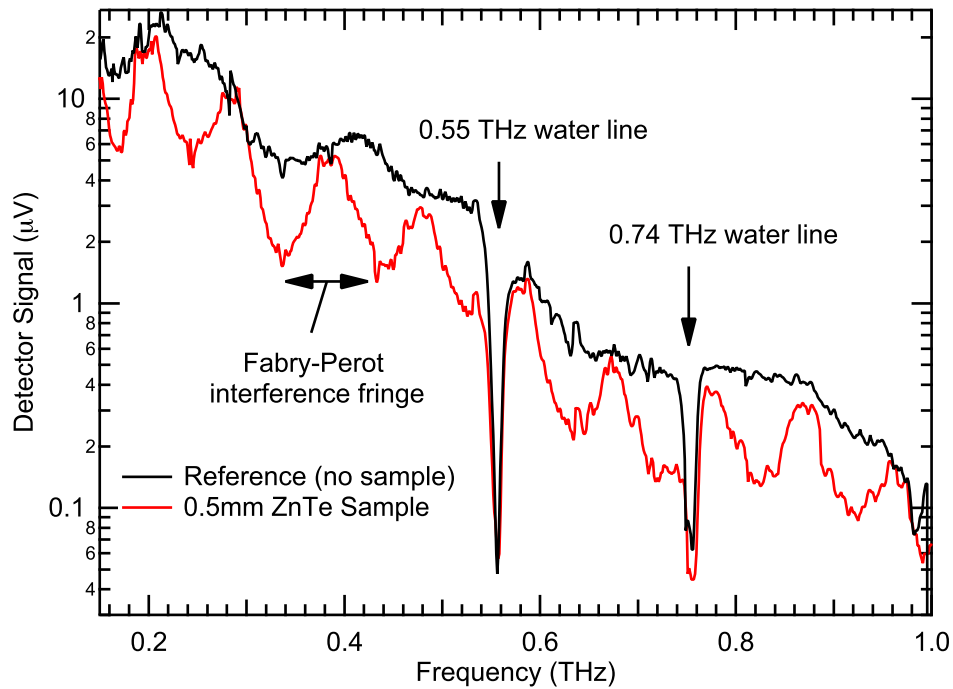
FIGURE 5.5: Transmission spectrum of 0.5 mm thick ZnTe wafer compared with background reference. Resolution is 1 GHz.

transmittance plots are attributed to random noise in the measurements. Points where the transmittance is greater than 1.0 occur when the sample measurements have experienced noise giving a higher signal relative to the reference measurement. In particular, there are consistent outliers at the 0.55 THz water absorption peak, when both the reference and sample spectra exhibit a low signal to noise ratio. When performing the fitting algorithm these points are masked (not included) to assist in a better fit. The theoretical fits to the transmittance data following the bootstrap procedure are overlaid on the data in Figure 5.6 and show superb agreement.

5.4.2 Statistical analysis of fits

Histograms of the parameter distributions are displayed for each sample in Figure 5.7. The bin width used for the histograms varies for each parameter as some parameters, such as $\epsilon(0)$, did not vary over a wide range of values. Using a larger bin width, such as that used for the $\epsilon(\infty)$ parameter, would group all the varied values for $\epsilon(0)$ into just one bin, which does not serve the purpose of graphically representing the statistical distribution.
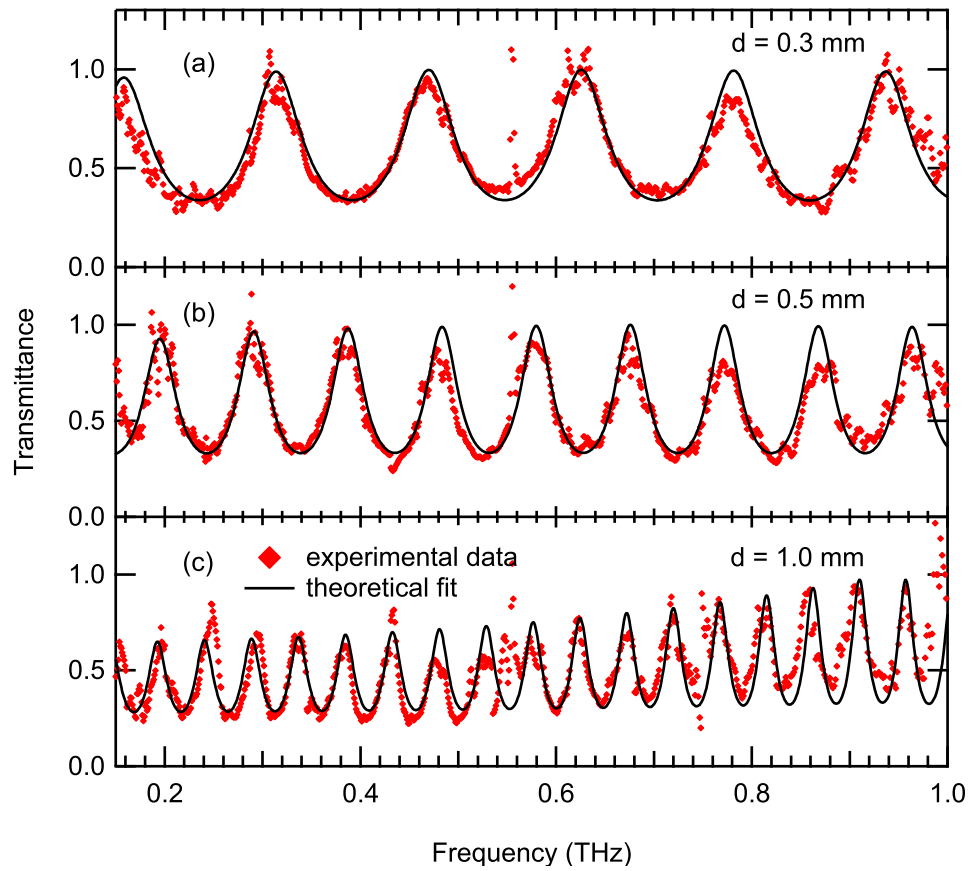
FIGURE 5.6: Transmittance measurements for three ZnTe wafers (solid diamonds) with thicknesses, d, of 0.3 mm (a), 0.5 mm (b), and 1.0 mm (c) fitted with theoretical curve (solid curve).

Therefore, the heights of the histograms for each parameter do not seem to match but this is only a result of different bin widths meaning a different frequency of values in a specific bin range. Nevertheless, as is intended by Figure 5.7, Gaussian like distributions can be seen for the variance in values of the different parameters.

The most accurate value for the parameters is taken as the one with the highest probability, or the mean. If the fitting procedure did not work correctly or the theoretical calculation was inaccurate, a randomised distribution for the fitted values would be expected. In some instances, such as Figures 5.7 (b) and (c), the distribution for γ and ω_{TO} appear asymmetric. This is most likely a result of cross-correlation with other parameters. What is also clear in the case of the $\epsilon(0)$ distributions (Figures 5.7 (a), (d), (g)), is the smaller variance of values relative to $\epsilon(\infty)$. This suggests that the transmittance function is more sensitive to $\epsilon(0)$ and has a lower tolerance to variability in this parameter. The plasma

frequency and its damping term, at least in the $d = 0.3$ and 0.5 mm cases have similar variability (Figures 5.7 (b), (e), (h)). Perhaps the greatest distribution is seen in ω_{TO}, with only a small variance in its associated damping factor (Figures 5.7 (c), (f), (i)).

As previously mentioned, when fitting experimental data simultaneously with multiple parameters, the cross-correlation between the various parameters must also be considered. The cross-correlation refers to when the variation in one parameter, which may improve the variance-of-fit, can be partially compensated for by a variation in one or more of the other parameters. Essentially, the parameters are coupled and the distribution of values are dependent on each other, leading to inaccuracies. This is generally not a problem if the compensation is low. Indeed, there will always be some cross-correlation due to the fact of fitting a complex equation to a small and finite number of data points. Considering that the physical origins of the parameters may also be correlated, such effects are expected here. However, if the correlation is nearly complete, then the fitting procedure will be unable to identify unique values for the parameters being estimated and their associated distributions become meaningless. To assess the degree of cross-correlation for the parameter values determined by the fits in this experiment, two techniques are employed.

The first technique is to calculate the matrix of cross-correlation coefficients C. Where,

$$C_{jk} = \frac{(M^{-1})_{jk}}{\sqrt{(M^{-1})_{jj}(M^{-1})_{kk}}}, \quad j \neq k. \tag{5.17}$$

The cross-correlation coefficients have a range of ± 1 with the optimal being zero. As a rule of thumb, if the magnitudes of the cross-correlation coefficients are less than approximately ± 0.97, the least-squares procedure can usually function adequately [250]. However, this rule of thumb should not be considered as an absolute threshold with everything acceptable below ± 0.97 and everything unacceptable outside of this range. Each case should be considered uniquely [250].

Therefore, the population of determined parameters also acts as an indication of cross-correlation effects by observing the distribution of their values with respect to each other [251]. This is the second technique employed and is achieved by plotting the array of values for one parameter against another. Uncorrelated parameter pairs will have circular
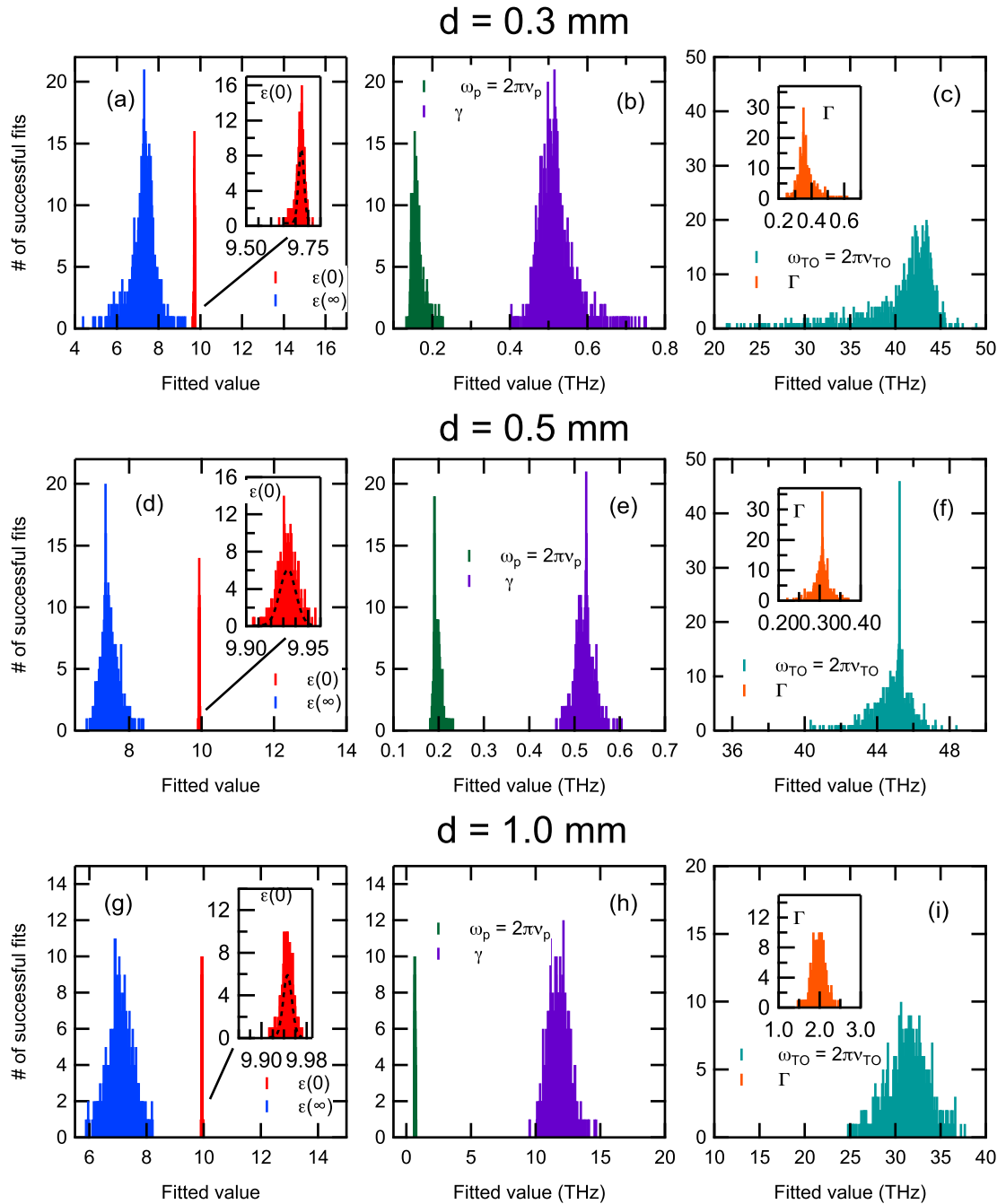
FIGURE 5.7: Histograms of parameter value populations for the 0.3 mm (a-c), 0.5 mm (d-f) and 1.0 mm (g-i) thick wafers.

distributions with Gaussian cross-sections while a correlated pair will feature a curve like dependence.

TABLE 5.2: Matrix of cross-correlation coefficients between fitted parameters for 0.3 mm sample.

	$\epsilon(0)$	$\epsilon(\infty)$	ω_{TO}	Γ	ω_{p}	γ
$\epsilon(0)$	1					
$\epsilon(\infty)$	0.27 ± 0.16	1				
ω_{TO}	0.16 ± 0.13	0.35 ± 0.27	1			
Γ	0.09 ± 0.09	0.17 ± 0.20	0.16 ± 0.18	1		
ω_{p}	0.11 ± 0.10	0.32 ± 0.27	0.26 ± 0.24	0.17 ± 0.20	1	
γ	0.18 ± 0.14	0.28 ± 0.25	0.29 ± 0.26	0.30 ± 0.26	0.18 ± 0.2	1

5.4.2.1 Cross-correlations in 0.3 mm sample

The correlation matrix for the 0.3 mm sample is given in Table 5.2. The matrix is symmetrical so only the lower diagonal is shown. Looking over the matrix elements, it can be seen that all of the cross-correlation coefficients are well below the 0.97 rule-of-thumb value for highly correlated parameters. The highest correlations occur between the ω_{TO} and $\epsilon(\infty)$ parameters, with a cross-correlation coefficient of 0.35 ± 0.27 and between ω_{p} and $\epsilon(\infty)$, with a cross-correlation coefficient of 0.32 ± 0.27. Within the limits of the uncertainties this can put the coefficients up to 0.62 and 0.59 respectively. This is still much lower than 0.97 but above 50%. Observing the co-parameter scatter plots in Figure 5.8, the cross-correlation effects are visualised. In particular, Figure 5.8 (f) shows that an increase in $\epsilon(\infty)$ is compensated for by a decrease in ω_{TO}. Similar dependences can be seen for many of the other parameter pairs but by and large the distributions have a clear circular distribution around the most probable values.

5.4.2.2 Cross-correlations in 0.5 mm sample

The cross-correlation coefficients for the 0.5 mm sample are given in Table 5.3. Again, the parameters with the highest correlation are ω_{TO}, ω_{p} and $\epsilon(\infty)$ with coefficients around 0.3 ± 0.3. This is still considered a relatively low correlation. The co-parameter scatter graphs support this assessment showing mostly circular distributions. Slight cross-correlations can be seen in particular for ω_{TO} and ω_{p} (Figure 5.9 (k)), where the ellipsoidal elongation of the scatter suggest that an increase in ω_{TO} is compensated by a reduction in ω_{p}.
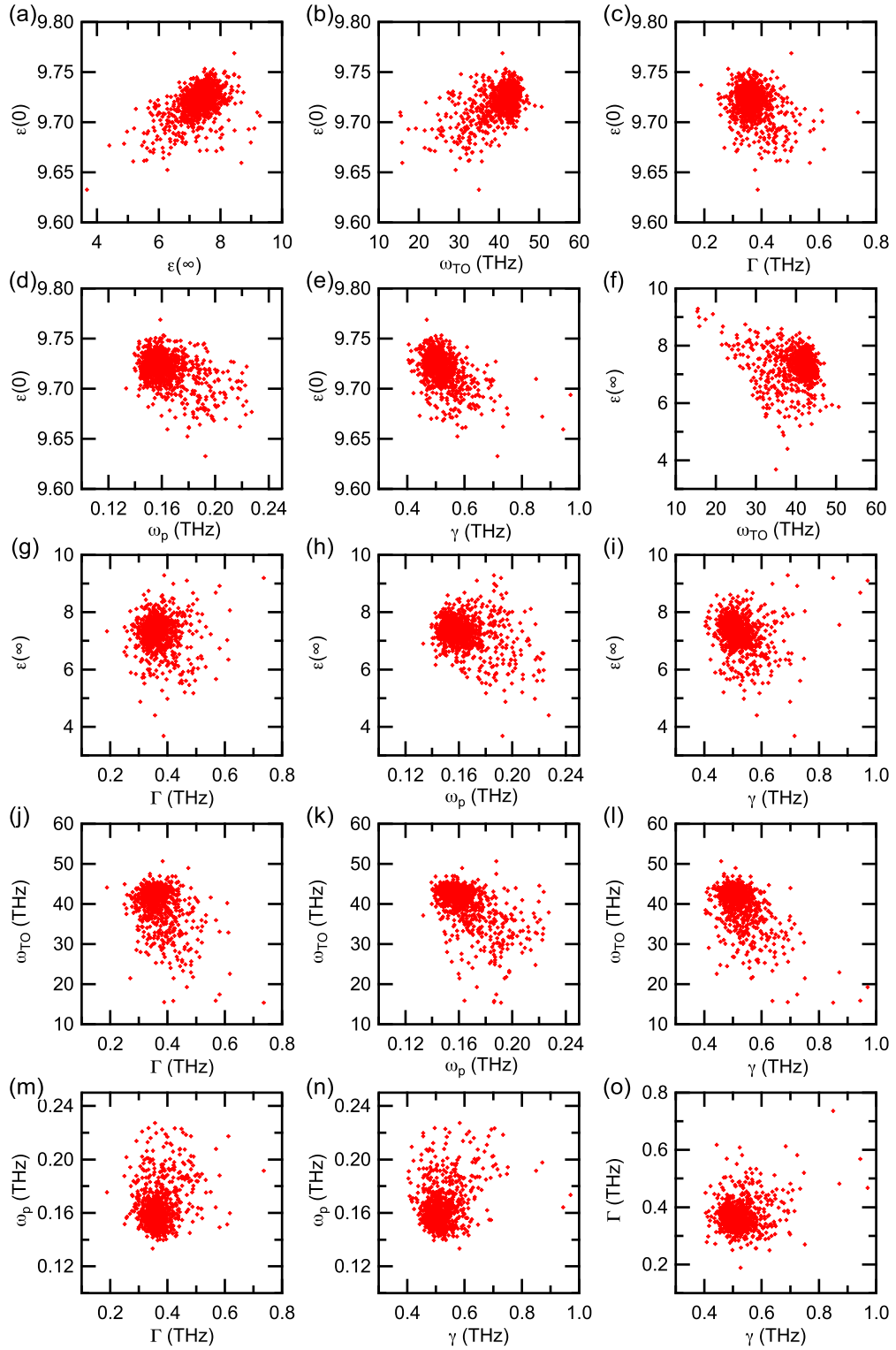
FIGURE 5.8: Visualisation of parameter cross-correlations for 0.3 mm wafer by co-parameter scatter graphs.
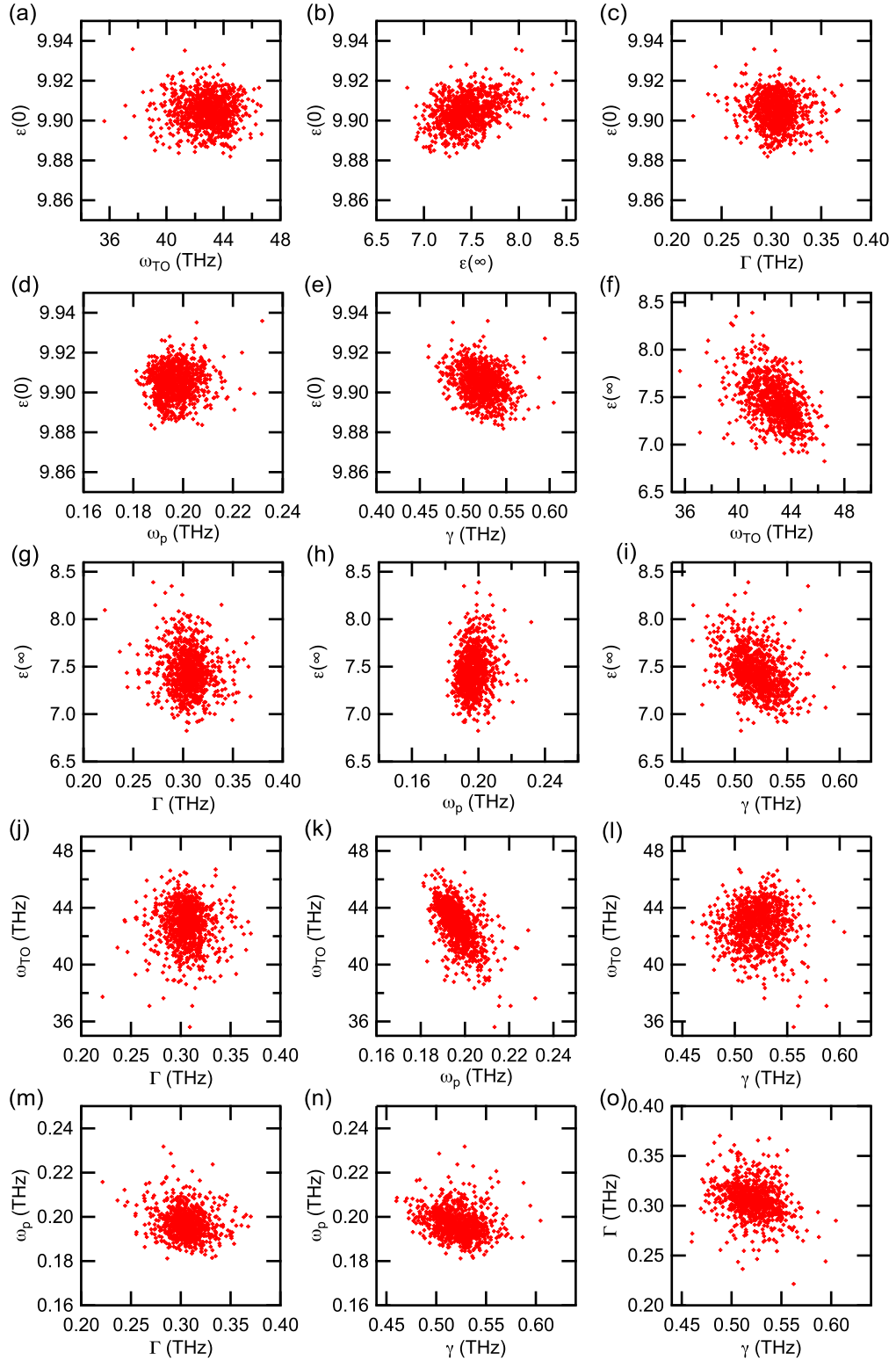
FIGURE 5.9: Visualisation of parameter cross-correlations for 0.5 mm wafer by coparameter scatter graphs.

TABLE 5.3: Matrix of cross-correlation coefficients between fitted parameters for 0.5 mm sample.

	$\epsilon(0)$	$\epsilon(\infty)$	ω_{TO}	Γ	ω_{p}	γ
$\epsilon(0)$	1					
$\epsilon(\infty)$	0.20 ± 0.13	1				
ω_{TO}	0.11 ± 0.10	0.30 ± 0.28	1			
Γ	0.08 ± 0.08	0.17 ± 0.22	0.17 ± 0.22	1		
ω_{p}	0.10 ± 0.10	0.31 ± 0.28	0.29 ± 0.28	0.17 ± 0.22	1	
γ	0.14 ± 0.12	0.30 ± 0.28	0.30 ± 0.29	0.28 ± 0.27	0.18 ± 0.22	1

5.4.2.3 Cross-correlations in 1.0 mm sample

The cross-correlation between the fitted parameters for the 1.0 mm sample appear higher than for the other two samples. Comparing the cross-correlation coefficients of Table 5.4, many of the parameters share coefficients greater than 0.5. The highest again being between ω_{TO} and $\epsilon(\infty)$ with 0.66 ± 0.21 which reaches 0.87 at the limits of its uncertainty. This higher level of cross correlation is reflected in the scatter graphs of Figure 5.10. Here, numerous parameter pairs feature ellipsoidal elongation away from the ideal circular scatter distribution. It is easy to see which parameter pairs are cross-correlated and which one are not. The higher level of cross-correlation is most likely due to a higher variability in the fitting procedure. With the same resolution used for the measurement of each sample spectrum, the same number of total data points are being fitted (898 points). However, the different samples have different numbers of interferences fringes ($\sim$5 for the 0.3 mm sample, $\sim$8 for the 0.5 mm sample and $\sim$17 for the 1.0 mm sample). Therefore the 1.0 mm sample, which has the most fringes, must be fit with less data points per fringe ($\sim$53 compared with 112 and 180 for the 0.5 and 0.3 mm samples respectively). The fringes are key features that the theoretical function must be fit to and the higher derivatives are crucial for determining the parameter values. It is well understood that quality of fit is reduced when less data points are available [251]. This therefore explains the increased uncertainty and cross correlation for the thicker samples. This problem could be easily rectified by performing higher resolution scans for the thicker samples, attempting to keep the points per fringe constant. Nevertheless, with cross correlation considered, the values obtained for the parameters of the 1.0 mm sample may still be considered accurate. No complete correlation is observed, which is the main problem when encountering cross-correlated parameters, and realistic values are obtained.
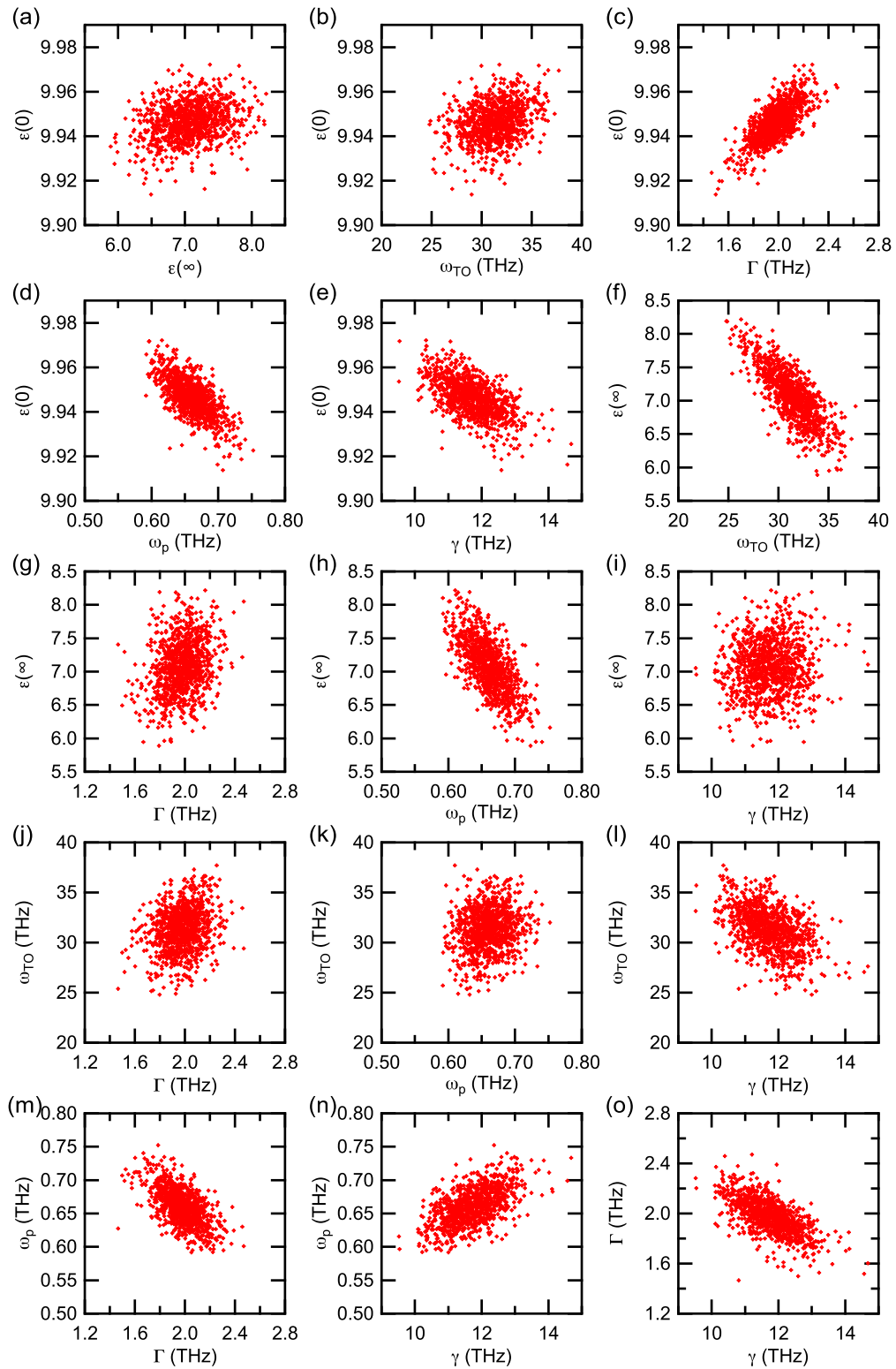
FIGURE 5.10: Visualisation of parameter cross-correlations for 1.0 mm wafer by co-parameter scatter graphs.

TABLE 5.4: Matrix of cross-correlation coefficients between fitted parameters for 1.0 mm sample.

	$\epsilon(0)$	$\epsilon(\infty)$	ω_{TO}	Γ	ω_{p}	γ
$\epsilon(0)$	1					
$\epsilon(\infty)$	0.29 ± 0.17	1				
ω_{TO}	0.30 ± 0.19	0.66 ± 0.21	1			
Γ	0.43 ± 0.18	0.32 ± 0.21	0.27 ± 0.20	1		
ω_{p}	0.57 ± 0.14	0.58 ± 0.21	0.27 ± 0.22	0.42 ± 0.21	1	
γ	0.43 ± 0.17	0.23 ± 0.20	0.43 ± 0.22	0.54 ± 0.21	0.50 ± 0.25	1
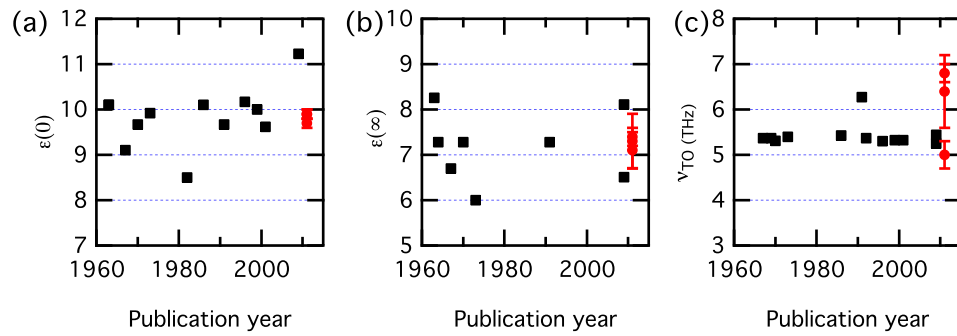
FIGURE 5.11: Historical comparison of the optical parameters of ZnTe presented in Table 5.5. Results from this work are shown in red. Previously reported values are in black

5.4.3 Dielectric parameters

The results of the bootstrap analysis are presented in Table 5.5. They represent the rounded average parameter values taken over 1000 bootstrap samples, with the uncertainty given as the standard deviation rounded to the nearest significant figure stated for the parameter value. The angular frequencies (ω) stated in Section 5.2 are converted to usual frequencies (ν) which are more often reported. Since the plasma frequency (ν_{p}), collision frequency (γ) and phonon damping (Γ) parameters all depend on an individual sample's doping and crystal imperfections, they are often not reported as a general result and thus have not been included in many of the previous reports. They have been left in this analysis to demonstrate the capability of this technique. Figure 5.11 displays the results in the context of the previously published values. A more detailed discussion of the results for each parameter follows.

TABLE 5.5: Optical parameters for ZnTe at room temperature determined by a statistical bootstrap analysis of the theoretical fits in Figure 5.6. The first three entries represent the results of this work. The results are compared with previous results from literature ($\nu_p = \omega_p/2\pi$, $\nu_{TO} = \omega_{TO}/2\pi$).

	$\epsilon(0)$	$\epsilon(\infty)$	ν_{TO} (THz)	Γ (THz)	ν_p (THz)	γ (THz)
0.3 mm	9.7 ± 0.1	7.3 ± 0.6	6.4 ± 0.8	0.4 ± 0.1	0.03 ± 0.01	0.5 ± 0.1
0.5 mm	9.9 ± 0.1	7.4 ± 0.2	6.8 ± 0.2	0.3 ± 0.1	0.03 ± 0.01	0.5 ± 0.1
1.0 mm	9.9 ± 0.1	7.1 ± 0.4	5.0 ± 0.3	2.0 ± 0.1	0.1 ± 0.1	11.7 ± 0.7
Aven[232]	10.1	8.26	-	-	-	-
Berlincourt[233]	10.1	-	-	-	-	-
Marple[235]	-	7.28	-	-	-	-
Manabe[236]	9.1	6.7	5.37	0.017	-	-
Mitra[237]	-	-	5.37	-	-	-
Rode[238]	9.67	7.28	-	-	-	-
Beserman[239]	-	-	5.31	-	-	-
Hattori[240]	9.92	6	5.40	-	-	-
Hidaka[241]	7 to 10	-	-	-	-	-
Peterson[242]	10.1	-	5.43	-	-	-
Ruda[243]	9.67	7.28	6.27	-	-	-
Oh[244]	-	-	5.37	-	-	-
Wu[116]	10.17	-	5.30	-	-	-
Gallot[245]	10.0	-	5.32	≤ 0.025	-	-
Schall[246]	9.62	-	5.32	-	-	-
Bignell[247]	11.23	8.11	5.25	0.04	-	-
Mnasri[248]	-	6.51	5.44	-	-	-

5.4.3.1 Low and high frequency dielectric constants

Both the low and high frequency dielectric constants are intrinsic optical properties of the crystal. It is for these parameters where there is the biggest variance in previously published values (Figure 5.11 (a) and (b)). Accurate results from the low frequency dielectric constant are expected due to the low frequency band, relative to the phonon frequency, that the spectra are measured in. This is evident in how the results compare with each other and the reviewed literature (Figure 5.11 (a)). By taking an average of the results for each wafer and using the upper and lower limits of their respective standard deviations as an uncertainty, the low frequency dielectric constant can be taken as $\epsilon(0) = 9.8 \pm 0.2$. When fitting this parameter, it was noticed that it was very stable relative to the other parameters, but depended strongly on the sample thickness. It was found that a change of 1% in d could effect $\epsilon(0)$ by up to 5% so it was important to have accurate measurements for d. The cross-correlation coefficients, with respect to the rest of the parameters, were

generally less than 0.1. The parameter value scatter graphs were mostly circular with cross-sections of approximate Gaussian distribution.

Even though the measurements were not performed at high frequency, reasonably accurate results were able to be obtained for the high frequency dielectric constant. This is attributed to the fringe depth and width being dependent on this parameter. The results fall within the spread of the previously published values and give an average value of $\epsilon(\infty) = 7.3 \pm 0.6$ with the uncertainty representing the upper and lower limits of the standard deviation from each wafer. The large uncertainty can be attributed to a higher cross-correlation, particularly with the transverse optical phonon and plasma frequencies. Average cross-correlation coefficients for these pairs of parameters were around 0.6 ± 0.2. This is expected as each of these parameters contribute to separate terms in the dielectric function model. This was also confirmed by observing a slight linear dependence in the scatter graphs for each of these parameter pairs. Nevertheless, since the fitting algorithm was able to converge and the cross-correlation coefficients were much lower than 0.97, the results can be considered accurate.

5.4.3.2 Transverse optical phonon and phonon damping frequencies

While the phonon frequency is an intrinsic property of the crystal, the damping constant will depend on the particular purity of the sample and is therefore not an intrinsic crystal property. Hence, most of the reviewed literature only reports on the phonon frequency. Whilst the previously reported results agree within the uncertainty of the values presented in this article, the large deviation from the general consensus evident in Table 5.5 and Figure 5.11 (c) of $\nu_{\mathrm{TO}} \approx 5.3\,\mathrm{THz}$ is notable. The accuracy does seem to increase with sample thickness. The uncertainty may be attributed to both the slight cross-correlation between the high frequency dielectric constant (described above) and the fact that the measurements have been taken in the sub-THz ($< 1.0\,\mathrm{THz}$) region. The sub-THz frequency region is an order of magnitude lower than the phonon resonance and therefore a much weaker coupling to the optical phonon is expected. Many of the previous measurements [236, 239, 247] were performed in reflection using far-infrared spectrometers which allows direct observation of the Reststrahlen band. From this, the optical phonon frequencies can

be directly determined with considerable accuracy as the actual structure of the resonance is observed. Taking an average of the results for each wafer gives $\nu_{\text{TO}} = 6.0 \pm 1.3\,\text{THz}$ with the uncertainty adjusted to encompass the full spread of the uncertainties for each wafer's results.

5.4.3.3 Plasma and collision frequencies

The plasma and collision frequencies represent the resonant frequency and damping of the charge carriers in the conduction band. As previously mentioned, these parameters are sample dependent and not intrinsic properties of the ZnTe crystal. This is why they do not appear in the reviewed literature. It could also explain the discrepancy between the results of the 1.0 mm sample compared to the others. While the 0.3 mm and 0.5 mm samples were obtained in the same order from the supplier, the 1.0 mm sample was obtained at a different time and could therefore be of a different purity. The results therefore support the application of THz spectroscopy in semiconductor quality control. Using the determined parameters, material properties of the samples such as resistivity or carrier concentration can be calculated. It should be noted however, that the uncertainty in the fit of ω_{p} for the 1.0 mm sample is as large as the determined value. This suggests that a good fit for this parameter was not achieved and the true value could indeed be more in line with the other samples.

5.4.3.4 Calculations of carrier concentration

Using the results of Table 5.5 and the form of the plasma frequency given earlier, ($\omega_{\text{p}}^2 = ne^2/m^*\epsilon_0\epsilon(\infty)$), an approximate carrier concentration for each sample is calculated. An effective charge carrier mass of $m^* = 0.151 m_{\text{e}}$, taken from Reference [238], is assumed. Rearranging the plasma frequency expression gives n in terms of known and measured constants,

$$n = \omega_{\text{p}}^2\epsilon(\infty)\frac{m^*\epsilon_0}{e^2}. \tag{5.18}$$

The results of the calculations are given in Table 5.6. The values of n are in agreement with concentrations for high resistivity ZnTe at room temperature obtained by theoretical

TABLE 5.6: Calculations of carrier concentration for the ZnTe wafers using results from Table 5.5.

wafer thickness d (mm)	carrier concentration n (m^{-3})
0.3	$(1.2\pm0.6)\times10^{19}$
0.5	$(1.5\pm0.5)\times10^{19}$
1.0	$(1.3\pm1.9)\times10^{20}$

and experimental transport models [243]. Again, the result for the 1.0 mm sample has a large uncertainty relative to the calculated value and this is related back to the quality of fit for ω_{p}. This shows that accurate determination of material properties relies crucially on well fitted data with correctly calculated errors.

5.5   Conclusions

In summary, the theory and formalism for THz transmission through plane parallel samples has been established. Using this theory, the transmittance of three ZnTe crystal wafers with different thicknesses was measured by continuous-wave THz radiation. The transmittance spectra of these wafers allow the determination of the optical parameters of ZnTe. This is achieved by fitting the experimental data with theoretical curves calculated using a simple Drude-Lorentz dielectric function. The optical parameters include the low and high frequency dielectric constants and plasma and phonon frequencies, as well as their damping constants.

Due to the non-linear dependence of the transmittance on the fitted parameters, a statistical approach such as the bootstrap method should be used to obtain accurate values with genuine uncertainties. The quality of fit is dependent on the number of data points per spectral feature, suggesting that better fits would be achieved with higher resolution measurements. The results fall within a broad range of acceptable values, which highlights the uncertainty in documented ZnTe optical parameters. Accurate knowledge of these parameters allows the calculation of sample electrical properties such as carrier concentration. This demonstrates how a two-colour photomixing THz source can perform as a semiconductor characterisation tool.

In contrast to traditional electrical transport measurements [232], this method does not require the attachment of electrodes, potentially damaging the sample. Previous optical methods for characterising ZnTe have had success using far infrared interference and grating spectrometers and applying Drude dispersion theory or the Kramers-Kronig dispersion relation [240]. However, these measurements often require either thin film samples for transmission measurements or complicated optical setups for reflection measurements [239, 240, 247]. THz time-domain spectroscopy measurements performed more recently have had success using transmission measurements due the low absorption of THz frequencies by ZnTe crystals [245, 246]. However, such setups have large startup costs due to the requirement of femtosecond lasers for their operation.

As photomixing technologies continue to be improved, through development of new materials able to photomix efficiently using telecommunication wavelengths [255], such two-colour systems will prove to be more widely accessible. And so the development of effective analysis techniques for use of their capabilities is beneficial for future industrial characterisation techniques. The excellent frequency precision, ability to perform contactless measurements, and low start up costs (particularly with their further developments to operate at telecommunication wavelengths) suggests that a two-colour THz spectrometer is a good candidate for industry application.

Chapter 6

Weak magnetic excitations in geometrically frustrated Cu$_3$Bi(SeO$_3$)$_2$O$_2$Cl

6.1 Introduction

In this chapter weak magnetic excitations in a novel layered compound Cu$_3$Bi(SeO$_3$)$_2$O$_2$Cl (CBSCl) are investigated at low temperature and with applied magnetic fields. Two magnetically active modes are identified and their applied field dynamics are used to extract the gyromagnetic factor and magnetic anisotropy of the magnetic ions in the material. The results suggest that the two modes arise from different copper sites and add to the understanding of the dynamics of the magnetism in this novel material. Within the context of this thesis, the results also establish the use of THz radiation in probing the magnetic excitations of novel single crystal materials.

Further motivation for the work is by the geometrically frustrated structure of CBSCl, and its magnetic ordering, leading to a canted spin lattice. As reviewed in Section 2.3.2, it is understood that such canting may produce non-collinear short-range magnetic orders [256], such as cycloidal or spiral spin systems. This is a hallmark of magneto-electric (ME) coupling in multiferroic materials [157]. A central issue in the research of multiferroics, is

the unique ME effects due to the collective modes (or elementary excitations) [257]. In the static ground state the properties of the ME coupling are relatively well understood, however, the effects can be rather weak. Enhanced coupling through mode excitation offers ways to further test the theories of the microscopic mechanisms of the ferroelectricity induced in such magnetically ordered materials [258]. Magnetic frustration is also of interest in the regime of quantum spin liquids and spin ices which result from large degeneracy in the magnetic ground state [259, 260]. Such novel and experientially understudied states have broad interest both fundamentally and in quantum device applications [259].

This work draws heavily from research performed in collaboration with K. H. Miller and published in Miller *et al.* (2012), *Infrared phonon anomaly and magnetic excitations in single-crystal* $Cu_3Bi(SeO_3)_2O_2Cl$ [261]. The collaboration with K. H. Miller, a visiting researcher to the University of Wollongong from Florida State University, occurred through the East Asia and Pacific Summer Institutes (EAPSI) program for US graduate students. The visit took place over 8 weeks from June to August of 2012. Prior to the collaborative work, Miller performed a thorough infrared analysis of the phonon spectrum in CBSCl. This work identified 36 of 38 predicted phonon modes for the $Pmmn$ space group of CBSCl selectively along the a, b and c crystal axes at room temperature. Remarkably, below 115 K, 16 new phonon modes were identified, which is indicative of a symmetry-lowering structural transition. However, an anomalous result was that subsequent powder x-ray diffraction measurements revealed the same structure existing both at 300 K and 85 K, which indicated no structural transition.

Preliminary Raman spectra taken at 300 K revealed five phonon modes with energies close to the new modes observed in the infrared spectra below 115 K. Raman exclusive modes in a centrosymmetric space group can become infrared active when the inversion centre is removed. Essentially, the local centres of symmetry about which all the Raman modes have zero net dipole moment disappear [262]. The identification of two non-centrosymmetric orthorhombic space groups ($Pm2_1n$ and $P2_1mn$) that have the same allowed Bragg reflection peaks as the 300 K $Pmmn$ structure, suggest that such a subtle second-order transition may occur. Hence, the subtle change in diffraction pattern would be below the resolution of the powder x-ray diffraction experiment and not detected. This hypothesis is consistent with optical birefringence measurements performed by Millet *et al.* [263],

where a continuous but rapid decrease in the difference in refractive index between the (011) and (100) planes was observed at $\sim$110 K. Such a result is indicative of a second order phase transition where a first order phase transition would feature a discontinuous change. The angle of index rotation was too small to detect (less than 1°) which also suggests the change in symmetry is within the framework of orthorhombic structures rather than a symmetry lowering from orthorhombic to monoclinic.

Interestingly, the potential lattice distortion manifests itself at the same temperature in the magnetic susceptibility as a change in the Curie-Weiss behaviour of the paramagnetic region, thus drawing suspicions of high-temperature ME coupling [261, 263]. The occurrence of high-temperature ME coupling in CBSCl would open up possibilities of spintronic application. The observation of the magnetic excitations presented in this chapter and published in References [261] and [99] reflects on the possibilities of electromagnons. Shortly following the publication of this work, a report on the magnetic excitations by THz radiation in isostructural $Cu_3Bi(SeO_3)_2O_2Br$ (CBSBr) was published [264]. In addition to being isostructural, CBSBr features similar magnetic properties to those of CBSCl, including the magnetic-ordering temperature, magnetic anisotropy, and a field-induced metamagnetic transition (rapid increase in magnetisation with small applied magnetic field) [263–265]. The results of Wang *et al.* corroborate well with those presented here with an analysis of the mode field dependence used to determine the magnetic anisotropy constant. A similar approach is applied here for CBSCl, which expands on the results published by Miller *et al.* [99, 261].

The chapter takes on the following structure: Section 6.2 provides specific details on the CBSCl compound including a brief history of its discovery and synthesis. Its novel magnetic properties are also detailed along with a description of the sample used in the experiments of this chapter. Section 6.3 outlines the details of the experimental setups used in the study. To access a broad range of frequencies, both the two-colour system and Polytec interferometer were implemented. Section 6.4 presents the spectroscopic results separated into subsections dedicated to each spectrometer. The results are then combined and discussed in Section 6.5.1. The gyromagnetic factor and magnetic anisotropy are extracted from the data. Section 6.6 concludes the chapter.

6.2 Crystal and magnetic properties of $Cu_3Bi(SeO_3)_2O_2Cl$

Single-crystal CBSCl is a relatively undocumented compound. It was first reported on by Pring, Gatehouse and Birch in 1990 [266], who identified the orthorhombic cell of the *Pmmn* space group by x-ray diffraction. The crystals characterised were natural formations obtained from the Iron Monarch iron deposit in South Australia. The compound is also known as francisite in honour of Glyn Francis' contribution to the submission of minerals for identification from the Iron Monarch ore body [266]. Millet *et al.* in 2001, performed the first synthesis of CBSCl single crystals [263]. They proceeded with a detailed structural study using x-ray diffraction along with magnetic, optical, and electron spin resonance measurements as a function of temperature.

It was shown that CBSCl crystallises in a layered structure, with two types of CuO_4 bonded plackets forming a buckled hexagonal lattice arrangement with two distinct $S = 1/2$ Cu^{2+} sites (Cu1 and Cu2) [263]. The buckled lattice is stacked along the c axis of the orthorhombic cell as in Figure 6.1 [265]. The layers are therefore reminiscent of the kagome lattice and result in strong magnetic frustration due to competing nearest-neighbour ferromagnetic and next-nearest–neighbour antiferromagnetic interactions of the $S = 1/2$ magnetic Cu^{2+} ions [267]. The spin frustration occurs because the neighbouring spins that seek to lower their energy by aligning ferromagnetically, cannot mutually do so incorporating an additional antiferromagnetic alignment with their next-nearest neighbours. This forces the canted state as the lowest energy arrangement for the Cu1 sites seen in Figure 6.2 (a) [265]. Additional super-super-exchange interactions across long Bi and Se bonds (Cu-O-X-O-Cu, where X = Se, Bi) may also be of importance, particularly concerning interlayer coupling [265].

The first magnetic investigations were performed by Millet *et al.* [263], who determined by susceptibility measurements that CBSCl was paramagnetic above ∼24 K and most likely a canted antiferromagnet below. However, it was Pregelj *et al.* [265] who gave a detailed analysis of the magnetic structure. This was achieved by magnetisation, magnetic susceptibility and neutron diffraction measurements on the isostructural CBSBr compound. Through these measurements, Pregelj *et al.* established the existence of alternating ferromagnetic ab layers individually exhibiting a canted structure. Recent calculations have

shown this magnetic state to be very fragile even for the extreme quantum-mechanical limit, with the lattice topology providing infinite degeneracy which acts to prevent long-range ordering [268]. Despite this, a weak antiferromagnetic interlayer coupling leads to the bulk antiferromagnetic ordering observed below $T_N = 24$ K along the c axis. The Dzyaloshinsky-Moriya (DM) interaction has been proposed as necessary to account for this peculiar magnetic ordering in a system that should otherwise remain unordered due to the infinite degeneracy of the ground states [268].

In the magnetically ordered ground state, the system undergoes a metamagnetic transition to ferrimagnetic order upon the application of a weak external magnetic field of 0.8 T along the c axis. Since the Br and Cl ions do not contribute to the magnetic ordering in CBSBr and CBSCl respectively, the analysis of Pregelj *et al.* can be applied directly to CBSCl. The magnetic structure along with the metamagnetic transition are represented graphically in Figure 6.2. The magnetisation of CBSCl along the c axis for increasing fields is shown in Figure 6.2 (c) and was provided by K. H. Miller. The effects of the metamagnetic transition are clearly seen where the magnetisation saturates above 0.8 T. Recently, the same magnetic ordering has been observed in the isostructural compound $Cu_3Y(SeO_3)_2O_2Cl$ [267]. Since Y is nonmagnetic, the substitution of Y for Sr only has the effect of a slight distortion to the crystal lattice. In this case, the same metamagnetic and anisotropic responses with an applied magnetic field were observed, adding a new member to the family of these novel francisite compounds.

The single crystal used in these experiments was provided by K. H. Miller and grown by H. Berger. The growth involved the use of standard chemical vapour-phase methods. Mixtures of analytical-grade purity CuO, SeO_2, and BiOCl powder in a molar ratio of 3:2:1 were sealed in quartz tubes with electronic-grade HCl as the transport gas for the crystal growth [261]. The ampoules were then placed horizontally into a tubular two-zone furnace and heated at $50°$ C/h to $450°$ C. The optimum temperatures at the source and deposition zones for the growth of single crystals were found to be $480°$ C and $400°$ C, respectively. After 4 weeks, many tabular green CBSCl crystals with a maximum size of $15 \times 12 \times 1$ mm^3 were obtained, which were identified as synthetic francisite on the basis of x-ray powder diffraction data [261]. The crystal appears a bright apple green colour. A
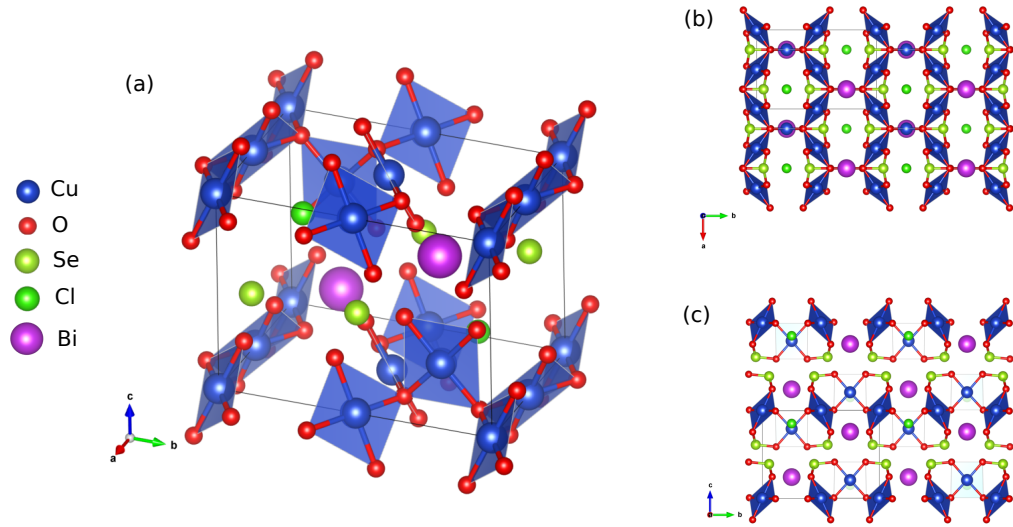
FIGURE 6.1: (a) Crystal structure of room temperature CBSCl (*Pmmn*) with the CuO_4 plackets identified as blue isosurfaces. The hexagonal kagome-like structure is evident in the *ab* plane (b). The buckled hexagonal lattice due to the different Cu sites appears in the *ac* plane (c). All graphics generated using VESTA [253] and information in Appendix B.2.

photograph of the grown crystals is shown in Figure 6.3. The specific sample used in this study was a thin *ab* plane wafer of dimensions $5.1 \times 3.5 \times 0.3\,\text{mm}^3$.

6.3   Experimental methodology

Prior to this work, K. H. Miller's infrared study on CBSCl covered the broad frequency span of 1.2–300 THz (40-10000 cm^{-1}). From ~1.2–30 THz (40-1000 cm^{-1}), strong phonon absorptions render the material opaque and the analysis of the phonon spectrum was performed in reflection geometry. Below 1.2 THz however, CBSCl transmits relatively well, allowing for transmission geometry measurements. Preliminary transmission measurements in the frequency interval 0.45-1.2 THz were performed by K. H. Miller at the National Synchrotron Light Source, Brookhaven National Laboratory in magnetic fields up to 10 T [261]. A detailed temperature survey demonstrated the formation of a magnetically active excitation in the vicinity of 1.0 THz. Another lower frequency mode was detected at high fields above 6 T around 0.45 THz. However, being right at the bandwidth limit of the spectrometer, the existence of the excitation was not conclusive.
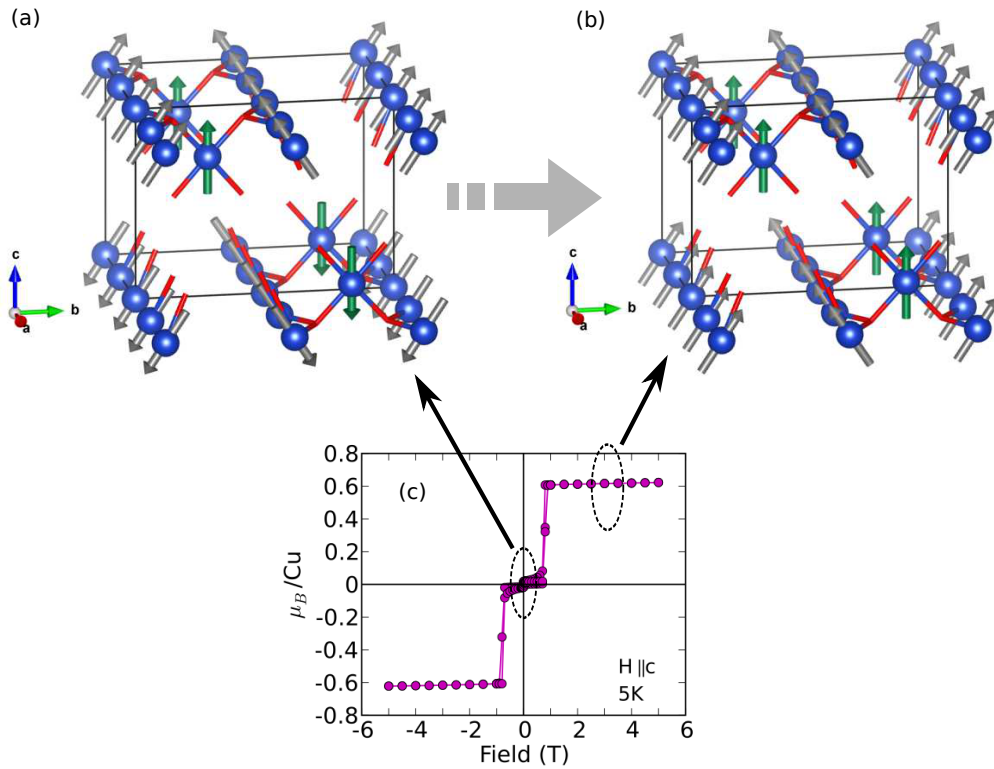
FIGURE 6.2: (a) The magnetic sublattice structure of CBSCl as described by Pregelj *et al.* [265] below $T_N = 24$ K. The silver spin sites are referred to as the Cu1 sites while the green spins are the Cu2 sites. (b) Metamagnetic transition following applied external B field above 0.8 T along c axis. (c) Magnetisation versus external field along c axis indicating metamagnetic transition and ferrimagnetic saturation above 0.8 T (figure courtesy of K. H. Miller [261]).
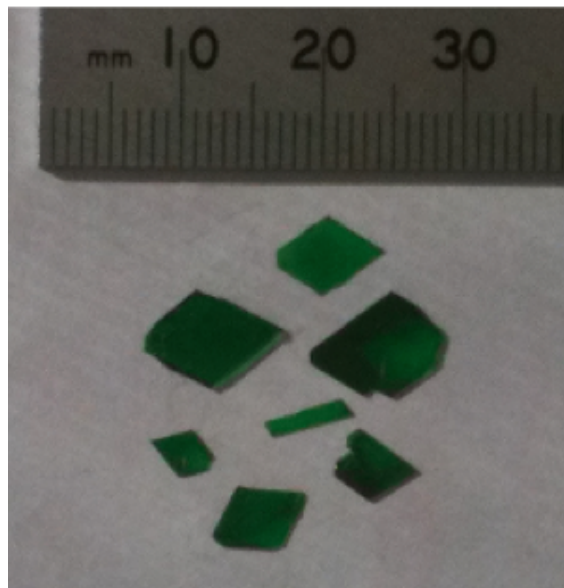
FIGURE 6.3: Photograph of CBSCl single crystals used in the experiment (figure courtesy of K. H. Miller).

The focus of the work in this chapter was therefore to confirm the existence of the low frequency mode, track its energy to zero fields and also identify any other modes at very low frequencies down to 0.1 THz. To achieve this, complementary spectroscopic techniques that utilised two separate sources of THz radiation were implemented. The two systems included the quasi-monochromatic two-colour system and broadband Polytec interferometer. For the purpose of tracking such low frequency excitations, the two-colour system is ideal, as its ability to access low frequencies at high resolution complements the higher frequencies achievable with the Polytec and synchrotron interferometers.

The sample was mounted in the variable temperature insert of the Oxford superconducting magnet with the incident radiation normal to the sample c axis. Magnetic fields up to 5.5 T were applied in the $\mathbf{B}||\hat{c}$ (Faraday) geometry. Sample temperatures from 5–300 K were achieved, but in general the sample was kept at 5 K, well below the magnetic ordering temperature of $T_{\mathrm{N}} = 24$ K. The temperature development of the higher frequency mode had already been established by K. H. Miller and so a detailed temperature survey of the modes identified in this work was not carried out.

The flexible placement of the two-colour system photomixer, due to its optical fibre tethering, allows easy interfacing to the Oxford magnet. A schematic of this novel setup is shown in Figure 6.4. The setup consists of the standard two-colour system coupled to a 24 m polarisation maintaining optic fibre, optimised for 850 nm radiation. The fibre carries the mixed laser light to the photomixer in position for use with the Oxford magnet. An approximate loss in optical power of 10% occurs in the 24 m fibre. The tapered laser amplifier is used to compensate for the small loss.

In the magnet setup, the optical fibre is fed through an evacuation port into the vacuum chamber of the Polytec interferometer. The photomixer is fixed in place with an appropriate adjustable mount and the THz radiation it produces is collimated by a removable gold-plated off-axis parabolic mirror. The removable mirror allows for easy switching between use of the Polytec interferometer and two-colour system. For measurements using the Polytec interferometer, the mercury arc lamp source was implemented in combination with the 70 μm beamsplitter. The bolometer detector was used in all measurements.
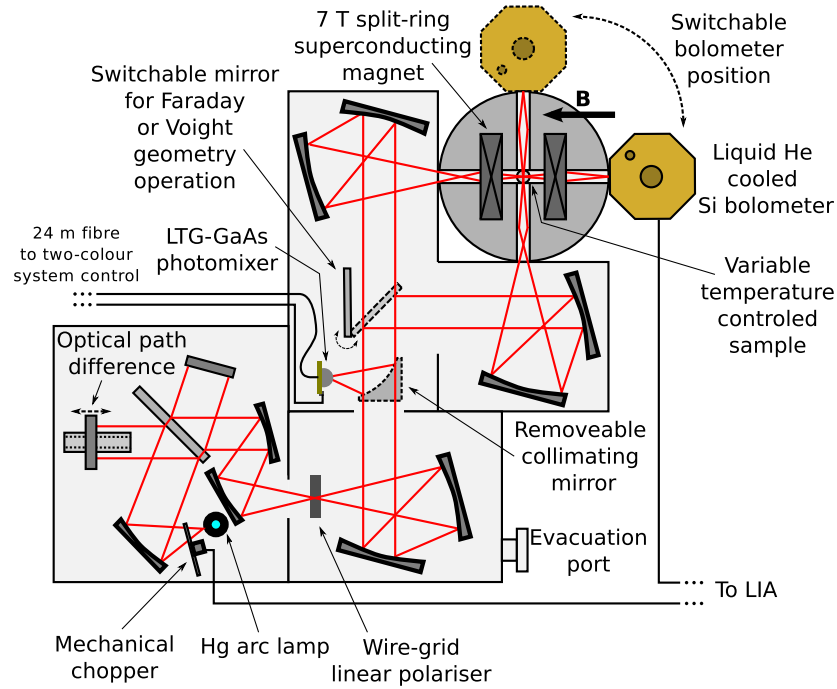
FIGURE 6.4: Schematic of the novel two-colour/magnet THz spectrometer setup interfaced with the Polytec interferometer. The photomixer is able to be placed directly near the magnet through the use of a long (24 m) optic fibre. This allows the spectrometer control system to be operated from a different room within the laboratory. Removing the parabolic mirror allows use of the Polytec interferometer.

6.4 Results

In the preliminary measurements of K. H. Miller, two modes were observed at low energies with frequencies that were shifted by external magnetic fields. One mode had a resonant frequency of $0.99\,\mathrm{THz}$ ($33.14\,\mathrm{cm^{-1}}$) at $0\,\mathrm{T}$ and $1.03\,\mathrm{THz}$ ($34.34\,\mathrm{cm^{-1}}$) at $10\,\mathrm{T}$. It will hence forth be referred to as the high frequency (HF) mode. The other mode, which will be referred to as the low frequency (LF) mode, had a resonant frequency of $0.45\,\mathrm{THz}$ ($14.92\,\mathrm{cm^{-1}}$) at $6\,\mathrm{T}$ and $0.58\,\mathrm{THz}$ ($19.27\,\mathrm{cm^{-1}}$) at $10\,\mathrm{T}$. Below $6\,\mathrm{T}$ the mode could not be tracked due to bandwidth limitations of the spectrometer used. This section presents measurements of the LF-mode down to $0\,\mathrm{T}$.

6.4.1 Quasi-monochromatic spectroscopy

The quasi-monochromatic two-colour system was the first spectrometer implemented to study the CBSCl crystal. As mentioned in Section 3.2.1.1, an initial attempt to reach

6.5 T on the Oxford split-ring superconducting 7 T magnet resulted in a quench of the superconducting coils. Therefore, applied fields were limited to 5.5 T. A broad spectrum measurement at 5.5 T was first attempted. The LF-mode was expected to occur close to the region where the mode was observed at 6 T by K. H. Miller. In addition, the broad spectrum should assist in identifying the presence of any other lower lying modes. Doing this at high fields is also beneficial as, under the correct geometry, the external field should act to lift the energies and increase the intensity of any prospective lower-lying modes, giving the maximum likelihood for identification.

Naturally, if the geometry of the external field is aligned such that it opposes the internal field acting on the spin arrangement, the external field would act to soften the mode. This could weaken the excitation beyond the limits of detection missing a chance for identification. The work of Pregelj *et al.* established that below the magnetic transition temperature, the anisotropy is strongest along the c axis with a weak component along the b axis [265]. The a axis was shown to be the *hard* axis. The experiment was set up so that the external field was applied parallel to the c axis. This ensures that the external field does not oppose the internal field and should act to raise the energies of the spin excitations rather than soften them.

The spectrum taken with the two-colour system is shown in Figure 6.5 (a). A weak feature at $\sim$0.45 THz is indicated in the vicinity of the same feature observed at 6 T by Miller *et al.* [261]. A spectrum at 0 T is also given that highlights the weak absorption feature in the 5.5 T plot. At 0 T the feature is expected to have shifted to lower energies. Transmittance spectra are shown in the inset. A feature does seem to be evident at $\sim$0.43 THz although it appears very weak and there is substantial noise in the spectrum. The noise is attributed to the low signal to noise ratio due to the small sample size with the beam significantly attenuated. The transmission of the crystal is also $\lesssim$20%.

A weak signature in the spectrum of the 0 T data may be evident at $\sim$0.27 THz but is not fully resolved. Indeed a similar feature appears at the same energy in the 5.5 T spectrum. However, linear extrapolation for the data by Miller *et al.* above 6 T suggests a zero field resonance energy of 0.285 THz, which is in close proximity to the feature observed here.

If the external field was applied in the opposite direction, the LF-mode would be softened and would not appear at 0.43 THz at 5.5 T. This confirms that the field orientation is correct for giving the maximum likelihood of observing other lower-lying modes. However, close analysis of Figure 6.5 (a) reveals no other clear resonance features in this spectral region. It should be noted that the large amount of experimental noise in the spectra, with some noise features having larger amplitude than the identified LF-mode, make these conclusions rather tentative. It is the systematic change in position of the LF-mode feature with changing field and agreement with higher field measurements by K. H. Miller, that allows its identification.

A series of spectra from 3–5 T are shown in Figure 6.5 (b). Since no other lower frequency modes were observed in Figure 6.5 (a), these spectra were obtained at high resolution but limited to a range from 0.3–0.5 THz. Since the frequency position of the mode moves rapidly with changing field and the absorption feature has narrow width, the spectra of the mode at different fields do not have frequency overlap. Therefore, the transmittance here may be calculated by a ratio of the spectra at 4 T, 4.5 T and 5 T with the spectra at 3 T. The spectra at 3 T and 3.5 T are ratioed with the spectra at 5 T. This has the effect of reducing noise due to Fabry-Perot fringes. It does however introduce artefact features at corresponding points in the spectra where a resonance feature exists. Nevertheless, a very narrow and weak feature is seen to increase from ∼0.38 THz at 3 T to ∼0.43 THz at 5 T. There is a considerable amount of noise in the spectrum which is compounded by the weak absorption of the mode making it difficult to resolve. Below 3 T the mode is too weak to observe.

In an attempt to observe the zero field resonance of the LF-mode, focus was given to the frequency range 0.15–0.35 THz. This was determined to be the most likely location of the mode from an extrapolation of the frequency/field dependence at higher fields. High resolution (1 GHz) and long integration time (1 s) scans were implemented to achieve the high sensitivity necessary for detecting the weak feature. Two spectra were taken at 0 T, one at 5 K and the other at 200 K. Above the long range magnetic ordering temperature (T_N=24 K), there should be no magnetic excitations in the 200 K spectrum. Therefore, a comparison between spectra at 5 K and 200 K should reveal any purely magnetic features.

The results of the measurements are shown in Figure 6.6. As can be seen, there is a clear difference in the signal of the 5 K spectrum centred around 0.28 THz. A ratio between the two spectra is shown in the inset. The central frequency of the dip is found to be 0.287 THz, in precise agreement with the linear trend of the LF-mode at higher magnetic fields. However, it should also be noted in reference back to Figure 6.5 (a), that this frequency span also corresponds to a minima in the power of two-colour system's characteristic spectrum. Therefore, there is a very low signal over this frequency span which introduces uncertainty in this assignment. Furthermore, the broad nature of the feature ($\sim$0.04 THz) with respect to the resonance modes observed at higher fields ($\sim$0.006 THz) raises questions. While it is understood that applying magnetic fields to the material sharpens the magnetic resonance, the difference in width of the mode at 1 T and 0 T is substantial. It is possible that below the metamagnetic transition there is a series of split modes due to the increased number of spin sublattices. For weak closely spaced resonance features, this would appear as a smeared out broad mode in the spectrum as observed here.

6.4.2   Fourier transform interferometry

The Polytec interferometer was implemented to complement the results obtained by the two-colour system. The mercury arc-lamp source has a higher and more stable power output than the two-colour system, so it is expected to reduce the noise associated with the two-colour system measurements. However, as displayed in Figure 3.10, the mercury arc lamp and 70 μm beamsplitter combination is limited to frequencies above 0.3 THz. Since the results of Figure 6.5 suggest that no lower frequency excitations exist below the LF-mode, measurements at 0.3 THz and above are sufficient. Detailed measurements of the LF-mode in low applied fields are difficult as the mode is expected to soften down to 0.287 THz at 0 T.

Representative spectra at 4 T and 5 T, as well as a reference, are shown in Figure 6.7. The LF-mode is clearly seen to shift from $\sim$0.40 THz at 4 T to $\sim$0.43 THz at 5 T. At 4 T, the HF-mode is also visible shifting only slightly from $\sim$1.0 THz to $\sim$1.01 THz at 5 T. Unfortunately, the frequency of the HF-mode at these field strengths corresponds to a feature in
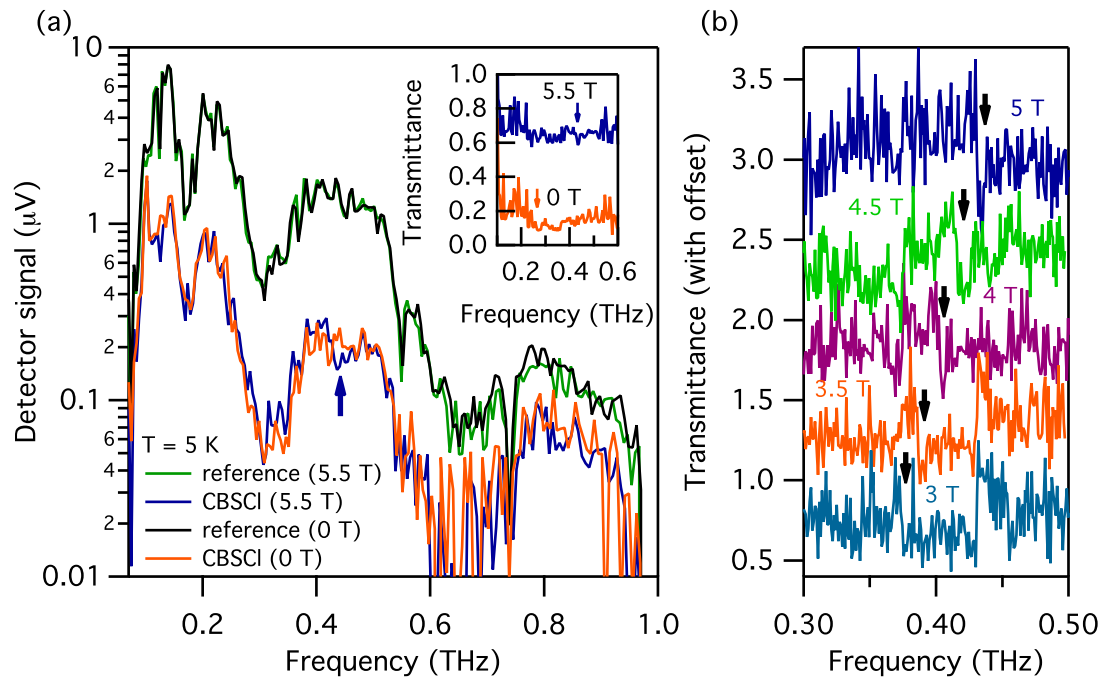
FIGURE 6.5: (a) Comparison of CBSCl and reference spectra at 0 T and 5.5 T. The spectra were taken using the two-colour system at a resolution of 5 GHz. The inset shows the calculated transmittance (5.5 T data is offset by 0.5). (b) High resolution (1 GHz) transmittance spectra of CBSCl from 3 T to 5 T. The spectra are increasingly offset by 0.5. The weak magnetic absorption is indicated by arrows.

the reference spectrum. This masks their true shape and makes it difficult to analyse the mode in detail. The Fabry-Perot oscillations in the spectra also make identification of the modes difficult. The large shift in frequency with changing field and narrow absorption band make it possible to build a reference spectrum from a combination of the spectra at different field strengths following the method described earlier in Section 4.3.

Taking the ratio with this constructed reference leaves only the magnetic effects that shift with magnetic field. The noise from the interference fringes is also filtered out. The results of these ratios are shown in Figure 6.8. The weak resonance the LF-mode is seen to increase linearly from ∼0.3 THz at 0.5 T to ∼ 0.44 THz at 5 T (Figure 6.8 (a)). This agrees nicely with the measurements taken using the two-colour system. Again, the weak nature of the mode makes it difficult to track through the spectra but a clear shift is seen. The inherent noise in each spectrum at low frequencies due to the limitations of the spectrometer bandwidth is reduced by the novel ratio method. This makes identification of the LF-mode close to 0.3 THz possible. However, below 1 T the mode becomes very weak
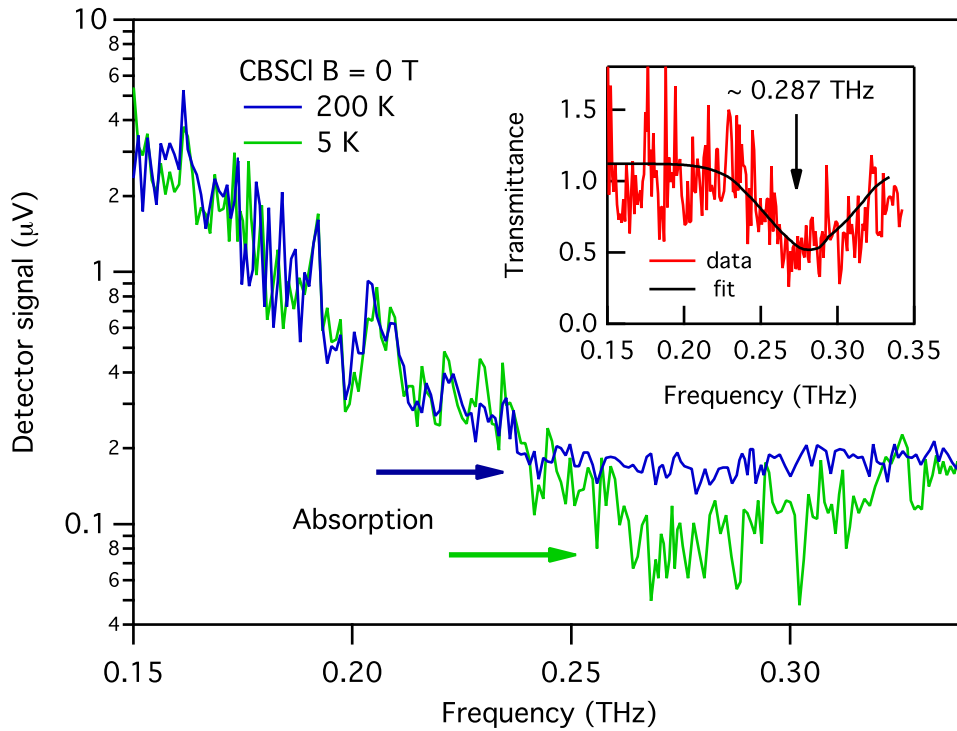
FIGURE 6.6: Spectra of CBSCl crystal at 0 T above (200 K) and below (5 K) the magnetic ordering temperature (24 K). The measurement attempts to identify the zero field resonance of the LF-mode. A ratio of the two spectra appears in the inset.

and the results for 0.5 T and 0.8 T are tentative. At 0 T the mode could not be observed at all. Also worthy of mention, is that there is no remarkable change in the LF-mode across the metamagnetic transition of $H_{MM} = 0.8$ T.

The analysis of the LF-mode in Figure 6.8 (a) also reveals a new possible excitation at $\sim$0.56 THz for the data above 2 T. While it does not shift with changing fields, its activation above 2 T suggests that it might have magnetic origin. This would be a peculiar result however, as the metamagnetic transition above 1 T acts to lower the number of magnetic sublattices. Therefore, less modes should be observed above 1 T. Furthermore, no features were observed over this spectral region by K. H. Miller with fields of 0–10 T. A likely explanation for this feature is that it is due to residual water vapour in the apparatus. This is reasoned because the frequency resembles that of the highly absorbing 0.55 THz water line.

A similar analysis is shown for the HF-mode in Figure 6.8 (b). The HF-mode is broad and does not shift much in frequency with applied field. Therefore, the same constructed
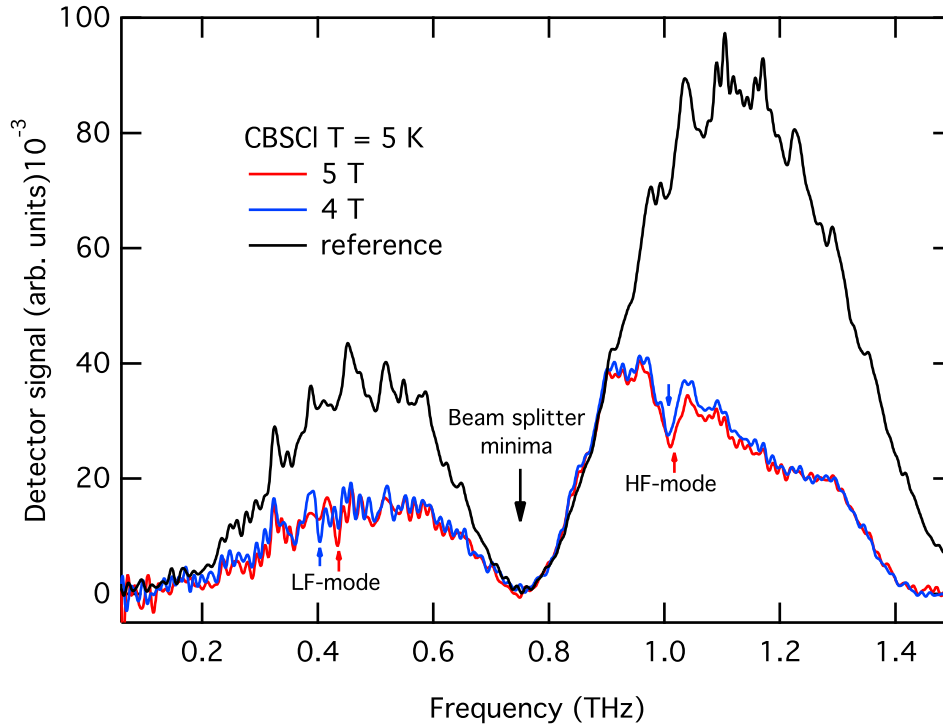
FIGURE 6.7: Spectra of CBSCl crystal with the Polytec interferometer using $70\,\mu$m beam-splitter at an unapodised resolution of $6\,$GHz ($0.2\,$cm^{-1}). The sample is at $5\,$K with magnetic fields of $4\,$T and $5\,$T showing a shift in the LF- and HF-modes. A reference is also shown.

reference, as used in the analysis of the LF-mode, cannot be used here. In this case, the standard reference spectrum taken with no crystal in the beam path (reference trace in Figure 6.7), is used for the ratio. As is seen, the HF-mode is also very weak and is only discernible for fields above $3\,$T.

6.5 Discussion and analysis

6.5.1 Origin of the excitations

To elucidate the nature of the magnetic excitations observed, Miller *et al.* compared the strength of the modes to the extensive literature on magnons and electromagnons in the domain [261]. In essence, it was suggested that the intensity of the LF and HF modes was far weaker than those of reported electromagnons and more consistent with pure magnons. Furthermore, it was shown that reflectivity spectra of the phonon modes measured at 7 K
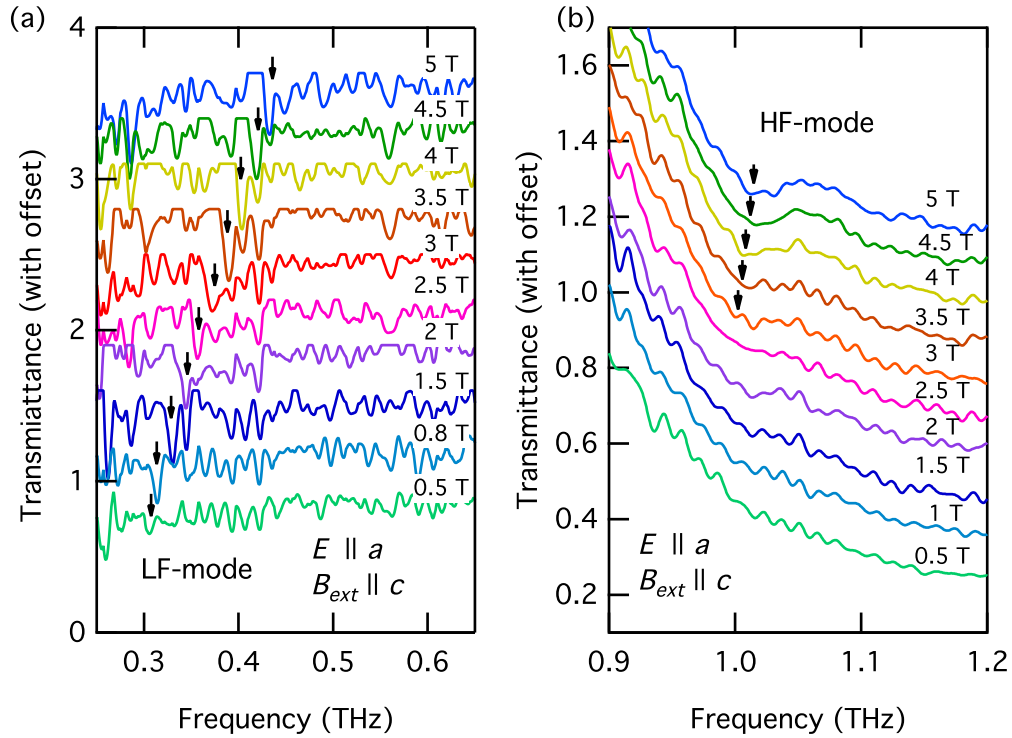
FIGURE 6.8: Magnetic field dependent transmittance spectra of CBSCl crystal using Polytec interferometer from 0.5–5 T. (a) Field dependence of LF-mode calculated by ratio with constructed reference from series of field dependent spectra. (b) Field dependence of HF-mode calculated by ratio with reference in Figure 6.7.

and 30 K (Below and above the magnetic transition), did not show any change associated with coupling to the magnetic excitations. This suggests that the magnetic excitations do not gain spectral weight from the low frequency infrared-active phonon modes.

Electromagnon excitations, extensively studied in the rare-earth manganites, have shown gains in spectral weight from dipole active excitations such as phonons [162]. In return, a loss of spectral weight is detected for the phonon. The absence of this observation for the LF and HF modes here, is a strong suggestion that they are pure spin-wave excitations. The same interpretation was also used by Wang *et al.* in their THz magnetooptical study of CBSBr. Due to the ferromagnetic arrangement of the interlayer Cu^{2+} spins and the canted nature of the hexagonally arranged interlayer spins, the magnetic excitations most likely resemble ferromagnetic resonance.

Spin waves resulting from ferromagnetic resonance typically occur at much lower frequencies because they must extrapolate linearly to zero frequency at zero applied magnetic field

[29]. It is therefore peculiar to observe ferromagnetic resonance above 0.3 THz in a 1 T external field. There is however precedence of an exceptional case involving a metamagnetic transition in $FeCl_2$, first observed by Jacobs *et al.* [193]. The metamagnetic transition in $FeCl_2$, involves a transition from a two-sublattice antiferromagnet to a ferromagnet above 1 T. Following the transition, the antiferromagnetic spin waves at 0.5 THz weaken in favour of a ferromagnetic resonance line around the same frequency. The high frequency of the ferromagnetic resonance line in $FeCl_2$ is explained by large magnetic anisotropy fields in the material with the result supported by theoretical calculations [269]. The two modes therefore proceed to be analysed as ferromagnetic spin-wave resonances above 1 T.

When comparing the field-dependent shifts in frequency of the LF-mode with the HF-mode, it is quite clear that the LF-mode has a much stronger field dependence. This suggests that the two modes result from different copper sites experiencing different magnetisations. Considering the energy of a dipole moment (μ) in a magnetic field ($\mathbf{B}$) is given by $\mu \cdot \mathbf{B}$, then a canted spin will have less energy than an uncanted spin. By associating the HF-mode with the canted Cu1 spin sites, it is expected that the energy (and therefore field dependent slope) is reduced by a factor of $\cos\theta$, where θ is the canting angle. The HF-mode is therefore assigned to the Cu1 with the LF-mode assigned to the Cu2 sites.

6.5.2 Calculations of gyromagnetic factor and magnetic anisotropy

The frequency position determined by a series of mathematical fits to the spectra in Figures 6.5–6.6 is shown in Figure 6.9. The results corroborate nicely with those measured by Miller *et al.* using synchrotron radiation [261]. While attempts were made to track the HF-mode below 5 T, the mode appeared too weak and fits were inaccurate. Approximate fits with large uncertainties were only achieved for 3.5 T, 4 T and 5 T. However, with the full dependence of this mode measured from 0-10 T by Miller *et al.* [261], a detailed analysis was not given to this feature.

The LF-mode shows a linear trend with applied field and good agreement between each of the spectrometers used. Using this field dependent data, the *g* factor and anisotropy energy of the easy axis can be determined by ferromagnetic resonance theory. The theory of ferromagnetic resonance for uniaxial or cubic ferromagnetic crystals was worked out by

Kittel [270] who showed that classically the resonance condition is given by,

$$\hbar\omega = g\mu_B B_{\text{eff}}, \tag{6.1}$$

where g is the g-factor and B_{eff} is the effective magnetic field. Considering easy axis anisotropy and demagnetisation effects from the sample geometry, when the external field is applied along the easy axis, B_{eff} is given by [29, 264],

$$B_{\text{eff}} = \sqrt{(\mu_0 B_{\text{ext}})^2 + A_1\mu_0 B_{\text{ext}} + A_2^2}, \tag{6.2}$$

where A_1 and A_2 are defined as

$$A_1 \equiv (N_x + N_y - 2N_z)\mu_0 M + 2\mu_0 B_A, \tag{6.3}$$

$$A_2 \equiv \mu_0\sqrt{[(N_x - Nz)M + B_A][(N_y - Nz)M + B_A]}. \tag{6.4}$$

Here, B_{ext} is the external applied field, M is the sample magnetisation and N_x, N_y and N_z are the sample dependent demagnetisation factors along the a, b, and c axes, respectively. The uniaxial magnetic anisotropy energy for an easy-axis magnetic material was given earlier in Equation 4.2.2. Neglecting higher-order terms, its effective magnetic field can be approximated as $B_A = 2K/\mu_0\mu_{\text{Cu}}$, where K is the anisotropy constant and μ_{Cu} is the magnetic moment per Cu ion [264]. The magnetisation, M, is in general a function of external field. However, as shown in Figure 6.4 (c), above the metamagnetic transition (0.8 T), the magnetisation reaches a saturation value. This corresponds to $\sim 0.6\mu_B$ per Cu ion [261] and can be considered a constant above 0.8 T.

Substituting Equation 6.2 into Equation 6.1, the data above 1 T in Figure 6.9 (a) is fit for the g, A_1 and A_2 constants. Being linear with respect to the higher order partial derivatives of the fitting constants, the fitting procedure converges with accurate uncertainty values. The results give $g = 2.16\pm0.22$, $A_1 = 17.2\pm5.6\,(\mu_0 T)^{-1}$ and $A_2 = 9.56\pm0.80\,(\mu_0 T)^{-1}$. The g-factor is consistent with typical values for Cu^{2+} ions [271]. Approximating the plate-like sample by an infinitely thin plate, the demagnetisation constants are set to $N_x = N_y = 0$ and $N_z = 1$. The values of A_1 and A_2 can then be used to separately approximate the anisotropy constant K. The value from A_1 gives $K = 0.15 \pm 0.05\,\text{meV}$ and from
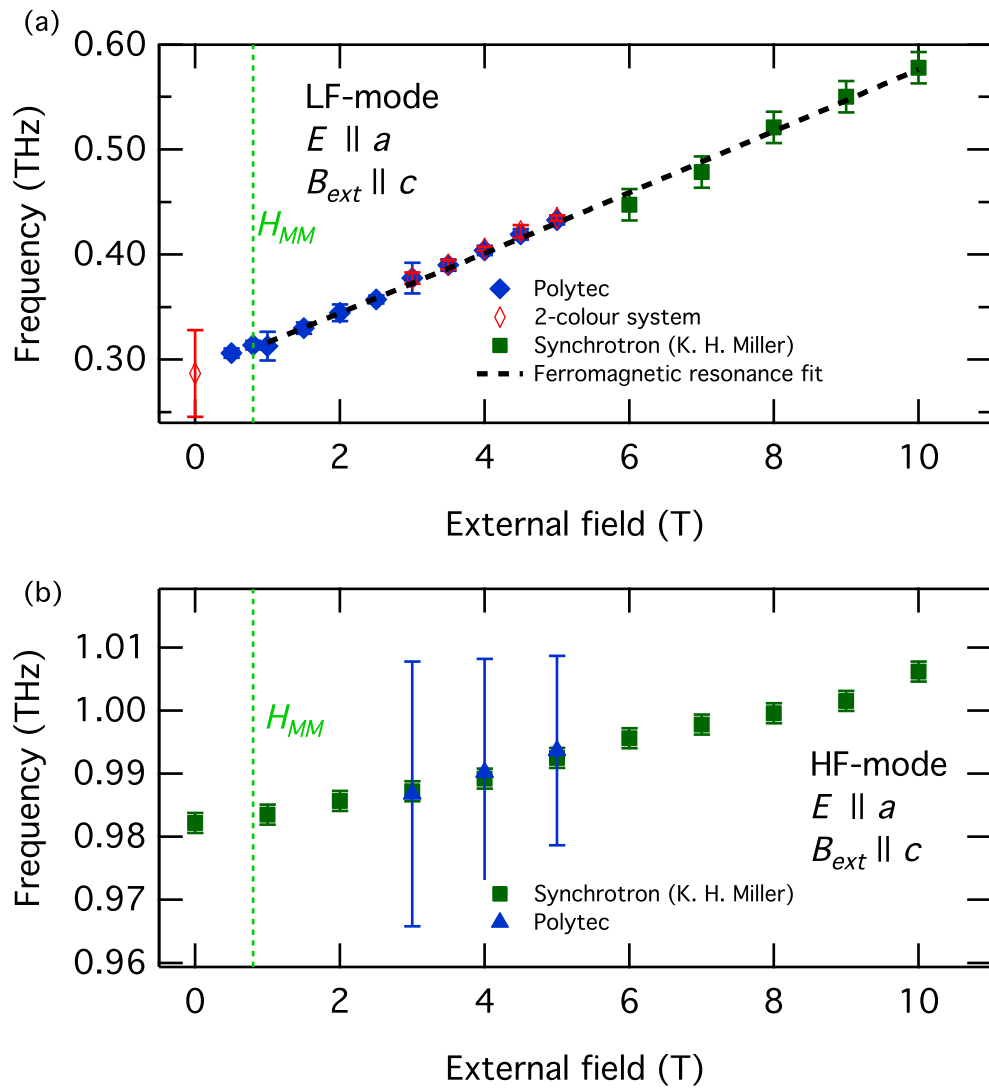
FIGURE 6.9: Magnetic field dependence of the LF- (a) and HF- (b) mode frequency for CBSCl at 5 K. The metamagnetic transition (H_{MM}) is identified at 0.8 T. The error bars represent the half width at half maximum of the fitted peaks. Equation 6.1 is fit to the data above 1 T in (a) for the calculation of g and K.

A_2 gives $K = 0.17 \pm 0.02$ meV. The magnetic anisotropy energies are consistent with values obtained for CBSBr by both THz ferromagnetic resonance [264] and magnetisation approximations [265].

6.6 Conclusions

In summary, THz spectroscopy in the frequency range of 0.1–1.2 THz of the geometrically frustrated CBSCl compound has revealed two magnetically active excitations. The excitations, named the LF and HF modes, have tentatively been assigned to spin-wave excitations in the Cu^{2+} magnetic sublattices. The possibility of electromagnon excitations resulting from potential ME coupling following a structural transition at 115 K that corresponds to a change in the magnetic susceptibility, remains. However, based on an analysis of the infrared phonon spectrum by K. H. Miller, no ME coupling is detected in these excitations.

Above 0.8 T applied along the c axis, CBSCl undergoes a metamagnetic transition where the alternating antiferromagnetically aligned layers flip forming a ferromagnetic or, more precisely, a ferrimagnetic arrangement. In the ferrimagnetic state, the field dependence of the LF-mode was analysed using ferromagnetic resonance theory and a fit to the field dependent data. The results revealed a g-factor value of $g = 2.16 \pm 0.22$ which encompasses the expected value of a spin half system (i.e Cu^{2+}), which is $g = 2.0$. The uniaxial anisotropy energy along the c axis was also determined from two different coefficients of the fit. The results gave values of $K = 0.15 \pm 0.05$ meV and $K = 0.17 \pm 0.02$ meV, which is consistent with magnetisation measurements of the isostructural and magnetically similar compound CBSBr. A similar analysis of the HF-mode by Miller *et al.* gave a g-factor value of ~ 0.4 [261]. The large difference compared to the LF-mode and the expectation of 2.0 reveals that the HF-mode likely results from the canted Cu1 spin sites with the LF-mode from the Cu2 sites.

Interestingly, even though there are 5 distinct magnetic sublattices above and 6 below the metamagnetic transition, only two excitations are observed where one might expect one mode per sublattice. While it is possible that the excitations are not optically active, calculations invoking the DM interaction have predicted up to 6 modes with frequencies ranging from 0.2 THz to 4 THz at the zone centre, which should be optically active [268]. Furthermore, the frequency positions of these predicted modes do not agree with the zero field extrapolations for the modes measured here. It is likely that a refinement of the model predicting these modes is required. However, there is also large uncertainty in the

observations of the magnetic excitations in this study due to the weak signals obtained. Attempts to measure the LF-mode at zero field revealed a broad and weak absorption which could be the result of a group of weak excitations overlapping each other. To better understand the spin-waves in this system, inelastic neutron scattering experiments are required to reveal the structure of the spin-wave dispersion. A full picture of the dispersion would complement the THz spectroscopy possibly revealing the 'hidden' spin-wave modes and refining the theoretical model involving the DM interaction. However, the growth of appropriately large crystals is a limiting factor for such measurements.

A polarisation study of the HF-mode by K. H. Miller identified that the excitation was isotropic (excited by all polarisations in the *ab* plane) [261]. This was interpreted as a crossing of two orthogonal spin-wave dispersions at the $k = 0$ zone centre. A similar phenomenon was observed by Kida *et al.* in $DyMnO_3$ [203]. However, such isotropic excitations can also be the result of a spiral-like layering of the spins along the *c* axis [272]. In such an arrangement, the spin waves will have left- and right-handed circular polarisation. The linear projection of the THz wave would couple the spins along all polarisations for $\mathbf{k}||\hat{c}$ measurements. This interpretation may also explain the very weak absorption properties of the excitations as only a small component of the spin wave absorbs the THz radiation.

A spiral like structure is inherently coupled to the layering of the crystal lattice and therefore the possibility of ME coupling exists. Magneto electric coupling is very appealing in CBSCl, since the occurrence of the metamagnetic transition for weak magnetic fields offers the potential of magnetic switching. In a ME coupled material one could envisage the manipulation of the magnetic switch by means of equally small electronic currents, a very desirable application indeed.

Chapter 7

Spin waves in canted antiferromagnet NdFeO$_3$

7.1 Introduction

In this chapter, polarisation sensitive THz spectroscopy is performed on a single crystal of the canted antiferromagnet NdFeO$_3$. Two orthogonal spin waves are observed and their frequencies are measured as a function of temperature and applied magnetic field. Many of the results in this chapter were published in Reference [40].

NdFeO$_3$ is part of the rare-earth orthoferrite (RFeO$_3$) series of materials, which have recently gained renewed scientific interest due to the discovery of multiferroic behaviour in DyFeO$_3$ [273], SmFeO$_3$ [274], and GdFeO$_3$ [275]. Most notably however, the RFeO$_3$ series are known for their complex range of magnetic properties, such as weak ferromagnetism and a temperature induced spin reorientation (SR) [276]. The SR involves a continuous and coherent rotation of the antiferromagnetic Fe–Fe spin lattice through 90° from alignment along one principal crystal axis to another.

The SR phenomenon has been the subject of numerous investigations [277–280]. However, its exact mechanism is still poorly understood. The two main theories developed attribute SR to either temperature-dependent anisotropic fields [278] or antisymmetric coupling between the Fe^{3+} and R^{3+} ions [279]. Both mechanisms have been supported by

various experimental results [197, 280, 281], but neither has been shown conclusively to be correct. The spin-wave dynamics measured in this and the proceeding chapter assist in understanding the nature of the SR in NdFeO$_3$. The results draw conclusions about the SR through calculations of the dynamic anisotropic energies.

The chapter is structured as follows: Section 7.2 is dedicated to background information regarding the RFeO$_3$ series. Details about the history of these compounds, their unique magnetic properties and recent interest in THz spectroscopy are covered. Section 7.3 provides specific details about the NdFeO$_3$ crystal used in the experiments. Its crystal and magnetic structure is defined. The sample face and chemical phase are determined by XRD and EDS studies. The magnetic Hamiltonian is also given along with the spin-wave equations. Three separate sections are then dedicated to THz spectroscopy performed using three complementary spectrometer systems. Section 7.4 covers the Zomega time-domain spectroscopy system, Section 7.5 covers the Polytec interferometer and Section 7.6 covers the two-colour system. Details about the specific experimental methodology are provided in each section. Section 7.7 then combines the data and provides a brief analysis. Section 7.8 summarises the chapter. Further analysis using complementary inelastic neutron scattering is covered in the next chapter (Chapter 8).

7.2 Rare earth orthoferrites (RFeO$_3$)

Following developments in the concept of antiferromagnetism by Néel in 1932, a hotbed of research through the 1940s and 50s matured around this new form of magnetism [282]. At the same time, availability of rare earth elements greatly improved as global production of rare earth ore increased substantially over this period [283]. One particular series of materials to emerge from this effort was the rare earth orthoferrites with the chemical formula RFeO$_3$ (where R represents one of the rare earth elements).

Early work on powdered polycrystalline forms of RFeO$_3$ were performed by Néel and Pauthenet in 1954 [194]. In 1956 single crystals were first produced by Remeika [284] and Geller promptly detailed the crystal structure of a representative compound, GdFeO$_3$ [285]. It was found that the orthoferrites crystallise in an orthorhombically distorted

perovskite structure belonging to space group D_{2h}^{16}-*Pbnm* with four Fe^{3+} ions and four R^{3+} ions per primitive cell. Neutron diffraction measurements performed by Koehler *et al.* demonstrated a G-type antiferromagnetic configuration (spins having six antiparallel nearest neighbours) of the Fe^{3+} magnetic ions with relatively high Néel temperatures in the vicinity of 600-800 K [286, 287]. At low temperatures the R^{3+} ions were also seen to order in $ErFeO_3$ (T_N = 4.3 K) and $HoFeO_3$ (T_N = 6.5 K). A detailed description of the crystal structure and magnetic arrangement of $NdFeO_3$ is provided in Section 7.3.

The early work on $RFeO_3$ established two principal areas of research focus:

1. A weak ferromagnetic moment had been demonstrated in the early magnetic torque measurements [288–290]. However, since the Fe^{3+} sublattice was antiferromagnetic and the R^{3+} sublattice did not order until very low temperature, the mechanism behind this was not immediately clear.

2. A temperature dependent and reversible rotation of the spin network from alignment along either the *a* or *c* crystal axis to alignment along the *c* or *a* axis respectively was consistently observed in many of the $RFeO_3$ compounds [277, 285, 289]. This was referred to as the spin reorientation.

Naturally, each of these phenomena are intimately related to each other. Here they are given a brief separate discussion, as each topic represents a natural progression in the understanding and development of research interest for the $RFeO_3$ series. A diagram displaying both phenomena in terms of the antiferromagnetically coupled Fe^{3+} spin moments is shown in Figure 7.1

7.2.1   Weak ferromagnetic moment and spin canting

As reviewed in Section 2.3, in an antiferromagnetic material the ordered spins are aligned in an antiparallel arrangement. As a result, the net magnetic moment must be zero. However, in the rare earth orthoferrites (like many other transition-metal oxides) a weak ferromagnetic moment is observed in the presence of antiferromagnetic ordering [288]. Initially, the presence of parasitic ferromagnetism or ferrimagnetism was suggested. However, in such cases the ferromagnetic moment must appear along the antiferromagnetic axis.
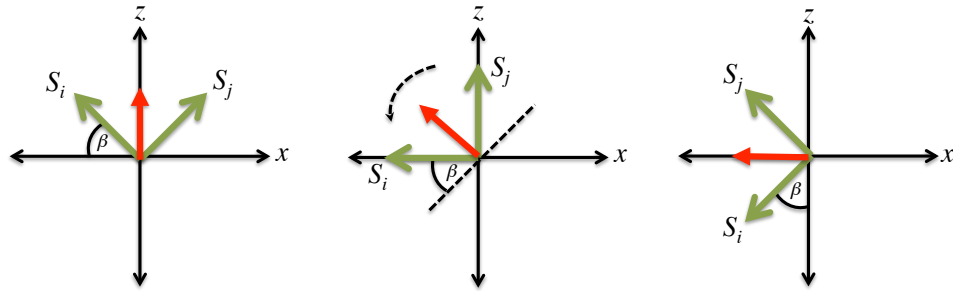
FIGURE 7.1: Diagram of weak ferromagnetic moment and spin reorientation in RFeO$_3$. The antiferromagnetically coupled Fe^{3+} spin moments represented as green arrows are designated S_i and S_j. The net ferromagnetic moment is displayed as a red arrow. β is the angle between the canted spin and the antiferromagnetic axis.

What would later become apparent with improved neutron diffraction studies, is that the antiferromagnetic axis and ferromagnetic moment were mutually perpendicular [287]. For example, as Koehler *et al.* observed in ErFeO$_3$ at room temperature, the antiferromagnetic axis lies along the [100] direction or a crystallographic axis. However, the ferromagnetic moment is along the [001] direction or c crystallographic axis [287]. It was thus suggested that the weak ferromagnetic moment was due to imperfections in an otherwise perfect antiferromagnetic alignment of the Fe^{3+} moments. Repeated accounts of the weak ferromagnetism by various groups, however, suggested that it was an intrinsic property.

During this period, the Dzyaloshinsky-Moriya (DM) exchange interaction was being developed [221, 222]. The DM interaction showed that it was possible to change the spin direction or magnitude, without departing from the symmetry of the original distribution, of antiferromagnetic spins through an energetically favourable antisymmetric spin exchange coupling. The DM interaction is prevalent in materials with a super-exchange across oxygen bonds and typically leads to a canted spin structure. Treves later developed magnetic torque methods to determine if the weak ferromagnetic moment in RFeO$_3$ was due to spin canting as a result of either single-ion magnetocrystalline anisotropy or an antisymmetric exchange interaction [277]. His results supported the antisymmetric exchange or DM interaction explanation. This was later confirmed using Mössbaur measurements that showed that the super-exchange and perturbing force had the same temperature dependence and were therefore part of the same interaction. In recent years, an inverse effect of the DM interaction has been proposed as responsible for the ferroelectric ordering observed in DyFeO$_3$ [273], SmFeO$_3$ [274], and GdFeO$_3$ [275].

7.2.2 Spin reorientation

Perhaps one of the most intriguing properties of the rare earth orthoferrites is the spin reorientation (SR) transition. The SR involves a temperature-driven rotation of the easy axis of magnetisation through $90°$ from one principal axis to another. It is observed in all of the rare earth orthoferrites for which the RFeO$_3$ ion has a magnetic moment. Therefore, it is not observed in LaFeO$_3$, YFeO$_3$ or LuFeO$_3$ [291]. In most cases (R = Yb, Tm, Er, Ho, Dy, Tb, Gd, Eu, Nd, Pr), the antiferromagnetic axis is in the c direction with the weak ferromagnetic moment in the a direction below the transition temperature [194, 291]. Above the transition temperature the antiferromagnetic axis rotates into the a direction with the ferromagnetic moment in the c direction. This is the opposite case for SmFeO$_3$. Typically, the rotation is continuous over a broad temperature range in the order of 10 K. The process starts at a temperature T_1 and the spin arrangement rotates until a temperature T_2. However, for DyFeO$_3$ the transition is observed as an abrupt rotation occurring at a single temperature T_r [279]. The doped compound Dy$_{0.5}$Pr$_{0.5}$FeO$_3$ features a two fold SR passing through an intermediate state with the antiferromagnetic axis aligned along the y direction [292].

The SR was initially observed as a rotation of the net magnetic moment in early magnetic torque measurements [288–290]. Neutron diffraction later identified the phenomenon as a rotation of the antiferromagnetic Fe^{3+} spin sublattice [293], [291]. It was also established through the absence of anomalies in specific heat measurements, that the transition was not crystallographic and thus second order in origin [294]. Considering this, two possible mechanisms for the reorientation were considered [295]:

1. A continuous and coherent rotation of all spins with change in temperature.

2. A discontinuous series of $90°$ spin flips in localised domains, the proportion of such domains being a function of temperature.

Angular dependent Mössbauer measurements on ErFeO$_3$ confirmed the absence of a first order transition. The results further demonstrated the transition to involve a continuous and coherent rotation of Fe^{3+} ion spins [295]. This was latter supported by sound velocity

measurements of shear waves, with a polarisation vector along the a axis [296] and by neutron diffraction of single crystals [293].

With the second order and coherent rotational nature established, discussion moved to the microscopic mechanism behind the reorientation. Early models for the mechanism of rotation involved the use of a dynamic anisotropy with magnitude and direction changing with temperature [297]. Shane improved this model with the concept of competing internal fields and a largely temperature independent fourth order anisotropy [278]. Shane's work predicted the occurrence of a soft resonance mode consistent with the spin-wave spectrum determined by Hermann [298] and resonant microwave measurements by LeCraw *et al.* [299]. The details were developed further by Levinson *et al.* [300], who argued that since the preferred direction of the magnetic moment is determined by the magnetic anisotropy, the easy-axis reorientation process must be governed by the temperature variation of this anisotropy. The key result of this work was the notion that the transition temperature is dictated through the cancellation of the fine structure and the dipolar contributions to the second-order anisotropy in the spin Hamiltonian. While this theory could also be applied to the similar canted antiferromagnetic, haematite (αFe_2O_3) [301], it fails to naturally explain the absence of a spin reorientation in the $RFeO_3$ compounds where the R^{3+} ions have no magnetic moment, e.g. $YFeO_3$.

To interpret their far infrared transmission data, Aring and Sievers suggested that the full Hamiltonian involving Fe^{3+}–R^{3+} as well as R^{3+}–R^{3+} magnetic exchange interactions were required to properly describe the spin-wave spectrum and macroscopic properties of the $RFeO_3$ series [281]. This was supported by inelastic neutron scattering measurements performed by Shapiro *et al.* who demonstrated that the simple two sublattice model was able to approximate the low energy acoustic spin-wave spectrum but not the high energy exchange modes [280].

In 1974, a model was developed by Yamaguchi showing that the anisotropic magnetic interactions between Fe^{3+} ions and R^{3+} ions, are generally responsible for both the rotational and the abrupt types of the spin-reorientations [279]. The model incorporates antisymmetric and the anisotropic-symmetric exchange interactions that produce an effective field on the spins in the direction perpendicular to their alignment. The field acts in different

directions for each Fe^{3+} sublattice. Ultimately, the interactions favour rotation of the spin lattice, retaining its original antiferromagnetic configuration. Thus, as the temperature is lowered, the effective field increases due to the increase of the rare earth magnetisation. When the interaction energy of the Fe^{3+} spins with the effective field exceeds the anisotropy energy of the system, SR takes place. The main attraction of this model is that it accounts for the lack of SR in non magnetic R^{3+} $RFeO_3$ compounds. However, the model is problematic at explaining the high temperatures of the SR ($\sim100\,\mathrm{K}$) since rare earth magnetisation does not occur until very low temperatures ($\lesssim5\,\mathrm{K}$).

7.2.3 Contemporary studies on RFeO₃

Interest in the $RFeO_3$ compounds was initially maintained by its potential application in magnetic bubble memory. The occurrence of strong magnetic anisotropy with substantial temperature dependence and a low value of magnetic saturation facilitated the formation of magnetic bubble domains in $RFeO_3$ single crystal wafers [302]. The bubble domains hold the magnetisation vectors normal to the large surfaces of wafer crystals and are exploited in non-volatile memory devices known as bubble memory [194, 303]. The promise of the $RFeO_3$ compounds for application in this technology was ultimately superseded by the more desirable properties of Yttrium iron garnet [303]. Finally, when magnetic bubble memory was overtaken by the cheaper and more efficient flash memory, interest in $RFeO_3$ declined.

Advancements in laser technology which led to the developments of improved Raman scattering techniques, opened the door once again for studying the spin dynamics of $RFeO_3$. A series of Raman experiments in the 1980's focused on observing the spin-wave temperature dependence [196–200]. The low frequency Raman scattering could track the spin waves as they rotated through $90°$ using polarisation sensitive techniques. The key developments to come from this research was the direct observation of spin-wave temperature-dependence and precise determination of the SR transition temperatures.

The more recent developments for THz technology have allowed direct measurement of the antiferromagnetic resonance due to the acoustic spin waves in the $RFeO_3$ series [40, 201, 210]. The THz frequency control of magnetisation by femtosecond laser pulses is also

possible, first demonstrated by Kimmel *et al.* for DyFeO$_3$ [207]. The concept of inertia-driven spin switching, therefore, has its basis in the THz frequency spin waves of RFeO$_3$ materials [42].

In terms of spectroscopy at THz frequencies, the work of Yamaguchi *et al.* [209, 210] (distinct from Yamaguchi of Reference [279]) has been pioneering. Establishing the coherent control of spin precession with half-cycle THz radiation, Yamaguchi *et al.* present the possibility of controlling spin diffusion for spintronic applications [209]. Using this technique, which consists of a polarised analysis of THz time-domain spectroscopy, the temperature dependence of the spin-wave modes in ErFeO$_3$ were tracked through the SR. Much of the work of Yamaguchi *et al.* was undertaken and published during the period of this doctoral study. As a result, similar concepts are presented in this chapter.

With this in mind, many RFeO$_3$ compounds still remain to be surveyed at THz frequencies. In this chapter, focus is given to NdFeO$_3$. In contrast to the work of Yamaguchi *et al.*, a number of complementary THz techniques are implemented in the study of RFeO$_3$ spin waves. Some of these results suggest a more conventional model of spin excitation than that claimed by Yamaguchi *et al.*

7.3   Neodymium iron oxide (NdFeO$_3$)

In spite of the long history of research on the RFeO$_3$ compounds, NdFeO$_3$ remains largely unstudied. This is in part due to unavailability of large, high quality crystals. The recent increased supply of neodymium for use in strong permanent magnets (NdFeB), has facilitated an increased availability of Nd based materials [283]. This chapter represents the first comprehensive THz study on NdFeO$_3$.

7.3.1   Crystal structure

NdFeO$_3$ crystallises in a distorted orthorhombic perovskite structure of the D_{2h}^{16} (*Pbnm*) space group [287]. The unit cell is pictured in Figure 7.2. The Fe^{3+} ions are surrounded by
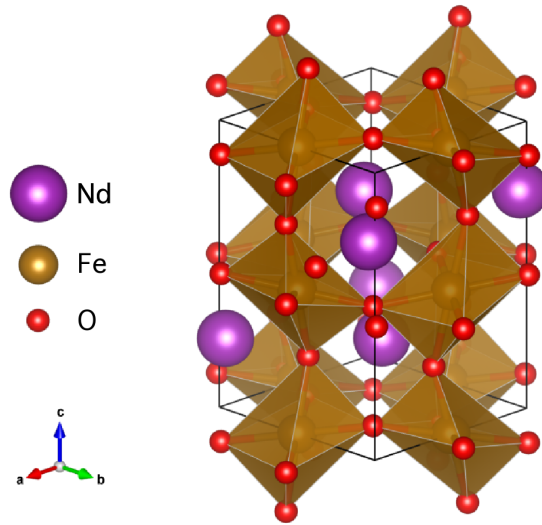
FIGURE 7.2: Orthorhombic *Pbnm* crystal structure of NdFeO₃. FeO₆ octahedra represented with brown isosurfaces (graphic generated using VESTA [253] and information in Appendix B.3).

six O^{2-} ions arranged in FeO₆ octahedra. The structural parameters near room temperature (290 K) are approximately $a = 5.45$ Å, $b = 5.59$ Å and $c = 7.76$ Å [304]. The similar values of a and b indicate only a slight orthorhombic distortion away from a tetragonal or pseudocubic perovskite structure. Along the RFeO₃ series, this distortion increases with increasing rare earth atomic number. The ratio of the b and a lattice constants changes from 1.017 for PrFeO₃ up to 1.064 for LuFeO₃. NdFeO₃ has a relatively small value of 1.024 [305].

7.3.2   Spin structure

There are two magnetic ion species in NdFeO₃, Nd^{3+} and Fe^{3+}. An isotropic super-exchange across the Fe-O-Fe bonds favours antiferromagnetic ordering of the Fe^{3+} ions below 670 K [304]. A weak ferromagnetic moment perpendicular to the antiferromagnetic ordering axis occurs due to subtle spin-canting of approximately 8.5 mrad from the parallel state [306]. As previously mentioned, this is a result of the anti-symmetric DM interaction [277]. At room temperature, the Fe^{3+} spin state equates to antiferromagnetic ordering along the a crystal axis, with the ferromagnetic moment directed along the c axis [304]. This is typically represented as $G_x F_z$ using the notation of Bertaut [307]. In this notation,
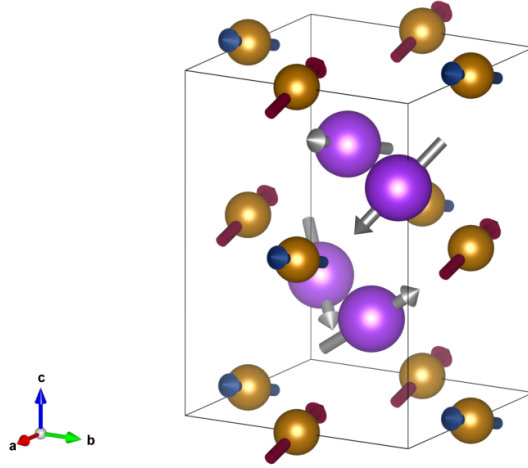
FIGURE 7.3: Spin structure of NdFeO$_3$ at room temperature. The Fe^{3+} ions are brown and the Nd^{3+} ions are purple. The two Fe^{3+} spin sublattices are indicated by the red and blue antiparallel spin moments. The spin ordering constitutes the G_xF_z state.

the magnetic axes x, y, and z are aligned with the crystallographic axes a, b, and c respectively. G_x refers to the "checker-board" style (G-type) antiferromagnetic ordering, aligned to the x and layered along the z axes. F_z refers to the ferromagnetic moment along the z axis from the canted spin structure.

Strictly speaking, there are four Fe^{3+} spin-sublattices due to the four inequivalent Fe^{3+} sites of the crystal lattice [298]. However, for the low energies considered in this study (on the order of $1\,\mathrm{THz}$ or $\lesssim 10\,\mathrm{meV}$), it has been established that a two sublattice model is an adequate simplification [280, 308]. Therefore at room temperature, the spin structure of NdFeO$_3$ appears as in Figure 7.3. This represents the G_xF_z state of the Fe^{3+} spin sublattice. The Nd^{3+} ions are represented as paramagnetic. This is a result of very weak exchange coupling partly due to relatively large nearest-neighbour spacing and no Nd-O-Nd super-exchange bonding. The magnetic contributions of the Nd^{3+} ions can therefore be neglected when considering the other dominant magnetic interactions associated with spin-wave modes in the THz energy range.

The magnetic Hamiltonian is then constructed with a single isotropic exchange interaction coupling nearest-neighbour Fe^{3+} ions and the Fe-O-Fe super-exchange induced antisymmetric DM interaction [298]. An effective second-order anisotropy is included to stabilise

the spin sublattices with respect to the crystal lattice. The effective anisotropy is chosen to represent the contribution of all the microscopic anisotropy sub-terms in the Hamiltonian. The Hamiltonian is then [197]:

$$H = 2J \sum_{ij} \mathbf{S}_i \cdot \mathbf{S}_j + \sum_{ij} (\mathbf{D} \cdot \mathbf{S}_i \times \mathbf{S}_j) + \sum_i (\mathbf{K}_{\text{eff}} \cdot \mathbf{S}_i)^2 . \tag{7.1}$$

Here J $(0.66\,\text{THz}/22\,\text{cm}^{-1}/2.7\,\text{meV})$ and D $(0.028\,\text{THz}/0.95\,\text{cm}^{-1}/0.1\,\text{meV})$ are the isotropic Heisenberg and antisymmetric DM exchange constants, S $(= 5/2)$ is the spin moment of the ith and jth nearest-neighbour Fe^{3+} ions, and $\mathbf{K}_{\text{eff}}$ is the effective anisotropy. Following the standard procedure, the magnetic axes are set along the crystallographic axes $(x||a, y||b, z||c)$. At room temperature, in the $G_x F_z$ state, $\mathbf{D} = D\hat{z}$. Neutron diffraction [287, 304] and magnetometry [306, 309] studies indicate that the rotation of the spin-moments is confined to the ac plane. Therefore, the anisotropy can be simplified to two perpendicular uniaxial terms, $\mathbf{K}_{\text{eff}} = (K_x, 0, K_z)$ where K_x and K_z are the second-order anisotropic field energies along the a and c crystal axes. Equation 7.1 then takes the form:

$$H = 2J \sum_{ij} \mathbf{S}_i \cdot \mathbf{S}_j + D \sum_{ij} \left(S_i^z S_j^x - S_i^x S_j^z \right)$$

$$+ K_x \left[\sum_i (S_i^x)^2 + \sum_j (S_j^x)^2 \right] + K_z \left[\sum_i (S_i^z)^2 + \sum_j (S_j^z)^2 \right] . \tag{7.2}$$

7.3.3 Spin waves

The time dependent solutions to Equation 7.2 were carried out by Tsang *et al.* [310]. For $k = 0$ the dispersion relation gives two orthogonal spin waves of the form:

$$\hbar \omega_{\text{F}} = \{24 JS \left[2 \left(K_x - K_z \right) S \right] \}^{1/2} \tag{7.3}$$

and

$$\hbar \omega_{\text{AF}} = \{24 JS \left[6 DS \tan \beta + 2 K_x S \right] \}^{1/2} , \tag{7.4}$$
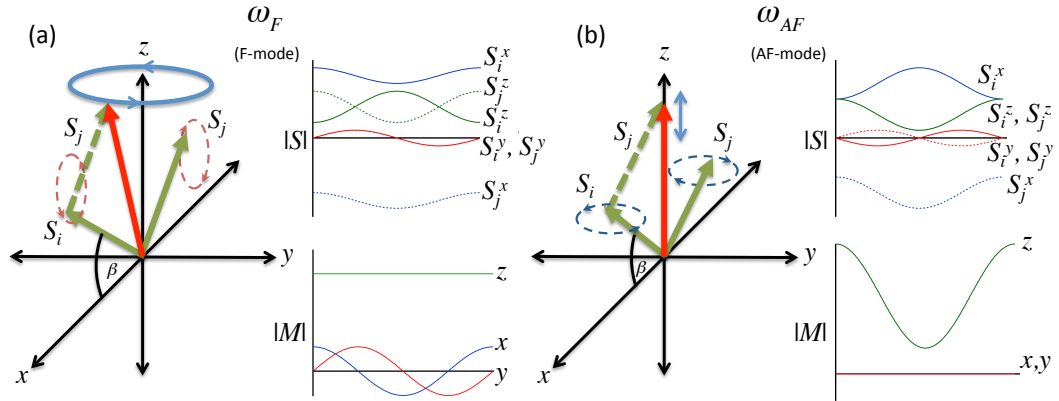
FIGURE 7.4: Optically active spin-wave modes in NdFeO$_3$. (a) ω_{F}, combines in-phase oscillations of the anti-parallel spin components (S_i and S_j) along the x and y axes with out-of-phase oscillations of the z components. The net effect is a low-frequency rotation of the weak ferromagnetic moment (M) around the z axis. (b) ω_{AF}, has out-of-phase oscillations of the anti-parallel x and y components and in-phase oscillations of the z components. This gives a net magnetic oscillation along the z axis

where β is the antiferromagnetic canting angle between the Fe^{3+} magnetic moments of each spin sublattice [197, 298]. The two modes are equivalent to those first derived by Herrmann and are displayed in Figures 7.4 (a) and 7.4 (b), respectively [298].

The spin-wave energies are governed by J, D, K_x and K_z. With $J = 0.66\,\mathrm{THz}$ ($22\,\mathrm{cm}^{-1}$ or $2.7\,\mathrm{meV}$) and $D = 0.028\,\mathrm{THz}$ ($0.95\,\mathrm{cm}^{-1}$ or $0.1\,\mathrm{meV}$) for NdFeO$_3$, this puts them within the THz domain [200, 306]. Using linearly polarised THz radiation, each mode can be excited separately. This is possible since the optically active components of the modes are in the xy plane for ω_{F} and along the z axis for ω_{AF}. As Figure 7.8 shows, ω_{F}, referred to as the F-mode, features a pseudo-excitation of the ferromagnetic moment. Given the rocking motion of the anti-parallel spin moments in the xz plane, the F-mode energy depends on the difference in the anisotropic fields (K_x-K_z). On the other hand, ω_{AF}, referred to as the AF-mode, features a twisting motion about the antiferromagnetic axis. Its energy is sensitive to both the forces along the antiferromagnetic axis (K_x) and the amount of spin canting ($D\tan\beta$).

7.3.4 Sample characterisation

The THz measurements were performed on a single crystal disk (7 mm diameter by 1.95 mm thick) of NdFeO$_3$. The sample was obtained through a collaboration with Shujuan Yuan,
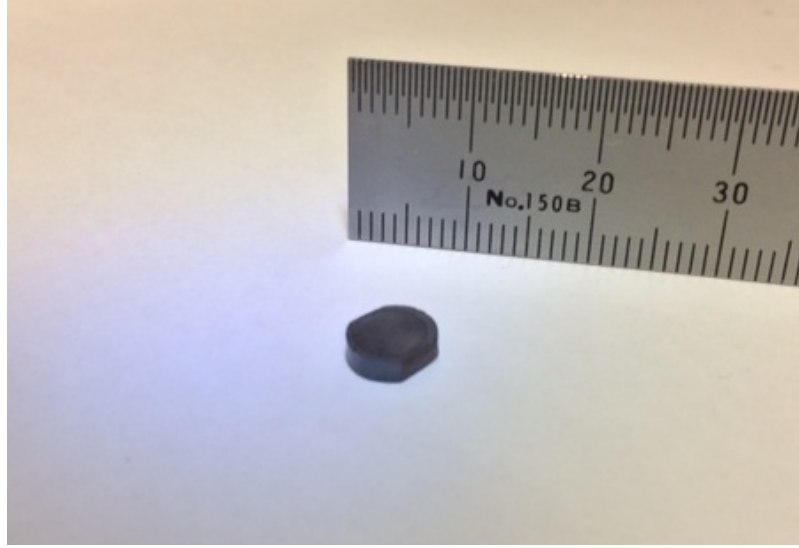
FIGURE 7.5: Photograph of NdFeO$_3$ single crystal used in optical measurements. The sample is approximately disk shaped with a diameter of 7 mm and thickness of 1.95 mm.

Shixun Cao and Guohong Ma of the Department of Physics, Shanghai University in the People's Republic of China. The single crystal was grown by the floating zone method, the details of which are described in Reference [309]. A photograph of the crystal is shown in Figure 7.5. The single crystal was obtained uncharacterised and required identification of the crystal face and confirmation of the chemical phase. This was achieved through the use of x-ray diffractometry (XRD) and energy-dispersive x-ray spectrometry (EDS).

7.3.4.1 X-ray diffractometry

An x-ray diffraction pattern of the sample face is shown in Figure 7.6. Orientation 1 refers to the flat face of the sample that the optical transmission measurements were performed normal to. As is seen in Figure 7.6, a strong diffraction peak is observed at $2\theta = 38°$. Comparison with the joint committee for powder diffraction standards (JCPDS) card number: 74-1473 for NdFeO$_3$, indicates that this scattering plane is (112). The higher order parallel plane (224) is also observed at $2\theta = {\sim}82°$. A smaller peak attributed to surface impurity or scattering off the sample holder is seen at $2\theta = 44°$.
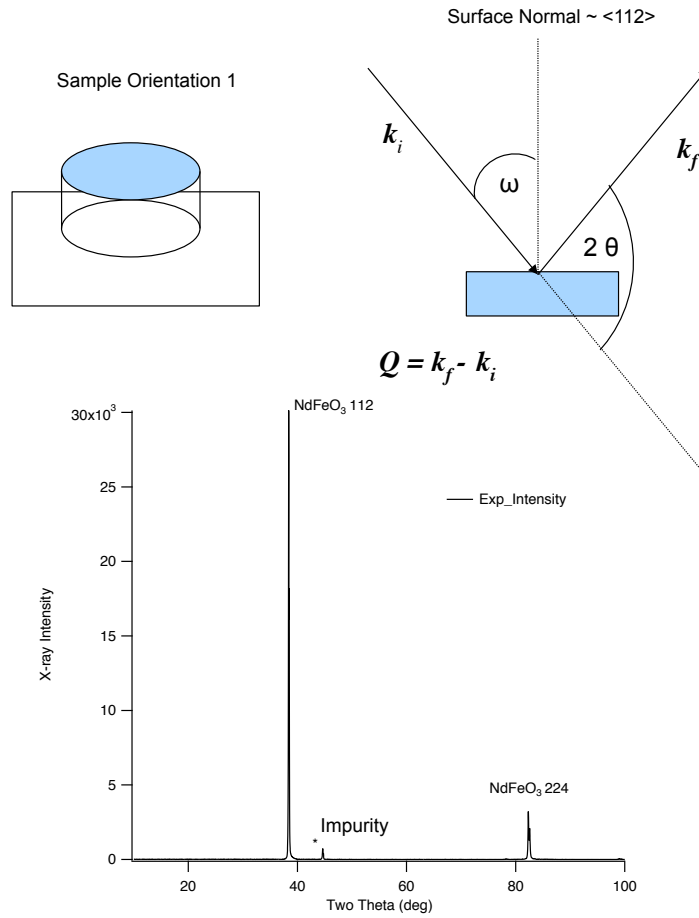
FIGURE 7.6: Schematic of XRD experiment on NdFeO₃ sample with diffraction pattern indicating (112) crystal face.

7.3.4.2 Energy-dispersive x-ray spectrometry

To ensure that the XRD scattering signal at $2\theta = 44°$ was not due to a major crystal imperfection or impurity and to confirm that the sample was in the NdFeO₃ phase, EDS measurements were performed on the (112) face. The results of EDS micrographs are displayed in Figure 7.7. The major elemental signals picked up from the measurements are indeed from Nd, Fe and O atoms. Figures 7.7 (a)-(c), indicate the uniform distributions of each atom. There are some minor depleted oxygen zones which are attributed to surface impurities. An SEM image of the same area is displayed in Figure 7.7 (d). This micrograph reveals the presence of surface debris and impurities, which match the oxygen depleted areas in Figure 7.7 (c). A combination of each EDS micrograph, overlayed with the SEM
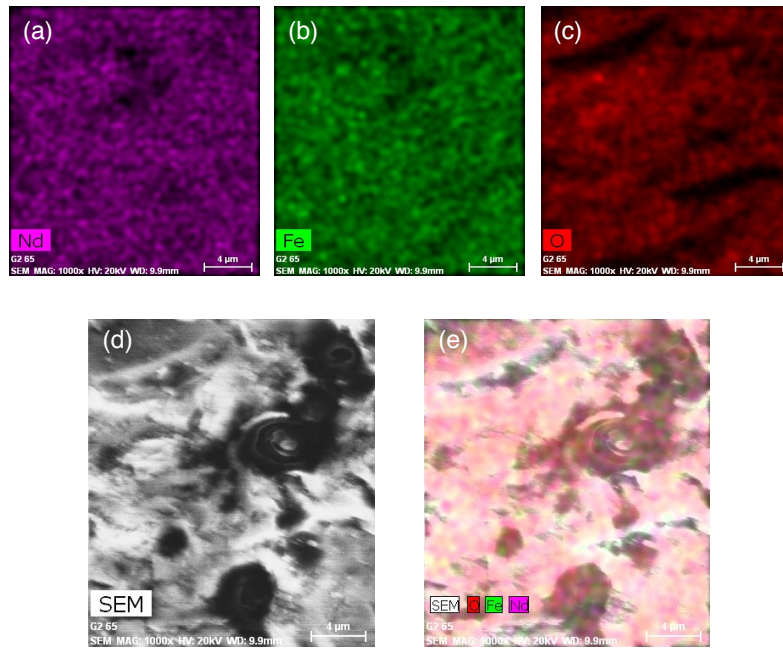
FIGURE 7.7: EDS micrographs of NdFeO₃ sample showing (a) neodymium, (b) iron and (c) oxygen contents. (d) SEM image of same area. (e) Combined micrograph of each content and SEM image.

micrograph, is displayed in Figure 7.7 (e). This demonstrates the uniformity of the Nd, Fe and O distributions away from the surface impurities.

A quantitative display of the EDS results is shown in Table 7.1. Comparing the normalised atomic percentages, it is seen that Nd accounts for $\sim \frac{1}{5}$, Fe for $\sim \frac{1}{5}$ and O for $\sim \frac{3}{5}$. This is equivalent to a Nd_1-Fe_1-O_3 phase as expected in a pure single phase sample. As Table 7.1 indicates, the EDS measurements also revealed some trace signatures of Si. This is attributed to surface contamination. Before the EDS measurement was taken, the sample had been covered in a silicon-oxide based thermal paste for temperature dependent measurements. It is therefore likely that some residue of silicon was left behind from this experiment. No THz signature is expected from the very small quantities of Si residue. The measurements were repeated at two other locations on the sample surface, producing repeatable results concurrent with a single phase crystal.

TABLE 7.1: Table of EDS results detailing elemental constituents of sample. Values are rounded to 6 significant figures. Weight, normalised and atomic are abbreviated as wt. norm. and at. respectively, with σ representing one standard deviation.

Element	Z	series	[wt.%]	[norm. wt.%]	[norm. at.%]	Error in wt.% (σ)
Neodymium (Nd)	60	L	52.9313	55.8480	18.5343	1.44454
Iron (Fe)	26	K	22.1294	23.3488	20.0133	0.61848
Oxygen (O)	8	K	19.1360	20.1905	60.4082	2.28720
Silicon (Si)	14	K	0.58072	0.61272	1.04431	0.05368
		Sum:	94.7774	100	100	

7.3.4.3 Polarised spin-wave orientation

With the crystal face identified as (112) and confirmation of single phase NdFeO$_3$ established, the planes for which the F- and AF-modes are excited by incident radiation can be determined. According to Keffer and Kittel [138], the two optically active spin-wave modes in a two-sublattice orthorhombic antiferromagnet should be mutually orthogonal. This means that radiation polarised to one axis should excite one mode and not the other and visa versa. This is consistent with the original resonant frequencies derived by Herrmann [298] for RFeO$_3$ and those derived by Tsang *et al.* given in Equation 7.4.

However, with a (112) cut orthorhombic crystal, there is no plane of polarisation for normal incident radiation that exclusively excites only one principal axes. Nevertheless, as is shown in Figure 7.8, the geometry of the oscillations allows for exclusive excitation using particular alignment of the incident radiation. As in Figure 7.8 (b), with polarised radiation incident on the (112) face of the sample, when **E** is confined to the $(1\bar{1}0)$ plane, **H** is in the $(11\bar{2})$ plane. In this orientation, **H** oscillates exclusively in the xy plane, with the x and y components out of phase by $\pi/2$. The optically active x and y components of the spin moments have the same time-dependent relationship and the ω_F mode is excited. Lacking a z component, ω_{AF} is not excited. A 90° rotation in polarisation puts **E** in $(11\bar{2})$ and **H** in $(1\bar{1}0)$. In this orientation, **H** has components along all three axes. The z component of **H** couples to the oscillating magnetic dipole of the ω_{AF} mode, which is now excited. At the same time, in the xy plane, the oscillations of the x and y components of **H** are in phase and this cancels the ω_F mode.

A (112)-cut crystal is thus ideal for measurement of the temperature dependence of the two modes, as each mode can be exclusively tracked through the SR using a single sample. For
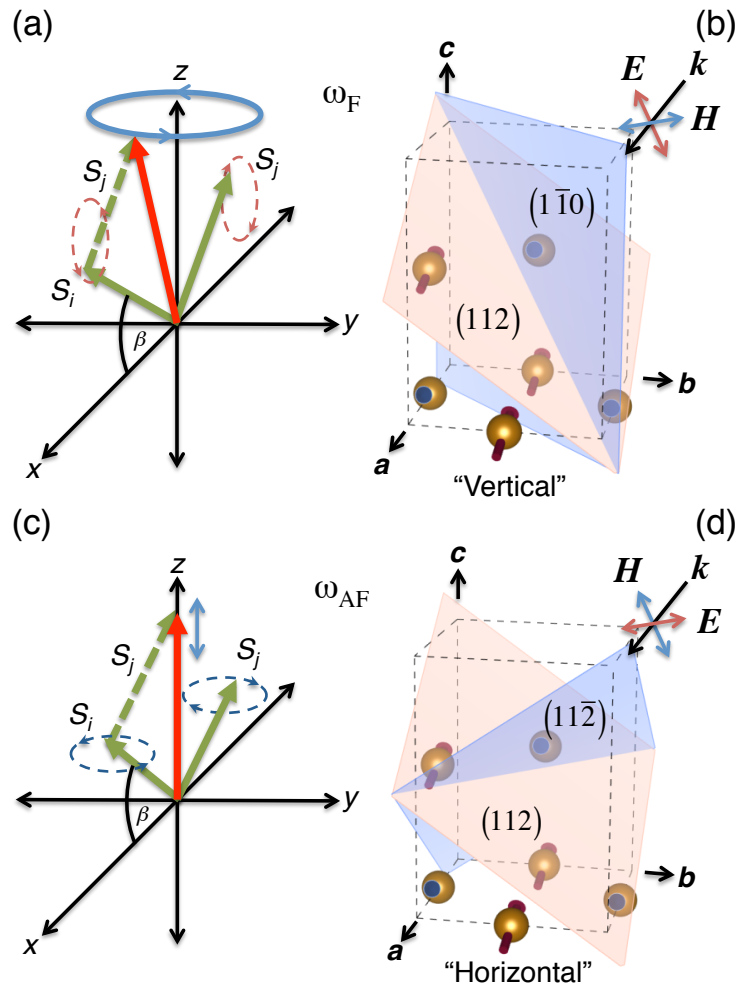
FIGURE 7.8: Optically active spin-wave modes in $NdFeO_3$ and their excitation planes. (a) ω_F, combines in-phase oscillations of the anti-parallel spin components (S_i and S_j) along the x and y axes with out-of-phase oscillations of the z components. The net effect is a low-frequency rotation of the weak ferromagnetic moment around the z axis. (b) Fe–Fe magnetic sublattices (at room temperature) sectioned along the (112) plane (pink surface), the sample face. Incident radiation polarised within ($1\bar{1}0$) (blue surface) excites the F-mode. (c) ω_{AF}, has out-of-phase oscillations of the anti-parallel x and y components and in-phase oscillations of the z components. This gives a net magnetic oscillation along the z axis (d) Incident radiation polarised within ($11\bar{2}$) excites the AF-mode.

simplicity in describing the orthogonal polarisations later, the polarisation of **E** confined to the ($1\bar{1}0$) plane is referred to as 'vertical'. The polarisation with **E** confined to the ($11\bar{2}$) plane is referred to as 'horizontal'. To assist in identifying the orientations in the figures, data shown in red is for the vertical polarisation, while data shown in blue is for the horizontal polarisation.

7.4   Time-domain spectroscopy

Time-domain THz spectroscopy measurements were undertaken to investigate the pulsed excitation of the spin waves in NdFeO₃. By pulsed excitation, the time delay of the transmitted THz field can also be used to calculated the refractive index. Furthermore, with the oscillations in the transmitted **E** field induced by magnetic resonance, it is possible to visualise the spin moment precession. The TDS measurements were performed using the Zomega system. As well as its pulsed wave capabilities, the Zomega system features a high signal to noise ratio of THz frequencies consistent with RFeO₃ spin waves. Spectral scans were taken with a time delay in the order of 50 ps, producing spectral resolutions of ~0.02 THz. In all cases, the sample was fixed to a 5 mm aperture and placed at the focal point of the Zomega's THz path. The setup was described in Section 3.1.2 and shown in Figure 3.6.

7.4.1   Refractive index and spin wave identification

Terahertz time-domain waveforms of the sample and an air reference are displayed in Figure 7.9. The spectrum of the sample is offset by 0.05. After the initial pulse at ~5 ps in the reference, the standard oscillations from water vapour absorption are observed. At ~26 ps the small localised peak due to reflections in the emitter lens is also evident. The spectrum through the sample shares both of these features. A secondary reflection from the parallel sample faces appears at 99 ps. Due to the longer optical path through the crystal, a time delay in the initial pulse is also observed. The time delay is measured to be $\Delta t = 27.44$ ps. The refractive index (η) of a material is related to the time it takes light to traverse a distance d through it, by the following expression,

$$\eta d = c\Delta t, \tag{7.5}$$

where c is the speed of light. Using this relationship, and the sample thickness of $d = 1.95$ mm, the refractive index of NdFeO₃ is found to be $\eta = 4.2$.

With a Néel temperature of 670 K, the magnetic ordering in the Fe–Fe sublattices is well established at room temperature. As a result, the spin-wave excitations must also be fully

developed. Figure 7.9 (b) and (c) demonstrate the general process for determining the transmittance and identifying the spin-wave modes at room temperature.

A Fourier transform of the time-domain waveform gives the frequency spectra seen in Figure 7.9 (b). By using a long delay time and including the secondary reflection in the Fourier transform, a high resolution spectrum is produced (purple trace). However, the spectrum is dominated by strong Fabry-Perot fringes. By truncating the time-domain waveform before the secondary reflection peak, the Fourier transform gives a smoother spectrum at a lower resolution (black trace). For the purposes of analysing spectral features of spin-wave resonance, the smoother low resolution spectrum is required. Subsequent time-domain measurements are therefore truncated before the secondary reflection. A ratio of the sample spectrum with the reference spectrum gives the transmittance (Figure 7.9 (c)). The sample transmits at about 45% below 0.5 THz. Above this frequency, the transmission begins to drop off approaching 0% by ∼2.0 THz. Above 2.0 THz the sample is opaque due to strong phonon absorptions. Most of the water line features are ratioed out although some artefacts still remain. A strong absorption at 0.16 THz is identified as a spin-wave resonance. This will later be assigned to the F-mode spin wave.

7.4.2 Spin-wave polarisation dependence

To determine the orientation associated with the excitation planes discussed in Section 7.3.4.3, spectra are taken at different orientations as the sample is rotated around its cylindrical axis. The angular dependent measurements are performed with the sample fixed to a 5 mm aperture on a rotating mount. A graphic of this concept is inset into Figure 7.10 (b) As the sample rotates, the projection of the **H** field on the excitation plane either increases or decreases. When the **H** field is aligned with the excitation plane, the projection is maximised and a maximum in the spin-wave absorption intensity is observed.

The results of this experiment are displayed in Figure 7.10. At specific orientations two different absorptions are now evident. One at low frequency (0.16 THz), assigned to the F-mode and on at high frequency (0.48 THz), assigned to the AF-mode. As is seen in Figure 7.10 (a), at different angles either the F-mode or the AF-mode are maximised. An intensity profile with a higher resolution of rotation-step-size is shown in Figure 7.10
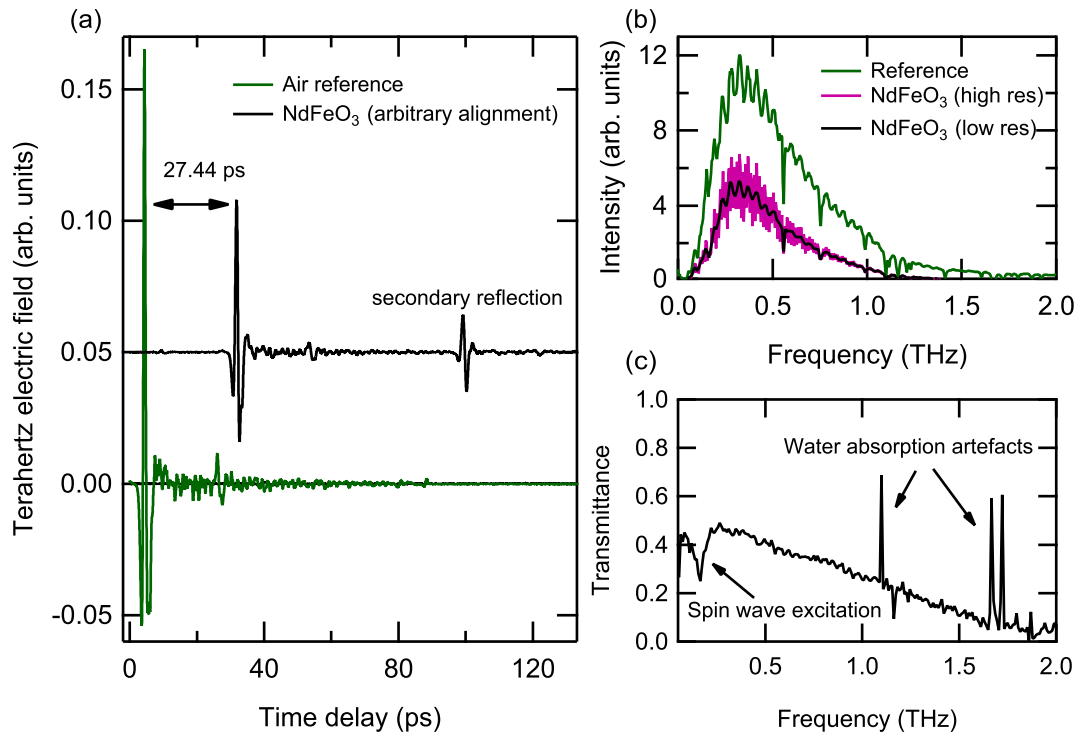
FIGURE 7.9: Process of calculating refractive index and identifying spin-wave excitations. (a) Time-domain waveforms of reference and sample showing time delay in sample. (b) Fourier transforms showing high resolution (purple trace, resolution of $5\,\mathrm{GHz}$) and low resolution (black trace, resolution of $10\,\mathrm{GHz}$) spectra. (c) Ratio of frequency domain spectra giving sample transmittance. Spin wave absorption is evident at $0.16\,\mathrm{THz}$

(b). From this it is established that an orientation of $150°$ maximises the AF-mode and therefore corresponds to $\mathbf{E}||(11\bar{2})$. As expected a $90°$ rotation from that corresponding to an orientation of $60°$ maximises the F-mode. This corresponds to an alignment of $\mathbf{E}||(1\bar{1}0)$.

The spectra of the maximised modes along with their equivalent excitation planes are shown in Figure 7.11. A periodic broad band absorption centred on $0.86\,\mathrm{THz}$ is also observed $90°$ apart at orientations of $110°$ and $20°$. The origin of the feature is currently unknown but could be due to Faraday rotation or birefringence effects. Since the geometry of the ZnTe detector is only sensitive to the fixed horizontal polarisation of the source, any rotation of the THz wave polarisation from the sample may cause losses in the detected signal. The feature is not well fitted by Gaussian or Lorentzian functions that are typically used to fit resonance features. This suggests that the feature is not associated with the spin waves.
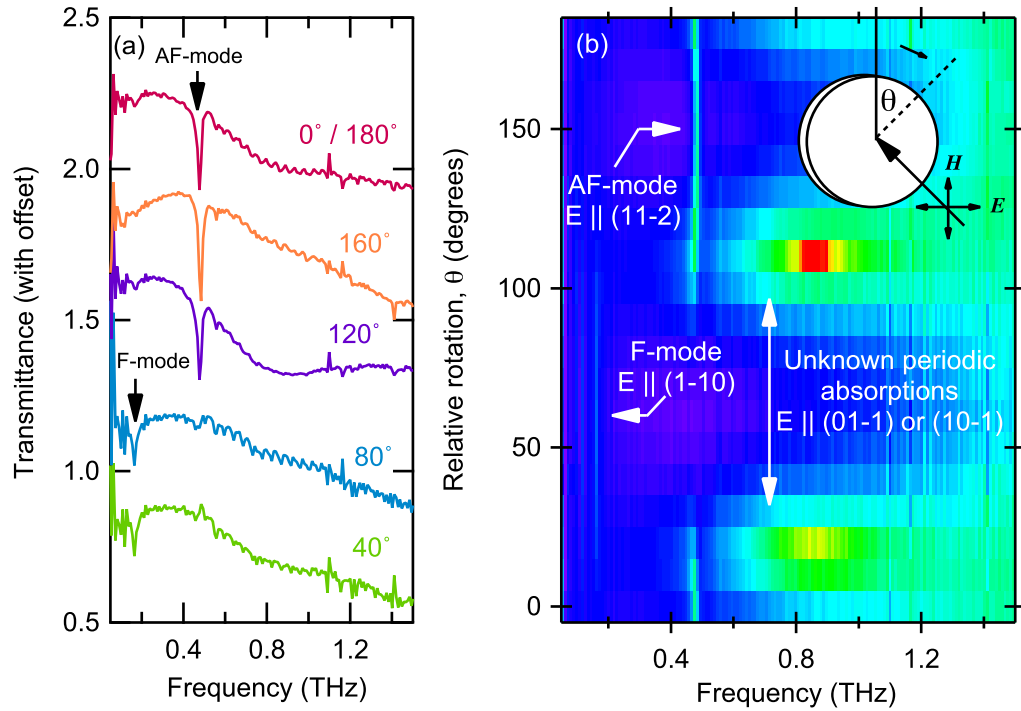
FIGURE 7.10: Rotation analysis of sample identifying $\mathbf{E}||(11\bar{2})$ and $\mathbf{E}||(1\bar{1}0)$ polarisation orientations for exclusively exciting the F- and AF-modes. Traces in (a) are offset by increasing transmittance values of 0.6.
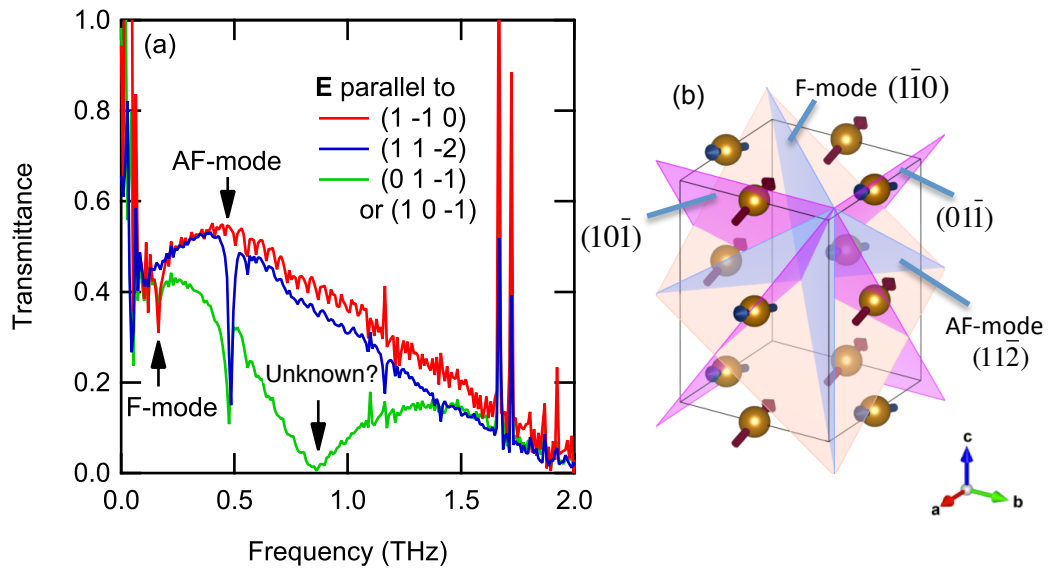
FIGURE 7.11: (a) Transmittance spectra with $\mathbf{E}||(11\bar{2})$ showing exclusive AF-mode excitation and $\mathbf{E}||(1\bar{1}0)$ showing F-mode excitation. $\mathbf{E}||(01\bar{1})$ and $\mathbf{E}||(10\bar{1})$ give an unknown absorption at ~0.85 THz. (b) Corresponding excitation planes relative to Fe^{3+} spin sub-lattices

7.4.3 Spin-wave oscillations

The oscillations of each mode in the time domain are now analysed individually. The compartment containing the optical path of the THz beam is filled with a nitrogen gas atmosphere to remove the spectral signs of water vapour. With the water vapour oscillations removed, the time-domain waveforms are dominated by the oscillating signature of the spin-wave modes. The results are shown in Figure 7.12. The periodic oscillations of the transmitted **E** field indicate absorption due to resonance of the F- and AF-modes. The period of the oscillation in the horizontal polarisation is equal to $\sim$2.06 ps while the period of the much weaker oscillation in the vertical polarisation is $\sim$6.06 ps. As seen in the insets of Figures 7.12 (a) and (b), these correspond to resonances at 0.485 THz and 0.165 THz. The frequencies agree with room temperature Raman scattering measurements of spin waves in NdFeO$_3$ [200]. No mixing of the modes in each polarisation is observed.

Recent experiments using THz TDS on ErFeO$_3$ have shown similar characteristic signals [210]. The oscillations were interpreted as the excitation and subsequent free induction decay of pumped spin-wave modes on femtosecond time-scales. If accurate, the mechanism promises new avenues to optically address specific spins and control spin diffusion. On the other hand, it is well known from the closely-related Raman [197, 200] and infrared [281] spectroscopy techniques, that absorption from magnetic substances may occur via more established and well-understood resonance mechanisms [138].

The measurements of Yamaguchi *et al.* rely on polarisation analysis of the transmitted THz wave [208, 209]. By setting an analysing polariser after the sample in standard transmission geometry, the vertical and horizontal components of the circularly polarised spin precession is extracted. The resulting time resolved **E** field is interpreted as the detection of a free-induction decay from the spin sublattice. This interpretation has shown success in controlled 'on/off' modulation of the spin precession [210]. However, the same results can be interpreted by standard Fourier analysis and far-field wave interference.

In this interpretation, the spin waves populate the system based on their thermodynamic distribution described by Bose-Einstein statistics. The spin waves absorb the transmitted radiation by excitation to higher energy states through a Zeeman coupling with the **H**

field of the radiation. Specific frequencies are absorbed, consistent with the spin wave resonant conditions. The transmitted broadband radiation has a discrete band of frequencies removed. Fourier theory states that a discrete band in frequency space is represented by a sinusoidal precession in phases space, or the time domain. Equivalently, the individual frequency components of the transmitted **E** field interfere generating the oscillations observed in the time domain. The same effect is observed for water vapour absorption and other discrete resonance features. Detecting a free induction decay of the microscopic magnetisation is also unlikely considering the small amplitudes of the spin precession, the low intensity of the THz radiation and small size of the samples used in these studies.

Nevertheless, the time resolved measurement of the **E** field oscillation is useful for visualising the spin precession. As shown in Figure 7.12 (c), extracting the oscillation for each mode gives the relative spin-wave amplitude as a function of time. Combining each oscillation in a three dimensional graphic shows the spin moment modulation as a function of time. Mapping the time dependent modulation to a spatial modulation over one cycle shows the precession of the net magnetic moment of an antiferromagnetic spin pair (Figure 7.12 (d)). Further development of this analysis technique may be beneficial for developing switching mechanisms in spintronic devices.

7.4.4 High temperature spin-wave dynamics

The resonant frequencies of the spin-wave modes are strongly temperature dependent and therefore can provide information regarding the underlying temperature-dependent physics of the Hamiltonian (Equation 7.2). The setup for the Zomega TDS system does not facilitate the use of a cryostat sample environment. Therefore, cooling measurements were not attempted on this system. However, the simple application of a resistive heating system allowed for measurements above room temperature [311].

To achieve this, the sample was mounted in a cavity between two aluminium blocks with centre apertures of 5 mm as shown in Figure 7.13. A series of 4 (5.6 Ω, 5 W) ceramic resistors, positioned in a channel cut into one of the Al blocks and driven by a variable current, provide the heat for the sample. The heating mount was placed in the standard
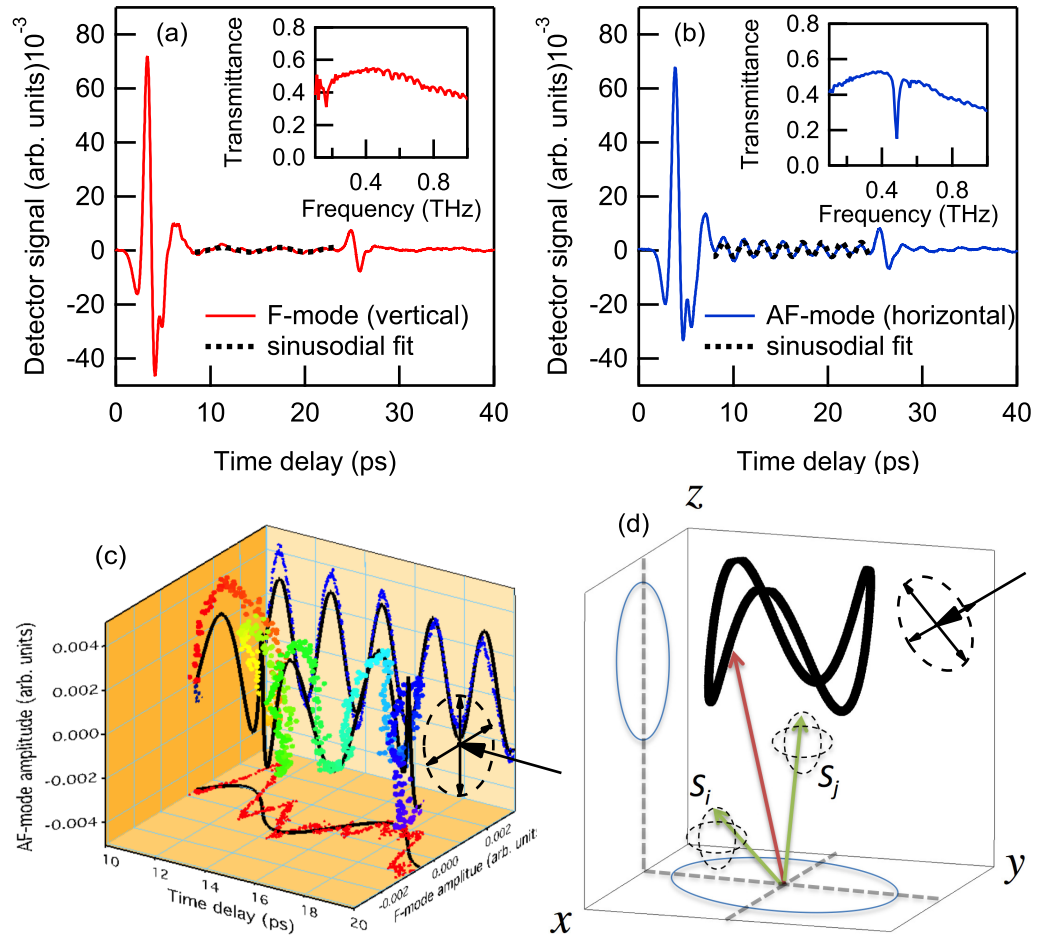
FIGURE 7.12: THz TD spectra of NdFeO$_3$ at 300 K for vertical (a) and horizontal (b) polarisations. (c) Visualisation of mixed modes by combining oscillations from (a) and (b). The blue curve represents the horizontal polarisation, the red represents the vertical polarisation. The rainbow curve is the combined polarisations representing time dependent motion of spin moment. (d) Model of precessing magnetic moment. The black curve is taken from one cycle of the mixed oscillation in (c)

transmission geometry for the Zomega system. Increasing the driving current of the resistors ($\sim$0–1 A) could produce sample temperatures from 300–470 K. A thermocouple was used to measure the sample temperature before and after each run. Only measurements that had consistent temperatures over the scan time were considered.

The transmittance spectra for each polarisation was calculated by a ratio of the sample spectrum with reference spectra taken through the heating mount without the sample. The results are shown in Figures 7.14 (a) and (b) with a reduced spectral range for clarity. An increasing offset of 0.1 in transmittance is applied to distinguish each spectra and highlight
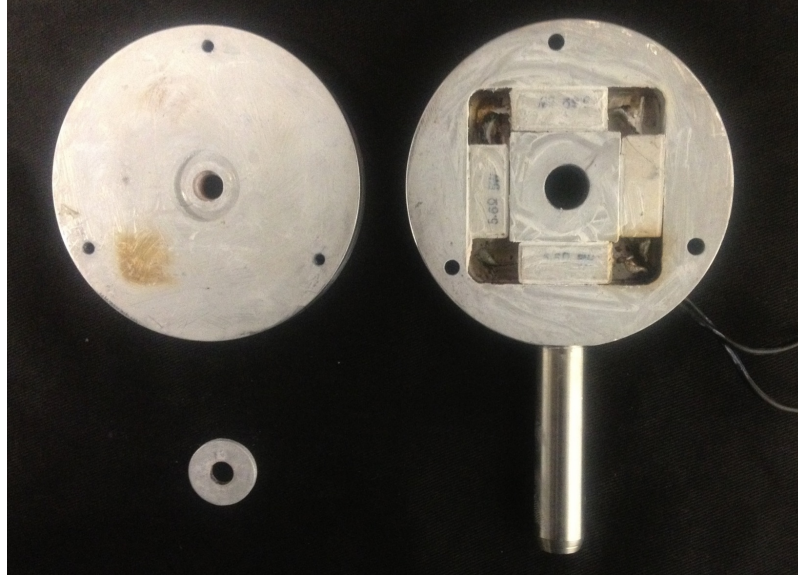
FIGURE 7.13: Photograph of aluminium sample holder used for high temperature measurements. The thermal energy is supplied by current through the series of $5.6\,\Omega$ $(5\,\text{W})$ ceramic resistors.

the frequency shift of the resonance. As can be seen, the F-mode hardens as the sample is heated from room temperature, reaching $0.19\,\text{THz}$ by $403\,\text{K}$. Above this temperature, the mode appears to reach a turning point were it then begins to soften to $0.185\,\text{THz}$ at $467\,\text{K}$. In the horizontal polarisation, the A-mode is seen to soften consistently over the temperature span from $0.48\,\text{THz}$ at room temperature to $0.40\,\text{THz}$ by $463\,\text{K}$.

As previously established, the resonant frequency of each mode is dependent on J, D, S, β, K_x and K_z. The temperatures probed in this experiment are still far below the Néel temperature which suggests that the values of J, D, S and β should remain fairly constant. The strong shift in the resonance frequency as the sample is heated is therefore most likely attributed to a temperature variable anisotropy. It is expected however, that at higher temperatures the exchange interaction will weaken due to increased thermal motion of the magnetic ions. As has been observed in other antiferromagnets [191], both modes should soften completely at the Néel transition.
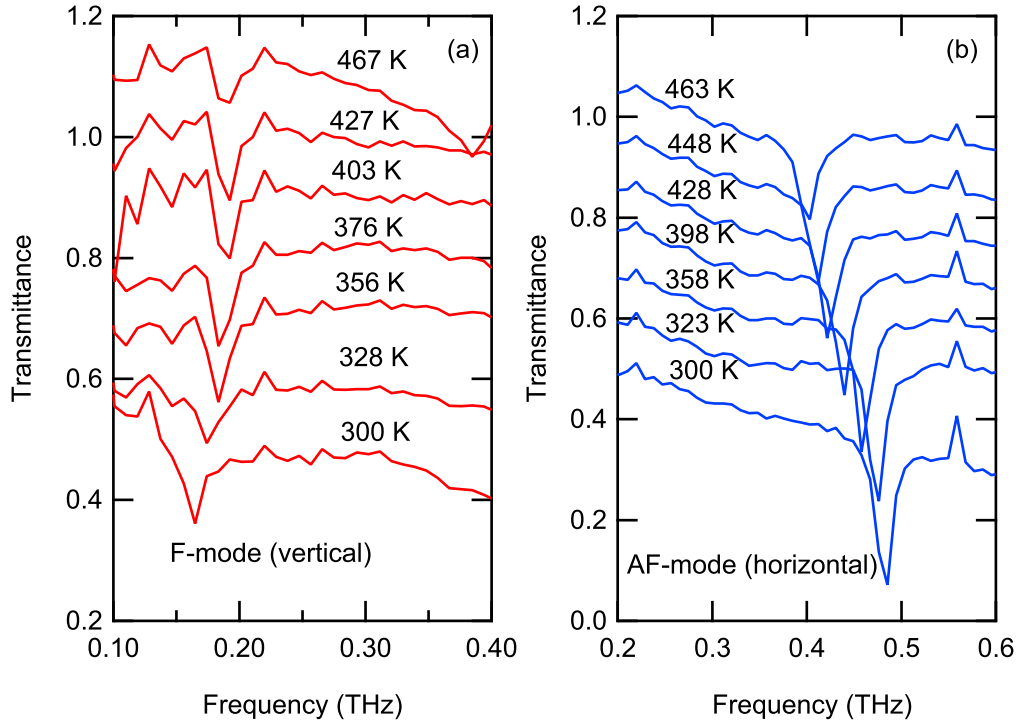
FIGURE 7.14: Transmittance spectra of heated NdFeO₃ single crystal in each polarisation (a) vertical (b) horizontal. Traces are offset by increasing transmittance values of 0.1.

7.4.5 Magnetic extinction coefficients and susceptibility

The large shift in resonance frequency for each mode at high temperatures is adequate for generating an effective crystal lattice reference, using the technique established in Section 4.3. The method is demonstrated in more detail in Figure 7.15. A lattice reference (I_{lat}) is constructed by taking the maximum signal at each frequency from the set of measured spectra. By rearranging Equation 4.32, an expression for the magnetic extinction coefficient in terms of the sample thickness d and a ratio between a measured spectrum and the constructed reference is found,

$$\alpha_{\text{mag}} = \frac{-1}{d} \ln \left[\frac{I_{\text{lat+mag}}}{I_{\text{lat}}} \right]. \tag{7.6}$$

Performing this analysis on the spectra in Figure 7.14 gave the results of Figure 7.16. At $300\,\text{K}$, the magnetic extinction coefficient of the AF-mode was found to be $584\,\text{m}^{-1}$, reducing to $412\,\text{m}^{-1}$ by $462\,\text{K}$. The magnetic extinction coefficient for the F-mode is much

weaker, equal to $140\,\text{m}^{-1}$ at $300\,\text{K}$ and reducing to 94^{-1} by $467\,\text{K}$. The extinction values are consistent with antiferromagnetic resonance in a similar canted antiferromagnet, NiF_2 [192]. The reduction in the extinction coefficient for each mode at high temperatures is attributed to spin-wave relaxation from increased phonon interactions [192]. The difference in the absorption strength of each mode results from different magnetic susceptibilities along the crystallographic directions. Since the F-mode oscillates in the ab plane, its amplitude is determined by the susceptibility χ_{xy}. The AF-mode oscillates along the c axis and its amplitude is determined by the susceptibility χ_{zz}.

The imaginary ac magnetic susceptibility and magnetic extinction coefficient are related through the following expression [312],

$$\alpha_{\text{mag}} = 8\pi^2 \eta_0 \omega \chi''(\omega), \tag{7.7}$$

where η_0 is the index of refraction in the absence of the magnetic interaction (the magnetic interaction giving it a negligible change). Using this expression, and the value of $\eta_0 = 4.2$ determined in Section 7.4.1, the imaginary ac magnetic susceptibility is calculated at room temperature for each polarisation (Figure 7.17). Richards provides a simple relationship between the real and imaginary parts of the complex susceptibility $\chi(\omega) = \chi'(\omega) - i\chi''(\omega)$ through the Kramers-Kronig transform [192],

$$\chi'(\omega') = \frac{2}{\pi} \int_0^\infty \frac{\omega \chi''(\omega) d\omega}{\omega^2 - \omega'^2}. \tag{7.8}$$

Choosing $\omega' = 0$, and assuming narrow resonant peaks in χ'' at ω_0, the expression simplifies to,

$$\int_0^\infty \chi''(\omega) d\omega = \frac{1}{2}\pi\omega_0 \chi'(0). \tag{7.9}$$

Integrating over the peaks in Figure 7.17 and substituting through Equation 7.9 the dc magnetic susceptibility is determined. Along the c axis the calculations gave $\chi'_{zz}(0) = 0.20$ and in the ab plane $\chi'_{xy}(0) = 0.05$.
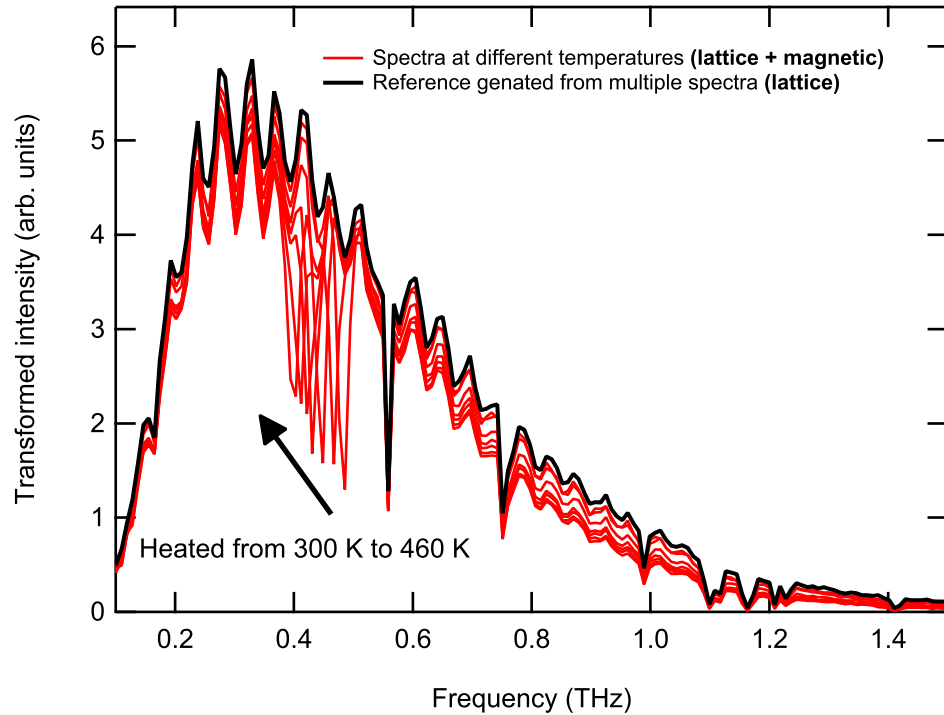
FIGURE 7.15: A series of spectra in the horizontal polarisation with increasing temperature. The shifting resonance of the AF-mode allows the construction of a lattice reference.

7.5 Fourier transform interferometry

Complementary to the Zomega system, the Polytec interferometer was used for the low temperature survey of the spin-wave modes. There were 3 main reasons for this,

1. Unlike the Zomega system, the Polytec interferometer is interfaced with the Oxford magnet. This allows for low sample temperatures down to 1.6 K and externally applied magnetic fields of up to 5.5 T.

2. The Polytec interferometer supports a broad bandwidth allowing access to frequencies above the 1 THz and 3 THz limits of the two-colour and Zomega systems respectively. This is beneficial in potentially identifying new modes that may appear at higher frequencies. Furthermore, at low temperatures the two modes harden considerably approaching the high frequency limits of the two-colour system.
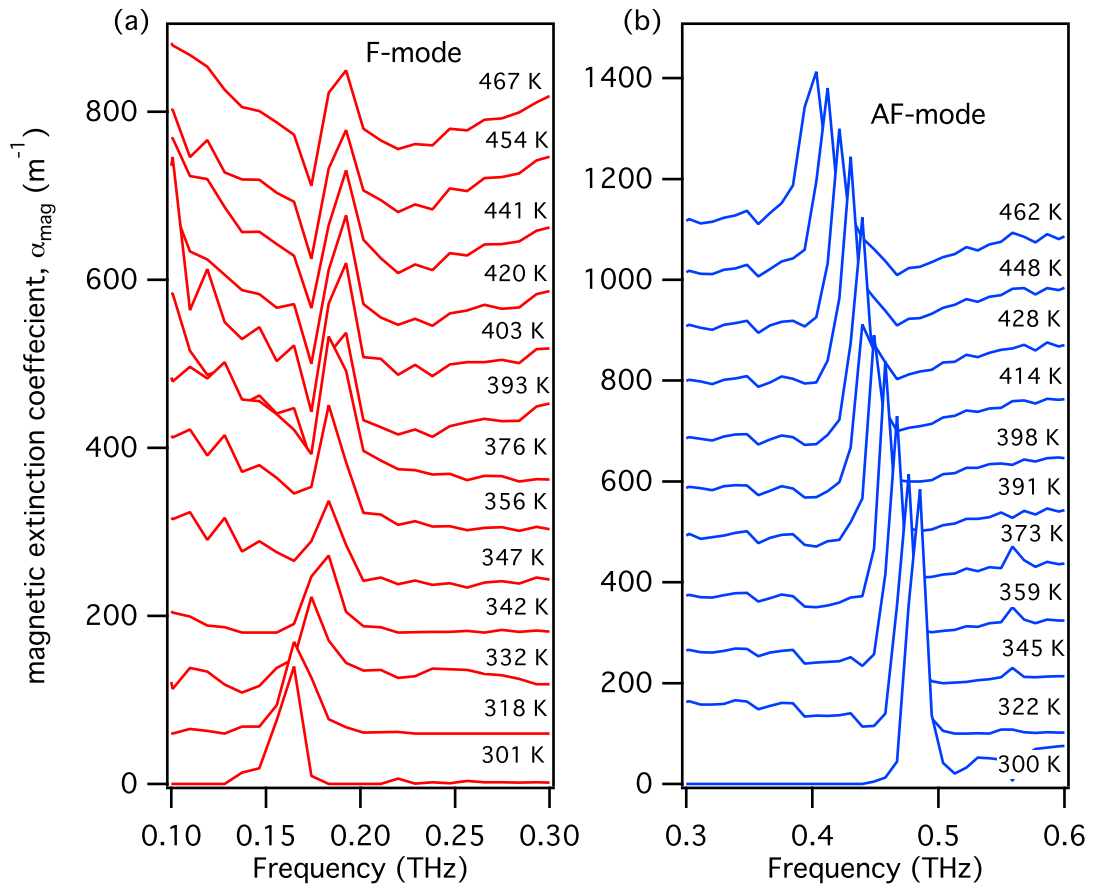
FIGURE 7.16: Magnetic extinction coefficient for NdFeO_3 from ~300–470 K for both F- and AF-modes. The traces are offset by increasing values of $60 \, \mathrm{m^{-1}}$.

3. The Polytec combines a continuous-wave source with phase space measurement of the interferogram. This provides an appropriate platform for identifying the differences with pulsed time-domain measurements using the Zomega system.

In all measurements the sample was fixed to the copper mount of the sample stick and inserted into the VTI of the Oxford magnet. The copper mount featured an aperture of $5 \, \mathrm{mm}$. The orientation of the sample was aligned so that the vertical and horizontal excitation planes were accessible by the gold-wire grid polariser. Interferograms were taken using an integration time of $300 \, \mathrm{ms}$ with a maximum path difference of 1–$2 \, \mathrm{cm}$ producing resolutions from $0.5 \, \mathrm{cm^{-1}}$ to $0.25 \, \mathrm{cm^{-1}}$ or $15 \, \mathrm{GHz}$ to $7.5 \, \mathrm{GHz}$.
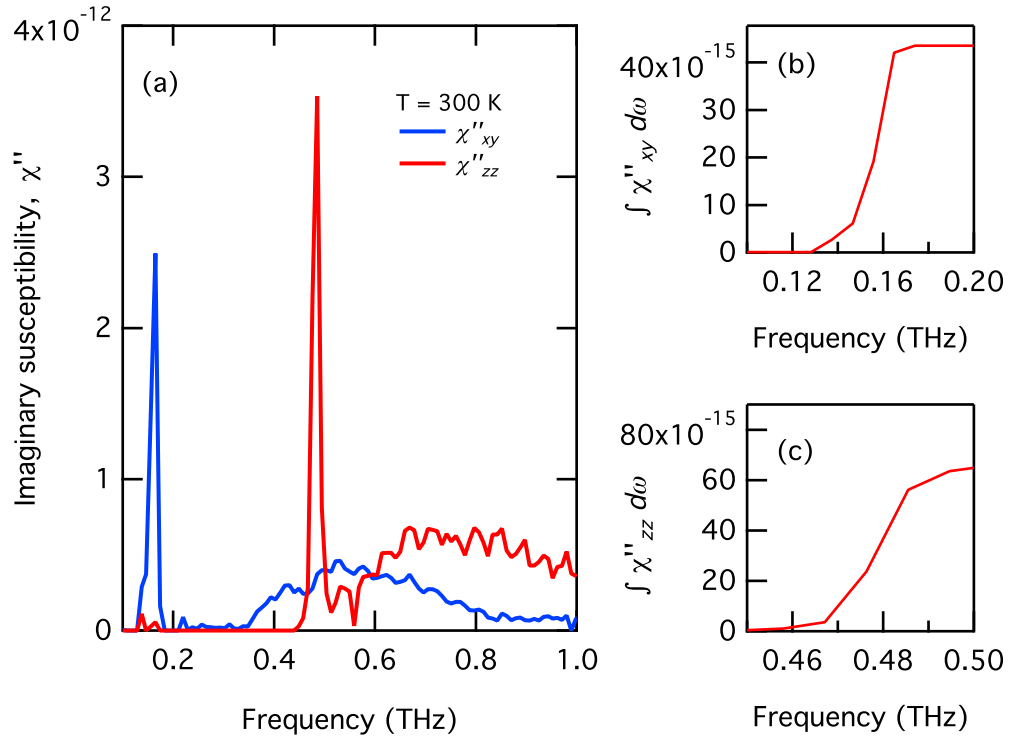
FIGURE 7.17: Imaginary magnetic susceptibility at room temperature along the *c* axis (χ''_{zz}) and in the *ab* plane (χ''_{xy}).

7.5.1 Spin oscillations by interferogram fringes

The interferograms of Figure 7.18 are provided to demonstrate that the oscillations observed in the TDS spectra are not unique to time-resolved measurements. The same F- and AF-modes are observed using conventional far-infrared Michelson interferometry. In Figure 7.18 (a) particularly, the wavelength of the oscillation is ∼0.0618 cm, which is equivalent to a resonance at $16.17\,\mathrm{cm}^{-1}$, or 0.485 THz and in agreement with the resonance shown in Figure 7.12 (b) by TDS. The F-mode could not be observed at this temperature as its low frequency falls below the spectral bandwidth of the interferometer. To observe both modes clearly by the interferometer, the sample must be <40 K (so that the F-mode frequency hardens to above 0.24 THz. Relative to room temperature, the two modes should have flipped in polarisation due to the 90° SR, and shift in frequency due to changes in the internal anisotropic fields. An interferogram for each polarisation at 7.5 K is shown in Figure 7.18 (b).

Figure 7.18 (c) is a zoomed-in section extracted from the full interferogram demonstrating the mode oscillation. Here, the wavelength of the oscillation for the AF-mode is now 0.0435 cm, equivalent to a resonance at 23 cm^{-1} or 0.69 THz. The F-mode oscillation wavelength is 0.0538 cm giving a resonance at 18.6 cm^{-1} or 0.56 THz. As seen in the inset of Figure 7.18 (a) there is now a trace of the F-mode in the vertical polarisation, which should be sensitive to the AF-mode only. On the other hand, there is no trace of the AF-mode in the horizontal polarisation. As can be seen in the three dimensional plot of the two modes (Figure 7.18 (d)), any polarisation orientation away from either vertical or horizontal should couple to both modes. Therefore, if the mixing of the F-mode in the vertical polarisation was due to a SR other than 90°, it would be expected that both modes would appear in each polarisation. The same argument can discount any effects due to polariser inefficiency. Therefore, this observation is attributed to the selection rules in the newly oriented geometry at temperatures below the SR. Below the SR the spin system is in the $G_z F_x$ state where the F-mode precesses around the z axis. The horizontal polarisation will couple to this mode. However, the vertical polarisation will also have a projection into the yz plane. Unlike in the $G_x F_z$ state at room temperature, here the **H**-field components do not fully cancel the F-mode and its signature can be seen in the vertical polarisation.

Figure 7.18 may also be used to visualise the time-resolved spin precession at 7.5 K. In the case of the interferometer, the time delay is represented by a spatial, rather than temporal, path difference. The two delay systems are equivalent, suggesting that one is able to visualise picosecond-time-scale magnetic excitations via conventional spectroscopy, as well as time-domain spectroscopy. Clearly, in this case, the spin system is not being pumped by a spontaneous kick from a short-pulse THz wave, since a broad spectrum blackbody source is used. This is therefore not a free-induction decay signal. Rather, what Figure 7.18 shows are the effects of interfering **E** field components with the spin-wave frequency filtered out. Applying the same analysis as in Figure 7.12 (c), a three dimensional depiction of the time dependent (measured through path difference) precession of the spin moment is generated. At 7.5 K, the precession appears more elliptical than at room temperature due the increased frequency and amplitude of the F-mode relative to the AF-mode.
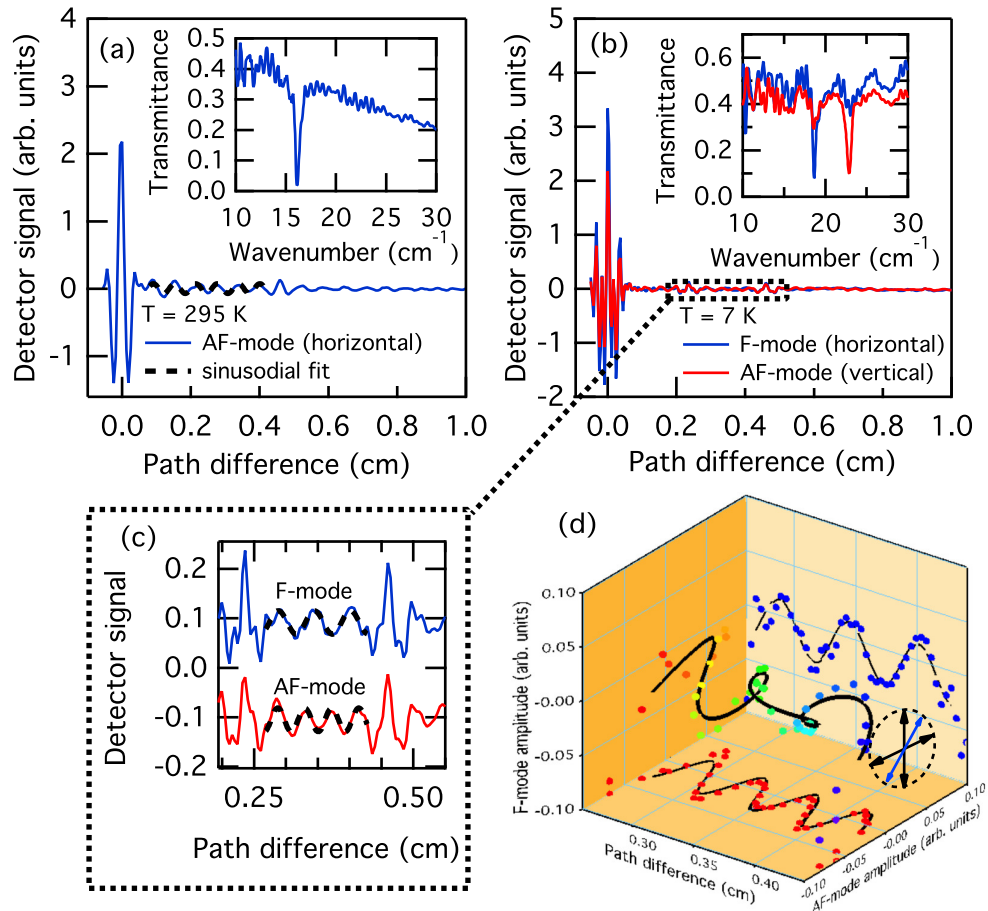
FIGURE 7.18: (a) Far-infrared interferogram for horizontal polarisation at 295 K with transmittance (inset). (b) Interferogram in both horizontal and vertical polarisations and equivalent transmittance spectra (inset) at 7.5 K. The two modes have swapped polarisation and hardened in resonant frequency. (c) Extracted section from (b) showing mode oscillation. The two traces are offset by ±0.1 for clarity. (d) Visualisation of mixed modes (at 7.5 K) for off axis polarisation. The interferogram oscillations may also act to visualise the spin moment precession. Path difference 0.25–0.45 cm is equivalent to a time delay of 8.3–15.0 ps.

7.5.2 Low temperature spin-wave dynamics

To observe the low temperature properties of the spin waves, spectra were taken in each polarisation at a series of temperatures from 290 K to 1.6 K. The temperature dependent transmittance spectra from 4.2–290 K, are displayed in Figure 7.19. In the vertical polarisation, above 170 K, no features are observed since the F-mode frequency is below the bandwidth of the spectrometer (Figure 7.19 (a)). At temperatures below 170 K, the SR begins to take place. As a result of the rotating spin lattice, the AF-mode excitation axis

begins to align with the horizontal polarisation. The AF-mode is first detected as a weak absorption at 0.49 THz at 160 K. On further cooling, the AF-mode increases in intensity and hardens considerably reaching 0.82 THz by 4.2 K.

In the horizontal polarisation (Figure 7.19 (b)), the AF-mode is observed at temperatures above the SR. As the sample is cooled the AF-mode first hardens, then softens and loses intensity during the SR transition, finally disappearing. Below the SR, the F-mode should be sensitive to the vertical polarisation. However, it is not until $\sim$40 K that the F-mode is detected, appearing at the limit of the spectrometer band width at 0.28 THz. As the sample is cooled further the F-mode hardens reaching 0.72 THz by 4.2 K.

To access lower temperatures, a low pressure bath of liquid helium was set up below the sample. Using this procedure, temperatures of 1.6 K and 1.8 K were achieved for measurements in the vertical and horizontal orientations respectively. The results are shown in Figure 7.20. At these temperatures both modes have increased frequencies of 0.88 THz for the F-mode and 0.98 THz for the AF-mode.

7.5.3 External magnetic field dependence

By applying external magnetic fields using the Oxford superconducting magnet, the field dependent properties of the spin waves were examined. The theory of field dependent antiferromagnetic resonance in an orthorhombic antiferromagnetic crystal was first derived by Keffer and Kittel [138]. In the orthorhombic symmetry, four spin-wave modes are present. However, two of these are degenerate, leaving only the two optically active modes described in Section 7.3.3. For external fields applied along the easy axis direction the resonance frequency dependence was given by,

$$\omega^2 = \gamma^2 B_{\text{ext}}^2 + A \pm \sqrt{C B_{\text{ext}}^2}, \tag{7.10}$$

where A and C are functions of the exchange field (B_{int}), anisotropic energies (K), sublattice magnetisation ($M_{1,2}$) and geometric demagnetisation effects ($N_{x,y,z}$). For the canted RFeO$_3$ antiferromagnetic system, Herrmann [298] derived the field dependence of the two modes including the important Dzyaloshinsky-Moriya interaction D separately from the
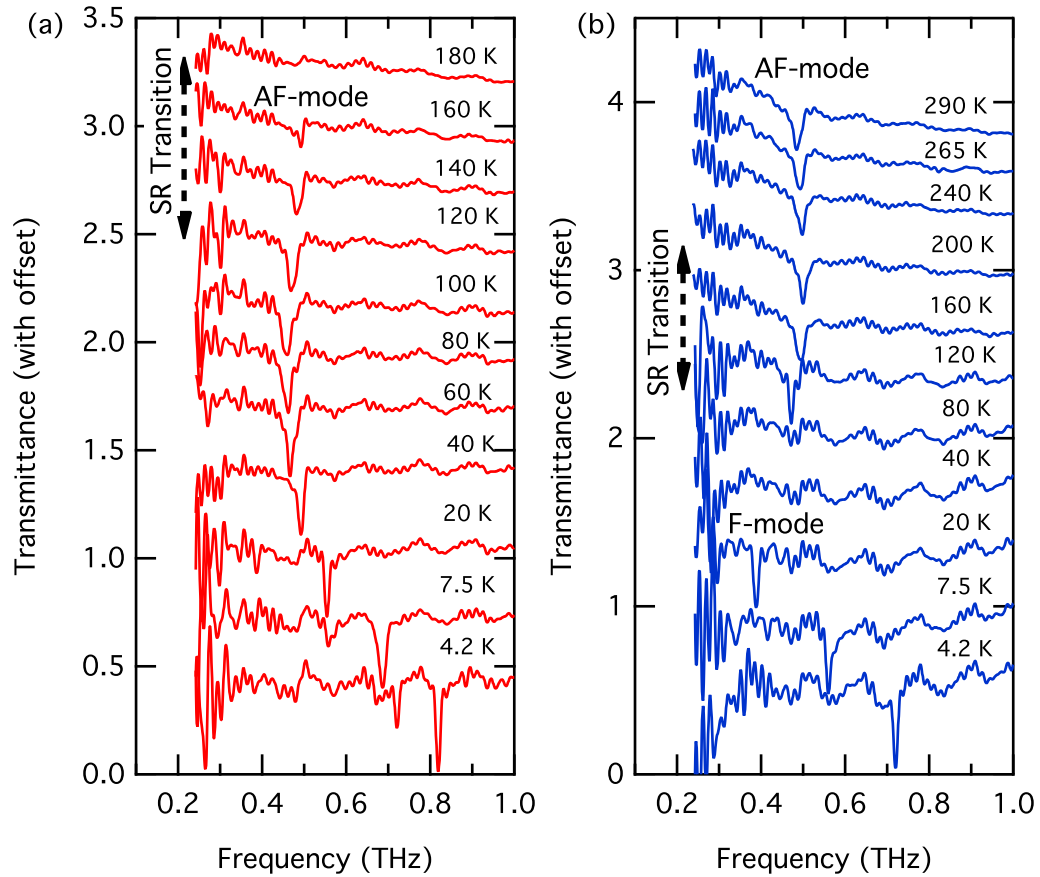
FIGURE 7.19: Temperature-dependent transmittance spectra of NdFeO₃ across the SR. The spectra are truncated below 0.24 THz due to noise. (a) Vertical orientation. Data above 180 K is omitted as no spectral features are evident. (b) Horizontal orientation. Traces are offset by increasing transmittance values of 0.4.
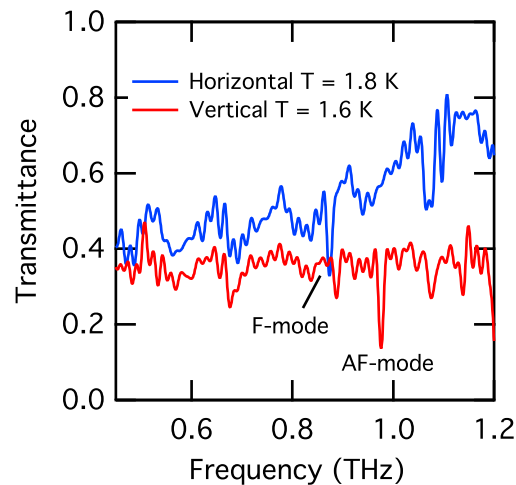
FIGURE 7.20: Transmittance spectra at sub liquid helium temperatures achieved by pumping on a helium bath.

effective anisotropy. The results gave linear coefficients for B_{ext} along z of $(5K_{xz} + D)$ and $(K_{xz} + D)$ for the F- and AF-mode respectively. Here, K_{xz} is an element of the anisotropy matrix representing anisotropy in the xz plane. The result allows easy determination of D and K_{xz} by external field measurements. With B_{ext} along y, the results gave more complicated non-linear dependence.

Due to the crystal orientation and geometry of the sample used in these experiments, $\mathbf{B}_{\text{ext}}$ could only be applied normal to the crystal face ($\mathbf{B}_{\text{ext}}||[112]$). The field dependence of $\mathbf{B}_{\text{ext}}$ along this higher order crystal direction features projections along each direction, x, y and z. Thus, deriving a dependence where the anisotropy and exchange parameters can be extracted, quickly becomes intractable. Nevertheless, field dependent measurements of the two modes at 10 K are shown in Figure 7.21 from 1–5 T. At this temperature, the spin system is in the $G_z F_x$ state.

The mixing of the F-mode in the vertical polarisation, as previously described, is clearly evident and both modes can be tracked in that polarisation. An approximate linear dependence is observed with the AF-mode increasing and the F-mode decreasing in frequency with higher fields. This agrees with the expected linear $\pm B_{\text{ext}}$ dependence. For completion purposes, spectra in the horizontal polarisation, where the F-mode is seen by itself, are also shown and give identical field dependence. The slope of each mode dependence is -28.8 ± 0.6 GHz T^{-1} and 10.6 ± 0.6 GHz T^{-1} for the F-mode and AF-mode respectively.

7.5.4 F-mode splitting

Over a very narrow temperature span around 15 K a peculiar result is obtained for the F-mode resonance. As is shown in Figure 7.22, at 14 K a second peak develops with an approximate shift of 0.016 THz from the normal F-mode. At 15 K, the two absorption peaks are most intense. By 16 K the original F-mode weakens while the second mode strengthens and continues on as the sample is heated further.

The origin of the F-mode splitting is currently not clear. There are no concurrent features that are observed in magnetometry data for NdFeO₃ over the same temperature span [309, 313]. Nor has there been any account of F-mode splitting in THz [210], Raman
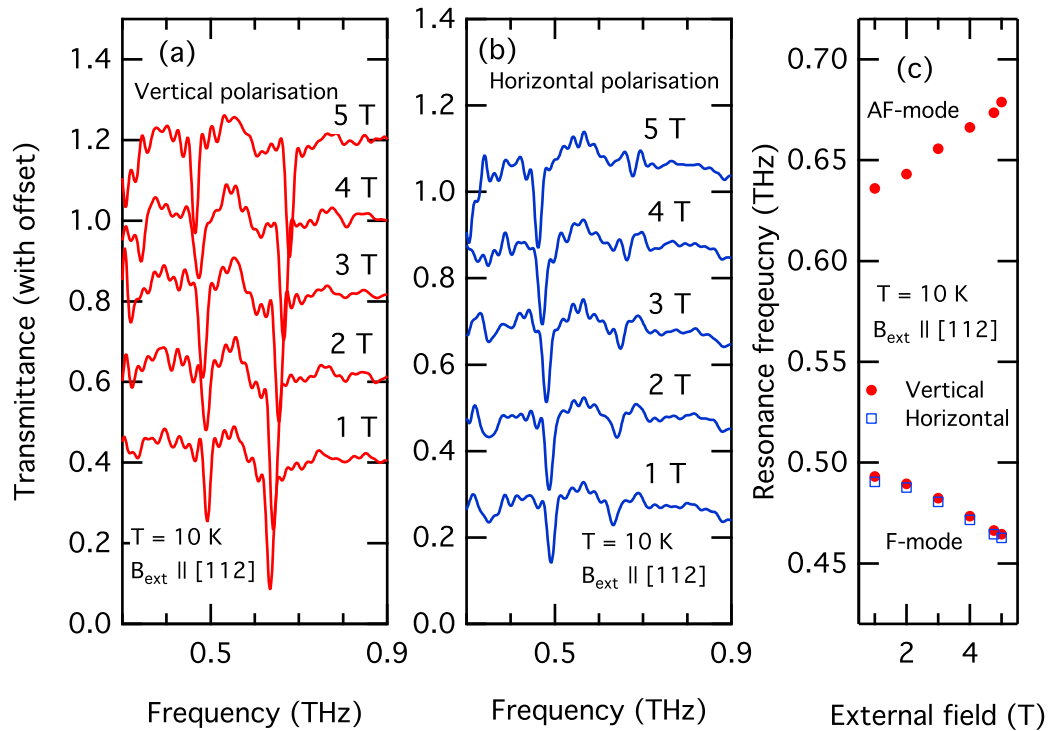
FIGURE 7.21: Magnetic field dependence measurements from 1–5 T of the F- and AF-modes in the vertical (a) and horizontal (b) polarisations. Data was taken at 10 K. Traces are offset by increasing transmittance values of 0.2. (c) Mode frequency dependence as a function of magnetic field shown linear splitting.

[197, 199, 200] and INS [280] studies of the spin waves in other RFeO$_3$ compounds. It is possible that the split mode is a brief raising of the degenerate spin waves calculated by Herrmann [298]. In this interpretation, the effective 2 sublattice model becomes a 3 or 4 sublattice model over a small temperature span. It should be noted however, that a similar splitting is not observed for the AF-mode nor is there a broadening of the resonant feature. If the 4 sublattice model was accurate one might expect a lift in the degeneracy of the AF-mode as well.

Field dependent measurements shown in Figure 7.23 indicate that a field of 1 T applied normal to the crystal (**B**||[112]) is sufficient to suppress the splitting. This is supportive of an interpretation involving an increased number of sublattices. An external field would act to align the spin moments effectively reducing the total number of sublattices. A similar metamagnetic transition was covered in Chapter 6. The mechanism behind any increase in the number of distinct sublattices may be tied to a phase transition in the crystal
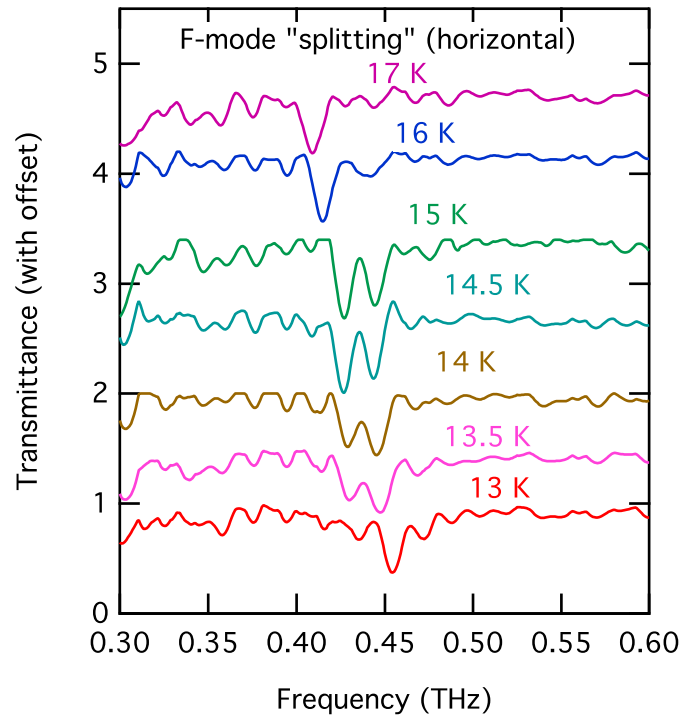
FIGURE 7.22: Transmittance spectra of F-mode in horizontal orientation. The spectra taken over 13–17 K show a small splitting of the excitation. The external magnetic field is zero. Traces are offset by increasing transmittance values of 0.5.

structure, but again no concurrent features are observed in the temperature dependent measurements of the lattice spacing for NdFeO₃ [304].

7.6   Low frequency quasi-monochromatic spectroscopy

In the temperature-dependent anisotropy model for SR of Shane [278], $(K_x\text{-}K_z)$ in Equation 7.3 is expected to reverse in sign over the SR transition. Therefore, one should observe complete softening of the F-mode. To observe this softening over 40–300 K, the two-colour system, boasting a lower-frequency limit and high resolution than the Polytec, was used. The process of obtaining spectra and analysing the results using the two-colour system is detailed in Figure 7.24.

As described in Chapter 5, collecting spectra of planar crystals directly in the frequency domain, as is done by the two-colour system, results in interference fringes inherent in the spectra. In Chapter 5, the fringes were useful in fitting a theoretical transmittance
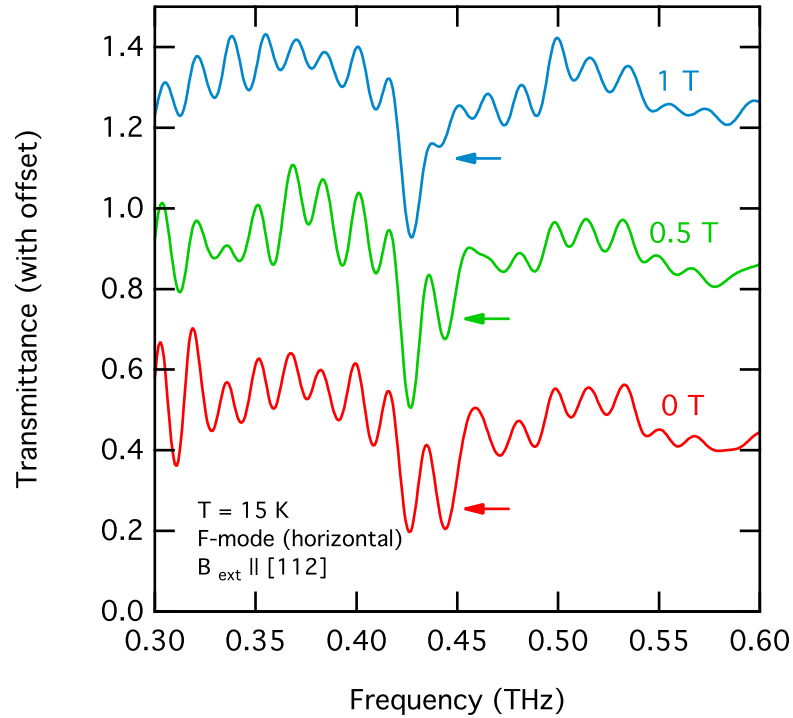
FIGURE 7.23: External field effects on split F-mode. By 1 T the splitting is suppressed. Traces are offset by increasing transmittance values of 0.4.

function. Here, they act to obscure the observation of the spin-wave excitations. The thick sample geometry ($d = 1.95\,\text{mm}$) and high refractive index ($\eta = 4.2$), means that the fringes in the spectra of NdFeO$_3$ are very narrow. A simple expression relating sample optical path difference to fringe spacing $\Delta\nu$ is given by

$$2\eta d = c/\Delta\nu. \tag{7.11}$$

Using this expression the fringe space should be in the order of 15 GHz.

For the pulsed-TDS or Fourier-space interferometer-type systems, the fringes are easily filtered out before the spectrum is Fourier transformed by truncation or attenuating the secondary reflection peak. For the two-colour system this can be achieved by limiting the resolution of a scan directly so the fringes are averaged out. However, the precision of the quasi-monochromatic source can often mean that one frequency step falls on a deconstructive trough while another falls on a constructive peak. Over the length of a scan this can lead to the appearance of considerable noise. Furthermore, this method

diminishes the high resolution appeal of the two-colour system. An alternative method implemented here, involves an extra inverse Fourier transform/re-transform step. To do this the complete spectrum is taken with the desired resolution as seen in Figure 7.24 (a) for the horizontal polarisation at room temperature. As is evident, the strong interference fringes obscure the signature of the F-mode. By performing a Fourier transform on this data the spectrum is converted into an inverse frequency spectrum (Figure 7.24 (b)).

The time delayed peak, associated with the internal reflection in the crystal, is easily identified in the inverse spectrum occurring at ∼69 ps in Figure 7.24 (b). The section of the inverse spectrum where the peak occurs is attenuated by 10 dB (data is multiplied by 0.1 over that section). This effectively dampens the reflection effects. When the inverse spectrum is re-transformed back into the frequency domain, the fringes are filtered out (Figure 7.24 (c)). The F-mode is now clearly resolved at 0.163 THz. The same is achieved with the vertical polarisation for the AF-mode. A ratio with the reference spectrum produces the transmittance data seen in Figure 7.24 (d). The AF-mode resonance is observed at 0.479 THz. The stability of the power and high resolution of the two-colour system still act to produce a considerably noisy spectrum. However, the information about the polarisation and frequency of each mode is still easily observed. Below the SR representative spectra at 40 K are shown in Figure 7.25 (a). As expected the F-mode (at 0.28 THz) and AF-mode (at 0.485 THz) have reversed in polarisation.

Applying the filtering method to temperature dependent measurements, the F-mode is tracked across the SR. Transmittance spectra in the horizontal polarisation from 40 K–90 K and in the vertical polarisation from 170 K–290 K are shown in Figure 7.25 (b) and (c). By 90 K and 170 K, the F-mode was observed to weaken below the detection limits. The rapid drop in frequency over this temperature span is highly suggestive of a soft mode over the SR transition.

7.7 Complete temperature analysis

Combining the temperature dependent results from each spectrometer gives a complete overview of the temperature characteristics of the spin-wave modes. In each case, the
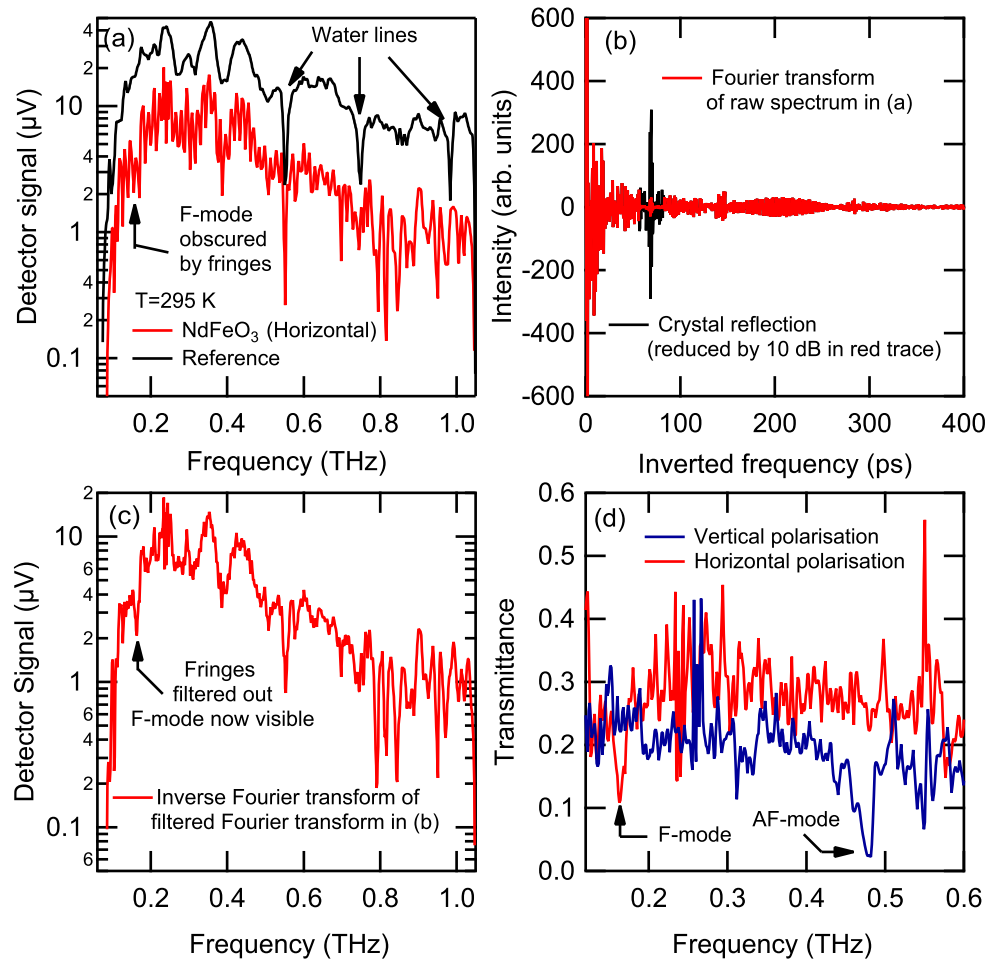
FIGURE 7.24: Method of filtering Fabry-Perot interference fringes from the NdFeO$_3$ sample using the two-colour system. (a) Raw spectrum taken in vertical polarisation at room temperature at a resolution of 0.001 THz. The F-mode is obscured by fringes. (b) Inverse transform of frequency spectrum. Reflection peak is attenuated by 10 dB. (c) Re-transformed spectrum with reduced fringe noise. The F-mode is now clearly visible. (d) Transmittance spectra calculated by ratio of filtered sample spectrum with reference.

spin-wave modes in the transmittance spectra were fit by Lorentzian functions using the WaveMetrics: Igor Pro graphing application. The absorption strength and frequency position were extracted from the fits. Uncertainties in the absorption strength represent quality of fits calculated by the fitting algorithm 'chi squared' variance. For the frequency position, the full width at half maximum is used as the uncertainty.

The absorption strength for the AF-mode as a function of temperature is shown in Figure 7.26 (a). As the temperature is reduced, spin-wave relaxation by phonon interaction
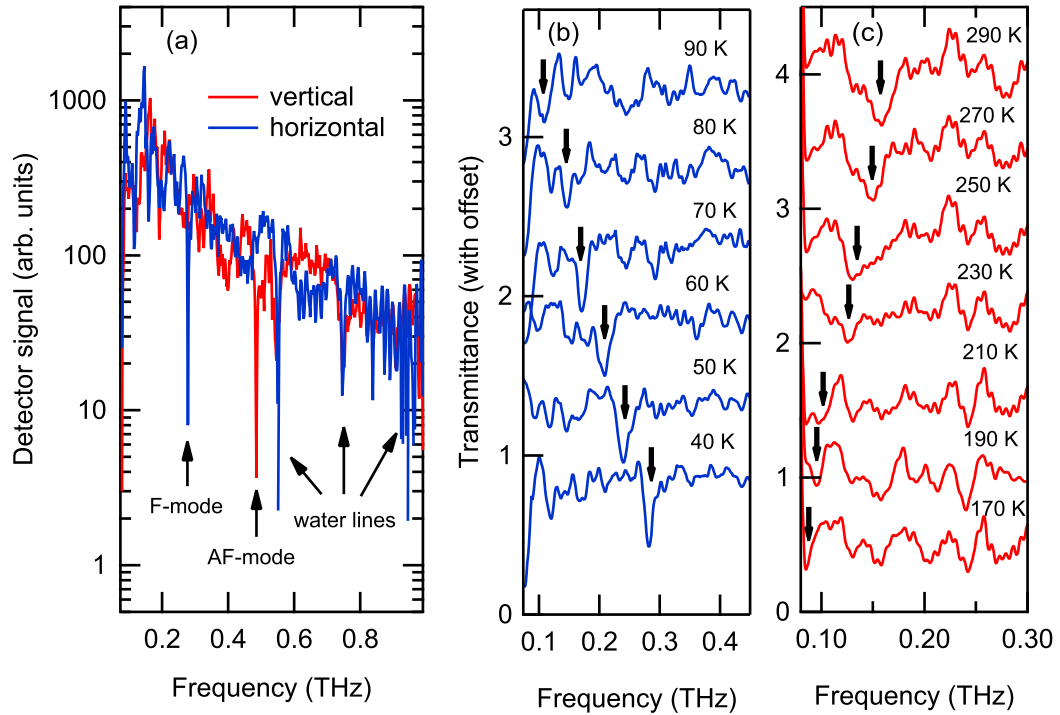
FIGURE 7.25: Transmittance spectra of the soft F-mode across the SR transition. (a) Spectra at 40 K using the two-colour system, in the horizontal and vertical polarisation orientations. Both the F-mode and AF-mode are observed at a high resolution of 1 GHz. (b) Temperature dependence of F-mode from 40–90 K and (c) from 170–290 K, showing mode softening. Traces are offset by increasing transmittance values of 0.5.

is limited and the mode's intensity strengthens. As the temperature of the sample approaches the SR transition, the polarisation sensitivity reveals the rotation of the spin system through a weakening of the AF-mode in this orientation due to a smaller projection of the spin moment in the $(1\bar{1}0)$ plane. Correspondingly, in the other orientation $((11\bar{2})$ plane), the AF-mode is seen to strengthen as the projection of the excited spin moment maximises its alignment with the THz **H** field. The sensitivity to the alignment of the spin sublattice allows precise identification of the temperatures $T_1 = 110$ K and $T_2 = 170$ K at the boundaries of the spin reorientation.

A rapid weakening is also observed for the measurements at 1.6 K and 1.8 K. Presently, it is not clear whether this is due to a reduced spin moment projection in the plane of polarisation (corresponding to another SR at lower temperatures), a reduction in the magnetic susceptibility of the Fe^{3+} sublattice or simply a measurement artefact. Recent studies have indicated that exchange coupling between the Nd^{3+} ions may produce antiferromagnetic

ordering in the Nd^{3+} sublattice at very low temperatures [304, 313–315]. Competition between the corresponding Fe^{3+} and Nd^{3+} sublattice magnetic moments gives rise to a particularly unstable magnetic state where either of these scenarios is a possibility.

The F-mode intensity over the same temperature span is shown in Figure 7.26 (b). The weak nature of this mode makes accurate fitting difficult in some of the spectra. Therefore the mode intensity features some degree of scatter and uncertainty. Nevertheless, the mode intensity does follow a similar trend as the AF-mode. Noticeably, the intensity at high temperature features a turning point at around 250 K. This is higher than the turning point of the AF-mode that marks the onset of the SR and may be due to a decrease in the susceptibility in the *ab* plane. At temperatures below 4.2 K, a rapid weakening is observed, similar to the AF-mode.

The complete temperature dependence, from 1.6–470 K, of the frequency position for both modes is shown in Figure 7.27. At high temperature (above $\sim$200 K) the AF-mode behaves much like antiferromagnetic resonance observed in typical antiferromagnets such as MnO, NiO, CoF_2 and NiF_2 [190, 316]. That is, as the temperature is reduced, the resonant frequency hardens from being zero at the Néel temperature. This generally results from an increase in the sublattice magnetisation due to increasing internal fields and a reduction in thermal disruptions. By a certain temperature above absolute zero, the magnetisation saturates and the resonant frequency plateaus to a constant value at lower temperatures. In Figure 7.27, the Néel temperature (T_N) is indicated at 670 K, presumably, if measurements were achievable above 500 K the F- and AF-modes would be observed to soften to zero by this temperature.

In the typical cases mentioned above, the high frequency mode hardens to its saturated value by $\sim$ 30% of T_N. In the case of NdFeO₃, $0.3T_N$ is equivalent to $\sim$200 K and the AF-mode frequency is seen to plateau at approximately this temperature. In YFeO₃ (T_N = 640 K) the same hardening and plateau at 200 K is also observed for the AF-mode [200]. However, no SR occurs for YFeO₃, a fact attributed to a lack of magnetic moment of the Y^{3+}. Therefore, in YFeO₃ the plateau in the AF-mode frequency persists below 200 K much like the typical antiferromagnets. Here, in the case of NdFeO₃, below 200 K the AF-mode begins to soften as the SR takes place. Since the YFeO₃ case establishes that
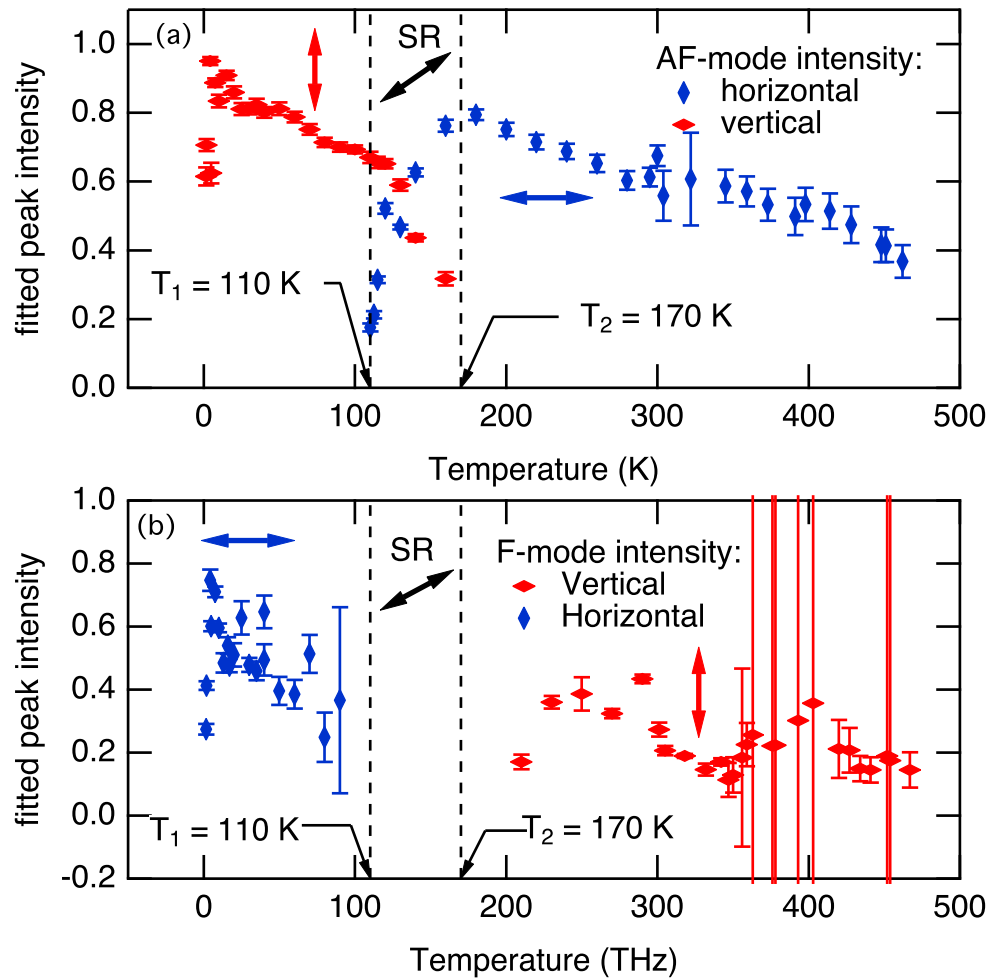
FIGURE 7.26: (a) Temperature dependence of absorption intensity for AF-mode. The SR is identified from 170–110 K. (b) F-mode intensity dependence (could not be tracked from 100–200 K).

the magnetisation in the Fe^{3+} magnetic sublattices has mostly stabilised below 200 K, the dramatically different behaviour of the AF-mode in NdFeO$_3$ below 200 K suggests that a new magnetic force linked to the Nd^{3+} ion develops at low temperatures.

At 200 K, the F-mode is seen to soften below the detection limits of the spectrometers used. This is suggestive of a crossing of the two anisotropy energies K_x and K_z in Equation 7.3, where $(K_x - K_z)$ and hence ω_F would equal zero. It is possible however, that the F-mode does not in fact soften completely and just reaches a turning point at low frequency within the microwave energy range. An absence of such complete softening has been observed in ErFeO$_3$ [197, 200, 210, 280], SmFeO$_3$ [200, 280] and TbFeO$_3$ [198] using Raman, THz,

and inelastic neutron scattering spectroscopies. White *et al.* [197] have suggested that the absence of complete F-mode softening may be a result of R^{3+}–Fe^{3+} coupling playing an important role in the low energy spin dynamics.

Below the SR, both modes harden considerably over a small temperature range, a feature not typical in other antiferromagnetic resonance systems that do not feature SR [190]. This observation gives support to the notion that another anisotropic force acting along the z axis competes with the x axis anisotropy, driving the SR. A detailed discussion along with calculations of the two anisotropy energies, K_x and K_z, are given in the proceeding chapter, following a series of complementary inelastic neutron scattering measurements.

Finally, in reference to the inset of Figure 7.27 the temperature dependence of the F-mode splitting is shown in detail. This seems to be the first account of spin-wave splitting at zero applied field in a $RFeO_3$ material. Antiferromagnetic spin-wave splitting in an applied field occurs when two degenerate states are separated. One mode typically increasing in frequency while the other decreases [191]. Here, the splitting bears resemblance to an anticrossing of degenerate states. Anticrossing occurs when the degeneracy of two states is lifted by a perturbation of the Hamiltonian describing them. The two states form branches of two hyperbolae that asymptotically approach the original unperturbed energy levels [148]. The impact of anticrossing in a degenerate two state system is the formation of a lower energy eigenstate which acts to increase stability of the system. Specific heat measurements performed on $NdFeO_3$ [309] show a minimum in the vicinity of $13\,K$ which the authors attribute to an interaction between the Nd^{3+} and Fe^{3+} ions. With the specific heat representing the number of available degrees of freedom in a system, it is possible that the Nd^{3+}–Fe^{3+} interaction causes a perturbation on the magnetic Hamiltonian that results in the formation of a lower eigenstate and anticrossing of the degenerate F-mode. Essentially a new sublattice is formed. However, the fact that the splitting does not persist to lower or higher temperatures and the absence of concurrent features in magnetisation measurements [309, 313], is unresolved. Similar splitting has currently not been observed in F-mode studies in other $RFeO_3$ compounds but may likely be due to resolution limitations since the splitting is only small and occurs over a very limited temperature span.
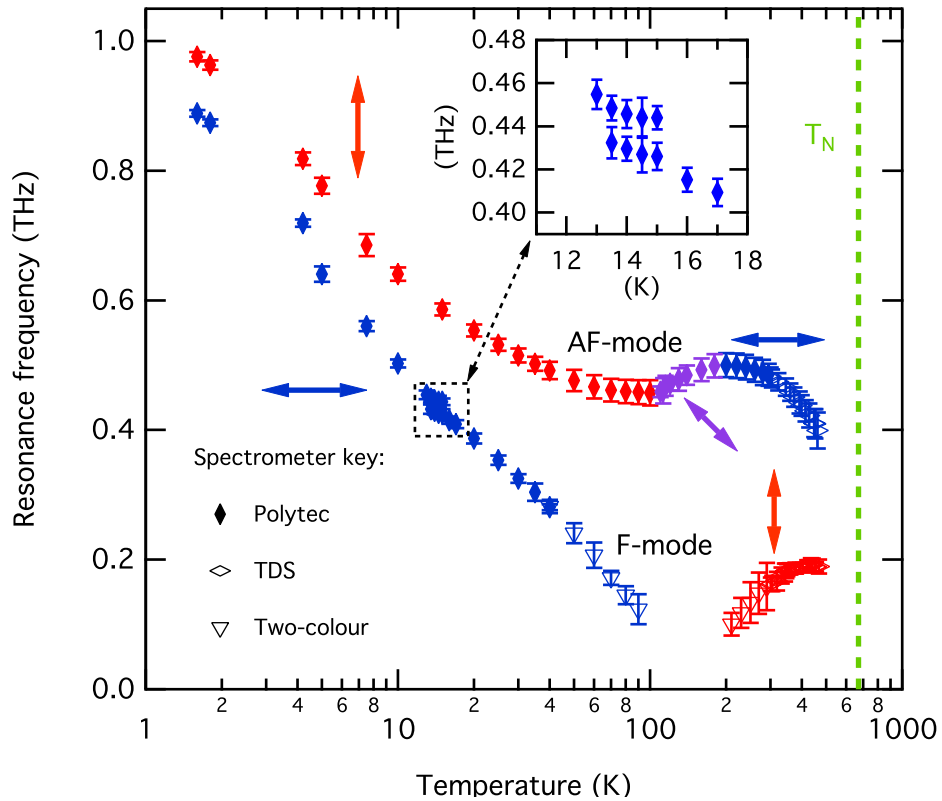
FIGURE 7.27: Combined temperature and polarisation dependence of frequency for both the F- and AF-modes from 1.6–467 K. The F-mode splitting shown in the inset resembles degenerate two state anticrossing. Uncertainties represent full widths at half maximum of fitted absorption features.

7.8 Conclusions

In summary, the rich magnetic interactions in NdFeO₃ provide a fascinating environment for spin wave study using THz radiation. Polarisation sensitive transmission spectroscopy has revealed two orthogonal antiferromagnetic spin-wave modes denoted the F-mode and AF-mode. The F-mode represents a lower frequency precession of the weak ferromagnetic moment in a plane parallel to the antiferromagnetic alignment. The AF-mode represents a higher frequency oscillation of the amplitude of the weak ferromagnetic moment perpendicular to the antiferromagnetic alignment. By studying oscillations from the spin-wave absorption in time-domain and interferogram waveforms, the spin moment precession can be visualised. This technique shows promise in applications of THz frequency magnetisation control.

Quantifying the magnetic extinction coefficients for the two modes shows that they are consistent with an interpretation of antiferromagnetic resonance. Frequency dependence on externally applied magnetic fields also supports this assignment. A relationship between the magnetic extinction coefficients and imaginary susceptibility is used to calculate the dc susceptibility along the c axis and in the ab plane at room temperature. The results reveal anisotropic susceptibility with the c axis susceptibility having a larger value than the ab plane. This accounts for the larger amplitude of the AF-mode relative to the F-mode as the spin moments are more easily deflected along the c axis.

Temperature dependent measurements reveal a strong influence on mode frequency, intensity and polarisation. Tracking the mode polarisation and intensity over a temperature span of 1.6–470 K exposes a 90° rotation of the spin lattice (spin reorientation) from 110 K to 170 K. The spin reorientation manifests itself in the THz spectra as a 90° rotation of the spin-wave polarisation. The frequency dependence of each mode over the same temperature span highlights a considerable temperature variability of the internal magnetic interactions. Across the spin reorientation both modes experience softening indicative of a phase transition likely associated with dynamic magnetic anisotropies along the crystal axes. Below the spin reorientation, both modes harden to high frequencies suggesting strong internal magnetic interactions possibly resulting from Nd–Fe coupling.

Over a very narrow temperature span of 13–17 K, the F-mode is seen to split forming two narrowly spaced resonance lines. The development of the split F-mode over this temperature span is reminiscent of anticrossing states. The observations represent the first documented zero field mode splitting in a RFeO$_3$ material and may be a result of an additional transient spin sublattice.

The combined use of an ultrafast pulsed THz source (Zomega system) and continuous THz absorption techniques (Polytec and two-colour systems) gave consonant results over the wide temperature range. This highlights suitability of THz spectroscopy for probing spin-wave dynamics in antiferromagnetic materials.

Chapter 8

Complementary inelastic neutron scattering and anisotropy calculations for NdFeO$_3$

8.1 Introduction

This chapter presents inelastic neutron scattering (INS) measurements of the rare earth orthoferrite NdFeO$_3$. The neutron scattering experiments were performed complementary to the THz study presented in Chapter 7. Combining both studies, the temperature variable magnetic anisotropy in NdFeO$_3$ is calculated as a function of temperature. The goals of the neutron study were to confirm the zone-centre acoustic spin-wave origin of the excitations observed using THz radiation. While the THz experiments gave results consistent with zone centre antiferromagnetic spin-wave resonance, magneto-electric coupling was not ruled out. Since multiferroic properties have been observed in other RFeO$_3$ compounds, it is beneficial to test the possibility of **E** field coupling to the magnetic excitations. This is difficult using a purely optical study.

Because of the electromagnetic nature of THz waves, the time-dependent **E** field couples to charge based dipolar moments within the material [163], just as the time-dependent **H** field couples to spin moments [138]. The observation of an external field dependent shift in a

resonant frequency may help to identify the magnetic origin of resonant features. However, in magneto-electrically coupled systems, the magnetism and crystal lattice are coupled and the manipulation of one will inherently affect the other [275]. Since the electromagnon is a manifestation of lattice coupled spin waves, their frequencies are shifted by both external electrical and magnetic fields [162]. Their frequencies also appear in the same energy region and may even be degenerate with purely magnetic spin waves [317].

Inelastic neutron scattering identifies magnetic excitations through its unique ability to collect scattered spectra at specific locations in the reciprocal space of the magnetic lattice [48]. Careful monitoring of the dispersion relation of excitations can confirm their origin [165, 211]. Thus, INS is a strong complementary technique to THz spectroscopy. Furthermore, the ability to study the spin-wave dispersion at k values away from the zone centre can reveal information about different contributions to the magnetic Hamiltonian [47], including in-plane anisotropy and low-dimensionality [318].

The results presented confirm the spin-wave nature of the excitations observed in Chapter 7 and reveal that there is a relation between a spin-wave gap that develops at low temperature and the spin reorientation (SR). This supports the presence of a temperature-variable magnetic anisotropy in the Hamiltonian, as previously proposed for this class of system [278, 300] and briefly discussed in Chapter 7. This provides the motivation for calculation of the anisotropy as a function of temperature. Much of the work presented was published along side the THz experiments in Reference [40].

The chapter takes the following structure: Section 8.2 provides and overview of the neutron scattering methodology. Section 8.3 presents the INS data and covers the analysis and interpretation of the results. Section 8.4 incorporates the temperature dependent THz data from Chapter 7 and provides calculations for the temperature variable magnetic anisotropy based on the experimental results. A detailed discussion of the results for the calculations is included. Further refinement of the calculations using temperature dependent spin moment data from Reference [304] are also presented. Section 8.5 concludes the chapter.

8.2 Experimental methodology

The inelastic neutron experiments were carried out on the Australian OPAL reactor TAIPAN triple-axis spectrometer. The theory behind elastic and inelastic neutron scattering of elementary excitations was covered in Section 3.2.3.2. A description of the neutron scattering instruments and facility was also given.

The sample used in these experiments was a disk (7 mm diameter, 5 mm thick) cut from the same boule as the sample used in the THz analysis of Chapter 7. The sample environment consisted of a Janis cryofurnace with an operating temperature range of ∼3–800 K. The sample was mounted on the cryofurnace cold finger within an aluminium compartment filled with a helium atmosphere to improve the cooling rate. Additional aluminium radiation shields around the helium compartment were also in place to reduce the cooling time. Under this configuration, the cryofurnace was able to achieve temperatures down to 3.6 K and as high as 300 K. The cryofurnace was mounted to the tilt stages of the AZ sample mounting stage of the TAIPAN beamline allowing rotations up to 20 degrees.

Scattering spectra were taken with a constant final energy, $E_\mathrm{f} \simeq 14.87$ meV and at a resolution of 0.25 meV (0.06 THz). Constant-energy Q-scans were performed at 175 K, 50 K, 25 K and 3 K, around the magnetic zone centre $\mathbf{Q} = (h01)$. This involved fixing the detected energy transfer and scanning the $\mathbf{Q}$ vector from (0.7 0 1) to (1.3 0 1). Repeating the $\mathbf{Q}$ scans at different energy transfers from 1–8 meV (0.24–1.93 THz) tracks the low energy spin-wave dispersion. Constant Q energy-scans from 0–15 meV (0–3.63 THz) were performed at the antiferromagnetic zone centre in the ac and bc planes at 11 temperature steps between 3 and 298 K. This is performed by fixing the $\mathbf{Q}$ vector (e.g $\mathbf{Q}= (101)$) and scanning through the energy transfer. This provides better resolution data of the excitations at the zone centre out to higher energies. In all cases, a statistical approach is taken for the neutron detection. The number of neutrons incident on the sample is monitored while the number of neutrons scattered at the specific $\mathbf{Q}$ and energy transfer are counted at the detector. When the number of incident neutrons reaches a predefined value of 10^6, the counting of the scattered neutrons stops. The standard deviation of the number of counts is then used as the statistical uncertainty for the data point.

The positions in Q space relative to the magnetic sublattice are determined by alignment of the instrument to elastic Bragg peaks from the NdFeO$_3$ crystal lattice. With the instrument aligned, the crystal and magnetic lattice parameters from Reference [304] are input into the spectrometer control program. The program converts the lattice information into a UB matrix which defines vectors within the scattering plane [319]. The spectrometer then operates within the coordinate space of these vectors. The process is automated by the instrument control program which drives the spectrometer to precise locations of **Q** and energy transfer as defined by the operator.

8.3   Inelastic neutron scattering results

8.3.1   Low energy spin-wave dispersion

The results from a series of INS constant energy **Q**-scans around the magnetic zone centre **Q** = (101) and at several temperatures across the SR are shown in Figure 8.1. Focus is given to energies less than 10 meV. The energies below 1.5 meV are obscured by the elastic Bragg peak near the zone centre due to the limited energy resolution of thermal neutrons. As the temperature is increased, the background signal is raised due to enhanced incoherent scattering. Despite these experimental limitations, the scattering experiments yield important information about the acoustic spin-wave dispersion.

At 175 K, just above the SR, the dispersion curve at the zone centre mixes with the Bragg peak. As the sample is cooled a gap forms between the ground state and $k = 0$ excited spin-wave state, most prominent in the data at 3 K. In the standard isotropic Heisenberg antiferromagnet, acoustic spin waves have zero energy at the zone centre. Their energies are lifted when in-plane anisotropies lower the magnetic symmetry [318]. The temperature development of a gapped dispersion therefore provides strong evidence for a temperature-dependent in-plane spin anisotropy. Its rapid increase at temperatures below the SR suggests that the temperature-dependent anisotropy drives the SR.

The excitation energy of the AF-mode by THz radiation is overlaid on the dispersion plots. As is seen, particularly in the data at 3 K, the AF-mode energy is consistent with the base of the dispersion or 'spin gap'. This confirms that both observations are part of

the same phenomenon. In multiferroics with non-collinear magnetic ordering, the magnetic Bragg sites are usually incommensurate to the crystal lattice. This means that the electro-active spin-wave dispersion will develop at off centre positions in the Brillouin zone [165, 211]. The centring of the excitation dispersion on the antiferromagnetic zone centre in Figure 8.1 is therefore more suggestive of a purely magnetic acoustic spin-wave interpretation. Furthermore, the steep dispersion relation ($\mathbf{Q}$ changing little with energy transfer) and resilience of the magnetic scattering over the broad temperature range is not consistent with more highly dispersed, low temperature electromagnons [165]. This is because the antiferromagnetic spin waves are dominated by the strong Fe-O-Fe super-exchange interaction, whereas the main coupling mechanism of electromagnons in other $RFeO_3$ compounds has been shown to be through the much weaker Dzyaloshinsky-Moriya interaction [273, 274].

In Figure 8.1, the development of two off-centre peaks ($\mathbf{Q} = (0.95\ 0\ 1)$ and $(1.2\ 0\ 1)$) with energies centred on $2.25\,\text{meV}$ is a peculiar result at these temperatures. The Nd^{3+} ions have not been observed to order for temperatures down to $<1.5\,\text{K}$ [314]. It is therefore unlikely that the peaks are due to coherent scattering of a newly-ordered state involving a Nd^{3+}–Nd^{3+} exchange interaction. For low energy transfer measurements, a small scattering angle is measured. This increases the likelihood of spurious neutron signals arriving at the spectrometer detector from unknown sources such as the sample environment. Such spurious signals are likely the origin of the off centre peaks. Since the peaks are separated from the zone centre and are therefore optically inactive, they cannot be probed by the THz techniques. Therefore, focus is given to the spin gap which relates to the spin anisotropy.

8.3.2 Spin gap

The spin gap is directly measured by constant-$\mathbf{Q}$ energy scans at the zone centre. The top panel of Figure 8.2 shows such a scan at room temperature ($298\,\text{K}$). A broad peak beginning at $\sim 2\,\text{meV}$ ($0.48\,\text{THz}$) and falling off at $15\,\text{meV}$ ($3.63\,\text{THz}$) is attributed to magnetic scattering as the scan cuts through the spin-wave dispersion. The prominent peak at $10.3\,\text{meV}$ ($2.37\,\text{THz}$) is attributed to the Nd^{3+} crystal field excitation [320]. As the sample is cooled below the SR to $3\,\text{K}$ (bottom panel of Figure 8.1), the broad peak
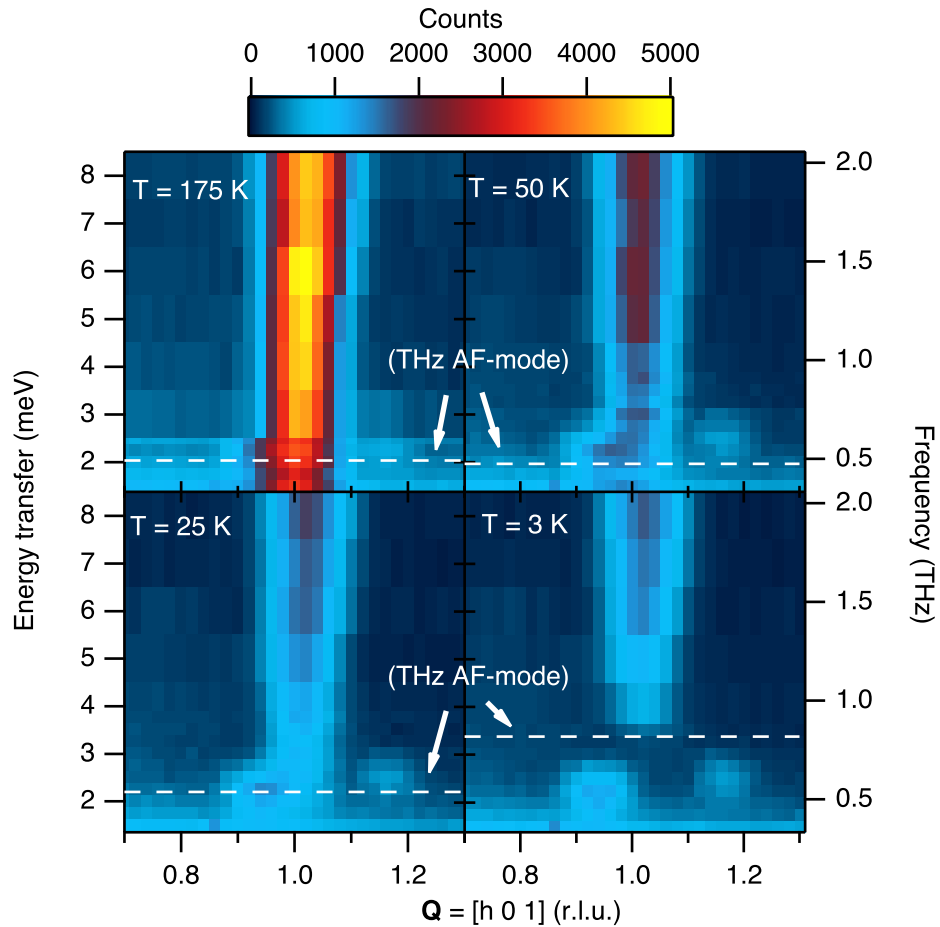
FIGURE 8.1: Temperature evolution of low-energy spin-wave dispersion constructed from a series of **Q** scans at the magnetic zone centre **Q** = (101). **Q** = (*hkl*) is given in reciprocal lattice units (r.l.u.). The series demonstrates the development of a spin gap that is formed as the sample is cooled through the SR. The dashed lines indicate the resonant frequency of the AF-mode as measured by the optical THz techniques for the equivalent temperatures (the AF-mode at 4.2 K is used for the 3 K dispersion plot).

shifts to higher energies, now beginning at ∼3.75 meV (0.91 THz). This is consistent with the development of the spin gap in Figure 8.1. A background scan taken at 3 K with **Q** = (0.9 0 0.9) reveals the non-spin-wave contributions. Subtraction of the background gives zero readings below the spin-gap energy. This demonstrates both the magnetic nature of the features at the zone centre and that the intensity across the spin gap is consistent with background levels.

Figure 8.3 displays a series of the temperature-dependent measurements for the spin gap, attributed to the anisotropy-lifted spin waves. Here, the constant **Q** scattering spectra are
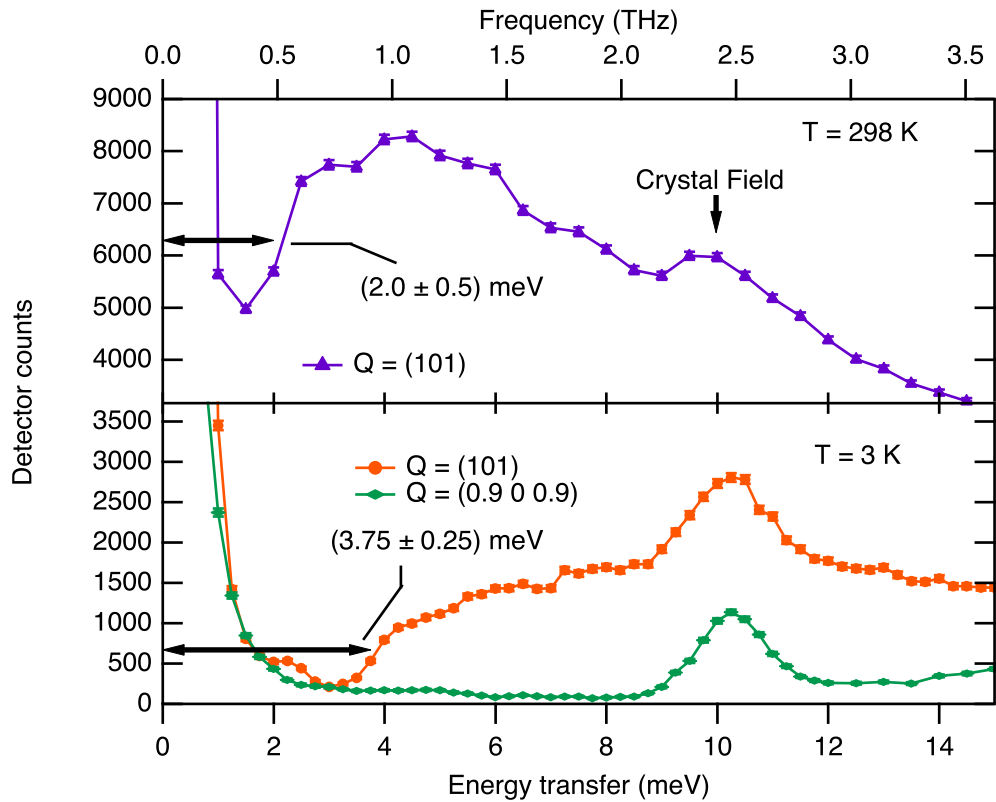
FIGURE 8.2: Constant **Q** energy scans of the magnetic zone centre **Q** = (101) at 298 K and 3 K. A background scan away from the zone centre **Q** = (0.9 0 0.9) is also shown in the bottom panel. Lines between data points are included as a guide for the eye. The error bars of the data points represent the standard deviation of the statistical neutron counts (in most cases the error bars are obscured by the markers). The spin-gap energy is calculated as the inflection point of a polynomial fit to the leading edge of the magnetic peak. The uncertainties of the spin gaps represent the resolution of the data points. The non-magnetic crystal field excitation is isotropic and does not shift with temperature or **Q**.

taken at the magnetic scattering vector **Q** = (011). Shapiro *et al.* [280] have shown in other RFeO₃ compounds, that spin waves in the (0*kl*) scattering plane feature an identical frequency dependence on temperature behaviour to the (*h*0*l*) scattering plane shown in Figure 8.1. The spin gap is determined by a polynomial fit to the scattering data points. The zero-crossing point of a second order differential gives the inflection point. The process is shown in Figure 8.4 for the data at 15 K. The shift in the inflection point with reduced temperature is attributed to the changing magnetic anisotropy. When compared to the frequency of the AF-mode as determined by THz spectroscopy, the inflection point energy shows striking agreement (Figure 8.5).

In both the dispersion (Figure 8.1) and spin gap (Figures 8.2 and 8.3) measurements, no signature of the F-mode is detected. This most likely results from a combination of 3 limitations:

1. At temperatures above $20\,\mathrm{K}$ the F-mode energy is less than $1.5\,\mathrm{meV}$. This means that its signature will be obscured by the broad elastic Bragg peak at these temperatures.

2. Below $20\,\mathrm{K}$ the F-mode energy rapidly increases with reduced temperature. By $4.2\,\mathrm{K}$ the two modes are separated by $0.4\,\mathrm{meV}$ which is within an uncertainty overlap of the INS resolution.

3. The strength of the F-mode appears weaker than the AF-mode. This means that there will be less states to scatter the neutrons resulting in a very weak signature. This would require much longer counting statistics to detect above the levels presented in the data.

Nevertheless, the measurement of the AF-mode spin gap provides an encouraging outcome and motivation to pursue a temperature variable magnetic anisotropy interpretation.

8.4 Magnetic anisotropy calculations

The strong temperature dependence of spin-wave modes, their relation with a temperature variable spin gap and the intriguing process of the SR, provides the backdrop for calculations of magnetic anisotropy in NdFeO₃. The results presented in this section represent the first calculations for the magnetic anisotropy terms along the x (K_x) and z (K_z) magnetic axes as a function of temperature for NdFeO₃. The calculations are performed using Equations (7.3 and 7.4) with the data of Figure 8.5.

Starting with Equation 7.3, the expression is rearranged for $(K_x - K_z)$,

$$\hbar\omega_{\mathrm{F}} = \left\{ 24JS\left[2\left(K_x - K_z\right)S\right]\right\}^{1/2},$$

$$(\hbar\omega_{\mathrm{F}})^2 = 48JS^2\left(K_x - K_z\right),$$

$$(K_x - K_z) = \frac{(\hbar\omega_{\mathrm{F}})^2}{48JS^2}. \tag{8.1}$$
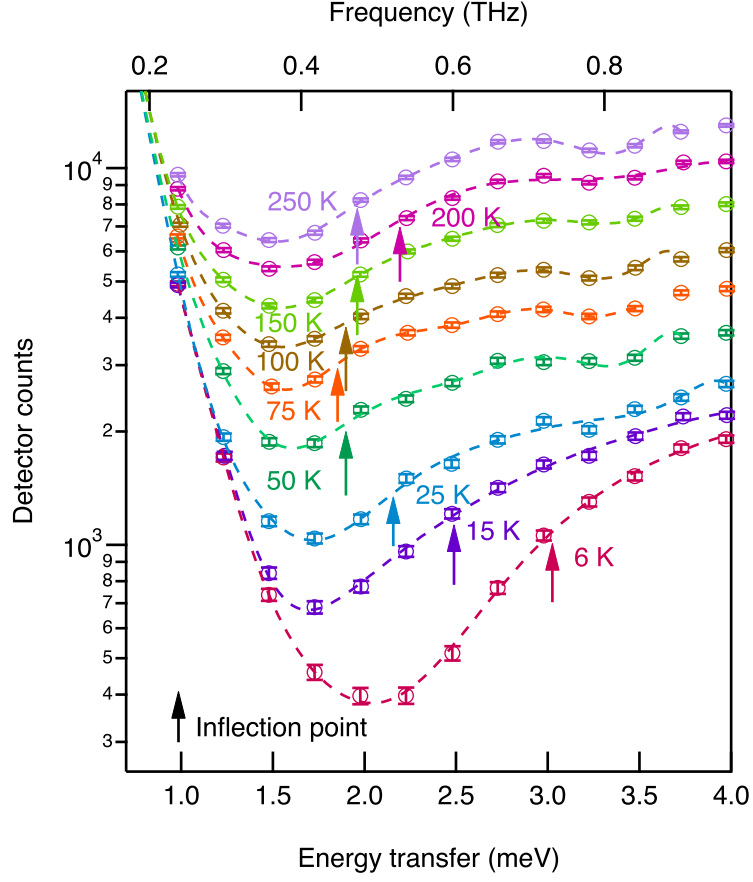
FIGURE 8.3: Constant **Q** energy scans of the magnetic scattering vector **Q** = (011) show-
ing expansion of the spin gap with reducing temperature. Dashed black lines represent
polynomial fits. Arrows show inflection point of fits representing the spin-gap energies.

The same is done for Equation 7.4 to give K_x,

$$\hbar\omega_{\mathrm{AF}} = \left\{24JS\left[6DS\tan\beta + 2K_xS\right]\right\}^{1/2},$$

$$(\hbar\omega_{\mathrm{AF}})^2 = 48JS^2\left[3D\tan\beta + K_x\right],$$

$$K_x = \frac{(\hbar\omega_{\mathrm{AF}})^2}{48JS^2} - 3D\tan\beta. \tag{8.2}$$

K_z is then given by the following expression,

$$K_z = K_x - (K_x - K_z),$$

$$= \frac{(\hbar\omega_{\mathrm{AF}})^2}{48JS^2} - 3D\tan\beta - \frac{(\hbar\omega_{\mathrm{F}})^2}{48JS^2},$$

$$= \frac{1}{48J}\left(\frac{\hbar}{S}\right)^2\left[\omega_{\mathrm{AF}}^2 - \omega_{\mathrm{F}}^2\right] - 3D\tan\beta. \tag{8.3}$$
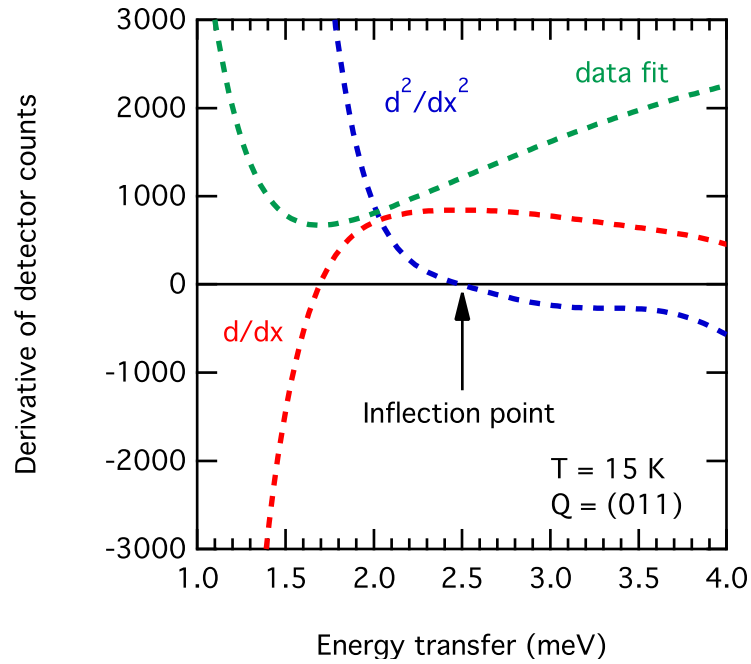
FIGURE 8.4: Process for determining spin gap by inflection point. Neutron scattered data is fit by a polynomial function. The second derivative of the polynomial is calculated and the zero crossing of second derivative gives the inflection point. The data shown here is for the scan at 15 K. The spin gap is 2.5 meV (0.60 THz).
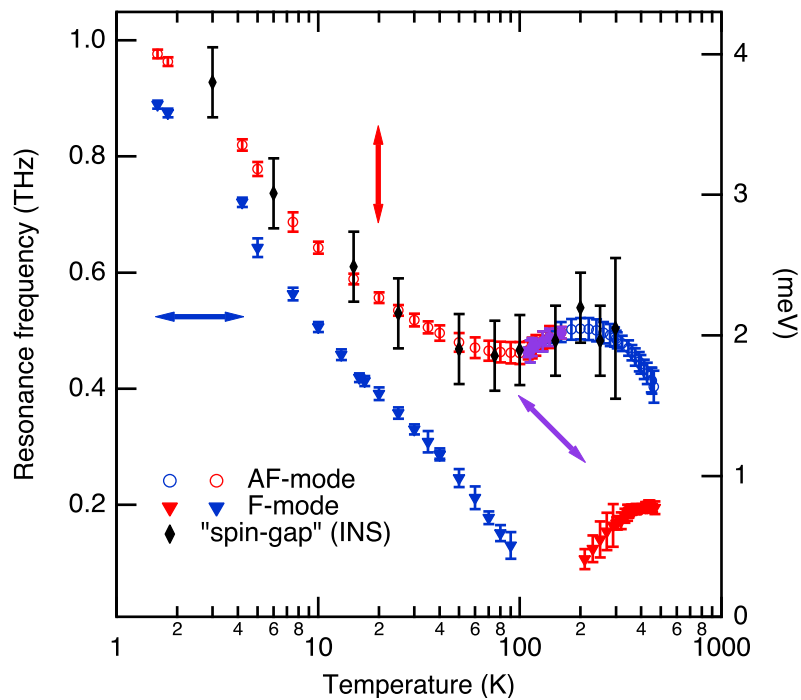
FIGURE 8.5: Temperature dependence of the spin gap from the INS results overlaid on the results obtained by THz spectroscopy. The F-mode splitting is left out and is represented by just a few data points.

Substituting the values for ω_{AF} and ω_{F} from Figure 7.27 as well as values presented in the literature for J ($0.66\,\mathrm{THz}/22\,\mathrm{cm}^{-1}/2.7\,\mathrm{meV}$), S (5/2), D ($0.028\,\mathrm{THz}/0.95\,\mathrm{cm}^{-1}/0.1\,\mathrm{meV}$) and β ($8.5\,\mathrm{mrad}$) [200, 306], the values for K_x and K_z are calculated from 1.6–465 K. The values for J, S, D and β are assumed to change little over the temperature range considered here based on magnetisation and neutron scattering studies [304, 309]. From the polarisation sensitive THz measurements, the fact that the anisotropic field acting on the AF-mode switches from K_x to K_z during the SR transition is taken into account. At the same time, $(K_x - K_z)$, acting on the F-mode, switches sign. The calculation could not be carried out from 90 to 210 K for the F-mode as the optical data required are not available.

The results are presented in Figure 8.6. As expected, due to the polarisation dependence of the two spin-wave modes, at temperatures above the SR, $K_x > K_z$, and at temperatures below the SR, $K_z > K_x$. The result is also in concordance, with the general understanding of a $G_x F_z \rightarrow G_z F_x$ phase transition across the SR, established by magnetisation and elastic neutron scattering measurements [287, 306, 309, 313]. In general, the values represent the effective anisotropies along the a and c crystal axes. The result strongly suggests that the change in size of K_x over K_z (favouring antiferromagnetic alignment along x over z) is the effective driving mechanism of the SR. At high temperatures, as the temperature is reduced, K_z is seen to go from negative to positive. While a positive value favours ordering along that direction, a negative value represents a *hard* axis, indicating that above 425 K internal magnetic forces oppose ordering in the z direction.

A graphical depiction of the SR process influenced by the dynamic anisotropic terms is approximated in Figure 8.7. At high temperatures, in the $G_x F_z$ state, K_x dominates. The Nd^{3+} moments are paramagnetically arranged. As the temperature is lowered, reduced thermal effects help to let the Nd^{3+} moments polarise to the weak ferromagnetic moment of the canted Fe^{3+} sublattices. This interaction facilitates an increase in the K_z term which at 170 K, overcomes the K_x term and the SR initiates. Below the SR, K_z dominates and the Fe^{3+} sublattices favour ordering in the $G_z F_x$ state.
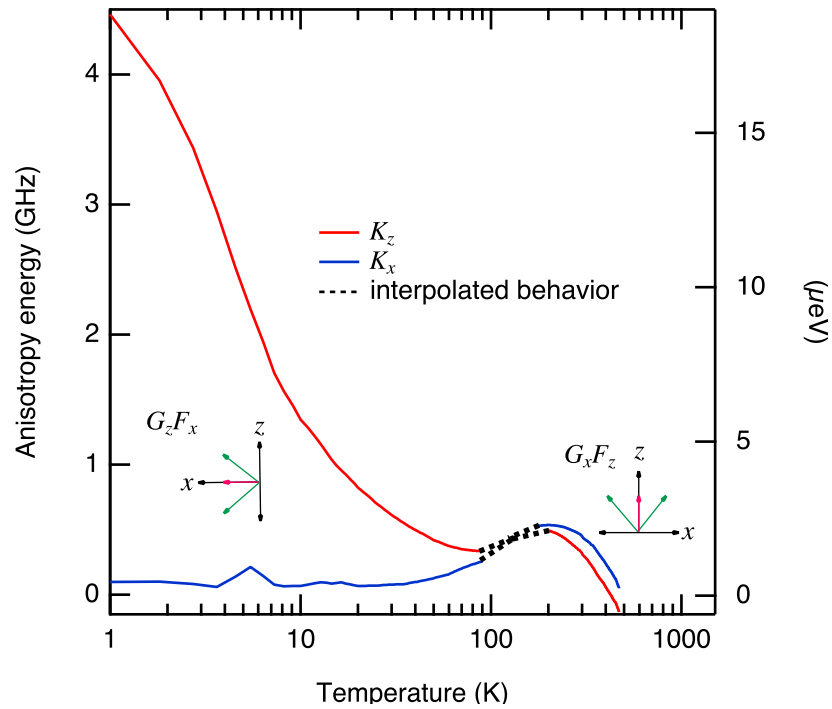
FIGURE 8.6: Calculated temperature dependence of the effective magnetic anisotropy energy. The net anisotropy is seen to shift from $K_x > K_z$ to $K_z > K_x$ as the sample is cooled through the SR, which is consistent with the 90° rotation of the spin-lattice from alignment with the a axis to the c axis. The dashed line represents the predicted trend as the F-mode softens over these temperatures and solutions to Equations 7.3 and 7.4 are unavailable.
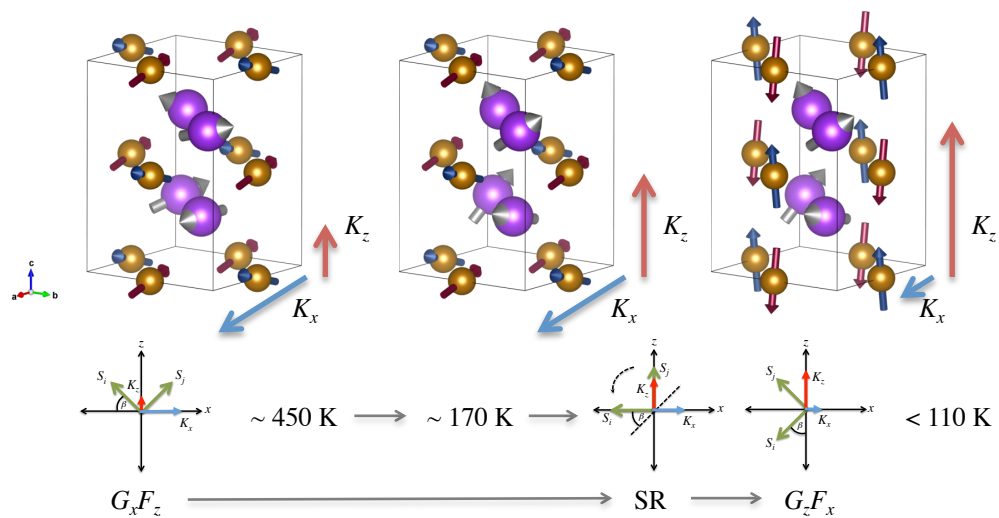
FIGURE 8.7: Spin reorientation process shown by the effect of dynamic anisotropy on the Fe^{3+} spin sublattices.

8.4.1   Calculation refinements

A complete assessment of the microscopic anisotropy contributions requires separate treatment of each term in the Hamiltonian. In reality, there may be numerous sources for anisotropic effects at the microscopic level. Some terms typically considered important in the literature involve second- and fourth-order single ion anisotropies, as well as dipole-dipole spin interactions, giving an anisotropic contribution to the Hamiltonian of the form [300]:

$$H_{\mathrm{anisotropy}} = \sum_i \left(\mathbf{K}_2 \cdot \mathbf{S}_i\right)^2 + \sum_i \left(\mathbf{K}_4 \cdot \mathbf{S}_i\right)^4 + \sum_i \left(\mathbf{K}_{\mathrm{DP}} \cdot \mathbf{S}_i\right)^2. \qquad (8.4)$$

Here K_2 and K_4 are the second- and fourth-order single ion anisotropies, and K_{DP} is the effective dipole-dipole interaction anisotropy.

It should also be noted that each of these terms may carry some form of temperature dependence. Even the quantum mechanical spin moment S is observed to deviate from the ionic expectation of $5/2$ for Fe^{3+}. In practice, this value is modified due to more complicated non-classical electronic effects [28]. For example in NdFeO₃, using neutron diffraction techniques, Sławiński *et al.* [304] find a magnetic moment of $\sim 4.2\,\mu_{\mathrm{B}}$ which would imply a spin moment of $4.2/2 = 2.1$ rather than $S = 5/2 = 2.5$.

In the absence of large structural or electronic transitions, the values for J and D detailed in Equation 7.2 are expected to be approximately constant, and only perhaps depend weakly on the expansion or contraction of the lattice with temperature. Therefore, the prominent temperature dependency in the Hamiltonian should be contained within the anisotropic terms. With $K_2 \gg K_4$, and K_4 usually considered temperature-independent [278, 300], containing the temperature dependence within an effective second-order anisotropy is a good approximation.

The effects of the temperature dependence on the spin moment and its deviation from the ionic expectation of $5/2$ can be modelled from published temperature dependence data of the total Fe^{3+} magnetic moment (μ_S). The temperature dependence of the total ordered Fe^{3+} magnetic moment and its M_x and M_z components were calculated by Sławiński *et al.* for NdFeO₃ by Rietveld refinement of neutron powder diffraction patterns (see Figure 5 in Reference [304]). The digitalised results of μ_S are displayed in Figure 8.8 (a). Assuming a
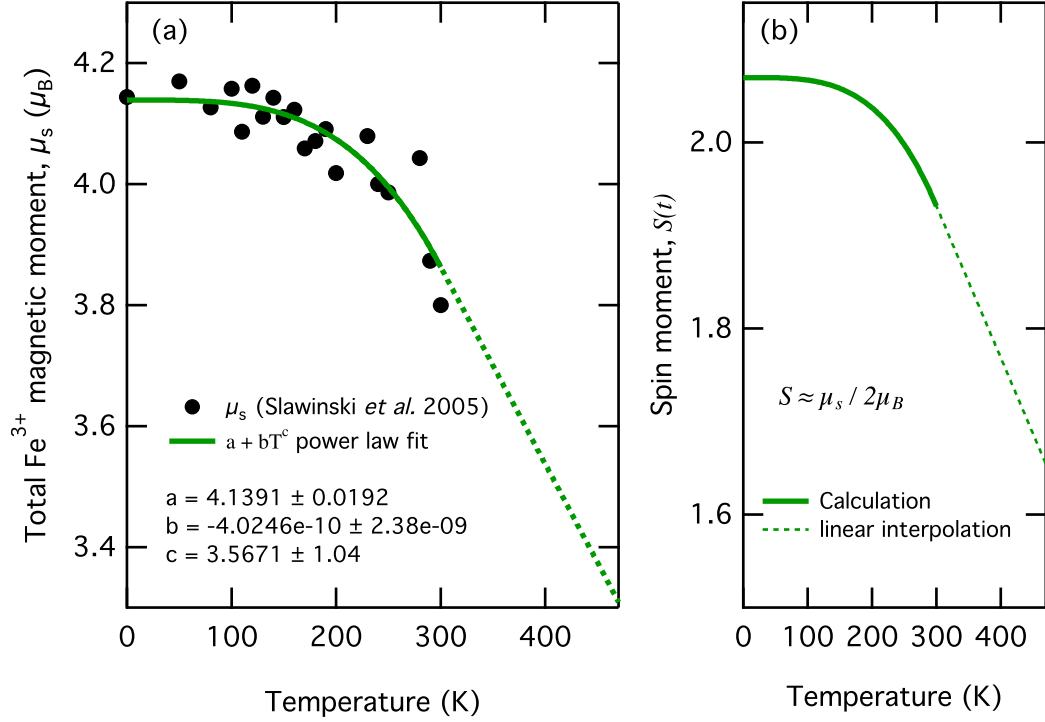
FIGURE 8.8: Temperature dependence of total Fe^{3+} magnetic moment for calculation of spin moment temperature dependence. (a) Data taken from [304] is fit to obtain $\mu_S(T)$. (b) The fit of $\mu_S(T)$ is used for temperature correction of $S(T)$.

T^x temperature dependence, the magnetic moment is fit with a simple power law function of $a + bT^c$ where a, b and c are all constants. With no data above $300\,\mathrm{K}$ available, the magnetic moment is linearly interpolated to $470\,\mathrm{K}$ to be used with the THz data for the spin-wave frequencies. The spin magnetic moment (μ_S) and the spin moment vector ($\mathbf{S}$) are related through the following expression,

$$\mu_S = g\frac{q}{2m}\mathbf{S} \tag{8.5}$$

$$\approx 2\mu_\mathrm{B}\mathbf{S}, \tag{8.6}$$

where g is the gyromagnetic ratio (≈ 2), q is the electron charge and m is the electron mass. Using this expression, the values for $S(T)$ are calculated across the temperature span considered in the THz and INS measurements (Figure 8.8 (c)). It should be noted that the linear interpolation for values greater than $300\,\mathrm{K}$ are likely not accurate and only included to show potential changes at high temperatures.
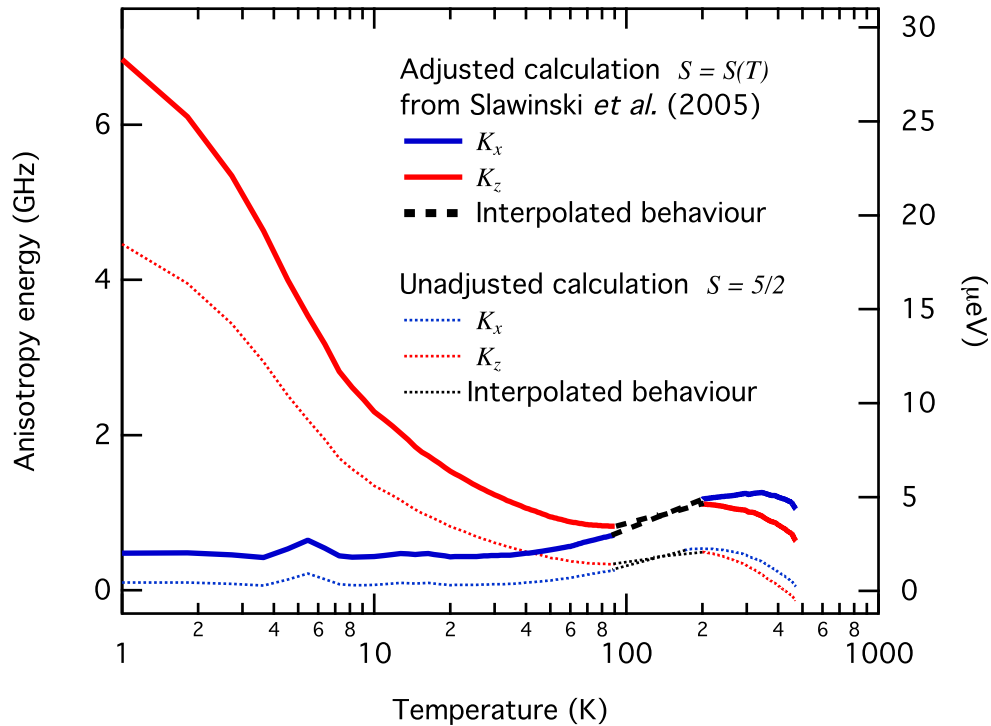
FIGURE 8.9: Refined magnetic anisotropy energies along x and z calculated with temperature dependent spin-moment correction.

The temperature dependent spin moment correction is applied to Equations 8.2 and 8.3. The refinements of the calculations for K_x and K_z are shown in Figure 8.9. The net effect is to generally raise the values for the two anisotropy energies. The roll-off in $S(T)$ at high temperatures leads to a greater separation of the two energies above the SR and K_z no longer appears negative above 425 K, suggesting that c may indeed not be a *hard* axis at high temperatures. Again, the linear interpolation of $S(T)$ above 300 K means that the calculations in this temperature range should be taken only as an approximation.

8.4.2 Discussion of anisotropy contributions

With the anisotropic energies calculated, some discussion on potential microscopic contributions is now given. It is the competition between the internal microscopic anisotropy forces that equates to temperature dependent changes in the effective anisotropies along the x and z directions. For example, calculations performed by Bidaux *et al.* [321] show that the dipole-dipole interactions for the Fe–Fe sublattices in RFeO$_3$ strongly favour an

x direction of antiferromagnetism as seen in NdFeO$_3$ above the SR. Therefore, a considerable contribution to the temperature dependence of the experimentally determined K_x value is likely the dipole-dipole interactions between the Fe–Fe sublattices. At the same time, upon cooling, reduced thermal interactions may allow polarisation of the Nd^{3+} ions with the weak ferromagnetic moment of the Fe–Fe sublattices, as supported by recent magnetometry results [313, 322].

This form of R-Fe coupling may drive a modulation of the spin-lattice coupling, which in turn facilitates the onset of a new anisotropy along the z direction. The rapid increase of the experimentally determined K_z value should contain the information about this net effect. The mathematical details for this mechanism were first laid out in detail by Yamaguchi [279]. The absence of a SR in YFeO$_3$ supports this mechanism since the Y^{3+} ions have no magnetic moment. However, no evidence of rare earth ordering has yet been observed at the high temperatures associated with the SR transitions via diffraction techniques [287, 320], which would be expected if pronounced R-Fe coupling were present. Therefore the specific details for the microscopic mechanism that drives the SR is still in question.

Individual anisotropy terms, such as the dipole-dipole interaction, may be modelled using mean field theory and Monte Carlo simulations. Using these measurements, it is conceivable that one could subtract theoretically modelled sources of anisotropy, thus revealing the contributions of presently unknown interactions to better understand the underlying mechanism of SR.

As shown by Tachiki and Nagamiya [323] using the molecular field approximation invoking a statistical approach to the spin ensemble, the temperature dependence of the dipolar anisotropy is proportional to the square of the spin moment expectation value ($\langle S \rangle^2$) where,

$$\langle S \rangle^2 = S^2 B_S(X) \propto K_{\text{dip}}. \tag{8.7}$$

Here, $B_S(X)$ is the Brillouin function [29],

$$B_S(X) = \frac{2S+1}{2S} \coth\left(\frac{2S+1}{2S}X\right) - \frac{1}{2S} \coth\left(\frac{1}{2S}X\right) \tag{8.8}$$

with

$$X = \frac{g\mu_{\mathrm{B}}SB_{\mathrm{int}}}{k_{\mathrm{B}}T}. \tag{8.9}$$

B_{int} is the internal field magnitude and k_{B} is the Boltzmann constant.

There is a relation between X, T and the Néel temperature T_{N}, given as,

$$\frac{T}{T_{\mathrm{N}}} = \frac{3S}{(S+1)}\frac{B_S(X)}{X}. \tag{8.10}$$

B_{int} is governed by the sublattice magnetisations and will have some form of temperature dependence changing rapidly around the Neèl temperature. Fortunately, there are approximations to these equations at high temperatures. As $T \to T_{\mathrm{N}}$ $X \to 0$ and Equations 8.8 and 8.10 can be expanded in powers of X. This gives,

$$\langle S \rangle^2 = \frac{(S+1)^2}{9}X^2, \tag{8.11}$$

and

$$X^2 = \frac{30S^2}{(S+1)^2 + S^2}\frac{T_{\mathrm{N}} - T}{T_{\mathrm{N}}}. \tag{8.12}$$

Therefore, there is a relation for the dipolar contribution at high temperatures in the vicinity of T_{N},

$$K_{\mathrm{dip}} \propto \frac{30}{9}\frac{S^2(S+1)^2}{(S+1)^2 + S^2}. \tag{8.13}$$

At lower temperatures the same approximation cannot be made. Therefore, the full expression for the Brillouin function should be used. However, since it is established that at sufficient temperatures below the Néel temperature ($\sim 0.3T_{\mathrm{N}}$), the magnetisation is saturated, a constant value for B_{int} can be assumed in Equation 8.9. Combining the low and high temperature K_{dip} approximations (Equations 8.7 and 8.13) a temperature dependent model of the dipolar anisotropy is constructed. The results are shown in Figure 8.10. To achieve this, the value of B_{int} was adjusted until the plot in Figure 8.10 resembled the anisotropy profile of K_x. The general shape bears striking resemblance to the K_x value determined from the calculations and shown in Figures 8.6 and 8.9. This may be expected as Bidaux *et al.* show that the energy is minimised for the Fe^{3+} sublattice in YFeO$_3$ for a dipolar alignment in the x direction. Bidaux *et al.* also calculate an easy axis in the

z direction, with the y axis being hard. It is therefore expected that there will be some smaller dipolar contribution in K_z and the high temperature profile of the determined value for K_z in Figure 8.9 seems to agree with this notion. At lower temperatures, as the SR begins, the shape of K_z changes considerably increasing rapidly as the temperature is cooled.

The single ion anisotropy originates from the spin-orbit coupling and in the absence of electronic reconfiguration at low temperatures, should remain mostly temperature independent when neglecting minor alterations due to lattice spacing contraction with cooling. At the same time, it has been suggested that reduced thermal interactions allow polarisation of the Nd^{3+} ions with the weak ferromagnetic moment of the Fe–Fe sublattice [313]. The effects of this may drive a modulation of the spin-lattice coupling, which may intern facilitate the onset of a strong temperature dependent single ion anisotropy along the z direction. The rapid increase of the experimentally determined K_z value should contain the information about this net effect.

Tachiki and Nagamiya [323] show that the single ion (or fine structure) contribution to the total anisotropy has the following proportionality,

$$K_{\mathrm{SI}} = \propto \frac{1}{2} \left[3 \left\langle S^2 \right\rangle - S(S+1) \right] \tag{8.14}$$

$$= S(S+1) - \frac{3}{2} S B_S(X) \coth \left(\frac{X}{2S} \right). \tag{8.15}$$

Here, the single ion contribution is proportional to the expectation value for the square of the spin moment ($\left\langle S^2 \right\rangle$). Considering that this effect only seems to take hold at temperatures in the vicinity of the SR and below, the assumption that B_{int} remains constant is utilised in the Brillouin function once again. Adjusting values for B_{int} to produce a similar profile as the calculations for K_z gives the result shown in Figure 8.11.

Combining the two models and considering only dipolar effects along the x direction and dipolar and single ion effects along the z direction, the two effective anisotropies along x and z are shown in Figure 8.12. The results have a resemblance to the determined values of K_x and K_z featuring a crossing between $100\,\mathrm{K}$ and $200\,\mathrm{K}$ as would be expected during the SR. It should be noted however, that the models presented only represent a proportionality

to the anisotropy terms. The actual physical energies have not been extracted and only conclusions about the general temperature profile can be made. The values of B_{int} used in the plots therefore have not been given as they do not represent physical values with real units. Furthermore, the interpretation of the rapid increase in single ion anisotropy in the z direction considered an interaction of the Nd^{3+} ions, yet the single ion model only concerns the Fe^{3+} sublattice. This was justified, however, by the notion that the Nd^{3+} interaction would affect the spin-orbit coupling of the Fe^{3+} sublattice where single ion anisotropy originates, effectively influencing the Fe^{3+} sublattice anisotropy. A more thorough model should include the magnetic interactions between the Nd^{3+} and F^{3+} ions. These interactions must be of importance since recent results on $Dy_{0.5}Pr_{0.5}FeO_3$, featuring two types of rare earth ions, show remarkably different SR properties involving three separate phases rather than the usual two [292]. Moreover, the magnetisation of the rare earth sublattice in $DyFeO_3$ may contribute to the magnetoelectric coupling observed in this compound facilitating the onset of multiferroicity at low temperatures [324]. Nevertheless, with more refinement, this technique could eventually be used to extract the physical contributions of the different anisotropic terms and lead to conclusions on the microscopic mechanism of the SR phenomenon.

8.5   Conclusions

In summary, inelastic neutron scattering measurements have been performed on the canted antiferromagnet NdFeO₃. The neutron scattering was primarily used to probe the magnetic zone centre $\mathbf{Q} = (101)$. A temperature profile of the low energy dispersion at the zone centre confirmed the magnetic origin of the excitation features in the THz spectra of Chapter 7. The dispersion of the magnetic excitation was consistent with an interpretation of acoustic spin waves dominated by the exchange interaction. No evidence of magneto-electric coupling was found.

A spin gap between the ground state and spin-wave dispersion was observed to increase at low temperatures. Measurement of the spin-gap temperature dependence showed excellent agreement with the temperature dependence of the AF-mode measured by THz spectroscopy. The correlation between the spin gap in the spin-wave dispersion and the
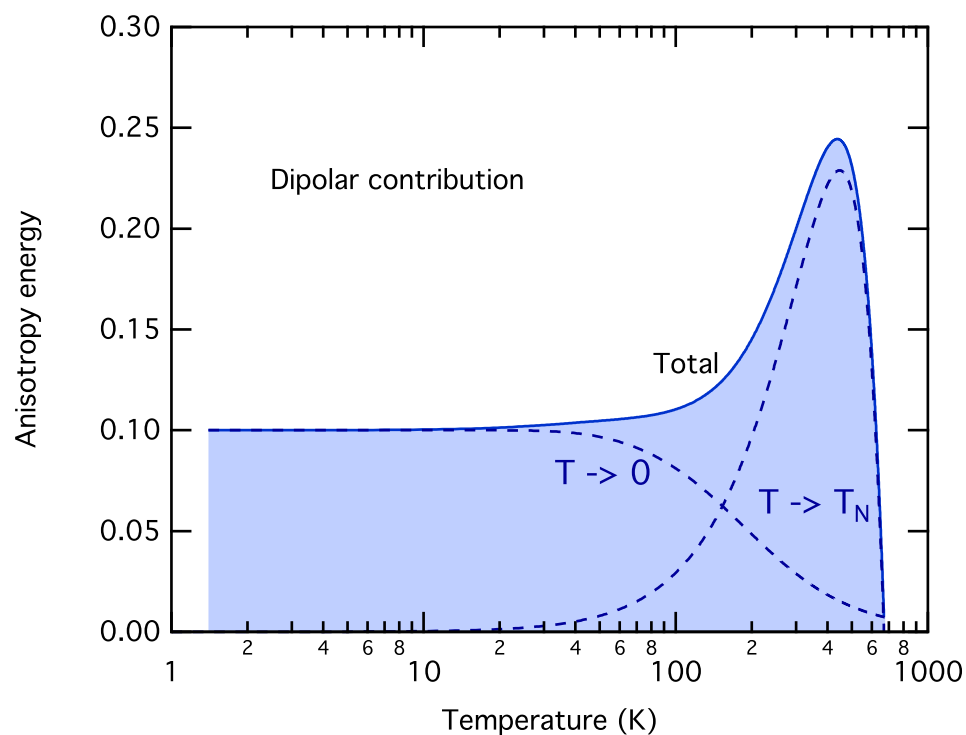
FIGURE 8.10: Model of the dipolar contribution to the K_x anisotropy energy.
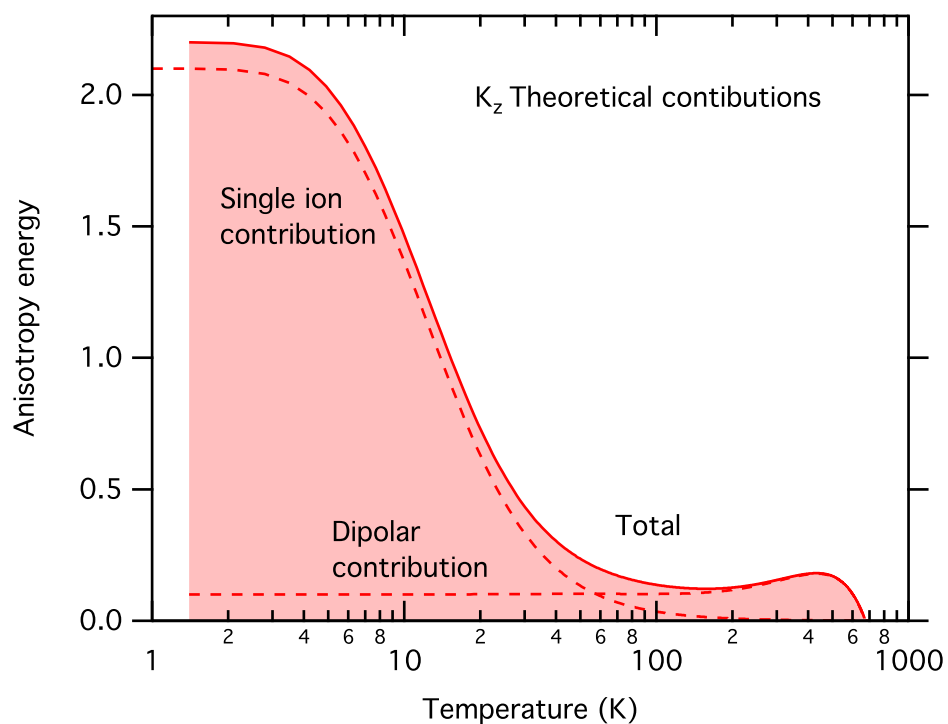
FIGURE 8.11: Model of the dipolar and single ion contributions to the K_z anisotropy energy.
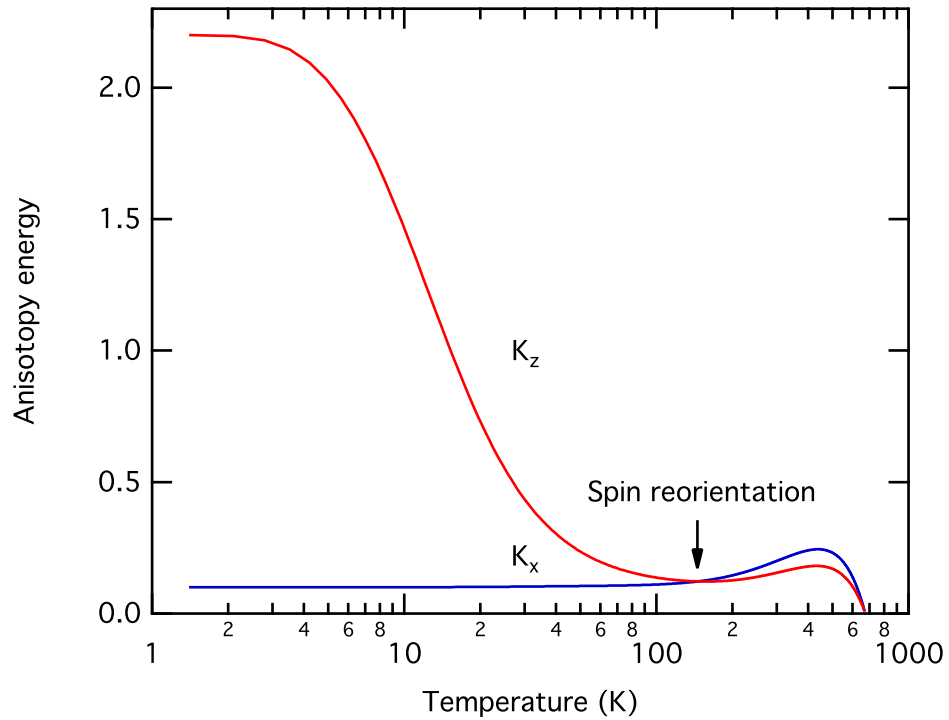
FIGURE 8.12: Theoretical model for the temperature profile of the K_x and K_z anisotropy energies, using contributions from dipolar and single ion approximations.

optically-detected spin-wave modes provided a link between the spin reorientation and a temperature variable magnetic anisotropy.

Using the temperature dependence of the spin-wave frequency the temperature variable anisotropy was calculated for contributions along the x (K_x) and z (K_z) magnetic axes. The results reveal that the SR transition occurs when K_x is overcome by K_z. Using a more physically representative temperature dependent spin moment, the calculations for K_x and K_z can be further refined. Modelling the anisotropic contributions suggests that an interplay between dipolar and single ion anisotropies is responsible for the temperature dependence of the SR.

The further development of the analysis could be used to extract precise values of the microscopic magnetic interactions. Such information could assist in the future engineering of desired anisotropic properties in spintronic devices.

Chapter 9

Anisotropic transmission and excitations in quantum spin ladder Sr$_{14}$Cu$_{24}$O$_{41}$

9.1 Introduction

This chapter presents THz spectroscopy of the low-dimensional quantum spin ladder system Sr$_{14}$Cu$_{24}$O$_{41}$ using synchrotron radiation. The results reveal highly anisotropic transmittance properties and a diverse range of resonant excitations. The high flux of the synchrotron source allows for transmission measurements of small lightly conducting samples. The experiments present a unique opportunity to probe low dimensional spin dynamics in a high temperature superconductor-type material.

Low-dimensional Heisenberg magnetic systems consist of a series of isotropic exchange interacting spins. In the one-dimensional case, the spins are arranged into chains and in the two-dimensional case they form planes. Such systems have been the subject of considerable theoretical investigation for over 70 years [325, 326]. Initially, low-dimensional spin systems offered a simplified way of understanding basic magnetic interactions. However, it soon became apparent that energy gaps in the spin excitation spectra could exist when an even number of spin chains are linked together into ladder-like structures [327]. An

implication for this was the possibility of superconducting phases and so rapid uptake in the experimental study of spin ladder systems took hold [328].

In parallel, following the discovery of high-temperature superconductivity (HTS) in the two-dimensional CuO_2 systems or cuprates in 1986 [329], a rapid increase in the research of two dimensional systems also took hold. Perhaps the major driving force behind these studies was the desire to better understand HTS, a phenomenon that had begun to appear more and more distinct from standard Bardeen-Cooper-Schrieffer (BCS) superconductivity. Shortly after the initial discovery of superconductivity in the Ba-La-Cu-O compound, with a critical temperature of $T_c = 30\,K$, further efforts in crystal synthesis were able to push T_c up to $90\,K$ in the Y-Ba-Cu-O compound [330]. This was a technological milestone as the T_c was now beyond the temperature of liquid nitrogen ($77\,K$). The high T_c values achieved in these compounds, and the considerably different thermal physics that exists at those temperatures compared with traditional low temperature superconductors, was intriguing. It became apparent that even the refined BCS theory, with a theoretical limit of $\sim 40\,K$, could not explain superconductivity in these materials [331].

In a superconductor, the charge carriers are not considered individually but rather as a collective state occurring with the formation of Cooper pairs [332]. In standard BCS theory, electrons form the collective Cooper pair state through phonon exchange. There is a single energy level associated with this collective state. This energy is lower than the 'normal' state energy and there is an energy gap between the superconducting and normal states. Cooper pairs are continuously formed and destroyed within this state, but their density remains well defined. A minimum energy is required to displace the Cooper-pair state, which presents a limit to the maximum temperature the T_c can be.

The critical temperatures achieved by the new HTS cuprates were far greater than the temperatures able to support superconductivity in the refined BCS theory. It was soon proposed, due to the strong magnetic correlations in these materials, that the superconductive state may involve so called 'd-wave pairing'. In this case, Cooper pairs are formed in the two-dimensional CuO_2 planes by spin-wave fluctuations in the d-orbitals of the Cu^{2+} ions [333, 334]. Essentially, the role of the phonon in a conventional superconductor is replaced by a spin-density wave, where an electron moving through the material may

distort the spin sublattice. This in turn causes a nearby electron to couple to the spin wave. However, while progress in the understanding of this phenomenon has been made in subsequent years [331], a universal and robust theory of the microscopic mechanism of the HTS state in the copper oxide family remains to be developed. Part of the reasons for this is that the multi-layered crystals of the HTS cuprates are generally very complex making theoretical modelling difficult.

The prospect of superconductivity in related, but more simplified one-dimensional materials such as $Sr_{14}Cu_{24}O_{41}$ is therefore of considerable interest in the development of theories for HTS in the broader sense. Terahertz spectroscopy presents a method for probing the low energy spin and phonon dynamics associated with such states which may help to reveal information about the microscopic interactions. It is revealed in the experiments presented here, that temperature and hence phonon interaction plays an important role in the charge dynamics of $Sr_{14}Cu_{24}O_{41}$.

The chapter is structured as follows: Section 9.2 addresses specific details about the $Sr_{14}Cu_{24}O_{41}$ compound studied. This includes a brief review of its historical background, its physical properties as well as some recent research outcomes. The characteristics of the specific sample measured are also given. Section 9.3 presents the experimental methodology involving the synchrotron radiation source. The results with accompanying discussions are covered in Section 9.4. Here, transmission spectra are shown for two principal polarisation orientations over a temperature span of 6–300 K. A large number of absorption features are observed in the spectra. Section 9.5 is dedicated to a discussion of the various possibilities for assignment of the absorption features. Section 9.6 summarises the chapter.

9.2 Strontium copper oxide spin ladder system ($\mathbf{Sr_{14}Cu_{24}O_{41}}$)

Following the rapid search for HTS materials in the late 1980's, many new and rather complex copper oxides were developed. $Sr_{14}Cu_{24}O_{41}$ is one such compound to come from this hotbed of materials development. First synthesised in 1988 [335], $Sr_{14}Cu_{24}O_{41}$ consists of alternating layers of Sr_2 planes, two-leg Cu_2O_3 ladders and CuO_2 chains.
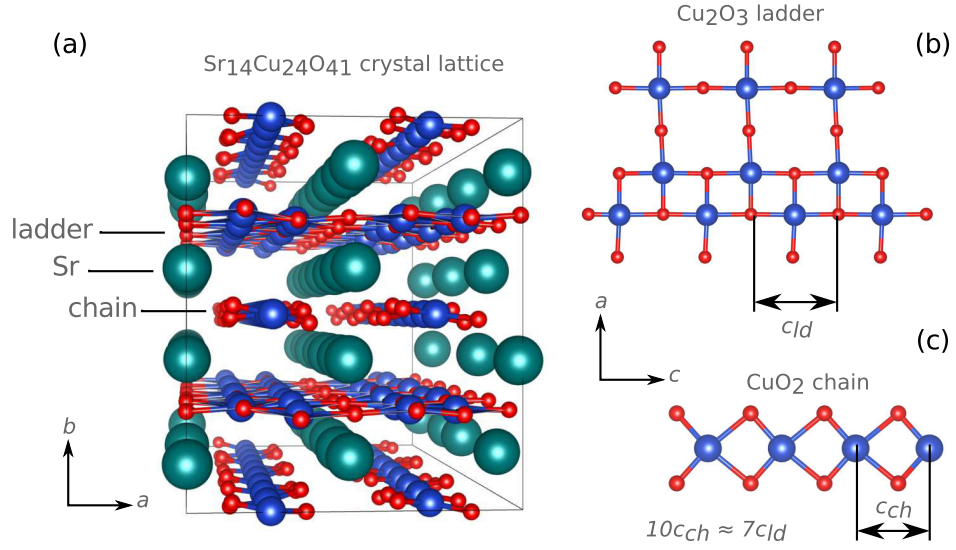
FIGURE 9.1: Crystal structure of $Sr_{14}Cu_{24}O_{41}$. (a) Large layered unit cell. (b) Cu_2O_3 two-leg ladder. (c) CuO_2 chain. Graphics generated using VESTA [253] and information in Appendix B.4.

9.2.1 Crystal structure

A diagram of the layered structure of $Sr_{14}Cu_{24}O_{41}$ is shown in Figure 9.1. Due to the free arrangement of two CuO_2 chains for each ladder and the periodic stacking, the lattice parameters a (11.47 Å) and b (13.41 Å) remain constant in each layer.

However, with near 180° Cu-O-Cu bonding in the legs of the ladder and 90° Cu-O-Cu bonding in the links of the chain, the two layers have different c parameters [336]. With $c_{ld} = 3.95$ Å and $c_{ch} = 2.75$ Å, the two layers feature an incommensurate (non-integer) repeating structure containing the Sr_2 - Cu_2O_3 and CuO_2 sublattices [337, 338]. Since $c_{ld} \simeq \sqrt{2}c_{ch}$, this gives an effective $c = 27.5$Å $\simeq 10c_{ch} \simeq 7c_{ld}$ and leads to the large unit cell.

9.2.2 Electronic properties

Electronically, $Sr_{14}Cu_{24}O_{41}$ is a 'self-doped' system with the nominal Cu valence of $+2.25$ [41(O) + 14(Sr)]/24(Cu), instead of $+2$ [328]. The charge carriers consist of roughly 6 holes per unit formulae located on the CuO_2 chains [339]. The one-dimensional nature of the chains facilitate highly anisotropic transport properties, insulating along the a and b directions and conducting along the c direction [340, 341]. When the temperature is

reduced, the resistivity increases non linearly and there is a metal-insulator transition for the c axis [342]. This phase change is attributed to a charge ordering transition, where below the transition temperature (T_{co}) the holes are localised in the lattice due to the highly correlated spin network in the chains and ladders. For $Sr_{14}Cu_{24}O_{41}$, this has been found to occur at $T_{co} = 200\,K$ [343].

The mechanism for this involves the formation of Zhang-Rice singlets, where the unpaired holes with $S = 1/2$ situated on the oxygen sites, form a tightly bound singlet state with a neighbouring $S = 1/2$ Cu^{2+} ion, essentially forming a $S = 0$ Cu^{3+} site [344, 345]. The Zhang-Rice singlets separate the remaining Cu^{2+} ions which then form antiferromagnetic spin dimers through a super-exchange across the Cu-O-Cu bond. Denoting the Zhang-Rice singlet as 0 and the $S = 1/2$ and $S = -1/2$ Cu^{2+} sites as $\uparrow$ and $\downarrow$ respectively, the dimerised magnetic arrangement leading to charge ordering is pictured below in two proposed models [337]:

$$\uparrow 0 \downarrow 00 \uparrow 0 \downarrow 00 \uparrow 0 \downarrow 0..., \tag{9.1}$$

which corresponds to dimers of two spins coupled across one hole. Neighbouring dimers are separated by two successive holes. Or,

$$\uparrow 0 \downarrow 0 \uparrow 0 \downarrow 0 \uparrow 0 \downarrow 0..., \tag{9.2}$$

which corresponds to alternating occupation by spins and singlets. This magnetic arrangement produces a singlet ground state for the chain system. While the correlations (coupling strength) between neighbouring spins is large, the correlations between separated spins, $S(x)$ and $S(x')$, decreases to zero for large distances ($|x - x'|$). Therefore, these states do not constitute long-range order.

The excited triplet state, where a singlet state transitions from $\downarrow\uparrow$ to $\uparrow\uparrow$, $\downarrow\downarrow$ or $\uparrow\downarrow$ requires an energy equivalent to the exchange coupling between the Cu^{2+} ions [328]. While the above magnetic arrangements do not strictly constitute long-range ordering, these local excitations feature energy-momentum dispersion. As they propagate along the chain, a spin gap forms which is the minimum of the dispersion at zero momentum [328]. The existence of spin gaps in HTS materials is thought to be of considerable importance to the mechanism behind their superconductivity. Both nuclear magnetic resonance (NMR)

[343] and inelastic neutron scattering (INS) [336, 346, 347] experiments have shown results consistent with the above magnetic models, observing periodic excitation of the excited triplet state with a spin gap energy around 10 meV (2.42 THz).

The magnetic arrangement in the ladders is very similar to that of the chains, only that there is now exchange coupling across the Cu-O-Cu bonds both along the ladder legs and rungs [327]. As is demonstrated in the simplified diagram of Figure 9.2 (a), Cu^{2+} singlet states are formed along the rungs since the exchange coupling across them (90° Cu-O-Cu bonding) is far greater than that along the legs (180° Cu-O-Cu bonding) [328]. The stronger coupling and stability in this singlet arrangement, compared to the spin-dimer network of the chain, requires a much larger energy to excite the triplet states. As a result, the spin gap of the ladder should be at much higher energy, which has been confirmed through INS experiments and observed with an energy of 32.5 meV (7.86 THz) [348].

When holes are introduced into the ladder network, they form Zhang-Rice singlets (Figure 9.2 (b)), which break the local Cu^{2+} singlet states on the rung they occupy raising the energy of the system. In the absence of strong thermal disruptions, the Zhang-Rice singlets will localise by occupying the same rung to reduce the energy of the system. This form of charge ordering is particularly special, as the paired holes now resemble the formation of Cooper pairs (Figure 9.2 (c)). It has been demonstrated that this magnetic arrangement produces the required 'd-wave' pairing necessary for HTS [327].

9.2.3   Doped compounds and superconductivity

The holes confined to the chains in $Sr_{14}Cu_{24}O_{41}$, are in fact promoted into the ladder network through substitution of Sr with Ca in the $Sr_{14-x}Ca_xCu_{24}O_{41}$ compound [349]. The Ca doping does not introduce new holes into the system but acts to reduce the spacing between the chains and ladders, allowing holes to transition from the chain into the improved conductive channel of the ladder. Such doping greatly increases the conductivity, with as little doping as $x = 3$ producing metallic transport properties along both the a and c axis at room temperature [350]. It has been shown that charge ordering is maintained up to $x = 2$, with the charge ordered state destroyed at higher Ca concentrations [351].
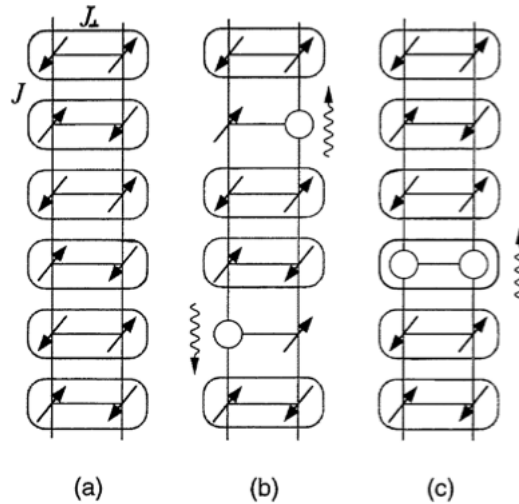
FIGURE 9.2: Simplified diagram of dimerisation of spin-singlets on the ladders of $Sr_{14}Cu_{24}O_{41}$. (a) No holes present produces a stable dimerised state. (b) Holes introduced to ladder form $S = 0$ Zhang-Rice singlets breaking local dimers raising energy of system. (c) With reduced thermal fluctuations holes localise to the same rung lowering the energy of the system and forming a charge ordered state. Figure adapted from Reference [328].

Nevertheless, in 1996 with a Ca concentration of $x = 13.6$ and under a hydrostatic pressure of 3 GPa, it was shown by Uehara *et al.* that $Sr_{14-x}Ca_xCu_{24}O_{41}$ would superconduct.

This was the first result for superconductivity in the spin-ladder systems. It constitutes an important result for the further development of HTS theory, as now a simple one-dimensional system had shown HTS properties. Since then, others have shown superconductivity in $Sr_{14-x}Ca_xCu_{24}O_{41}$ at lower doping concentrations [352]. The results of Isobe *et al.* [352] are complemented with temperature dependent x-ray diffraction measurements. The results revealed that no distinct structural transition exists under the pressure required for superconductivity. This suggests that there is no transition from the one-dimensional chain/ladder structure into a two-dimensional state typical of other HTS cuprates. However, this notion remains a debated topic [345]. Recently, Rusydi *et al.* have demonstrated by resonant x-ray scattering that hole doping in the ladder network acts to reduce nearest-neighbour Coulomb repulsion increasing magnetic exchange and promoting hole pairing [353]. This supports the notion of superconductivity by paired holes on the ladder rungs.

9.2.4 Optical investigations and excitations

In this chapter, the transmission properties of the undoped $Sr_{14}Cu_{24}O_{41}$ system in the spectral region of 0.6–3.6 THz are investigated. The energies associated with this spectral range are ideal for probing the spin-dimer network on the chains [336], as well as exciting low-lying phonons that could be important in spin-phonon coupling. This has recently become an area of interest regarding the onset of the superconducting state in the HTS cuprates [354].

To date, optical studies have proven particularly fruitful in the study of $Sr_{14}Cu_{24}O_{41}$, revealing the presence of charge-density waves and pseudo gaps in the optical conductivity [355, 356]. Elementary excitations such as zone folded phonons [357], gapped sliding acoustic modes [38] and triplet excitations in the magnetic ordering [358] have also be observed. All of this, provides significant insight into the physical properties of the $Sr_{14}Cu_{24}O_{41}$ spin-ladder system and will be discussed in more detail in relation to the results presented in this chapter.

9.2.5 Sample details

A single crystal of $Sr_{14}Cu_{24}O_{41}$ was fabricated by G. Deng using the floating zone technique. An XRD pattern (Figure 9.3) of a polycrystalline sample was used to confirm the phase and structure of the material. The incommensurate layers generate many weak Bragg peaks. The peak positions were fit by G. Deng using a refined crystal model consisting of a composite of smaller well defined lattices. Details can be found in Reference [359].

The sample used in the experiments of this chapter was a single crystal cut from the crystal grown by G. Deng. The sample was a small rectangular wafer with dimensions $5.2 \times 3.5 \times 1.0 \, mm^3$. The sample face used for the optical measurements was in the *ac* plane. A photograph of the crystal can be seen in Figure 9.4.
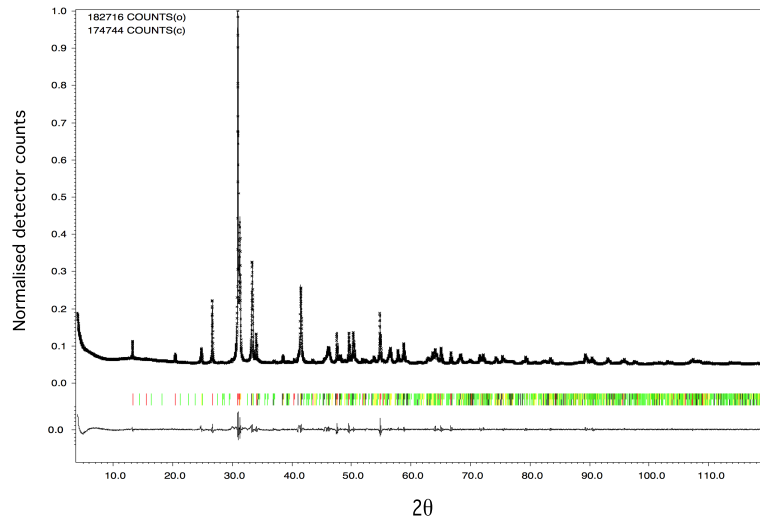
FIGURE 9.3: X-ray diffraction pattern of $Sr_{14}Cu_{24}O_{41}$ polycrystalline sample provided courtesy of G. Deng. The Bragg peaks were used to confirm the material phase using a refined composite crystal model.
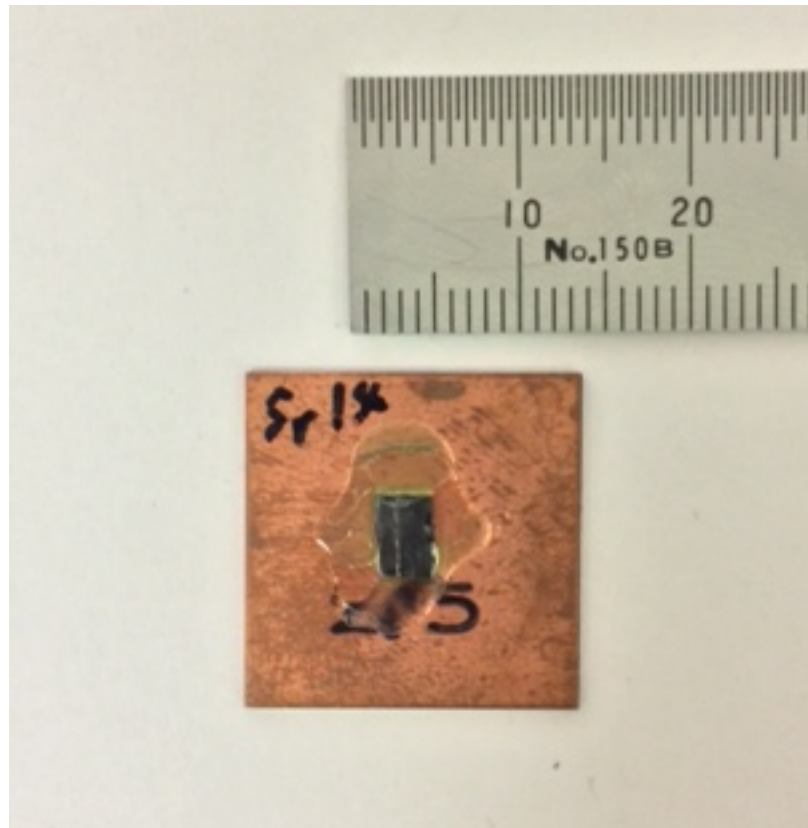
FIGURE 9.4: Single crystal of $Sr_{14}Cu_{24}O_{41}$ used in optical experiments. The crystal is mounted on a copper plate with 2.5 mm aperture for further mounting on the cold head of the cryostat.

9.3 Experimental methodology

Transmission measurements under ambient pressure and with no applied magnetic fields were performed at the Australian Synchrotron far-infrared beamline. The sample was fixed to a copper plate with a 2.5 mm aperture using nail polish as an adhesive around the edges of the crystal. The copper plate was then mounted to the cold head of the Cryo Industries closed cycle helium cryostat. The sample was cooled to a base temperature of 5.6 K and the temperature was regulated using a resistive heater element fixed to the sample mount. As discussed in Section 3.1.3.2, light from the synchrotron is elliptically polarised, with approximately 62% in the horizontal plane and 38% in the vertical plane. A gold-wire-grid polariser, positioned in the optical path before the cryostat, is fixed in the horizontal position to ensure that the light incident on the sample is horizontally polarised. The elliptical nature of the synchrotron radiation limits the ability to use a rotating polariser, since essential signal is lost when in the vertical orientation. To achieve measurements with $\mathbf{E}||\mathbf{c}$ and $\mathbf{E}||\mathbf{a}$, the sample was rotated on the sample mount, with the polarisation fixed in the horizontal plane. The most efficient technique was to complete a temperature survey, taking measurements in one orientation from 5.6–300 K. After that, the sample mount was removed, rotated, remounted and cooled back down to base temperature for the next polarisation survey.

Spectral scans were taken using the Brüker IFS125HR FTIR Michelson interferometer. The interferograms were averaged over 250 scans at a path length of 2 cm, providing a resolution of $0.5\,\mathrm{cm^{-1}}$ (15 GHz). A 75μm Mylar beam splitter was used, providing a usable spectral bandwidth from 0.6 THz to 3.6 THz (20–120 cm^{-1}). The background signal from the setup can be seen in Figure 9.5. Measurements were taken at temperature steps of 5 K from 10 K up to 50 K, with additional measurements at 5.6 K and 7 K. Measurements were then taken at 10 K intervals from 50 K to 300 K, with special focus around 80 K and 200 K. 80 K was chosen as a focus due to a characteristic decrease in the magnetic susceptibility at this temperature, likely related to interactions in the chain dimers [339, 360]. 200 K was chosen at it has been found to be the temperature where charge ordering onsets [343].

The high flux available at the Australian synchrotron assists in shorter scan times as less scans are needed to reduce noise. This is particularly important when dealing with small

and absorbing samples such as the $Sr_{14}Cu_{24}O_{41}$ crystal. This experimental ability allows for high resolution scans and a detailed temperature survey in an acceptable time frame.

9.4   Results

9.4.1   Characteristics and limitations of spectrometer setup

The characteristic transmission spectra of the $Sr_{14}Cu_{24}O_{41}$ sample, with both $\mathbf{E}||\mathbf{a}$ and $\mathbf{E}||\mathbf{c}$ orientations at 5.6 K, are shown in Figure 9.5. As can be seen in the background spectrum, the 75 μm beamsplitter gives usable signal from ∼0.6–3.6 THz. The interference fringes due to Fabry-Perot internal reflections, generate broad minima in the spectra. The two prominent minima appear between 1.2–1.35 THz and 2.52–2.67 THz. This limits the usable signal in these regions. Another broad absorption in the background appears at 2.17 THz and is due to a resonance absorption in the polyethylene windows used in the helium cryostat. Both orientations are considerably absorbing. Nevertheless, there is still adequate signal in the region to observe features in the sample spectra. As can be seen in Figure 9.5, the spectra in each polarisation are distinctly different, demonstrating considerable optical anisotropy with a number of distinct absorption features. Such anisotropy reflects the low-dimensionality of the material. Furthermore, a clear loss of signal is observed above 3.6 THz for either orientation which is not a result of the beam splitter minima. This suggests conductive properties at higher energies.

9.4.2   Transmittance spectra

Taking the ratio of the sample spectrum with the background gives the transmittance as seen in Figure 9.6. Three representative temperatures for each polarisation are displayed, demonstrating the general temperature dependence of the transmittance over this spectral range. The low signal at the first beamsplitter minimum produces a noise artefact centred on 1.29 THz and forces an omission of that portion of the spectrum. The periodic fringes superimposed on each spectrum are attributed to Fabry-Perot interference within the crystal.
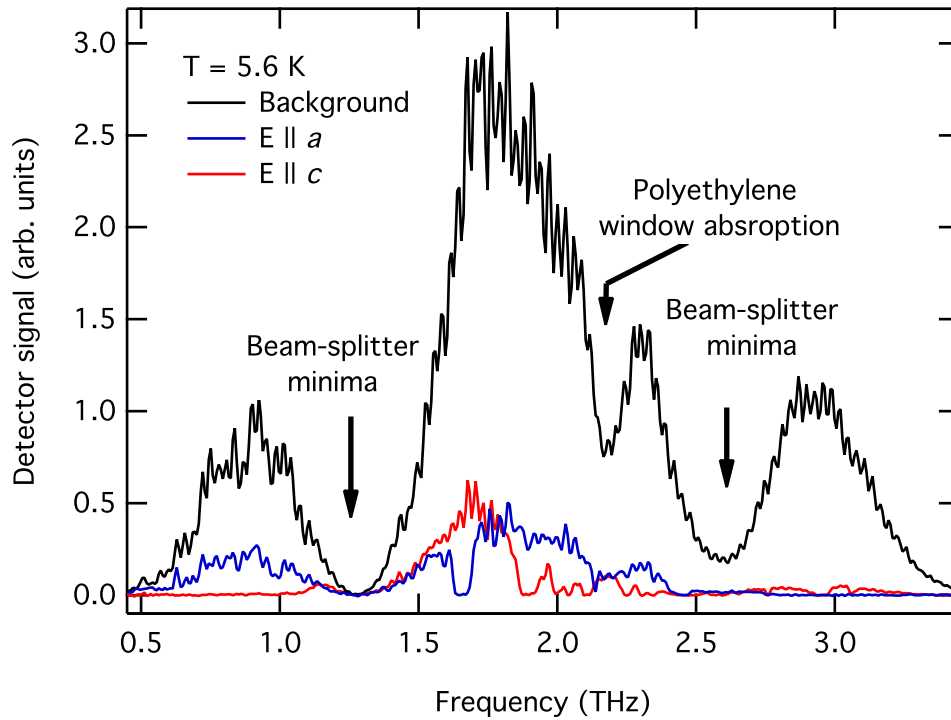
FIGURE 9.5: Characteristic transmission spectra of the background and sample at different orientations. Experimentally limiting features include spectral bandwidth, beam-splitter minima and sample absorption.

The two panels highlight the highly anisotropic nature of the material. With $\mathbf{E}||\mathbf{a}$, the $\mathbf{E}$ field is parallel to the rungs of the ladders and perpendicular to the chains, while the $\mathbf{H}$ field is parallel to the legs of the ladders and to the chains. Immediately, it is possible to draw conclusions about the different conductive nature of the directions along and perpendicular to, the ladders and chains.

At low temperature both orientations feature a high number of strongly absorbing excitation features. For now it is worth mentioning that the resonant features most likely do not represent spin-wave excitations. This is reasoned in two comments:

1. The frequencies of spin-wave excitations in antiferromagnetic materials tend to be in the region $\leq 1\,$THz due to the energies responsible for the spin coupling. The measurements shown here are all generally above 1 THz.

2. While short range antiferromagnetic order is observed in $Sr_{14}Cu_{24}O_{41}$, spin waves are excitations in the long range order of the magnetic sublattice. Therefore no

spin-waves states should exist in $Sr_{14}Cu_{24}O_{41}$.

The absorption features therefore likely have a range of origins. With that being said, the short range ordering does form a gapped state which can be excited optically [358]. So it is possible that some of the features do have magnetic origin but these are not spin waves.

9.4.2.1 Electric field parallel to ladder rungs (E||a)

In Figure 9.6 (a), at 5.6 K for **E**||**a**, 5 distinct absorption features are identifiable at 1.65 THz, 1.92 THz, 2.13 THz and 2.46 THz. There is a general trend in the transmission starting at ∼30% at 0.6 THz and falling to ∼5% by 2.7 THz. Above 2.7 THz the transmittance falls to zero indicating a conductive band edge. This is consistent with optical conductivity measurements that show a high density of peaks in conductivity above 3 THz ($100\,cm^{-1}$) [355, 356, 361–363]. In particular, Ruzicka *et al.* [355] observe a plasma edge in their reflectivity spectra for **E**||**a** above 0.01 eV (10 meV, 2.42 THz, $80\,cm^{-1}$), which corresponds to the roll off seen in the transmission for this orientation.

As the temperature is increased, the roll off is shifted to lower energies. At room temperature, the transmittance at 0.9 THz is half of its value at 5.6 K, with the roll off occurring at ∼1.5 THz. As previously mentioned, $Sr_{14}Cu_{24}O_{41}$ is a self doped system, with a small but finite density of charge carries which contribute to its conductivity, reducing the transmissive properties of the crystal [350]. Naturally, the charge ordering phenomenon localises these charges, increasing resistivity with reducing temperature. The decrease in resistivity as temperature is increased is demonstrated by Akimitsu *et al.* [342] and is consistent with the reduction in transmission. However, the occurrence of a plasma edge in this orientation is an interesting result. The low dimensionality of the ladder/chain system should largely confine the motion of the charge carries in one dimension, parallel to the ladder/chain lengths. Interchain charge-carrier transfer in similar one dimensional materials (the Bechgaard salts [364]), is quantified by a single-electron transfer integral (t_a) and offers an interesting comparison with the one-dimensional nature of the chains and ladders in the $Sr_{14}Cu_{24}O_{41}$ system. Specifically the interchain electron transfer in the Bechgaard salts was defined by an energy gap E_{gap} in the order of $100\,cm^{-1}$ (∼3 THz).

Optical frequencies above this energy produced a constant optical conductivity related to the metallic properties induced by the charge motion.

9.4.2.2 Electric field parallel to ladder legs (E||c)

For **E**||**c** (Figure 9.6 (b)) at 5.6 K, multiple absorption bands can be seen between 1.8 THz and 3.0 THz. At energies below 1.05 THz, the transmission is zero indicating high absorption. Between 1.05 THz and 1.2 THz, the transmission increases rapidly to ~30%, falling to ~10% by 1.8 THz, above which the spectrum is dominated by absorption bands. The highly absorbing region below 1.05 THz is likely a section of the Reststrahlen band stretching from 0.39 THz up to 1.05 THz as reported by Thorsmølle *et al.* [38]. Above 3 THz, as in the **E**||**a** orientation, the spectrum is dominated by a series of conductive bands due to either disorder induced localisation of carriers or pinned charge-density waves [355, 356]. In this orientation, the motion of charge carriers is less impeded since conduction is channelled down the chains and ladder legs. The fact that transmission occurs through the sample in this orientation at all results from the temperature dependent charge ordering.

As Figure 9.6 (b) shows, at a base temperature of 5.6 K there is transmission of around 10-30%. As the sample is heated, the transmission drops rapidly falling to zero by 170 K. This is consistent with the temperature dependence of the charge ordering in the chains [343]. As the temperature is increased, thermal disruptions break the localised ordering and the charge carriers are free to move along the chains and ladders. By ~200 K the charge ordering is completely annealed. With motion permitted along the chains and ladders (unlike for the **E**||**a** orientation), the material becomes metallic with Drude like behaviour along this direction and the broadband transmittance naturally falls to zero. Observing the 5.6 K spectrum of Figure 9.6 (b), the plasma edge roll-off at higher frequencies is obscured by the noise of the beamsplitter artefact. Nevertheless, referring back to Figure 9.5 one can see that for **E**||**c**, transmission has certainly fallen to zero above 3.6 THz.
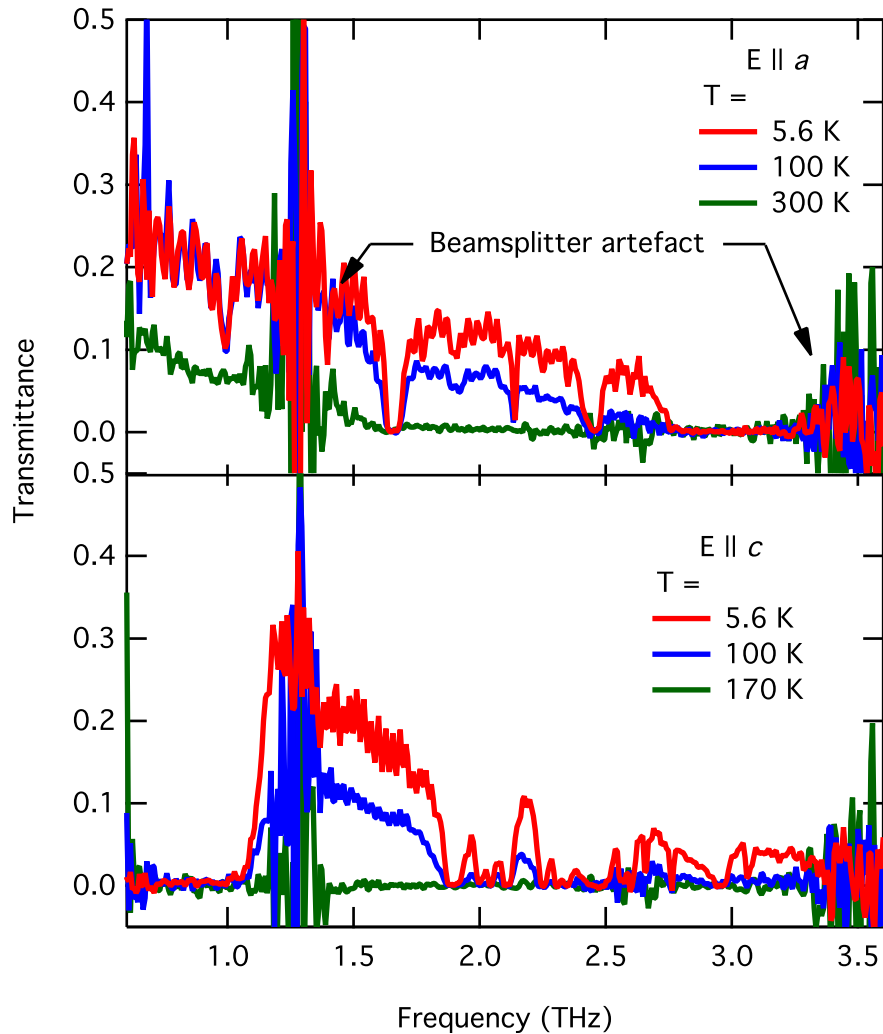
FIGURE 9.6: Comparison of the transmittance for $\mathbf{E}||\mathbf{a}$ and $\mathbf{E}||\mathbf{c}$ at 5.6 K, 100 K, 170 K ($\mathbf{E}||\mathbf{c}$ only) and 300 K ($\mathbf{E}||\mathbf{a}$ only).

9.4.2.3 Complete temperature profile

The complete temperature dependence of each orientation is presented in the colour-map of Figure 9.7. The figure may be used to more clearly see the dynamic and anisotropic nature of the transmission in each orientation. One of the notable features includes the shift in the high frequency roll-off for $\mathbf{E}||\mathbf{a}$ with increasing temperature. The different energies for when the plasma edge occurs in each orientation is a remarkable result considering this relates to energies in which the localised charges are freed by thermal excitations in the chains and ladders. In particular, at low temperature the roll-off for $\mathbf{E}||\mathbf{a}$ corresponds precisely with the sharp absorption line in $\mathbf{E}||\mathbf{c}$ at 2.76 THz. This energy is equivalent to
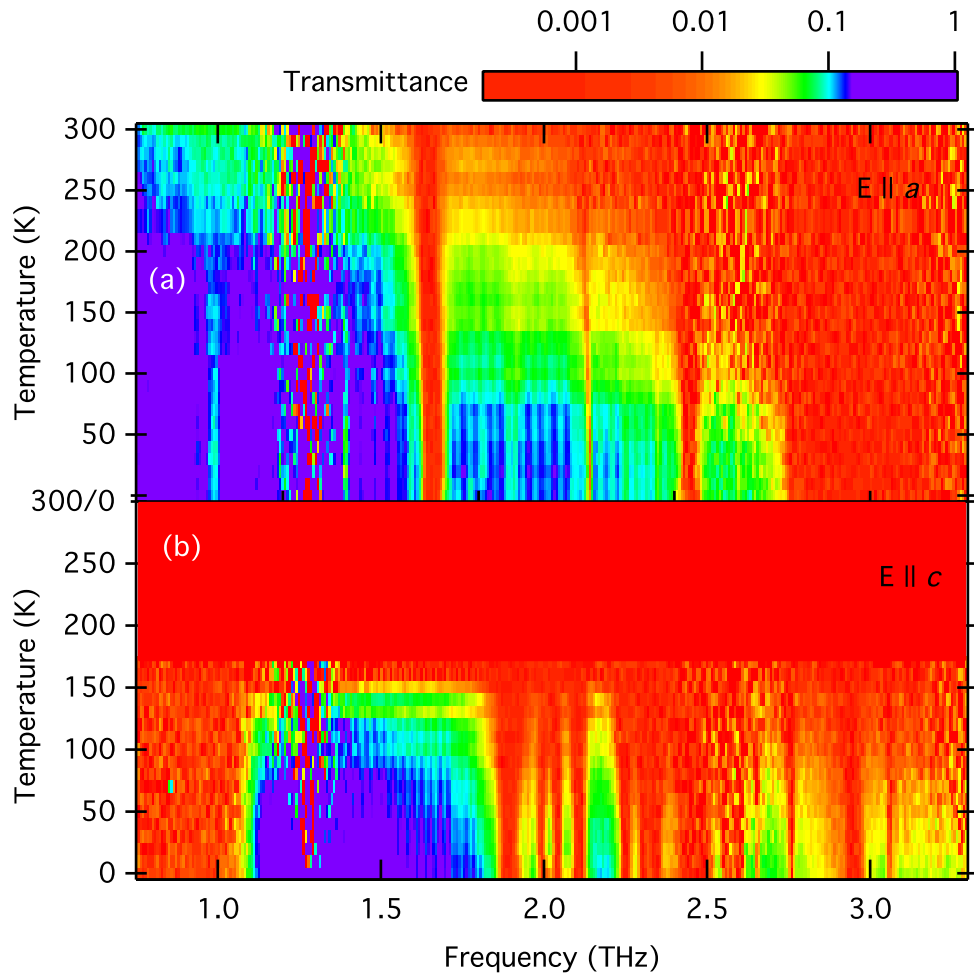
FIGURE 9.7: Colour map of temperature dependence of transmittance in $\mathbf{E}||\mathbf{a}$ (a) and $\mathbf{E}||\mathbf{c}$ (b) orientations. Data above 170 K in (b) was not measured as no signal was obtained. Here the data is represented as by a plain red shaded rectangle

11.4 meV, which is consistent with spin-dimer triplet excitations observed using inelastic neutron scattering [336, 347].

While the plasma edge remains at a constant frequency ($\sim$2.76 THz) at low temperatures, by $\sim$80 K the edge rapidly begins to shift to lower frequencies with increasing temperature. This is indicative of a phase transition centred around 80 K and could be related to the inter chain interactions. Other notable features include the abrupt insulator-metallic transition for $\mathbf{E}||\mathbf{c}$ above 150 K discussed above. The appearance of certain absorption peaks below 200 K is consistent with the charge ordering transition temperature. The subtle temperature dependence of peak position, width and spectral strength, is discussed further in Section 9.4.3.

A frequency-band slice of 6 data points from Figure 9.7, centred on 1.5 THz, is taken and averaged at each temperature. Plotting the value against the corresponding temperature gives a general indication of the transmittance dependence on temperature in each orientation. The result is displayed in Figure 9.8.

The data is fit well by a 3rd degree polynomial, suggesting that the transmittance has a T^2 temperature dependence. Since the transmittance is indicative of the conductive properties, this matches the non-linear dependence in resistivity reported by Akimitsu *et al.* who enlist the variable range hopping mechanism as an explanation [342]. From this relationship it is possible to draw conclusions about the temperature dependence of the charge ordering process and transport properties in $Sr_{14}Cu_{24}O_{41}$. For example, the most rapid change in transmittance occurs above 100 K consistent with the development of the charge ordering process. Judging from Figure 9.8, the charge ordering first occurs around 200 K when transmission in the $\mathbf{E}||\mathbf{c}$ orientation becomes non zero. The rapid increase in conductivity below this temperature suggests that charge ordering is not fully developed until ~50–80 K where the temperature dependence then begins to flatten off. Below this temperature the Zhang-Rice singlet states should be stabilised. Interestingly, at low temperatures ($<$20 K) the $\mathbf{E}||\mathbf{c}$ orientation transmits more than the $\mathbf{E}||\mathbf{a}$ orientation over this frequency span. This suggests that the charge ordered state has a considerable effect on the dielectric properties in each crystal direction.

While the d-wave coupling in the Zhang-Rice singlet states is related to the d-wave interactions considered responsible for HTS, the short range antiferromagnetic magnetic ordering of the Zhang-Rice singlets is a competing state for superconductivity [328]. Conductivity measurements of the doped compound $Sr_{14-x}Ca_xCu_{24}O_{41}$ show similar temperatures for charge ordering [342]. However, the superconductive states only occur at high doping concentrations, very low temperatures and large external pressures. This evidence suggests that the combination of these properties acts to saturate the conduction band with charge carriers that break the highly stabilised Zhang-Rice singlet state potentially forming the superconductive state. Further investigations into this effect is certainly worth pursuing, with recent results suggesting that the increased presence of holes on the ladders acts to reduce Coulomb repulsion of neighbouring magnetic ions encouraging hole pairing [353].
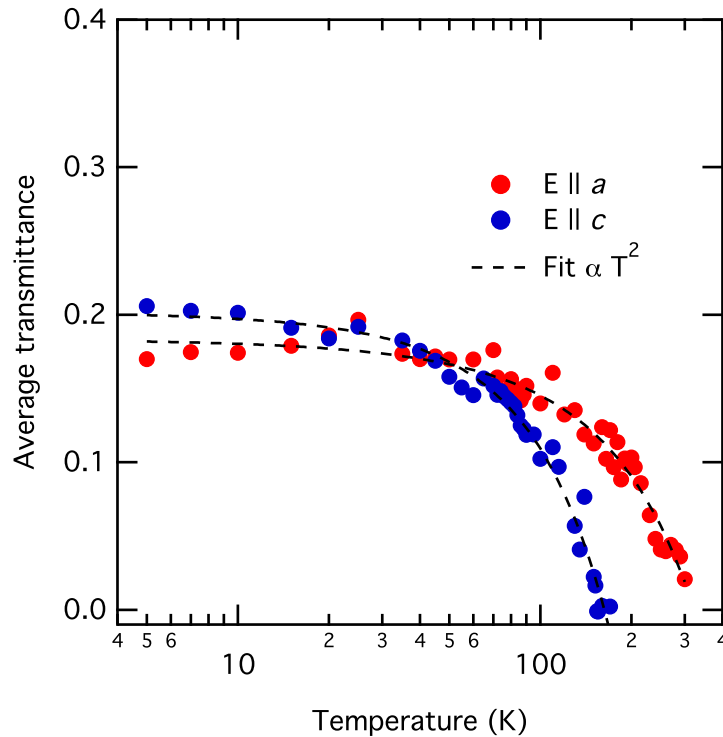
FIGURE 9.8: Temperature dependence of transmittance at 1.5 THz in both the **E**||**a** and **E**||**c** orientations.

9.4.3 Discrete excitations

The details of the absorption features in $Sr_{14}Cu_{24}O_{41}$ are obtained by fitting mathematical peaks to the spectral data. Figure 9.9 shows the results of a multi-peak fitting algorithm implemented in WaveMetrics' Igor Pro software package and applied to the transmittance spectrum of the **E**||**a** orientation at 5.6 K. From this procedure it is possible to identify 6 distinct absorption features labelled A–F. Features in the spectra from 1.20–1.35 THz are neglected due to the beamsplitter artefact. In the **E**||**c** orientation (Figure 9.10), the spectral features are much more dense and the high resolution used is necessary to discern individual excitations. Nevertheless, performing the same analysis on the transmittance data reveals 12 distinct resonance features between 1.8–3.0 THz labelled G–R. The feature designated Q has an asymmetric quality and requires an exponentially modified Gaussian peak to provide a good fit. In both cases, the mathematically equivalent peaks are shown (with the background removed) in panels below the spectral data. Here the relative spectral weight and position is easily compared. The peak parameters for each absorption at
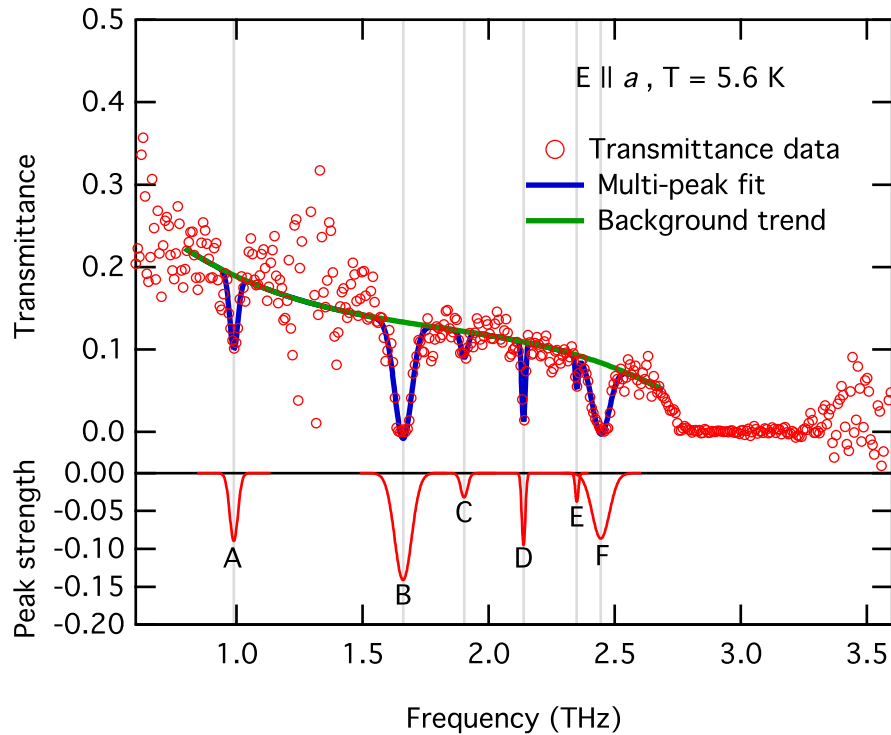
FIGURE 9.9: Multiple peak fit for **E**||**a** with cubic background trend.

5.6 K are summarised in Table 9.1. The amplitude and area values are scaled to the largest absorption feature (Peak G) for easy comparison.

By performing this analysis on both orientations for each of the spectra at different temperatures, the temperature dependence of the absorption peak properties can be observed. The fitting analysis allows for the determination of the peak position in the frequency domain, the peak amplitude, area and full width at half maximum (FWHM). The results are shown in Figures 9.11 and 9.12. At the scale of Figures 9.11 (a) and (b), no indication of strong frequency temperature dependence is seen. Closer inspection of each peak (Figures 9.13 and 9.14) does reveal some degree of temperature dependent shift. In particular, peaks B and D show softening as the temperature is increased. Peak C is seen to harden for increasing temperature. Peak A, apart from only appearing below 200 K, does not seem to show any temperature dependent shift. These differences provide information about the forces acting on the resonant feature and will be discussed further when considering peak assignment. The spectral intensity of the absorption lines is represented by considering the area of the fitted peak scaled to the base temperature value for the G
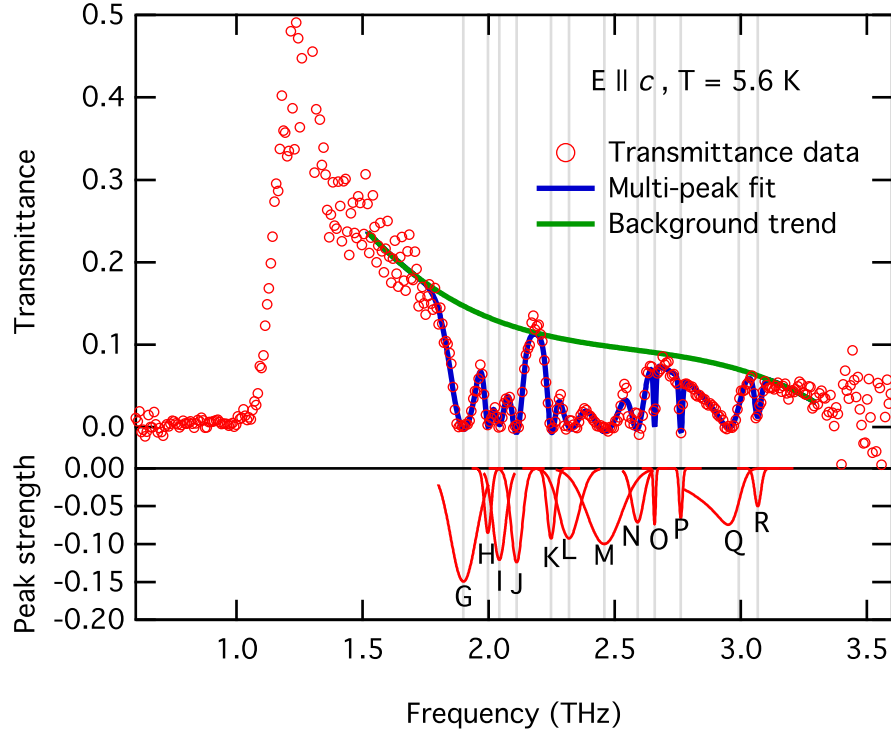
FIGURE 9.10: Multiple peak fit for **E**||**c** with cubic background trend.

TABLE 9.1: Table of fitted peaks in both at **E**||**a** and **E**||**c** orientations at 5.6 K

		Location (THz)	Scaled Amplitude	Scaled Area	FWHM (GHz)
E∥**a**	A	0.988±0.009	0.69±0.31	0.21±0.11	38±21
	B	1.657±0.002	1.15±0.08	0.08±0.05	89±5
	C	1.901±0.005	0.13±0.08	0.05±0.02	30±12
	D	2.137±0.001	0.69±0.08	0.09±0.02	16±3
	E	2.348±0.003	0.31±0.08	0.04±0.02	14±6
	F	2.443±0.003	0.69±0.08	0.46±0.04	82±7
E∥**c**	G	1.899±0.003	1.0±0.08	1.0±0.07	124±8
	H	1.995±0.005	0.62±0.23	0.16±0.09	32±9
	I	2.040±0.005	0.85±0.08	0.37±0.14	56±22
	J	2.109±0.005	0.85±0.08	0.40±0.09	58±10
	K	2.245±0.003	0.62±0.15	0.19±0.07	40±8
	L	2.316±0.008	0.62±0.08	0.51±0.23	102±31
	M	2.457±0.012	0.62±0.08	0.83±0.21	155±40
	N	2.588±0.004	0.46±0.08	0.21±0.07	56±11
	O	2.656±0.001	0.46±0.03	0.04±0.02	10±7
	P	2.760±0.002	0.38±0.08	0.05±0.02	15±4
	Q	2.951	0.46	0.67±0.04	155±68
	R	3.064±0.003	0.31±0.08	0.05±0.02	24±7
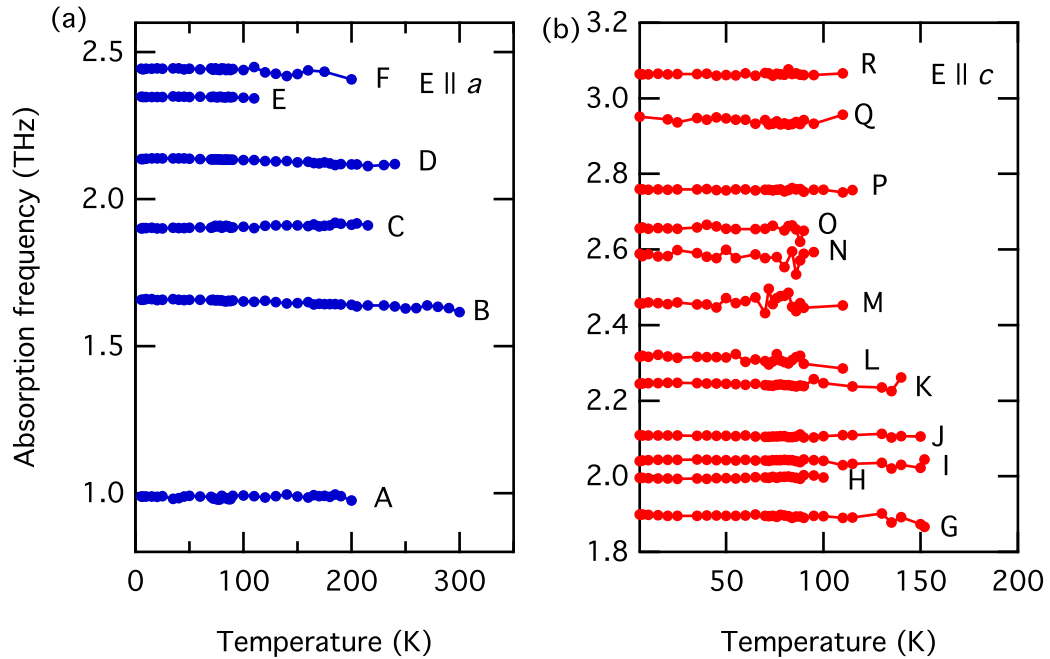
FIGURE 9.11: Temperature dependence of peak position for $\mathbf{E}||\mathbf{a}$ (a) and $\mathbf{E}||\mathbf{c}$ (b)

peak. As Figures 9.12 (c) and (d) indicate, the spectral weight of each peak increases with decreasing temperature. The trend follows a similar dependence as the overall transmittance in Figure 9.8. There is no clear exchange of one peak's spectral weight to another which might be expected if any of the modes were coupled. Some out lying data points are observed where the fitting function could not produce a well defined fit.

9.5 Absorption feature assignment and discussion

As mentioned earlier, the $Sr_{14}Cu_{24}O_{41}$ system features localised magnetic ordering in the form of spin dimers and singlets, which also results in charge ordering. Such transitions are known to have associated resonant features in the form of spin triplet excitations [336, 347, 358, 365] and charge-density waves [38, 356, 362, 366–368]. On top of that, one can expect phonon modes from the individual Sr, Cu and O ions as well as the numerous forms of Cu-O bonding in the chains and ladders [355–357, 361, 369–371]. The layering of the chains, ladders and Sr ions also results in inter-planer interactions which may produce phonon-like resonances [38]. In what follows, a discussion of the excitation peak assignment
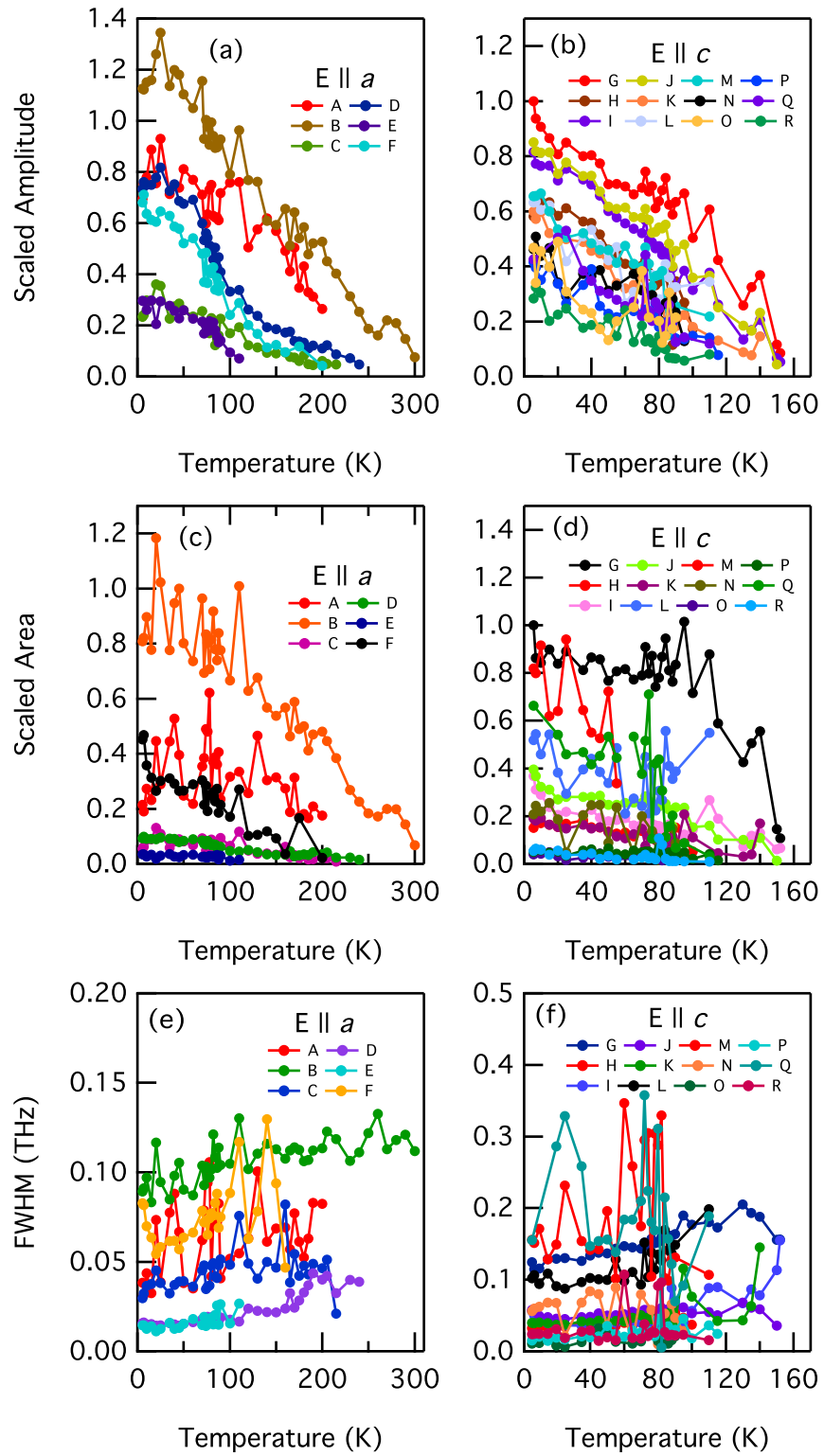
FIGURE 9.12: Temperature dependence of peak (a) $\mathbf{E}||\mathbf{a}$ amplitude. (b) $\mathbf{E}||\mathbf{c}$ amplitude. (c) $\mathbf{E}||\mathbf{a}$ area. (d) $\mathbf{E}||\mathbf{c}$ area. (e) $\mathbf{E}||\mathbf{a}$ FWHM. (f) $\mathbf{E}||\mathbf{c}$ FWHM. The amplitude and area values are scaled to the $5.6\,\mathrm{K}$ value of the G peak.
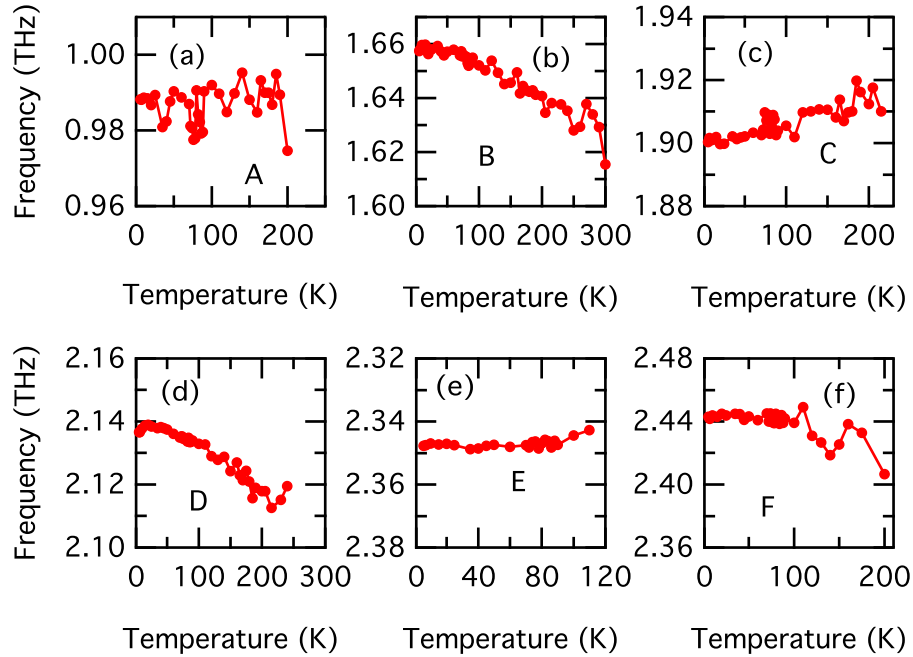
FIGURE 9.13: Zoomed-in temperature dependence of individual mode position for $\mathbf{E}||\mathbf{a}$

is given on each of the possible excitations mentioned above. Cases are often presented for and against each physical origin. This involves stating why a particular mechanism may be responsible for an excitation and discussing evidence that both supports and is contradictory to a possible assignment. Finally, a table is presented with the most likely assignments based on the discussion.

9.5.0.1 Low lying optical phonons

The incommensurate nature of the layering in $Sr_{14}Cu_{24}O_{41}$ produces a large unit cell, consisting of four formula units with 316 atoms in total [357]. Therefore a very large number of optically active modes due to the immense number of atoms in each unit cell is expected. Popović *et al.* report that, considering this, factor-group-analysis (FGA) of $Sr_{14}Cu_{24}O_{41}$ gives a representation consisting of 948 Raman and infrared active modes. However, treating the system as an ideal structure with two Cu-O sublattices of $Fmmm$ space group, reduces the number considerably, to 12 Raman active modes showing good agreement with experiment [369]. A more thorough approach undertaken by Popović *et al.*, is to separate the chains and ladders in to two different space groups, with the ladder
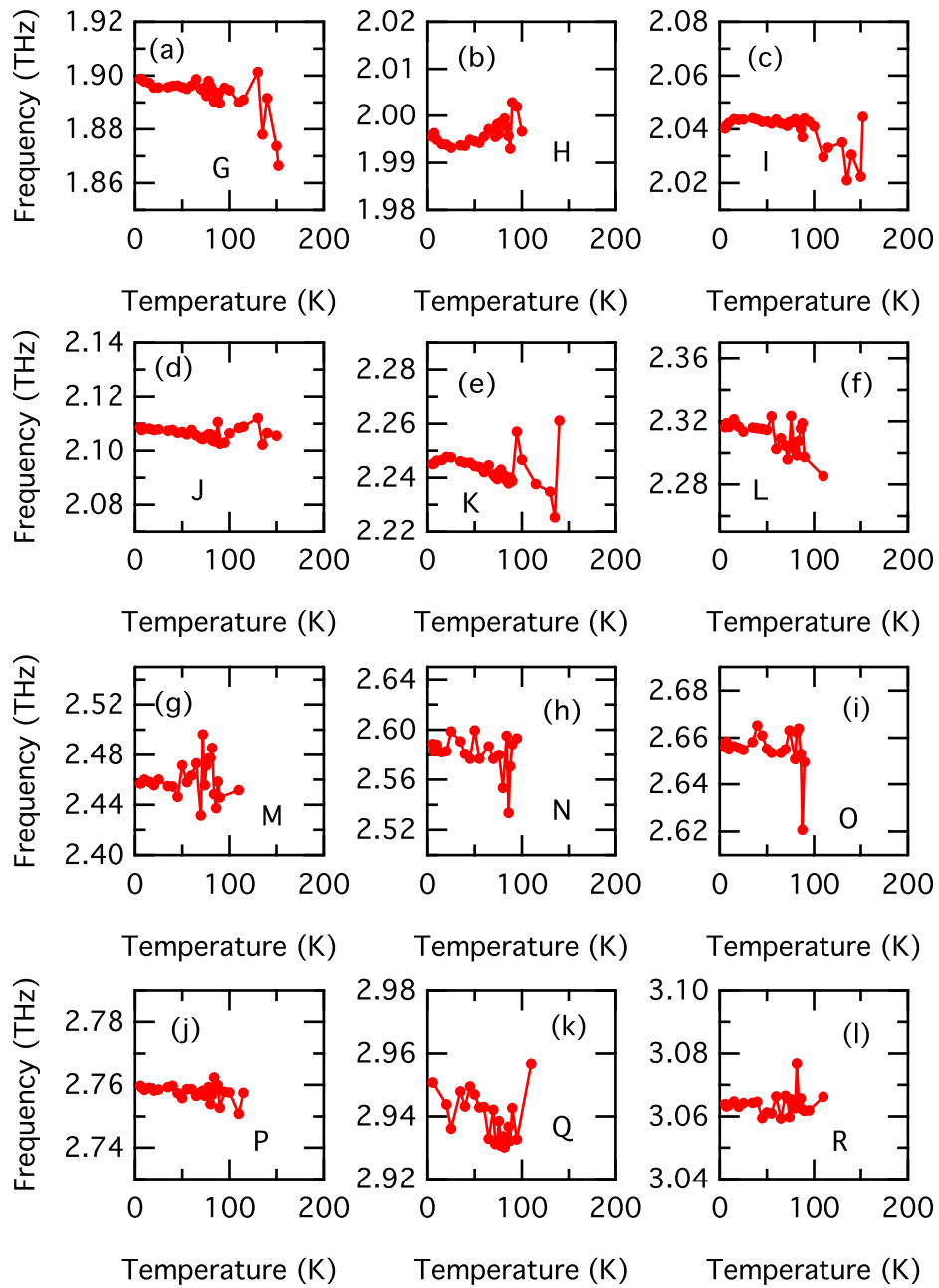
FIGURE 9.14: Zoomed-in temperature dependence of individual mode position for **E**||**c**

being a *Fmmn* space group and the chains being *Amma*. This method predicts close to 40 modes.

In these cases, assignment is achieved by comparison with existing studies on simplified systems with similar properties. Such systems include the Cu-O double layers in $SrCuO_2$ [372] and $YBa_2Cu_4O_8$ [373], as well as copper oxide squares present in CuO [374] and CuGeO [375]. These appear in the Cu-O chains of $Sr_{14}Cu_{24}O_{41}$ when the copper oxide squares form common edges [357]. Such an approach gives rather good agreement with assignment of the low frequency translational modes of the Sr, Cu and O ions at frequencies of 7.38 THz, 9.02 THz and 16.3–17.4 THz respectively. Based on these studies, the main features of the optical phonon spectrum, including the various stretching and breathing modes of the Cu-O bonds, exist between 3 THz to 21 THz. This is also supported by far-infrared reflection measurements [356]. Popović *et al.* suggest that all modes above 21 THz are in fact either second-order combinations (over-tones) of the low-energy phonon modes or two-magnon excitations.

The purpose of this discussion is to suggest that the features observed in the experiments of this chapter ($\lesssim 3$ THz) do not constitute typical optical phonons. While it is possible that the above mentioned optical studies on $Sr_{14}Cu_{24}O_{41}$ have not been sensitive enough in the sub 3 THz region and therefore missed assignment of these lower lying modes, review of literature on related HTS cuprates shows no sign of potentially related modes in that region. Low lying modes at 3.09 THz [376] and 2.49 THz [377] in YBCO compounds are typically attributed to the Ba ion as it is the heaviest ion in the system. Being below Sr in the periodic table, it is expected that its resonant energy is also much lower than that of Sr in $Sr_{14}Cu_{24}O_{41}$, which agrees with the conclusions of [357, 369].

However, calculations of chain-bending modes in Y-Ba-Cu-0 1:2:3 compounds, have given frequencies as low as 2.4 THz [373] and could be responsible for some of the features seen in the presented spectra. In a similar fashion, lattice-dynamics calculations in the HTS compound, $SrCuO_2$, predict the presence of a low-frequency B_{1g} mode at $\sim$2.3 THz [372]. In the calculation, all nearest all nearest Sr, O_{Sr}, Cu, and O_{Cu} atoms vibrate in-phase along a specific crystal axis. The process is explained by considering the crystal structure as one containing infinite $(Cu_2O_4)_n$ molecules with Sr atoms between them. A correlation

is made between the modes of the free infinite $(Cu_2O_4)_n$ molecule and the modes in the crystal. A molecular rotational mode around the molecular axis, features a considerably low frequency and is transformed into a B_{1g} crystal librational mode [372]. The authors note that similarity may be found between this mode and the zone boundary TA mode in the cubic SrO with out-of-phase translations of the adjacent Sr-O layers.

9.5.0.2   Brillouin zone folded phonons

Brillouin zone folding is observed when zone boundary phonon modes appear at the zone centre. For example, as demonstrated in Figure 9.15, an acoustic phonon at the zone centre has zero energy and is therefore optically inactive but hardens towards the zone boundary. When folded back to the zone centre, it may now become optically active. Likewise, an optical phonon that softens towards the zone boundary may appear at a lower energy if the zone is folded back to the zone centre. Typically, the zone folding phenomenon is triggered by a phase transition where the unit cell may double in size, halving the size of the reciprocal lattice, the symmetry points for the initial zone boundary are reflected back to the origin [378]. The phenomenon is well documented in the tetra-methyl-tetra-selena-fulvalene salts which have similar low dimensionality and charge ordering properties to $Sr_{14}Cu_{24}O_{41}$ [378, 379]. In these materials, the phase transition occurs when the tetra-hedral anions order in an alternating fashion along each crystal direction, forming a new unit cell double the original size. The results show a number of phonon modes developing in the 0.6–3 THz vicinity, below the ordering temperature.

Further, zone folding is also observed in pure CuO when it is cooled below its Néel temperature ($T_N = 213$ K), with the onset of long-range magnetic order and strong spin-lattice coupling effectively increasing the unit-cell dimensions [380]. Evidence of similar effects have been noted in $Sr_{14}Cu_{24}O_{41}$, with the appearance of new phonon like Raman modes below the charge ordering temperature (200 K), in the vicinity of 6–18 THz [357]. Modulation of the chains and ladders due to charge ordering has been found even though no rigid modulation of the chains and ladders is present [337], nor is there any first order structural transitions seen in any of the lattice constants [352]. However, no soft modes are observed in the spectra shown here.
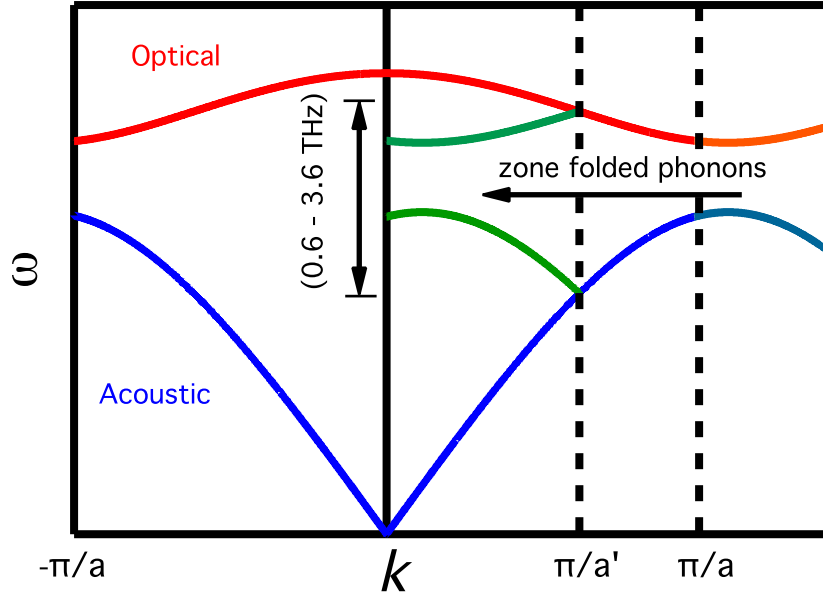
FIGURE 9.15: Diagram of zone folding effect in phonon dispersion. A transition may cause lattice parameter a to increase to a' where $a' > a$. A new zone boundary is created reflecting symmetries back to zone centre.

Charge ordering in the rare earth alkaline manganite $La_{1-x}Ca_xMnO_3$, is accompanied by a lattice superstructure which leads to zone folded phonons around 1.5 THz [381]. In $CuGeO_3$, the spin-Peierls phase transition, where a lattice distortion that occurs together with the formation of a spin-singlet ground state and the opening of an energy gap in the magnetic excitation spectrum, is known to produce zone folding [382]. The resulting deformation of the lattice is driven by the magnetic energy gain when the antiferromagnetic ions in the one-dimensional CuO_2 chains form dimerised pairs. In such cases folded phonons are also seen around 1.5 THz. In $Sr_{14}Cu_{24}O_{41}$ both the charge ordering and dimerisation on the chains and ladders are a closely linked phenomenon that constitute a second order transition. Therefore, one does not expect to see any strong structural change, rather the charge ordering and accompanying spin dimers will lock into regularly ordered positions in chains and ladders. The incommensurate nature of the chains and ladders with $10c_{ch}$ $\simeq 7c_{ld}$, will generate some translation symmetry breaking along the chains and ladders leading to a so called super structure. Certain symmetries can reflect back to the zone centre and therefore folded phonons are a likely outcome.

However, it is difficult to confirm whether the phonon-like features observed in these

spectra are due to zone-folded phonons without direct comparison to zone boundary measurements of the phonon dispersions using inelastic neutron scattering. Presently, no such experiments have been undertaken. Observing the appearance of potential zone folded phonons with changing temperature is also difficult for two reasons. Firstly, in the case of modes D, E and F, it is difficult to determine whether the appearance of the mode is associated with the zone folding phenomenon, or whether the mode becomes obscured by the plasma edge as it shifts to lower frequencies upon heating. This is especially true for all of the modes observed in the $\mathbf{E}||\mathbf{c}$ orientation, which is completely opaque due to conductive properties above the supposed zone folding transition. This would be consistent with the charge ordering transition. Secondly, mode A is observed to appear below T_{co} but in a frequency range that is transparent at room temperature. This is consistent with the onset of a zone folded phonon. However, it is possible to observe a feature related to a direct excitation of the charge ordered or spin dimer state. In fact, as will be discussed later, the energy of this mode is consistent with a magnetic peak observed in INS spectra [336].

In regards to folded optical phonons, the lack of disappearing counterpart modes at higher energies in both Raman [357] and infrared [355, 356] studies would suggest that the modes seen here cannot be zone folded optical modes. This is because it is expected that the modes at higher energies, which become the new zone folded modes, should disappear upon the transition. However, many of the features observed in Figure 9.7 are very sharp and weak and may not have been detected by other studies using lower resolution and sensitivity. Concerning folded acoustic modes, some studies on the phonon dispersion of related HTS cuprates [383, 384] do show zone boundary acoustic phonons with energies less than 3 THz. Such features could also be evident in $Sr_{14}Cu_{24}O_{41}$ and observed here as zone folded acoustic phonons. However, as is suggested by Thorsmølle *et al.* with $c \simeq 27.5\,\text{Å}$ and the sound velocity $v_s \simeq 13\,\text{km/s}$, the lowest energy acoustic phonon should have a frequency of approximately.

$$f = v_s/\lambda = 13 \times 10^3\,\text{ms}^{-1}/27.5 \times 10^{-10}\,\text{m} \simeq 4.7 \times 10^{12}\,\text{s}^{-1}, \qquad (9.3)$$

giving an equivalent mode at 4.7 THz. This implies that none of the features in the spectra presented here are a result of acoustic phonons. However, this calculation is still

rather approximate. With certainty, mode B which can be observed right through the charge ordering transition, must not be the result of a super structure forming below the transition creating a zone folded phonon and so an alternative explanation seems necessary.

9.5.0.3   Gapped sliding acoustic phonons

A final assignment of phononic origin involves the relative motion of the chains and ladders themselves. As far back as 1978, predictions were made concerning the existence of new normal modes of oscillation in ionic materials with incommensurate layers that have the ability to slip past each other [385]. These 'sliding' modes correspond to sliding of one sublattice relative to the other, with similar dynamics to the sliding motion in density wave systems [38]. In uncharged systems, the sliding modes have continuous symmetry in their motion with zero energy cost and the modes are therefore gapless at the zone centre [386]. However, for ionic crystals which feature long range Coulomb forces, displacement of the ions from their equilibrium positions will create net charges and electric fields that will oppose these displacements [387]. Analogous to a plasma frequency oscillation with conduction electrons moving relative to an ionic lattice, the restoring Coulomb forces for sliding ionic layers cost energy to excite and will induce a gap in the modes (see Figure 9.16).

Even though original calculations demonstrated through the structure factor that the phonon spectrum should be observable in neutron-scattering experiments [385], it wasn't until very recently that unambiguous experimental evidence of the sliding modes was claimed [38]. Indeed, the recent discovery of the sliding modes was accomplished using THz spectroscopy and Raman techniques in the frequency range 0.3–1 THz on the $Sr_{14}Cu_{24}O_{41}$ system. The two incommensurate subsystems of one-dimensional Cu_2O_3 ladders and CuO_2 chains in $Sr_{14}Cu_{24}O_{41}$ offers an ideal environment for the sliding modes [38]. Thorsmølle *et al.* identify one Raman and two infrared active modes at 5 K with frequencies of 0.36 THz, 0.38 THz and 0.25 THz respectively. Each of the modes shows considerable temperature dependence, either softening or hardening over ∼60 GHz from 300 K, with the lower frequency infrared mode only appearing below 100 K, far below the charge ordering transition. Little attention is given to the spectroscopic region above

1 THz, with only low resolution data shown. Therefore, the high resolution features observed in the spectra shown here, are not resolved. The above argument relating the sound velocity to zone boundary acoustic mode energies above 3 THz, is used to suggest that the modes are not zone folded phonons.

Applying the gap equation established by Theodoru [387], Thorsmølle *et al.* find a value of 0.88 THz for the higher frequency infrared mode assigned to out of phase oscillations of the chains and ladders. The almost $3\times$ difference in their experiment and calculation could suggest that indeed this mode is possibly more associated with the features observed in the $\mathbf{E}||\mathbf{c}$ spectra shown here. While it is tempting to associate mode A in $\mathbf{E}||\mathbf{a}$ orientation to this mode, it should be remembered that the equation established by Theodoru refers to sliding chains. In fact, Theodoru states that for polarisation perpendicular to the chain, the usual branches of optical and acoustical phonons should exist [385]. While this may be true for uncoupled ladders and chains, in $Sr_{14}Cu_{24}O_{41}$ it is possible to consider that for $\mathbf{E}||\mathbf{a}$, relative sliding of the ladder and chain planes as a hole may induce similar gapped modes.

In the presence of charge carriers, the carriers will follow the lattice motion and screen the interactions reducing the size of the gap [387]. This screening effect could explain the subtle softening in the modes observed as the sample is heated with the most prominent shifts occurring above the charge ordering transition (Figures 9.13 and 9.14). In fact, as noted by Thorsmølle *et al.* with the long-range hole ordering in the chains truly set in below 100 K, restoring Coulomb forces could oppose the out-of-phase oscillation of adjacent chains and ladders leading to the formation of new modes below this temperature. Such effects could explain the onset of modes A, E, H and L–R.

9.5.0.4 Charge-density waves

It has been established that collective charge excitations in the proximity of superconducting transitions may play a significant role in the pairing mechanism leading to HTS [388, 389]. As a result, many of the optical studies on $Sr_{14}Cu_{24}O_{41}$ have focused on the associated dynamics of screened density waves [356, 362, 366, 368]. The charge-density wave (CDW) state in $Sr_{14}Cu_{24}O_{41}$ represents standing waves or periodic modulations in
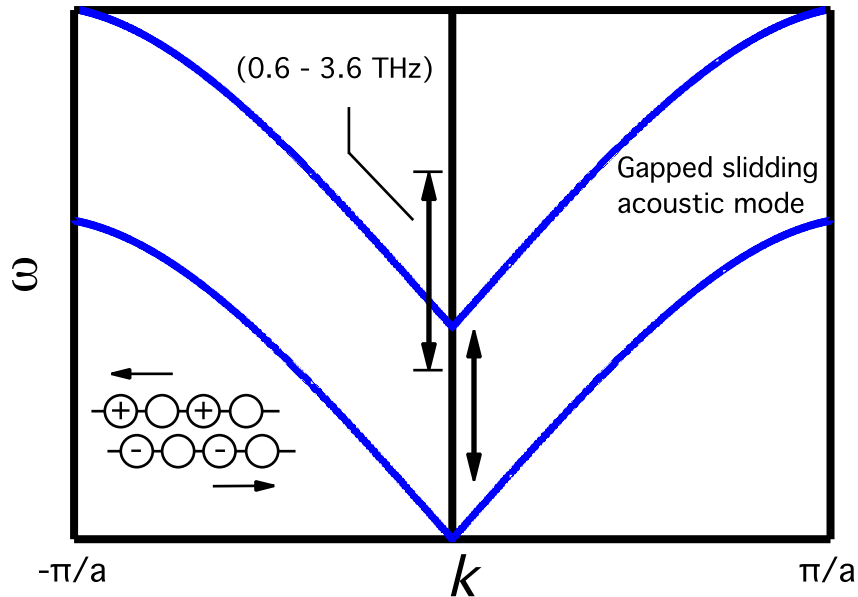
FIGURE 9.16: Diagram of gapped acoustic phonon mode due to relative sliding motion of charged chains.

the density of charge carriers, or holes in this case and is known to form before the onset of charge ordering at around 210 K [389]. The CDW interacts with crystal impurities and other irregularities, such as buckling caused by the incommensurate ratio of ladder and chain cell lengths pinning the CDW to finite frequencies. Therefore, the condensed holes do not participate in the conduction process for small dc electric fields and unlike a plasma or Drude response, which tend to be broadband features, they can appear as sharp resonances lifted into the infrared region [366]. Using polarized inelastic neutron scattering, Lorenzo *et al.* have shown that a CDW forms on the ladders of $Sr_{14}Cu_{24}O_{41}$ below 210 K [390]. The energy of the CDW was measured as 32.5 meV or 7.86 THz. The results also suggest strong electronic coupling between the ladders and chains which could pin CDWs on the chains at lower energies. Therefore, the possibility remains that at least some of the features observed in these spectra, could be due to pinned CDWs.

It should be noted that carrier dynamics along the *a* direction are impeded by the isolation of the chains and ladders. Osafune *et al.* observe a conductivity pseudo-gap in this orientation which is consistent with the formation of the plasma edge in the spectra shown here [356]. The gap could be pinned due to a modulation in potential provided by the

decoupled chains. For $\mathbf{E}||\mathbf{c}$ a sharp peak is observed, which is assigned to a CDW and is consistent with the onset of the pseudo-gap [356]. In the spectra here, this feature could be observed in mode Q which features an asymmetric Fano-type line shape, consistent with a mode strongly correlated to a charge carrier (or spin) background [391].

In the case of a CDW, strong dependence on temperature should be observed as the system is cooled through the charge ordering temperature, since its dynamics will change substantially when the holes are no longer condensed into their paired state [356]. Only subtle temperature dependence is noted for the observed modes and mode B for example, maintains a strong presence even above the charge ordering temperature, suggesting that it may not be linked to this phenomenon. As with previous infrared reflection measurements at higher energies, observations of the effects of Ca doping on the observed modes should reveal some details as to whether the features are due to charge carrier dynamics or phonon modes [356]. Ca doping has the effect of reducing the spacing between neighbouring planes of ladders and chains prompting the transfer of holes from the chains to the ladders increasing the conductive properties. The doping should therefore have little effect on the phonon modes but greatly affect the CDW dynamics. In the experiments detailed here, samples of $Sr_{14-x}Ca_xCu_{24}O_{41}$ with Ca concentrations of $x = 7$ and $x = 11$ were also measured. However the conductive properties appeared too high even at low temperature to observe any THz transmission in either orientation.

9.5.0.5   Singlet-triplet and other magnetic excitations

As detailed in Section 9.2, the chains and ladders of $Sr_{14}Cu_{24}O_{41}$ feature strongly correlated localised spin ordering in the form of dimerised singlet states, particularly at low temperatures. It has been predicted by theory and observed experimentally, that a diverse spectrum of possible magnetic excitations exists. The magnetic spectrum is of considerable interest due to its association with 'd-wave' pairing in HTS and potential for magnetic heat transport in a non conducting material [392].

The absence of true long range magnetic ordering inhibits the formation of ferromagnetic or antiferromagnetic spin waves. However, collective excitations in the dimers from the singlet state ($\uparrow\downarrow$) to the triplet state ($\uparrow\uparrow$, $\downarrow\uparrow$ or $\downarrow\downarrow$) are allowed and this constitutes the

energy of the spin gap. With the net spin of the singlet state $S = 0$, magnetic dipole transitions between singlet and triplet states are forbidden providing no coupling through the **H** field component of the THz photon [393]. Similarly, the **E** field component cannot directly couple to a spin system. However, when considering spin-phonon coupling, which can lead to an antisymmetric Dzyaloshinsky-Moriya (DM) interaction mixing the singlet-triplet states, it is possible for the **E** field to excite the triplet states [394]. In this mechanism, the **E** field couples to a phonon mode that lowers the symmetry of the lattice generating the antisymmetric DM interaction which couples singlet and triplet states [358]. This mechanism has been successful in explaining observed electric dipole transitions in $SrCu_2(BO_3)_2$ [393, 394] and α'-NaV_2O_5 [395] as well as in $Sr_{14}Cu_{24}O_{41}$ where Hüvonen *et al.* identify two triplet states at 2.33 THz and 2.63 THz. The **E**-field polarisation plays an important role in the excitation of these states, with the dynamic DM vector **D** perpendicular to **E**. In this case in the **E**||**a** orientation, an intradimer dynamic DM interaction is created along the c axis and with **E**||**c**, the intradimer dynamic DM interaction along the a axis must occur across neighbouring chains and ladders. Evidence of interchain dimerisation has been shown [365] and so an intradimer dynamic DM interaction across the chains is a possibility.

Referring back to the spectra of Figure 9.9, with **E**||**a**, here the concern is with intradimer interactions along the chains and legs of the ladders. While the spin gaps observed in the ladder dimer states have been shown to have much higher energies in the region of 35 meV or 8 THz [348], these are associated with the ladder rungs which have higher exchange coupling [328]. The interaction along the ladder legs is considered much lower and could lead to spin gaps in the 10 meV or 2 THz range. Mode A, which forms below the onset of charge ordering and is therefore related to the formation of spin dimers, is a strong candidate for such an excitation. A report by Eccleston *et al.* using INS on powdered samples of $Sr_{14}Cu_{24}O_{41}$, located a clear magnetic peak at $\sim$4 meV (0.97 THz) [336]. which is consistent with the energy of mode A at 0.99 THz. Magnetic peaks at this energy have not been identified in subsequent INS measurements on single crystals [346, 347, 396] and this is perhaps because these studies focused on the dimerisation along the ladders with appropriate scattering vectors for its geometry.

The powdered and single crystal studies were in agreement with identifying magnetic

peaks around 10 meV (2.4 THz), which were attributed to the spin dimer spin gap of the chains. These energies are consistent with modes E and F and far-infrared measurements performed by Hüvonen *et al.*, as mentioned above [358]. Splitting of the magnetic peak upon cooling was attributed to the development of two-dimensional properties as the interchain dimer interactions took hold [347]. Such splitting could explain the broad nature of mode F, as well as its unmatched frequency compared to the work of Hüvonen *et al.* (2.63 THz compared to 2.43 THz for mode F). The work of Hüvonen *et al.* was also limited to energies above 2.1 THz with orientations of $\mathbf{E}||\mathbf{a}$ and $\mathbf{E}||\mathbf{b}$ and so did not detect any of the modes observed here below this frequency or in the $\mathbf{E}||\mathbf{c}$ geometry.

The electric dipole coupling mechanism, as discussed above, relies on spin-phonon coupling to lower the symmetry of the lattice, invoking the DM interaction. Therefore, a local phonon should be present to facilitate this interaction. Hüvonen *et al.* note that they were unable to identify such a phonon and it is possible that mode B could be the required excitation. Mode B (at 1.65 THz) bears a striking resemblance to a strong absorption peak seen in $SrCu_2(BO_3)_2$ at 1.56 THz [393, 394]. The 1.56 THz mode in $SrCu_2(BO_3)_2$ is reported to loose intensity in strong magnetic fields (above 8 T), which could be a sign of phonon coupling to the magnetic lattice. However, Rõõm *et al.* use this property to argue against the feature being of phonon origin and state that the magnetic field effect more likely attributes it to two simultaneous triplet excitations [393]. The lack of such a feature in INS measurements of $Sr_{14}Cu_{24}O_{41}$ however does not agree with this scenario.

As stated earlier and also discussed by Rõõm *et al.*, the lack of a transition temperature for this ambiguous mode makes it unlikely to be a zone folded phonon, but its energy is consistent with the sliding gapped modes previously mentioned. $SrCu_2(BO_3)_2$ is a two-dimensional layered structure, so such a mode would require relative sliding of the $CuBO_3$ planes. Since the mode appears in the $\mathbf{E}||\mathbf{a}$ orientation in $Sr_{14}Cu_{24}O_{41}$, a decent argument that in this case it would require relative sliding of the planes of chains and ladders could be made. Under high magnetic fields the dimer network would likely become considerably disrupted to allow increased charge carrier motion adding to a screening of the plane sliding and weakening the mode, which could explain the magnetic field effect on the mode. Through this argument it is possible that mode B is the same mode observed at 1.56 THz in $SrCu_2(BO_3)_2$ and is the phonon responsible for the electric dipole excitation

of the triplet states in $Sr_{14}Cu_{24}O_{41}$ for $\mathbf{E}||\mathbf{a}$. Weak resonances at $1.29\,\mathrm{THz}$, $2.07\,\mathrm{THz}$ and $2.52\,\mathrm{THz}$ are also observed in $SrCu_2(BO_3)_2$ and are attributed to singlet resonances, which could be equivalent to some of the other modes observed here in both $\mathbf{E}||\mathbf{a}$ and $\mathbf{E}||\mathbf{c}$ orientations.

The spectra of Figure 9.10 features $\mathbf{E}||\mathbf{c}$, producing the DM interaction in the a axis and here it is expected that the electric dipole couples to interchain and interladder dimers. As mentioned earlier, INS measurements reveal magnetic peaks around $10\,\mathrm{meV}$ ($2.42\,\mathrm{THz}$) attributed to two-dimensional magnetic interactions across the chains [347], which could be assigned to any of the modes from M to P in the spectra. The high resolution of the spectroscopy presented here allows the observation of the fine structure and it is possible that these details are missed in the low resolution available to INS measurements. In other words, there could be a number of triplet transitions here in close proximity to each other. The $2.33\,\mathrm{THz}$ triplet excitation observed in the $\mathbf{E}||\mathbf{b}$ orientation of Hüvonen *et al.* matches that of mode L here. Hüvonen *et al.* attribute this mode to a zone folded acoustic triplet with reference to the dispersion relation of chain dimers determined using INS measurements [347, 365]. In this orientation, mode G is the most likely candidate for the spin-phonon coupling required to excite the triplet states, based on its proximity and resemblance to mode B, which suggests that they could be of similar origin.

To truly identify and better understand the magnetic features of the spectra in both Figures 9.9 and 9.10, a series of measurements under applied magnetic fields is required. Such measurements were performed by Hüvonen *et al.* and the results showed clear splitting of the ($\uparrow\uparrow$) and ($\downarrow\downarrow$) triplet states with the orientation of B_{ext} and the $\mathbf{E}$ field polarisations revealing the selection rules for the DM interaction singlet-triplet state mixing [358].

9.5.1   Table of possible assignments

Considering all of the arguments presented above, some suggestions for the assignments of absorption features in $Sr_{14}Cu_{24}O_{41}$ are given in Table 9.2.

TABLE 9.2: Table of suggested excitation assignments for $Sr_{14}Cu_{24}O_{41}$ in the spectra region of $\sim$1–3 THz.

		Possible assignment	Reasoning
E∥a	A	Spin triplet	Peak develops below charge ordering and spin dimmer formation ($<$200 K). Is consistent with INS magnetic peak in Reference [336].
	B	Phonon (low-lying optical or gapped acoustic)	Strongly absorbing and present at room temperature. Slight hardening at low temperatures.
	C	Phonon (gapped acoustic) or CDW	Mode appears below 200 K. Is very weak and softens at low temperatures. Could be isotropic component of G but has different temperature dependence. Might be isotropic component of H.
	D	Phonon (low-lying optical or gapped acoustic)	Forms before onset of charge ordering. Has strong absorption and similar temperature dependence to B.
	E	Spin triplet	Peak develops below 200 K and agrees with spin triplet in Reference [358].
	F	Spin triplet or phonon	Peak develops below 200 K. Frequency is close to spin triplet in Reference [358] but not exact. Peak is very broad and isotropic with M.
E∥c	G	Anisotropic shift of B	Identical to B with slight shift in frequency.
	H	Anisotropic shift of C	Weak absorbing with similar frequency and temperature dependence to C.
	I	Phonon (zone folded or gapped acoustic)	Strongly absorbing with similar temperature dependence to B. Not in energy range of INS spin triplet excitations [347].
	J	Phonon (zone folded or gapped acoustic)	See reasoning for I.
	K	Phonon (zone folded or gapped acoustic)	See reasoning for I.
	L	Phonon (zone folded or gapped acoustic)	See reasoning for I.
	M	Isotropic with F	See F.
	N	Phonon (zone folded or gapped acoustic or spin triplet)	Similar properties to I but in range of magnetic INS excitations.
	O	Spin triplet	Sharp but weak absorption in range of magnetic INS excitations.
	P	Spin triplet	See reasoning for O. Also same frequency as conduction band edge in **E∥a**.
	Q	CDW	Strongly absorbing Fano-type line shape consistent with strong correlations to a charge carrier background as in Reference [391].
	R	Spin triplet or optical phonon	Is in range of magnetic INS excitations but also approaching optical phonon frequencies.

9.6   Conclusions

In summary, the quantum spin ladder $Sr_{14}Cu_{24}O_{41}$ is an excellent candidate for spectroscopic studies at THz frequencies, with the prospects of revealing important details about low dimensional magnetism and high temperature superconductivity. In particular, it has been shown that transmission through the *ac* plane is highly anisotropic. At room temperature, with the **E** field parallel to the ladder legs and chains, the free motion of charge carriers absorbs radiation blocking transmission. When **E** is perpendicular to the ladder legs and chains, the inhibited charge flow allows transmission. The system therefore acts very much like a broad spectrum polariser although would not likely be useful for such applications as the transmission percentage in the transparent orientation is still low ($\sim$10%).

As the material temperature is reduced the transmissive properties improve. By 200 K weak antiferromagnetic coupling of neighbouring spins on the chains and ladders facilitates the formations of Zhang-Rice singlet states. These dimerised spin states seek to lower the system energy by inhibiting the flow of charge carrying holes. This process is known as charge ordering where free holes are bound to specific locations on the crystal lattice. By 150 K this effect allows transmission of THz radiation parallel to the ladder legs and chains. Below 100 K the charge ordered state appears fully formed with marginal increases in transmission with further reduced temperature.

The relatively high temperature onset of charge ordering compared to the low temperatures required for superconductivity in doped compounds, suggests that the superconducting state is formed when the highly stable charge ordered state is broken by a high density of charge carriers. The two states are therefore intimately related and further study of the charge dynamics in $Sr_{14}Cu_{24}O_{41}$ and its Ca doped compounds at THz frequencies could prove important for a better understanding of HTS physics.

Related to the low dimensional anisotropic properties, a high density of absorption features are present in the spectra from $\sim$1–3 THz. At 5.6 K, 6 excitations are observed in the **E**||**a** orientation while 12 are observed in the **E**||**c** orientation. There are many possibilities for the origins of the observed excitations. Such possibilities include, very low frequency

optical phonons; zone-folded phonons due to the large crystal lattice and charge ordering phases transition; gapped acoustic phonons from relative motion of chains and ladders; charge-density waves due to pinned charges in the charge ordered state and spin triplet excitations of the locally ordered spin dimers. Analysis of the frequency position and temperature dependence of the excitations gave some insight into their nature. With reference to complementary work in the literature, many of the modes were tentatively assigned to one of the above possibilities.

Further study of the $Sr_{14}Cu_{24}O_{41}$ system is certainly required to unambiguously assign the excitations. The application of spectroscopy with external magnetic fields should help to identify excitations with magnetic origin. While inelastic neutron scattering has measured the spin-dimer dispersion, which agrees with theory and some of the excitations observed in this study, a neutron study on the phonon dispersion is still required to lock down the dynamics of zone boundary phonons. Such experiments would likely reveal the if zone fold did occur or not.

Chapter 10

Conclusion

10.1 Summary

The results presented in this thesis have covered a broad range of measurements using THz spectroscopy generally focused on the study of magnetic materials. Hopefully it has been evident that such fundamental spectroscopic investigations have revealed intriguing details about the underlying physical interactions that give these novel materials their unique properties. Naturally, one may ask: What is the point? To this, I respond that at the beginning of the 20th century, the development of quantum mechanics lead to a revolution in the fundamental research of materials and their properties. By the 1950s, based on fundamental work performed by countless scientists around the world, the first integrated circuits were developed. Sixty or so more years of research, allowing for improvements and miniaturisation, and modern society is now graced with a powerful and interconnected network of devices that has transformed the daily lives of many. In principle, it can be seen that the applications of fundamental research are often not recognised and until many years after that research is performed.

Humankind's desire for fundamental understanding and ever improving technology has not ceased. The next generation of technology will incorporate the emerging technologies of photonics and spintronics with existing electronic functionality. This will require

considerable developments in the current understandings and properties of candidate materials. The novel materials studied and physical properties probed in this thesis represent foundational work towards this goal.

Specifically, in Chapter 5 continuous wave THz spectroscopy is presented as an effective method for characterising the optical and electronic properties of materials. In this case the semiconductor ZnTe was studied. It is shown that a statistical analysis is required in the fitting of nonlinear functions with respect to the fitted parameters. This concept is not well established in condensed matter physics research. Chapter 6 established two spin-wave excitations in the layered geometrically frustrated compound, $Cu_3Bi(SeO_3)_2O_2Cl$. Magnetic field dependent measurement allowed for the extraction of the magnetic parameters such as anisotropy and the gyromagnetic factor. The occurrence of a metamagnetic transition, where the antiferromagnetically ordered spins transition into a ferromagnetic state with the application of a weak external field, is particularly interesting. In the absence of the external field the low frequency spin wave is seen to weaken and broaden considerably. It is reasoned that it may split into many weak excitations at zero applied field due to a larger number of spin sublattices. The possibility of magneto-electric coupling through the frustrated structure presents an appealing possibility of controlling the number of spin excitation states with electric fields.

In Chapter 7, a far more robust spin system is studied featuring canted antiferromagnetism. Namely, the rare earth orthoferrite $NdFeO_3$. Terahertz spectroscopy is used to observe the dynamics of two orthogonal spin waves across a broad temperature range. A novel technique is used to visualise the spin moment precession as a result of each spin-wave oscillation. Polarisation sensitive measurements are required to isolate each mode. This also allows the identification of a spin reorientation where the spin sublattice rotates its orientation through 90 degrees over a finite temperature span. The results are combined with complementary inelastic neutron scattering measurements in Chapter 8. The neutron scattering confirms the spin-wave origin as acoustic antiferromagnetic oscillations under the influence of a strong temperature variable magnetic anisotropy. This information is used in conjunction with theoretical spin-wave equations to extract the temperature dependent anisotropy along two principal crystallographic axes. Analysis of the magnetic

anisotropies reveals information about the microscopic magnetic interactions. The technique presents the possibility of better understanding how to design magnetic materials with certain desired properties.

Finally, the low dimensional quantum spin ladder $Sr_{14}Cu_{24}O_{41}$ was studied in Chapter 9. Not only does $Sr_{14}Cu_{24}O_{41}$ offer the possibility of probing low dimensional spin systems, but it also features high-temperature superconductor-like properties. Highly anisotropic transmittance reveals the rather contrasting transport properties of polarisations perpendicular and parallel to the ladder and chain structures within the material. At low temperatures the transport properties are influenced strongly by localised antiferromageitc spin coupling, a competing but related state to high-temperature superconductivity. A diverse range of excitations are observed and tentatively assigned to unconventional phonon modes, charge-density waves and spin triplet excitations. The $Sr_{14}Cu_{24}O_{41}$ compound presents an excellent model for better understanding the properties of high-temperature superconductivity and its relation to spin and lattice coupled states.

10.2 Future outlook

Following the results that have been presented in this thesis, are the foundations for further investigation. A list of potential developments and experiments that would expand on the physics probed in this study follows:

- Inelastic neutron scattering of the spin-wave excitations in $Cu_3Bi(SeO_3)_2O_2Cl$.

    – Obtaining a full dispersion relation for the spin waves should reveal more details about their relation to the frustrated spin lattice as well as providing information relating to potential spin lattice coupling.

- Refinement of the models for contribution to the magnetic anisotropy in $NdFeO_3$.

    – Including Nd-Fe coupling in the analysis of the anisotropy energies could provide better information relating to the precise mechanism for the spin reorientation.

- Magnetic field dependent spectroscopy of the F-mode splitting.

– Performing spectroscopy with well defined external magnetic fields on a single crystal of $NdFeO_3$ cut to a low index plane could help to define the selection rules for its excitation. An understanding of this may help reveal the origin of the anticrossing splitting.

- Magnetic field dependent spectroscopy of $Sr_{14}Cu_{24}O_{41}$.

  – Field dependent measurements will reveal the excitations that have magnetic origin.

- High pressure spectroscopy of $Sr_{14}Cu_{24}O_{41}$.

  – Performing spectroscopy on $Sr_{14}Cu_{24}O_{41}$ under pressures of up to $5\,GPa$ would provide information about the excitations and charge transport properties in a state similar to that of the superconducting state in the doped compounds.

- Inelastic neutron scatting of the phonon modes in $Sr_{14}Cu_{24}O_{41}$.

  – Obtaining the full dispersion relation for the phonon modes in $Sr_{14}Cu_{24}O_{41}$ will reveal if any zone folding occurs and where the zone boundary energies are expected.

- Nonlinear studies of quantum spin systems.

  – Growing interest in the nonlinear properties of quantum spin systems provides interesting potential for further studies under high-power THz fields. The developments of coherent synchrotron radiation and free electron laser sources means that such measurements are now becoming feasible.

Appendix A

Transmittance and boostrap error analysis source code

The fitting procedure and error analysis implemented in Chapter 5 used a unique statistical approach. The details of this method are discussed within that chapter. Here the source code used to perform the analysis is presented. The code was implemented in the WaveMetrics: Igor Pro software package and is written in a native coding language for that package. The code is commented to assist in its readability. The comment tag in the native igor programming language is '`//`'. In general the executed code is justified to the left of the page with the comments kept to the right. In some cases the executed code will span an entire line. In these cases, the comment is given above the line of code it explains.

The analysis uses two separate coded functions to execute. The first is the transmittance function as defined by Equation 5.11. The second is the statistical fitting procedure which calls the transmittance function when performing each fit.

A.1   Transmittance fitting function

```
#pragma rtGlobals=1                        // Use modern global access method.

Function Transmittance( w, x ) : FitFunc   // Name of function (: Fitfunc allows it to be called by igor fitting function).

Wave w                                     // Declare that w is a wave (of the fitting parameters).
Variable x                                 // Declare that x is a variable.
```

```
Variable c                                     // Declare c as a variable.
c = 2.99792458E-4                              // Set c to speed of light (m/ps).


Variable eps1                                  // Declare dielectric function variables epsilon 1 and 2
Variable eps2


                                               // Define the real and imaginary parts of the dielectric function,
                                               // with fitting parameters from wave w.

eps1 = w[1]
     + (((w[3])^2*((w[3])^2-(2*pi*x)^2)*(w[2]-w[1]))/(((w[3])^2-(2*pi*x)^2)^2+(2*pi*x)^2*w[5]^2))
     - (w[1]*(w[4])^2)/((2*pi*x)^2+w[6]^2)


eps2 = (2*pi*x*w[1]*(w[4])^2*w[6])/((2*pi*x)^4+(2*pi*x)^2*w[6]^2)
     - (w[5]*2*pi*x*(w[3])^2*(w[2]-w[1]))/(((w[3])^2-(2*pi*x)^2)^2+(2*pi*x)^2*w[5]^2)


Variable n                                     // Declare complex refractive index.
Variable k
n = (((eps1^2+eps2^2)^0.5+eps1)/2)^0.5         // Set real and imaginary parts of refractive index
k = (((eps1^2+eps2^2)^0.5-eps1)/2)^0.5         // based on dielectric constant.


Variable r                                     // Declare reflectance and phase.
Variable Phase
r = (((1-n)^2+k^2)/((1+n)^2+k^2))^0.5          // Set reflectance and phase based on real and imaginary refractive index.
phase = atan(2*k/(1-n^2-k^2))


Variable Trans                                 // Declare transmittance function.


                                               // Set transmittance as a function of the above variables.

Trans= exp(-2*((2*pi*x)/c)*k*w[0])*((1-r^2)^2+4*r^2*(sin(phase))^2)
      /((1-r^2*exp(-2*((2*pi*x)/c)*k*w[0]))^2+4*r^2*exp(-2*((2*pi*x)/c)*k*w[0])*(sin(((2*pi*x)/c)*n*w[0]+phase))^2)


return Trans                                   // Update value of 'Trans'.


end                                            // End function.
```

A.2   Bootstrap fitting procedure

```
#pragma rtGlobals=1                                    // Use modern global access method.


function testFit(Ywave, Xwave, Mask)                   // Name of function (input names for Ywave etc...).


Wave Ywave; Wave Xwave; Wave Mask                      // Declare Ywave, XWave and W_coef as waves.


Wave res_synthdata, w_resampled                        // Declare waves for residual and resampled data.
Wave M_Covar, CorMat                                   // Declare waves for covarience and cross-correlation parameters.


                                                       // Make waves for array of well fitted parameters.


make /O /N=(loopNum+1)  permInfValues, perm0Values, omegaTValues, omegapValues, g1Values, g2Values


                                                       // Make waves for arrays of correlation coeffecients.


make /O /N=(loopNum+1)  corCoef12, corCoef13, corCoef14, corCoef15, corCoef16
make /O /N=(loopNum+1)  corCoef23, corCoef24, corCoef25, corCoef26
```

```
make /O /N=(loopNum+1)  corCoef34, corCoef35, corCoef36
make /O /N=(loopNum+1)  corCoef45, corCoef46
make /O /N=(loopNum+1)  corCoef56


Make/O/D/N=7 W_coef                                          // Make waves for parameter fits,
duplicate/O Ywave, Fit_Y, SynthData, res_synthdata, Fit_SynthData, Synth    // synthetic and residual data,
duplicate/O W_coef params                                   // initial parameter sttings.


variable i, j, loopNum                                      // Declare loop variables.


i = 0                                                       // Set loop variables.
j = 0
loopNum = 1000


Variable d, perm_inf, perm_0, omega_T, omega_p, g1, g2      // Declare fitting variables.


d = 0.0009908                                              // Set fixed sample thickness in metres.
perm_inf = 7                                               // Set initial fitting parameter values.
perm_0 = 10
omega_T = 33
omega_p = 0.6
g1 = 3
g2 = 9
W_coef[0] = params                                         // Store initial fitting parameter values in wave.


variable V_FitError, V_FitQuitReason                       // Declare fit-error indication variables.


                                                           // Execute built-in igor fitting function
                                                           // calling 'Transmittance' function on real data.


FuncFit/H="1000000"/M=2/NTHR=0 /Q Transmittance W_coef  Ywave /X=Xwave /D=Fit_Y /M=Mask


Params = W_coef                                            // Update parameter values based on new fit.
res_synthdata = Ywave - Fit_Y                             // Set residual dataset.
Synth = Transmittance(W_coef, Xwave)                      // Call theoretical 'Transmittance' function
                                                           // and create transmittance wave based on new fitted parameters.


do                                                        // Start bootstrap loop.


V_FitError=0                                              // Set initial fit-error indication variables.
V_FitQuitReason = 0


statsresample /N=(numpnts(synthData)) res_synthdata       // Sample with replacement from resdiual dataset.
synthData = Synth+w_resampled                            // Create synthetic transmittance data
                                                           // from theoretical fit and resampled residuals.
W_coef = Params                                          // Update parameter values based on new fit.


                                                           // Execute built-in igor fitting function
                                                           // calling 'Transmittance' function on synthetic data.


FuncFit/H="1000000"/M=2/NTHR=0 /Q Transmittance W_coef  synthData /X=Xwave /D=Fit_SynthData


Duplicate/O M_Covar, CorMat                              // Create correlation matix.
CorMat = M_Covar[p][q]/sqrt(M_Covar[p][p]*M_Covar[q][q])  // Calculate correlation matrix.


                                                           // If fit is good based on convergence
                                                           // and realistic parameter values,
                                                           // proceed to next line of code,
                                                           // otherwise proceed to next 'else' command.
```

```
if (V_FitError == 0 && V_FitQuitReason != 3 &&  W_coef[1]<W_coef[2] && W_coef[1]>0 && W_coef[2]>0
                    && W_coef[3]>0 && W_coef[3]<150 && W_coef[4]>0 && W_coef[5]>0 && W_coef[6]>0)


permInfValues[i] = W_coef[1]                               // Store fitted values in statistical arrays.
perm0Values[i] = W_coef[2]
omegaTValues[i] = W_coef[3]
omegapValues[i] = W_coef[4]
g1Values[i] = W_coef[5]
g2Values[i] = W_coef[6]


corCoef12[i] = abs(CorMat[1][2])                          // Store the correlation coeffecients in statistical arrays.
corCoef13[i] = abs(CorMat[1][3])
corCoef14[i] = abs(CorMat[1][4])
corCoef15[i] = abs(CorMat[1][5])
corCoef16[i] = abs(CorMat[1][6])
corCoef23[i] = abs(CorMat[2][3])
corCoef24[i] = abs(CorMat[2][4])
corCoef25[i] = abs(CorMat[2][5])
corCoef26[i] = abs(CorMat[2][6])
corCoef34[i] = abs(CorMat[3][4])
corCoef35[i] = abs(CorMat[3][5])
corCoef36[i] = abs(CorMat[3][6])
corCoef45[i] = abs(CorMat[4][5])
corCoef46[i] = abs(CorMat[4][6])
corCoef56[i] = abs(CorMat[5][6])


i += 1                                                    // Advance loop by one iteration.
print "Good fit!"                                         // Give feedback of well executed fit.
                                                          // OK to return to start of 'do' loop.


else                                                      // If fit was not good, set parameter values back to last good fit.


W_coef[0] = {d, permInfValues[i-1], perm0Values[i-1], omegaTValues[i-1], omegapValues[i-1], g1Values[i-1], g2Values[i-1]}


j += 1                                                    // Advance 'unstable fitting loop' by one integer.
                                                          // OK to return to start of 'do' loop.


                                                          // If 20 unstable fits occur in a row,
                                                          // set parameter values back to values from initial fit.


if(cos(2*pi*j/20) == 1)
W_coef[0] = {d, permInfValues[1], perm0Values[1],omegaTValues[1], omegapValues[1], g1Values[1], g2Values[1]}


endif


print "Bad Fit =["                                        // Give feedback of bad fit.
                                                          // OK to return to start of 'do' loop.
endif


printf "Iteration: %g\r", i                               // Give feedback of iteration number.
printf "Singular Matix error: %g\r", V_FitError           // Give feedback if a singular matix error occured.
printf "Did not converge: %g\r",  V_FitQuitReason         // Give feedback if fit was not able to converge.


while(i <= loopNum)                                       // Check loop number.


end                                                       // End bootstrap program after predefined number of loops.
```

Appendix B

Crystallographic Information Files

The crystal lattice graphics presented for each material studied were generated using the VESTA software package [253]. VESTA is able to convert the crystallographic information in a `.cif` or crystallographic information file into a three-dimensional visualisation. The `.cif` is administered by the International Union of Crystallography (IUCr) and is a standard file format for representing crystallographic information. In this appendix the `.cif` file information is provided for each material studied.

B.1   Zinc telluride (ZnTe)

As defined by Wyckoff [397].

```
================================================================================
Title           Te Zn


Lattice type       F
Space group name   F -4 3 m
Space group number 216
Setting number     1

Lattice parameters

    a        b        c       alpha     beta     gamma
 6.08900  6.08900  6.08900  90.0000  90.0000  90.0000


Unit-cell volume = 225.755308 Å^3


Structure parameters

                     x        y        z       Occ.    B   Site   Sym.
```

```
      1 Zn  Zn       0.00000    0.00000    0.00000    1.000    1.000    4a    -43m
      2 Te  Te       0.25000    0.25000    0.25000    1.000    1.000    4c    -43m
============================================================================
```

B.2   Francisite ($Cu_3Bi(SeO_3)_2O_2Cl$)

As defined by Millet *et al.* [263].

```
============================================================================
Title           Francisite

Lattice type    P
Space group name    P m m n
Space group number  59
Setting number      1 (origin choice 1)

Lattice parameters

   a       b       c     alpha    beta    gamma
 6.35200 9.63259 7.23235 90.0000 90.0000 90.0000

Unit-cell volume = 442.520120 Å^3

Structure parameters

                    x         y         z       Occ.     U    Site   Sym.
      1 Bi  Bi     0.00000   0.00000   0.24101   1.000  0.005   2a    mm2
      2 Se  Se     0.50000   0.19230   0.38953   1.000  0.007   4e    m..
      3 Cu  Cu1    0.25000   0.25000   0.00000   1.000  0.012   4c     -1
      4 Cu  Cu2    0.50000   0.50000   0.20786   1.000  0.011   2a    mm2
      5 Cl  Cl     0.50000   0.00000  -0.14900   1.000  0.032   2b    mm2
      6 O   O1     0.00000   0.13690  -0.00940   1.000  0.007   4e    m..
      7 O   O2     0.29240   0.16650   0.24250   1.000  0.007   8g     1
      8 O   O3     0.50000   0.36450   0.40770   1.000  0.007   4e    m..
============================================================================
```

B.3   Neodymium orthoferrite ($NdFeO_3$)

As defined by Streltsov and Ishizawa [398].

```
============================================================================
Title           Fe1 Nd1 O3

Lattice type    P
Space group name    P b n m
Space group number  62
Setting number      3

Lattice parameters

   a       b       c     alpha    beta    gamma
 5.45040 5.58350 7.76020 90.0000 90.0000 90.0000
```

```
Unit-cell volume = 236.160791 A^3

Structure parameters


                  x          y          z         Occ.     B    Site    Sym.
   1 Fe  Fe1     0.50000    0.00000    0.00000    1.000   1.000   4b      -1
   2 Nd  Nd1     0.00890    0.04850    0.25000    1.000   0.570   4c      .m.
   3 O   O1     -0.09210    0.48100    0.25000    1.000   0.390   4c      .m.
   4 O   O2      0.70840    0.28550    0.04240    1.000   0.370   8d       1
==================================================================================
```

B.4 $Sr_{14}Cu_{24}O_{41}$

Provided through collaboration with G. Deng. Further details can be found in Reference [359].

```
==================================================================================
Title              Ca1 Cu1 O1 Sr1


Lattice type       P
Space group name   P 1
Space group number 1
Setting number     1


Lattice parameters


   a        b        c      alpha    beta    gamma
11.46320 13.40410 27.19000  90.0000  90.0000  90.0000


Unit-cell volume = 4177.849046 Å^3

Structure parameters


                   x          y          z         Occ.     U    Site    Sym.
   1 Cu  Cu2a1     0.25000    0.50000    0.03528    1.000   0.029   1a       1
   2 Cu  Cu2a2     0.25000    0.50000    0.13528    1.000   0.029   1a       1
   3 Cu  Cu2a3     0.25000    0.50000    0.23528    1.000   0.029   1a       1
   4 Cu  Cu2a4     0.25000    0.50000    0.33528    1.000   0.029   1a       1
   5 Cu  Cu2a5     0.25000    0.50000    0.43528    1.000   0.029   1a       1
   6 Cu  Cu2a6     0.25000    0.50000    0.53528    1.000   0.029   1a       1
   7 Cu  Cu2a7     0.25000    0.50000    0.63528    1.000   0.029   1a       1
   8 Cu  Cu2a8     0.25000    0.50000    0.73528    1.000   0.029   1a       1
   9 Cu  Cu2a9     0.25000    0.50000    0.83528    1.000   0.029   1a       1
  10 Cu  Cu2a10    0.25000    0.50000    0.93528    1.000   0.029   1a       1
  11 Cu  Cu2b1     0.25000    0.00000    0.08528    1.000   0.029   1a       1
  12 Cu  Cu2b2     0.25000    0.00000    0.18528    1.000   0.029   1a       1
  13 Cu  Cu2b3     0.25000    0.00000    0.28528    1.000   0.029   1a       1
  14 Cu  Cu2b4     0.25000    0.00000    0.38528    1.000   0.029   1a       1
  15 Cu  Cu2b5     0.25000    0.00000    0.48528    1.000   0.029   1a       1
  16 Cu  Cu2b6     0.25000    0.00000    0.58528    1.000   0.029   1a       1
  17 Cu  Cu2b7     0.25000    0.00000    0.68528    1.000   0.029   1a       1
  18 Cu  Cu2b8     0.25000    0.00000    0.78528    1.000   0.029   1a       1
  19 Cu  Cu2b9     0.25000    0.00000    0.88528    1.000   0.029   1a       1
  20 Cu  Cu2b10    0.25000    0.00000    0.98528    1.000   0.029   1a       1
  21 Cu  Cu2b11    0.25000    1.00000    0.08528    1.000   0.029   1a       1
  22 Cu  Cu2b12    0.25000    1.00000    0.18528    1.000   0.029   1a       1
```

23 Cu	Cu2b13	0.25000	1.00000	0.28528	1.000	0.029	1a	1
24 Cu	Cu2b14	0.25000	1.00000	0.38528	1.000	0.029	1a	1
25 Cu	Cu2b15	0.25000	1.00000	0.48528	1.000	0.029	1a	1
26 Cu	Cu2b16	0.25000	1.00000	0.58528	1.000	0.029	1a	1
27 Cu	Cu2b17	0.25000	1.00000	0.68528	1.000	0.029	1a	1
28 Cu	Cu2b18	0.25000	1.00000	0.78528	1.000	0.029	1a	1
29 Cu	Cu2b19	0.25000	1.00000	0.88528	1.000	0.029	1a	1
30 Cu	Cu2b20	0.25000	1.00000	0.98528	1.000	0.029	1a	1
31 Cu	Cu2c1	0.75000	0.50000	0.06472	1.000	0.029	1a	1
32 Cu	Cu2c2	0.75000	0.50000	0.16472	1.000	0.029	1a	1
33 Cu	Cu2c3	0.75000	0.50000	0.26472	1.000	0.029	1a	1
34 Cu	Cu2c4	0.75000	0.50000	0.36472	1.000	0.029	1a	1
35 Cu	Cu2c5	0.75000	0.50000	0.46472	1.000	0.029	1a	1
36 Cu	Cu2c6	0.75000	0.50000	0.56472	1.000	0.029	1a	1
37 Cu	Cu2c7	0.75000	0.50000	0.66472	1.000	0.029	1a	1
38 Cu	Cu2c8	0.75000	0.50000	0.76472	1.000	0.029	1a	1
39 Cu	Cu2c9	0.75000	0.50000	0.86472	1.000	0.029	1a	1
40 Cu	Cu2c10	0.75000	0.50000	0.96472	1.000	0.029	1a	1
41 Cu	Cu2d1	0.75000	0.00000	0.01472	1.000	0.029	1a	1
42 Cu	Cu2d2	0.75000	0.00000	0.11472	1.000	0.029	1a	1
43 Cu	Cu2d3	0.75000	0.00000	0.21472	1.000	0.029	1a	1
44 Cu	Cu2d4	0.75000	0.00000	0.31472	1.000	0.029	1a	1
45 Cu	Cu2d5	0.75000	0.00000	0.41472	1.000	0.029	1a	1
46 Cu	Cu2d6	0.75000	0.00000	0.51472	1.000	0.029	1a	1
47 Cu	Cu2d7	0.75000	0.00000	0.61472	1.000	0.029	1a	1
48 Cu	Cu2d8	0.75000	0.00000	0.71472	1.000	0.029	1a	1
49 Cu	Cu2d9	0.75000	0.00000	0.81472	1.000	0.029	1a	1
50 Cu	Cu2d10	0.75000	0.00000	0.91472	1.000	0.029	1a	1
51 Cu	Cu2d11	0.75000	1.00000	0.01472	1.000	0.029	1a	1
52 Cu	Cu2d12	0.75000	1.00000	0.11472	1.000	0.029	1a	1
53 Cu	Cu2d13	0.75000	1.00000	0.21472	1.000	0.029	1a	1
54 Cu	Cu2d14	0.75000	1.00000	0.31472	1.000	0.029	1a	1
55 Cu	Cu2d15	0.75000	1.00000	0.41472	1.000	0.029	1a	1
56 Cu	Cu2d16	0.75000	1.00000	0.51472	1.000	0.029	1a	1
57 Cu	Cu2d17	0.75000	1.00000	0.61472	1.000	0.029	1a	1
58 Cu	Cu2d18	0.75000	1.00000	0.71472	1.000	0.029	1a	1
59 Cu	Cu2d19	0.75000	1.00000	0.81472	1.000	0.029	1a	1
60 Cu	Cu2d20	0.75000	1.00000	0.91472	1.000	0.029	1a	1
61 O	O3a1	0.13750	0.51056	0.09310	1.000	0.017	1a	1
62 O	O3a2	0.13750	0.47792	0.19310	1.000	0.017	1a	1
63 O	O3a3	0.13750	0.50692	0.29310	1.000	0.017	1a	1
64 O	O3a4	0.13750	0.51661	0.39310	1.000	0.017	1a	1
65 O	O3a5	0.13750	0.47994	0.49310	1.000	0.017	1a	1
66 O	O3a6	0.13750	0.49927	0.59310	1.000	0.017	1a	1
67 O	O3a7	0.13750	0.52064	0.69310	1.000	0.017	1a	1
68 O	O3a8	0.13750	0.48440	0.79310	1.000	0.017	1a	1
69 O	O3a9	0.13750	0.49171	0.89310	1.000	0.017	1a	1
70 O	O3a10	0.13750	0.52217	0.99310	1.000	0.017	1a	1
71 O	O3b1	0.13750	0.02209	0.04310	1.000	0.017	1a	1
72 O	O3b2	0.13750	0.02140	0.34310	1.000	0.017	1a	1
73 O	O3b3	0.13750	0.01811	0.64310	1.000	0.017	1a	1
74 O	O3b4	0.13750	0.00458	0.74310	1.000	0.017	1a	1
75 O	O3b5	0.13750	0.01262	0.94310	1.000	0.017	1a	1
76 O	O3b6	0.13750	0.98952	0.14310	1.000	0.017	1a	1
77 O	O3b7	0.13750	0.98621	0.24310	1.000	0.017	1a	1
78 O	O3b8	0.13750	0.99686	0.44310	1.000	0.017	1a	1
79 O	O3b9	0.13750	0.98109	0.54310	1.000	0.017	1a	1
80 O	O3b10	0.13750	0.97826	0.84310	1.000	0.017	1a	1
81 O	O3c1	0.36250	0.48944	0.09310	1.000	0.017	1a	1
82 O	O3c2	0.36250	0.52208	0.19310	1.000	0.017	1a	1
83 O	O3c3	0.36250	0.49308	0.29310	1.000	0.017	1a	1

84 O	O3c4	0.36250	0.48339	0.39310	1.000	0.017	1a	1
85 O	O3c5	0.36250	0.52006	0.49310	1.000	0.017	1a	1
86 O	O3c6	0.36250	0.50073	0.59310	1.000	0.017	1a	1
87 O	O3c7	0.36250	0.47936	0.69310	1.000	0.017	1a	1
88 O	O3c8	0.36250	0.51560	0.79310	1.000	0.017	1a	1
89 O	O3c9	0.36250	0.50829	0.89310	1.000	0.017	1a	1
90 O	O3c10	0.36250	0.47783	0.99310	1.000	0.017	1a	1
91 O	O3d1	0.36250	0.01048	0.14310	1.000	0.017	1a	1
92 O	O3d2	0.36250	0.01379	0.24310	1.000	0.017	1a	1
93 O	O3d3	0.36250	0.00314	0.44310	1.000	0.017	1a	1
94 O	O3d4	0.36250	0.01891	0.54310	1.000	0.017	1a	1
95 O	O3d5	0.36250	0.02173	0.84310	1.000	0.017	1a	1
96 O	O3d6	0.36250	0.97791	0.04310	1.000	0.017	1a	1
97 O	O3d7	0.36250	0.97860	0.34310	1.000	0.017	1a	1
98 O	O3d8	0.36250	0.98189	0.64310	1.000	0.017	1a	1
99 O	O3d9	0.36250	0.99542	0.74310	1.000	0.017	1a	1
100 O	O3d10	0.36250	0.98738	0.94310	1.000	0.017	1a	1
101 O	O3e1	0.86250	0.48627	0.00690	1.000	0.017	1a	1
102 O	O3e2	0.86250	0.52142	0.10690	1.000	0.017	1a	1
103 O	O3e3	0.86250	0.49678	0.20690	1.000	0.017	1a	1
104 O	O3e4	0.86250	0.48113	0.30690	1.000	0.017	1a	1
105 O	O3e5	0.86250	0.51816	0.40690	1.000	0.017	1a	1
106 O	O3e6	0.86250	0.50450	0.50690	1.000	0.017	1a	1
107 O	O3e7	0.86250	0.47828	0.60690	1.000	0.017	1a	1
108 O	O3e8	0.86250	0.51269	0.70690	1.000	0.017	1a	1
109 O	O3e9	0.86250	0.51168	0.80690	1.000	0.017	1a	1
110 O	O3e10	0.86250	0.47807	0.90690	1.000	0.017	1a	1
111 O	O3f1	0.86250	0.00700	0.05690	1.000	0.017	1a	1
112 O	O3f2	0.86250	0.01655	0.15690	1.000	0.017	1a	1
113 O	O3f3	0.86250	0.02061	0.45690	1.000	0.017	1a	1
114 O	O3f4	0.86250	0.02216	0.75690	1.000	0.017	1a	1
115 O	O3f5	0.86250	0.97990	0.25690	1.000	0.017	1a	1
116 O	O3f6	0.86250	0.99935	0.35690	1.000	0.017	1a	1
117 O	O3f7	0.86250	0.98434	0.55690	1.000	0.017	1a	1
118 O	O3f8	0.86250	0.99179	0.65690	1.000	0.017	1a	1
119 O	O3f9	0.86250	0.99067	0.85690	1.000	0.017	1a	1
120 O	O3f10	0.86250	0.98522	0.95690	1.000	0.017	1a	1
121 O	O3g1	0.63750	0.51373	0.00690	1.000	0.017	1a	1
122 O	O3g2	0.63750	0.47858	0.10690	1.000	0.017	1a	1
123 O	O3g3	0.63750	0.50323	0.20690	1.000	0.017	1a	1
124 O	O3g4	0.63750	0.51887	0.30690	1.000	0.017	1a	1
125 O	O3g5	0.63750	0.48184	0.40690	1.000	0.017	1a	1
126 O	O3g6	0.63750	0.49550	0.50690	1.000	0.017	1a	1
127 O	O3g7	0.63750	0.52172	0.60690	1.000	0.017	1a	1
128 O	O3g8	0.63750	0.48731	0.70690	1.000	0.017	1a	1
129 O	O3g9	0.63750	0.48832	0.80690	1.000	0.017	1a	1
130 O	O3g10	0.63750	0.52193	0.90690	1.000	0.017	1a	1
131 O	O3h1	0.63750	0.02010	0.25690	1.000	0.017	1a	1
132 O	O3h2	0.63750	0.00065	0.35690	1.000	0.017	1a	1
133 O	O3h3	0.63750	0.01566	0.55690	1.000	0.017	1a	1
134 O	O3h4	0.63750	0.00821	0.65690	1.000	0.017	1a	1
135 O	O3h5	0.63750	0.00933	0.85690	1.000	0.017	1a	1
136 O	O3h6	0.63750	0.01478	0.95690	1.000	0.017	1a	1
137 O	O3h7	0.63750	0.99300	0.05690	1.000	0.017	1a	1
138 O	O3h8	0.63750	0.98345	0.15690	1.000	0.017	1a	1
139 O	O3h9	0.63750	0.97939	0.45690	1.000	0.017	1a	1
140 O	O3h10	0.63750	0.97784	0.75690	1.000	0.017	1a	1
141 Sr	Sr1a1	0.49652	0.37826	0.04248	1.000	-0.001	1a	1
142 Sr	Sr1a2	0.50415	0.37998	0.17528	1.000	-0.001	1a	1
143 Sr	Sr1a3	0.49546	0.37896	0.33615	1.000	-0.001	1a	1
144 Sr	Sr1a4	0.50464	0.37921	0.46630	1.000	-0.001	1a	1

145	Sr	Sr1a5	0.49557	0.37974	0.62783	1.000	-0.001	1a	1
146	Sr	Sr1a6	0.50394	0.37847	0.75936	1.000	-0.001	1a	1
147	Sr	Sr1a7	0.49681	0.38041	0.91756	1.000	-0.001	1a	1
148	Sr	Sr1b1	0.50260	0.87800	0.10498	1.000	-0.001	1a	1
149	Sr	Sr1b2	0.49846	0.88074	0.25803	1.000	-0.001	1a	1
150	Sr	Sr1b3	0.50038	0.87774	0.40066	1.000	-0.001	1a	1
151	Sr	Sr1b4	0.50080	0.88081	0.54587	1.000	-0.001	1a	1
152	Sr	Sr1b5	0.49807	0.87788	0.69649	1.000	-0.001	1a	1
153	Sr	Sr1b6	0.50293	0.88048	0.83406	1.000	-0.001	1a	1
154	Sr	Sr1b7	0.49625	0.87837	0.99148	1.000	-0.001	1a	1
155	Sr	Sr1c1	0.00260	0.38056	0.11391	1.000	-0.001	1a	1
156	Sr	Sr1c2	0.00038	0.38082	0.40197	1.000	-0.001	1a	1
157	Sr	Sr1c3	0.00080	0.37776	0.54862	1.000	-0.001	1a	1
158	Sr	Sr1c4	0.00293	0.37808	0.84415	1.000	-0.001	1a	1
159	Sr	Sr1c5	0.99846	0.37782	0.25273	1.000	-0.001	1a	1
160	Sr	Sr1c6	0.99807	0.38069	0.68986	1.000	-0.001	1a	1
161	Sr	Sr1c7	0.99625	0.38019	0.97859	1.000	-0.001	1a	1
162	Sr	Sr1d1	0.00415	0.87859	0.18955	1.000	-0.001	1a	1
163	Sr	Sr1d2	0.00464	0.87935	0.48225	1.000	-0.001	1a	1
164	Sr	Sr1d3	0.00394	0.88010	0.77292	1.000	-0.001	1a	1
165	Sr	Sr1d4	0.99651	0.88030	0.03049	1.000	-0.001	1a	1
166	Sr	Sr1d5	0.99546	0.87961	0.32054	1.000	-0.001	1a	1
167	Sr	Sr1d6	0.99557	0.87883	0.61259	1.000	-0.001	1a	1
168	Sr	Sr1d7	0.99681	0.87816	0.90658	1.000	-0.001	1a	1
169	Sr	Sr1e1	0.49740	0.61944	0.11391	1.000	-0.001	1a	1
170	Sr	Sr1e2	0.50154	0.62218	0.25273	1.000	-0.001	1a	1
171	Sr	Sr1e3	0.49962	0.61918	0.40197	1.000	-0.001	1a	1
172	Sr	Sr1e4	0.49920	0.62224	0.54862	1.000	-0.001	1a	1
173	Sr	Sr1e5	0.50193	0.61931	0.68986	1.000	-0.001	1a	1
174	Sr	Sr1e6	0.49707	0.62191	0.84415	1.000	-0.001	1a	1
175	Sr	Sr1e7	0.50375	0.61980	0.97859	1.000	-0.001	1a	1
176	Sr	Sr1f1	0.50349	0.11970	0.03049	1.000	-0.001	1a	1
177	Sr	Sr1f2	0.49585	0.12141	0.18955	1.000	-0.001	1a	1
178	Sr	Sr1f3	0.50454	0.12039	0.32054	1.000	-0.001	1a	1
179	Sr	Sr1f4	0.49536	0.12065	0.48225	1.000	-0.001	1a	1
180	Sr	Sr1f5	0.50443	0.12117	0.61259	1.000	-0.001	1a	1
181	Sr	Sr1f6	0.49606	0.11990	0.77292	1.000	-0.001	1a	1
182	Sr	Sr1f7	0.50319	0.12184	0.90658	1.000	-0.001	1a	1
183	Sr	Sr1g1	0.00348	0.62174	0.04248	1.000	-0.001	1a	1
184	Sr	Sr1g2	0.00454	0.62104	0.33615	1.000	-0.001	1a	1
185	Sr	Sr1g3	0.00443	0.62026	0.62783	1.000	-0.001	1a	1
186	Sr	Sr1g4	0.00319	0.61959	0.91756	1.000	-0.001	1a	1
187	Sr	Sr1g5	0.99585	0.62002	0.17528	1.000	-0.001	1a	1
188	Sr	Sr1g6	0.99536	0.62079	0.46630	1.000	-0.001	1a	1
189	Sr	Sr1g7	0.99606	0.62153	0.75936	1.000	-0.001	1a	1
190	Sr	Sr1h1	0.00154	0.11926	0.25803	1.000	-0.001	1a	1
191	Sr	Sr1h2	0.00193	0.12212	0.69649	1.000	-0.001	1a	1
192	Sr	Sr1h3	0.00375	0.12163	0.99148	1.000	-0.001	1a	1
193	Sr	Sr1h4	0.99740	0.12200	0.10498	1.000	-0.001	1a	1
194	Sr	Sr1h5	0.99962	0.12226	0.40066	1.000	-0.001	1a	1
195	Sr	Sr1h6	0.99920	0.11919	0.54587	1.000	-0.001	1a	1
196	Sr	Sr1h7	0.99707	0.11952	0.83406	1.000	-0.001	1a	1
197	Cu	Cu1a1	0.33292	0.25356	0.11269	1.000	0.004	1a	1
198	Cu	Cu1a2	0.33292	0.24794	0.25862	1.000	0.004	1a	1
199	Cu	Cu1a3	0.33292	0.25043	0.40456	1.000	0.004	1a	1
200	Cu	Cu1a4	0.33292	0.25122	0.55049	1.000	0.004	1a	1
201	Cu	Cu1a5	0.33292	0.24720	0.69642	1.000	0.004	1a	1
202	Cu	Cu1a6	0.33292	0.25420	0.84235	1.000	0.004	1a	1
203	Cu	Cu1a7	0.33292	0.24468	0.98828	1.000	0.004	1a	1
204	Cu	Cu1b1	0.33292	0.74504	0.03973	1.000	0.004	1a	1
205	Cu	Cu1b2	0.33292	0.75587	0.18566	1.000	0.004	1a	1

206	Cu	Cu1b3	0.33292	0.74361	0.33159	1.000	0.004	1a	1
207	Cu	Cu1b4	0.33292	0.75650	0.47752	1.000	0.004	1a	1
208	Cu	Cu1b5	0.33292	0.74381	0.62345	1.000	0.004	1a	1
209	Cu	Cu1b6	0.33292	0.75548	0.76938	1.000	0.004	1a	1
210	Cu	Cu1b7	0.33292	0.74559	0.91532	1.000	0.004	1a	1
211	Cu	Cu1c1	0.16708	0.25496	0.03973	1.000	0.004	1a	1
212	Cu	Cu1c2	0.16708	0.24413	0.18566	1.000	0.004	1a	1
213	Cu	Cu1c3	0.16708	0.25639	0.33159	1.000	0.004	1a	1
214	Cu	Cu1c4	0.16708	0.24350	0.47752	1.000	0.004	1a	1
215	Cu	Cu1c5	0.16708	0.25619	0.62345	1.000	0.004	1a	1
216	Cu	Cu1c6	0.16708	0.24452	0.76938	1.000	0.004	1a	1
217	Cu	Cu1c7	0.16708	0.25441	0.91532	1.000	0.004	1a	1
218	Cu	Cu1d1	0.16708	0.74644	0.11269	1.000	0.004	1a	1
219	Cu	Cu1d2	0.16708	0.75206	0.25862	1.000	0.004	1a	1
220	Cu	Cu1d3	0.16708	0.74957	0.40456	1.000	0.004	1a	1
221	Cu	Cu1d4	0.16708	0.74878	0.55049	1.000	0.004	1a	1
222	Cu	Cu1d5	0.16708	0.75280	0.69642	1.000	0.004	1a	1
223	Cu	Cu1d6	0.16708	0.74580	0.84235	1.000	0.004	1a	1
224	Cu	Cu1d7	0.16708	0.75532	0.98828	1.000	0.004	1a	1
225	Cu	Cu1e1	0.66708	0.75482	0.03324	1.000	0.004	1a	1
226	Cu	Cu1e2	0.66708	0.74423	0.17917	1.000	0.004	1a	1
227	Cu	Cu1e3	0.66708	0.75635	0.32510	1.000	0.004	1a	1
228	Cu	Cu1e4	0.66708	0.74349	0.47103	1.000	0.004	1a	1
229	Cu	Cu1e5	0.66708	0.75625	0.61696	1.000	0.004	1a	1
230	Cu	Cu1e6	0.66708	0.74441	0.76290	1.000	0.004	1a	1
231	Cu	Cu1e7	0.66708	0.75455	0.90883	1.000	0.004	1a	1
232	Cu	Cu1f1	0.66708	0.24627	0.10620	1.000	0.004	1a	1
233	Cu	Cu1f2	0.66708	0.25226	0.25214	1.000	0.004	1a	1
234	Cu	Cu1f3	0.66708	0.24936	0.39807	1.000	0.004	1a	1
235	Cu	Cu1f4	0.66708	0.24898	0.54400	1.000	0.004	1a	1
236	Cu	Cu1f5	0.66708	0.25262	0.68993	1.000	0.004	1a	1
237	Cu	Cu1f6	0.66708	0.24596	0.83586	1.000	0.004	1a	1
238	Cu	Cu1f7	0.66708	0.25520	0.98179	1.000	0.004	1a	1
239	Cu	Cu1g1	0.83292	0.75373	0.10620	1.000	0.004	1a	1
240	Cu	Cu1g2	0.83292	0.74774	0.25214	1.000	0.004	1a	1
241	Cu	Cu1g3	0.83292	0.75064	0.39807	1.000	0.004	1a	1
242	Cu	Cu1g4	0.83292	0.75102	0.54400	1.000	0.004	1a	1
243	Cu	Cu1g5	0.83292	0.74738	0.68993	1.000	0.004	1a	1
244	Cu	Cu1g6	0.83292	0.75404	0.83586	1.000	0.004	1a	1
245	Cu	Cu1g7	0.83292	0.74480	0.98179	1.000	0.004	1a	1
246	Cu	Cu1h1	0.83292	0.24518	0.03324	1.000	0.004	1a	1
247	Cu	Cu1h2	0.83292	0.25577	0.17917	1.000	0.004	1a	1
248	Cu	Cu1h3	0.83292	0.24365	0.32510	1.000	0.004	1a	1
249	Cu	Cu1h4	0.83292	0.25651	0.47103	1.000	0.004	1a	1
250	Cu	Cu1h5	0.83292	0.24375	0.61696	1.000	0.004	1a	1
251	Cu	Cu1h6	0.83292	0.25559	0.76290	1.000	0.004	1a	1
252	Cu	Cu1h7	0.83292	0.24544	0.90883	1.000	0.004	1a	1
253	O	O1a1	0.16947	0.24453	0.11270	1.000	0.003	1a	1
254	O	O1a2	0.16947	0.25247	0.25863	1.000	0.003	1a	1
255	O	O1a3	0.16947	0.25070	0.40456	1.000	0.003	1a	1
256	O	O1a4	0.16947	0.24618	0.55049	1.000	0.003	1a	1
257	O	O1a5	0.16947	0.25669	0.69642	1.000	0.003	1a	1
258	O	O1a6	0.16947	0.24087	0.84236	1.000	0.003	1a	1
259	O	O1a7	0.16947	0.26097	0.98829	1.000	0.003	1a	1
260	O	O1b1	0.16947	0.76039	0.03973	1.000	0.003	1a	1
261	O	O1b2	0.16947	0.73821	0.18566	1.000	0.003	1a	1
262	O	O1b3	0.16947	0.76242	0.33160	1.000	0.003	1a	1
263	O	O1b4	0.16947	0.73776	0.47753	1.000	0.003	1a	1
264	O	O1b5	0.16947	0.76127	0.62346	1.000	0.003	1a	1
265	O	O1b6	0.16947	0.74044	0.76939	1.000	0.003	1a	1
266	O	O1b7	0.16947	0.75723	0.91532	1.000	0.003	1a	1

267 O	O1c1	0.33053	0.23960	0.03973	1.000	0.003	1a	1
268 O	O1c2	0.33053	0.26179	0.18566	1.000	0.003	1a	1
269 O	O1c3	0.33053	0.23758	0.33160	1.000	0.003	1a	1
270 O	O1c4	0.33053	0.26224	0.47753	1.000	0.003	1a	1
271 O	O1c5	0.33053	0.23873	0.62346	1.000	0.003	1a	1
272 O	O1c6	0.33053	0.25956	0.76939	1.000	0.003	1a	1
273 O	O1c7	0.33053	0.24277	0.91532	1.000	0.003	1a	1
274 O	O1d1	0.33053	0.75547	0.11270	1.000	0.003	1a	1
275 O	O1d2	0.33053	0.74753	0.25863	1.000	0.003	1a	1
276 O	O1d3	0.33053	0.74930	0.40456	1.000	0.003	1a	1
277 O	O1d4	0.33053	0.75382	0.55049	1.000	0.003	1a	1
278 O	O1d5	0.33053	0.74331	0.69642	1.000	0.003	1a	1
279 O	O1d6	0.33053	0.75913	0.84236	1.000	0.003	1a	1
280 O	O1d7	0.33053	0.73903	0.98829	1.000	0.003	1a	1
281 O	O1e1	0.83053	0.74188	0.03323	1.000	0.003	1a	1
282 O	O1e2	0.83053	0.76025	0.17917	1.000	0.003	1a	1
283 O	O1e3	0.83053	0.73830	0.32510	1.000	0.003	1a	1
284 O	O1e4	0.83053	0.76240	0.47103	1.000	0.003	1a	1
285 O	O1e5	0.83053	0.73771	0.61696	1.000	0.003	1a	1
286 O	O1e6	0.83053	0.76138	0.76289	1.000	0.003	1a	1
287 O	O1e7	0.83053	0.74027	0.90882	1.000	0.003	1a	1
288 O	O1f1	0.83053	0.25833	0.10620	1.000	0.003	1a	1
289 O	O1f2	0.83053	0.24429	0.25213	1.000	0.003	1a	1
290 O	O1f3	0.83053	0.25273	0.39806	1.000	0.003	1a	1
291 O	O1f4	0.83053	0.25043	0.54399	1.000	0.003	1a	1
292 O	O1f5	0.83053	0.24644	0.68993	1.000	0.003	1a	1
293 O	O1f6	0.83053	0.25646	0.83586	1.000	0.003	1a	1
294 O	O1f7	0.83053	0.24105	0.98179	1.000	0.003	1a	1
295 O	O1g1	0.66947	0.74168	0.10620	1.000	0.003	1a	1
296 O	O1g2	0.66947	0.75571	0.25213	1.000	0.003	1a	1
297 O	O1g3	0.66947	0.74727	0.39806	1.000	0.003	1a	1
298 O	O1g4	0.66947	0.74957	0.54399	1.000	0.003	1a	1
299 O	O1g5	0.66947	0.75356	0.68993	1.000	0.003	1a	1
300 O	O1g6	0.66947	0.74354	0.83586	1.000	0.003	1a	1
301 O	O1g7	0.66947	0.75894	0.98179	1.000	0.003	1a	1
302 O	O1h1	0.66947	0.25812	0.03323	1.000	0.003	1a	1
303 O	O1h2	0.66947	0.23976	0.17917	1.000	0.003	1a	1
304 O	O1h3	0.66947	0.26170	0.32510	1.000	0.003	1a	1
305 O	O1h4	0.66947	0.23760	0.47103	1.000	0.003	1a	1
306 O	O1h5	0.66947	0.26229	0.61696	1.000	0.003	1a	1
307 O	O1h6	0.66947	0.23862	0.76289	1.000	0.003	1a	1
308 O	O1h7	0.66947	0.25973	0.90882	1.000	0.003	1a	1
309 O	O2a1	0.50000	0.24394	0.10945	1.000	0.020	1a	1
310 O	O2a2	0.50000	0.25690	0.25538	1.000	0.020	1a	1
311 O	O2a3	0.50000	0.24271	0.40131	1.000	0.020	1a	1
312 O	O2a4	0.50000	0.25721	0.54724	1.000	0.020	1a	1
313 O	O2a5	0.50000	0.24335	0.69318	1.000	0.020	1a	1
314 O	O2a6	0.50000	0.25567	0.83911	1.000	0.020	1a	1
315 O	O2a7	0.50000	0.24569	0.98504	1.000	0.020	1a	1
316 O	O2b1	0.50000	0.74517	0.03648	1.000	0.020	1a	1
317 O	O2b2	0.50000	0.75329	0.18241	1.000	0.020	1a	1
318 O	O2b3	0.50000	0.74847	0.32835	1.000	0.020	1a	1
319 O	O2b4	0.50000	0.74967	0.47428	1.000	0.020	1a	1
320 O	O2b5	0.50000	0.75217	0.62021	1.000	0.020	1a	1
321 O	O2b6	0.50000	0.74613	0.76614	1.000	0.020	1a	1
322 O	O2b7	0.50000	0.75531	0.91207	1.000	0.020	1a	1
323 O	O2c1	0.00000	0.25483	0.03648	1.000	0.020	1a	1
324 O	O2c2	0.00000	0.24671	0.18241	1.000	0.020	1a	1
325 O	O2c3	0.00000	0.25153	0.32835	1.000	0.020	1a	1
326 O	O2c4	0.00000	0.25033	0.47428	1.000	0.020	1a	1
327 O	O2c5	0.00000	0.24783	0.62021	1.000	0.020	1a	1

328 O	O2c6	0.00000	0.25387	0.76614	1.000	0.020	1a	1
329 O	O2c7	0.00000	0.24469	0.91207	1.000	0.020	1a	1
330 O	O2c8	1.00000	0.25483	0.03648	1.000	0.020	1a	1
331 O	O2c9	1.00000	0.24671	0.18241	1.000	0.020	1a	1
332 O	O2c10	1.00000	0.25153	0.32835	1.000	0.020	1a	1
333 O	O2c11	1.00000	0.25033	0.47428	1.000	0.020	1a	1
334 O	O2c12	1.00000	0.24783	0.62021	1.000	0.020	1a	1
335 O	O2c13	1.00000	0.25387	0.76614	1.000	0.020	1a	1
336 O	O2c14	1.00000	0.24469	0.91207	1.000	0.020	1a	1
337 O	O2d1	0.00000	0.75606	0.10945	1.000	0.020	1a	1
338 O	O2d2	0.00000	0.74310	0.25538	1.000	0.020	1a	1
339 O	O2d3	0.00000	0.75729	0.40131	1.000	0.020	1a	1
340 O	O2d4	0.00000	0.74279	0.54724	1.000	0.020	1a	1
341 O	O2d5	0.00000	0.75665	0.69318	1.000	0.020	1a	1
342 O	O2d6	0.00000	0.74433	0.83911	1.000	0.020	1a	1
343 O	O2d7	0.00000	0.75431	0.98504	1.000	0.020	1a	1
344 O	O2d8	1.00000	0.75606	0.10945	1.000	0.020	1a	1
345 O	O2d9	1.00000	0.74310	0.25538	1.000	0.020	1a	1
346 O	O2d10	1.00000	0.75729	0.40131	1.000	0.020	1a	1
347 O	O2d11	1.00000	0.74279	0.54724	1.000	0.020	1a	1
348 O	O2d12	1.00000	0.75665	0.69318	1.000	0.020	1a	1
349 O	O2d13	1.00000	0.74433	0.83911	1.000	0.020	1a	1
350 O	O2d14	1.00000	0.75431	0.98504	1.000	0.020	1a	1

==

Bibliography

[1] I. Newton. *Opticks: or a Treatise of the Reflections, Refractions, Inflections & Colours of Light.* Dover Publications Inc., London, 4th edition, 1730.

[2] J. C. D. Brand. *Lines of Light: The Sources of Dispersive Spectroscopy, 1800–1930.* Gordon and Breach Publishers, Amsterdam, 1995.

[3] I. Newton. A letter of Mr. Isaac Newton, professor of the mathematicks in the University of Cambridge; containing his new theory about light and colors: Sent by the author to the publisher from Cambridge, Febr. 6. 1671/72; in order to be communicated to the R. Society. *Philosophical Transactions of the Royal Society of London*, 6:3075–3087, 1671.

[4] J. A. Gonzalo, J. de Frutos, and J. García. *Solid State Spectroscopies Basic Principles and Applications.* World Scientific Publishing, Singapore, 2002.

[5] R. A. Lewis. *Terahertz Physics.* Cambridge University Press, United Kingdom, 2012.

[6] Y.-S. Lee. *Principles of Terahertz Science and Technology.* Springer, New York, 2009.

[7] K. Sakai. *Terahertz Optoelectronics.* Springer, New York, 2005.

[8] S. A. Wolf, D. D. Awschalom, R. A. Buhrman, J. M. Daughton, S. von Molnár, M. L. Roukes, A. Y. Chtchelkanova, and D. M. Treger. Spintronics: A spin-based electronics vision for the future. *Science*, 294:1488–1495, 2001.

[9] I. Žutić, J. Fabian, and S. Das Darma. Spintronics: Fundamentals and applications. *Reviews of Modern Physics*, 76:323–410, 2004.

[10] Fabio Pulizzi. Spintronics. *Nature Materials Insight*, 11:367, 2012.

[11] W. Herschel. Experiments on the refrangibility of the invisible rays of the sun. By William Herschel, LL. D. F. R. S. *Philosophical Transactions of the Royal Society of London*, 90, 1800.

[12] J. W. Ritter. Experiments on the invisible rays of the solar spectrum. *Journal of Natural Philosophy (Nichalson's Journal)*, 5:255, 1803.

[13] T. Young. Outlines of experiments and inquiries respecting sound and light. By Thomas Young, M. D. F. R. S. In a letter to Edward Whitaker Gray, M. D. Sec. R. S. *Philosophical Transactions of the Royal Society of London*, 90:106, 1800.

[14] J. C. Maxwell. A dynamical theory of the electromagnetic field. *Philosophical Transactions of the Royal Society of London*, 155:459–512, 1865.

[15] M. K. E. L. Planck. Nobel prize lecture 1918. Nobelprize.org. Nobel Media AB 2014, [Online accessed: 6-Oct-2014]. URL http://www.nobelprize.org/nobel_prizes/physics/laureates/1918/.

[16] A. Einstein. Nobel prize lecture 1921. Nobelprize.org. Nobel Media AB 2014, [Online accessed: 14-Oct-2014]. URL http://www.nobelprize.org/nobel_prizes/physics/laureates/1921/.

[17] L. de Broglie. Nobel prize lecture 1929. Nobelprize.org, Nobel Media AB 2014, [Online accessed: 6th-Oct-2014]. URL http://www.nobelprize.org/nobel_prizes/physics/laureates/1929/.

[18] Penn State Unsiversity. Electromagnetic radiation (light). [Online accessed: 28-Oct-2014]. URL http://www2.astro.psu.edu/users/cpalma/astro1h/class5.html.

[19] N. Karpowicz, H. Zhong, C. Zhang, K.-I. Lin, J.-S. Hwang, J. Xu, and X.-C. Zhang. Compact continuous-wave subterahertz system for inspection applications. *Applied Physics Letters*, 86:054105, 2005.

[20] V. P. Wallace, A. J. Fitzgerald, S. Shankar, N. Flanagan, R. Pye, J. Cluff, and D. D. Arnone. Terahertz pulsed imaging of basal cell carcinoma *ex vivo* and *in vivo*. *British Journal of Dermatology*, 151:424–432, 2004.

[21] T. Kleine-Ostmann and T. Nagatsuma. A review on terahertz communications research. *Journal of Infrared, Millimeter, and Terahertz Waves*, 32:143–171, 2011.

[22] M. King. THz radiation systems market to reach a value of $195.3 million by 2018. Companies and Markets, October 2013, [Online accessed: 4-Oct-2014]. URL http://www.companiesandmarkets.com/News/Information-Technology/THz-radiation-systems-market-to-reach-a-value-of-195-3-million-by-2018/NI8274.

[23] The Southeastern Universities Research Association (SURA). Chart of the electromagnetic spectrum. 2010, [Online accessed: 4-Oct-2014]. URL http://www.sura.org/commercialization/terahertz.html.

[24] J. J. Thomson. Cathode rays. *Philosphical Magazine Series 5*, 44:293–316, 1897.

[25] E. Rutherdord. The scattering of α and β particles by matter and the structure of the atom. *Philosphical Magazine Series 6*, 21:669–688, 1911.

[26] N. Bohr. On the constitution of atoms and molecules. *Philosphical Magazine Series 6*, 26:1–25, 1913.

[27] N. Bohr. On the constitution of atoms and molecules part II. systems containing only a single nucleus. *Philosphical Magazine Series 6*, 26:476–502, 1913.

[28] D. J. Griffiths. *Introduction to Quantum Mechanics*. Pearson Prentice Hall, 2nd edition, 2005.

[29] C. Kittel. *Introduction to Solid State Physics*. John Wiley & Sons Inc., 2005.

[30] S. O. Kasap. *Principles of Electronic Materials and Devices*. McGraw-Hill, 3rd edition, 2006.

[31] W. Shockley. The path to the conception of the junction transistor. *IEEE Transactions on Electron Devices*, ED-31:1523–1546, 1984.

[32] M. Becker and H. Y. Fan. Optical properties of semiconductors. III. Infra-red transmission of silicon. *Physical Review*, 76:1531–1532, 1949.

[33] W. H. Brattain and H. B. Briggs. The optical constants of germanium in the infra-red and visible. *Physical Review*, 75:1705–1710, 1949.

[34] B. N. Murdin, J. Li, M. L. Y. Pang, E. T. Bowyer, K. L. Litvinenko, S. K. Clowes, H. Engelkamp, C. R. Pidgeon, I. Galbraith, N. V. Abrosimov, H. Riemann, S. G. Pavlov, H.-W. Hübers, and P. G. Murdin. Si:P as a laboratory analogue for hydrogen on high magnetic field white dwarf stars. *Nature Communications*, 4:1469, 2013.

[35] R. A. Lewis, A. Bruno-Alfonso, G. V. B. de Souza, R. E. M. Vickers, J. A. Colla, and E. Constable. Spherical, cylindrical and tetrahedral symmetries; hydrogenic states at high magnetic field in Si:P. *Scientific Reports*, 3:3488, 2013.

[36] A. J. Powner. Periodic table & periodic law. [Online accessed: 6-Oct-2014]. URL http://mr.powner.org/c/lessons/c_images/spectroscopy.jpg.

[37] L. Shore, P. Doherty, and T. Brady. Exploratorium teacher institute workshop 5: Stars. 2011, [Online accessed: 6-Oct-2014]. URL http://www.exo.net/~pauld/workshops/Stars/Stars.htm.

[38] V. K. Thorsmølle, C. C. Homes, A. Gozar, G. Blumberg, J. L. M. van Mechelen, A. B. Kuzmenko, S. Vanishri, C. Marin, and H. M. Rønnow. Phonon energy gaps in the charged incommensurate planes of spin-ladder $Sr_{14}Cu_{24}O_{41}$ compound by Raman and infrared spectroscopy. *Physical Review Letters*, 108:217401, 2012.

[39] D. A. Turton, H. M. Senn, T. Harwood, A. J. Lapthorn, E. M. Ellis, and K. Wynne. Terahertz underdamped vibrational motion governs protein-ligand binding in solution. *Nature Communications*, 5:3999, 2014.

[40] E. Constable, D. L. Cortie, J. Horvat, R. A. Lewis, Z. Cheng, G. Deng, S. Cao, S. Yuan, and G. Ma. Complementary terahertz absorption and inelastic neutron study of the dynamic anisotropy contribution to zone-center spin waves in a canted antiferromagnet $NdFeO_3$. *Physical Review B*, 90:054413, 2014.

[41] T. Kampfrath, A. Sell, G. Klatt, A. Pashkin, S. Mährlein, T. Dekorsy, M. Wolf, M. Fiebig, A. Leitenstorfer, and R. Huber. Coherent terahertz control of antiferromagnetic spin waves. *Nature Photonics*, 5:31–34, 2010.

[42] A. V. Kimel, B. A. Ivanov, R. V. Pisarev, P. A. Usachev, A. Kirilyuk, and Th. Rasing. Inertia-driven spin switching in antiferromagnets. *Nature Physics*, 5:727–731, 2009.

[43] S. Wienholdt, D. Hinzke, and U. Nowak. THz switching of antiferromagnets and ferrimagnets. *Physical Review Letters*, 108:247207, 2012.

[44] D. Talbayev, S. A. Trugman, S. Lee, H. T. Yi, S.-W. Cheong, and A. J. Taylor. Long-wavelength magnetic and magnetoelectric excitations in the ferroelectric anti-ferromagnet $BiFeO_3$. *Physical Review B*, 83:094403, 2011.

[45] S. Mangin, D. Ravelosona, D. A. Katine, M. J. Carey, B. D. Terris, and E. E. Fullerton. Current-induced magnetization reversal in nanopillars with perpendicular anisotropy. *Nature Materials*, 5:210–215, 2006.

[46] H. Béa, M. Gajek, M. Bibes, and A. Barthélémy. Spintronics with multiferroics. *Journal of Physics: Condensed Matter*, 20:434221, 2008.

[47] J. Jeong, E. A. Goremychkin, T. Guidi, K. Nakajima, G. S. Jeon, S.-A. Kim, S. Furukawa, Y. B. Kim, S. Lee, V. Kiryukhin, S.-W. Cheong, and J.-G. Park. Spin wave measurments over the full Brillouin zone of multiferroic $BiFeO_3$. *Physical Review Letters*, 108:077202, 2012.

[48] M. Matsuda, R. S. Fishman, T. Hong, C. H. Lee, T. Ushiyama, Y. Yanagisawa, Y. Tomioka, and T. Ito. Magnetic dispersion and anisotropy in multiferroic $BiFeO_3$. *Physical Review Letters*, 109:067205, 2012.

[49] C. Ederer and N. A. Spaldin. Weak ferromagnetism and magnetoelectric coupling in bismuth ferrite. *Physical Review B*, 71:060401(R), 2005.

[50] M. R. Freeman and Z. Diao. All-optical spin-wave control. *Nature Photonics*, 6:643, 2012.

[51] K. D. Möller and W. G. Rothschild. *Far-Infrared Spectroscopy*. Wiley-Interscience, USA, 1971.

[52] E. K. Plyler, D. J. C. Yates, and H. A. Gebbie. Radiant energy from sources in the far infrared. *Journal of the Optical Society of America*, 52:859–861, 1962.

[53] M. Seo, M. Urteaga, J. Hacker, A. Young, Z. Griffith, V. Jain, R. Pierson, P. Rowell, A. Skalare, A. Peralta, R. Lin, D. Pukala, and M. Rodwell. InP HBT IC technology for terahertz frequencies: Fundamental oscillators up to 0.57 THz. *IEEE Journal of Solid-State Circuits*, 46:2203–2214, 2011.

[54] R. Köhler, A. Tredicucci, F. Beltram, H. E. Beere, E. H. Linfield, A. G. Davies, D. A. Ritchie, R. C. Iotti, and F. Rossi. Terahertz semiconductor-heterostructure laser. *Nature*, 417:156–159, 2002.

[55] D. H. Auston. Picosecond optoelectronic switching and gating in silicon. *Applied Physics Letters*, 26:101–103, 1975.

[56] C. H. Lee. Picosecond optoelectronic switching in GaAs. *Applied Physics Letters*, 30:84–86, 1977.

[57] D. E. Spence, P. N. Kean, and W. Sibbett. 60-fsec pulse generation from a self-mode-locked Ti:sapphire laser. *Optics Letters*, 16:42–44, 1991.

[58] M. van Exter, Ch. Fattinger, and D. Grischkowsky. Highbrightness terahertz beams characterized with an ultrafast detector. *Applied Physics Letters*, 55:337–339, 1989.

[59] Ch. Fattinger and D. Grischkowsky. Terahertz beams. *Applied Physics Letters*, 54: 490–492, 1989.

[60] M. V. Exter and D. R. Grischkowsky. Characterization of an optoelectronic terahertz beam system. *IEEE Transactions on Microwave Theory and Techniques*, 28:1684–1691, 1990.

[61] R. A. Lewis. A review of terahertz sources. *Journal of Physics D: Applied Physics*, 47:374001, 2014.

[62] P. H. Siegel. Terahertz technology in biology and medicine. *IEEE Transactions on Microwave Theory and Techniques*, 52:2438–2447, 2004.

[63] J. F. Federici, B. Schulkin, F. Huang, D. Gary, R. Barat, F. Oliveira, and D. Zimdars. THz imaging and sensing for security applications — explosives, weapons and drugs. *Semiconductor Science and Technology*, 20:S266, 2005.

[64] M. L. Smith, R. Mendis, R. E. M. Vickers, and R. A. Lewis. Comparison of photoexcited p-InAs THz radiation source with conventional thermal radiation sources. *Journal of Applied Physics*, 105:063109, 2009.

[65] J. M. Byrd, W. P. Leemans, A. Loftsdottir, B. Marcelis, M. C. Martin, W. R. McKinney, F. Sannibale, T. Scarvie, and C. Steier. Observation of broadband self-amplified spontaneous coherent terahertz synchrotron radiation in a storage ring. *Physical Review Letters*, 89:224801, 2002.

[66] P. A. Tipler and R. A. Llewellyn. *Modern Physics*. W. H. Freeman and Company, 5th edition, 2008.

[67] K. Charrada, G. Zissis, and M. Aubes. Two-temperature, two-dimensional fluid modelling of mercury plasma in high-pressure lamps. *Journal of Physics D: Applied Physics*, 29:2432–2438, 1996.

[68] N. Zamdmer, Q. Hu, K. A. McIntosh, and S. Verghese. Increase in response time of low-temperature-grown GaAs photoconductive switches at high voltage bias. *Applied Physics Letters*, 75:2313, 1999.

[69] P. Mounaix, M. Tondusson, N. Chimot, J. Mangeney, K. Blary, and J. F. Lampin. High emission and detection efficiency of terahertz beam with heavy-ion-irradiated InP material excited at 0.8 μm. *Electronics Letters*, 42:879–880, 2006.

[70] J. N. Heyman, N. Coates, A. Reinhardt, and G. Strasser. Diffusion and drift in terahertz emission at GaAs surfaces. *Applied Physics Letters*, 83:5476, 2003.

[71] J. Lloyd-Hughes, S. K. E. Merchant, L. Fu, H. H. Tan, C. Jagadish, E. Castro-Camus, and M. B. Johnston. Influence of surface passivation on ultrafast carrier dynamics and terahertz radiation generation in GaAs. *Applied Physics Letters*, 89: 232102, 2006.

[72] R. McLaughlin, A. Corchia, M. B. Johnston, Q. Chen, C. M. Ciesla, D. D. Arnone, A. G. Davies G. A. C. Jones, E. H. Linfield, and M. Pepper. Enhanced coherent terahertz emission from indium arsenide in the presence of a magnetic field. *Applied Physics Letters*, 76:2038–2040, 2000.

[73] H. Takahashi, Y. Suzuki, A. Quema, M. Sakai, T. Yano, S. Ono, N. Sarukura, M. Hosomizu, T. Tsukamoto, G. Nishijima, and K. Watanabe. Magnetic-field-induced enhancement of THz-radiation power from femtosecond-laser-irradiated InAs up to 27 T. *Japanese Journal of Applied Physics*, 42:L532–L534, 2003.

[74] G. Klatt, F. Hilser, W. Qiao, M. Beck, R. Gebs, A. Bartels, K. Huska, U. Lemmer, G. Bastian, M. B. Johnston, M. Fischer, J. Faist, and T. Dekorsy. Terahertz emission from lateral photo-Dember currents. *Optics Express*, 18:4939–4947, 2010.

[75] T. Yajima and N.Takeuchi. Far-infrared difference-frequency generation by picosecond laser pulses. *Japanese Journal of Applied Physics*, 9:1361–1371, 1970.

[76] K. Radhanpura, S. Hargreaves, R. A. Lewis, L. Sirbu, and I. M. Tiginyanu. Heavy noble gas (Kr, Xe) irradiated (111) InP nanoporous honeycomb membranes with enhanced ultrafast all-optical terahertz emission. *Applied Physics Letters*, 97:181921, 2010.

[77] C. Kübler, R. Huber, and A. Leitenstorfer. Ultrabroadband terahertz pulses: Generation and field-resolved detection. *Semiconductor Science and Technology*, 20: S128–S133, 2005.

[78] I. Katayama, R. Akai, M. Bito, H. Shimosato, K. Miyamoto, H. Ito, and M. Ashida. Ultrabroadband terahertz generation using 4-N,N-dimethylamino-4'-N'-methyl-stilbazolium tosylate single crystals. *Applied Physics Letters*, 97:021105, 2010.

[79] K. Y. Kim, A. J. Taylor, J. H. Glownia, and G. Rodriguez. Coherent control of terahertz supercontinuum generation in ultrafast laser–gas interactions. *Nature*, 2: 605–609, 2008.

[80] D. J Cook and R. M. Hochstrasser. Intense terahertz pulses by four-wave rectification in air. *Optics Letters*, 25:1210–1212, 2000.

[81] M. Kress, T. Löffler, S. Eden, M. Thomson, and H. G. Roskos. Terahertz-pulse generation by photoionization of air with laser pulses composed of both fundamental and second-harmonic waves. *Optics Letters*, 29:1120–1122, 2004.

[82] X. Xie, J. Dai, and X.-C. Zhang. Coherent control of THz wave generation in ambient air. *Physical Review Letters*, 96:075005, 2006.

[83] H. G. Roskos, M. C. Nuss, J. Shah, K. Leo, D. A. B. Miller, A. M. Fox, S. Schmitt-Rink, and K. Köhler. Coherent submillimeter-wave emission from charge oscillations in a double-well potential. *Physical Review Letters*, 68:2216, 1992.

[84] T. Dekorsy, H. Auer, C. Waschke, H. J. Bakker, H. G. Roskos, H. Kurz, V. Wagner, and P. Grosse. Emission of submillimeter electromagnetic waves by coherent phonons. *Physical Review Letters*, 74:738, 1995.

[85] M. Hangyo, S. Tomozawa, Y. Murakami, M. Tonouchi, M. Tani, Z. Wang, K. Sakai, and S. Nakashima. Terahertz radiation from superconducting $YBa_2Cu_3O_7 - \delta$ thin films excited by femtosecond optical pulses. *Applied Physics Letters*, 69:2122, 1996.

[86] E. Beaurepaire, G. M. Turner, S. M. Harrel, M. C. Beard, J.-Y. Bigot, and C. A. Schmuttenmaer. Coherent terahertz emission from ferromagnetic films excited by femtosecond laser pulses. *Applied Physics Letters*, 84:3465, 2004.

[87] S. Preu, G. H. Döhler, S. Malzer, L. J. Wang, and A. C. Gossard. Tunable, continuous-wave terahertz photomixer sources and applications. *Journal of Applied Physics*, 109:061301, 2011.

[88] C.-S. Friedrich, C. Brenner, S. Hoffmann, A. Schmitz, I. C. Mayorga, A. Klehr, G. Erbert, and M. R. Hofmann. New two-color laser concepts for THz generation. *IEEE Journal of Selected Topics in Quantum Electronics*, 14:270–276, 2008.

[89] E. R. Brown, K. A. McIntosh, K. B. Nichols, and C. L. Dennis. Photomixing up to 3.8 THz in low-temperature-grown GaAs. *Applied Physics Letters*, 66:285–287, 1995.

[90] K. A. McIntosh, E. R. Brown, K. B. Nichols, O. B. McMahon, W. F. DiNatale, and T. M. Lyszczarz. Terahertz photomixing with diode lasers in low-temperature-grown GaAs. *Applied Physics Letters*, 67:3844–3846, 1995.

[91] J. Sigmund, J. Lampin, V. Ivannikov, C. Sydlo, M. Feiginov, D. Pavlidis, P. Meissner, and H. Hartnagel. Low-temperature grown GaAs with sub-picosecond photocarrier

lifetime for continuous-wave terahertz measurements. *The Institute of Electronics, Information and Communication Engineers, Transactions, Electronics*, E91-C:1058–1062, 2008.

[92] S. Matsuura, M. Tani, H. Abe, K. Sakai, H. Ozeki, and S. Saito. High-resolution terahertz spectroscopy by a compact radiation source based on photomixing with diode lasers in a photoconductive antenna. *Journal of Molecular Spectroscopy*, 187: 97–101, 1998.

[93] G. Mouret, S. Matton, R. Bocquet, F. Hindle, E. Peytavit, and J. F. Lampin. Far-infrared cw difference-frequency generation using vertically integrated and planar low temperature grown GaAs photomixers: Application to H_2S rotational spectrum up to 3 THz. *Applied Physics B*, 79:725–729, 2004.

[94] H. Page, S. Malik, M. Evans, I. Gregory, I. Farrer, and D. Ritchie. Waveguide coupled terahertz photoconductive antennas: Toward integrated photonic terahertz devices. *Applied Physics Letters*, 92:163502, 2008.

[95] R. Mendis, C. Sydlo, J. Sigmund, M. Feiginov, P. Meissner, and H. L. Hartnagel. Spectral characterization of broadband THz antennas by photoconductive mixing: Toward optimal antenna design. *IEEE, Antennas and Wireless Propagation Letters*, 4:85–88, 2005.

[96] E. Peytavit, G. Mouret, J. F. Lampin, S. Arscott, P. Masselin, L. Desplanque, O. Vanbelsien, R. Bocquet, F. Mollot, and D. Lippens. Terahertz electromagnetic generation via optical frequency difference. *Institute of Electrical Engineers Proceedings Optoelectronics*, 149:82–87, 2002.

[97] E. R. Brown. THz generation by photomixing in ultrafast photoconductors. *International Journal of High Speed Electronics and Systems*, 13:497, 2003.

[98] J. Liu, H. Schmutz, and F. Merkt. Generation of widely tunable Fourier-transform-limited terahertz pulses using narrowband near-infrared laser radiation. *Journal of Molecular Spectroscopy*, 22:1–7, 2009.

[99] K. H. Miller, E. Constable, H. Berger, D. B. Tanner, and R. A. Lewis. Complementary techniques for probing terahertz magnetic excitations in $Cu_3Bi(SeO_3)_2O_2Cl$. In

International Conference on Infrared, Millimeter, and Terahertz Waves (IRMMW-THz), Wollongong, Australia, 2012. doi: 10.1109/IRMMW-THz.2012.6380234.

[100] M. Martin, J. Mangeney, P. Crozat, Y. Chassagneux, R. Colombelli, N. Zerounian, L. Vivien, and K. Blary. Gigahertz modulation of tunable terahertz radiation from photomixers driven at telecom wavelengths. *Applied Physics Letters*, 93:131112, 2008.

[101] P. H. Siegel. THz technology: An overview. *International Journal of High Speed Electronics and Systems*, 13:351, 2003.

[102] V. L. Bratman, Y. K. Kalynov, and V. N. Manuilov. Large-orbit gyrotron operation in the terahertz frequency range. *Physical Review Letters*, 102:245101, 2009.

[103] W. He, C. R. Donaldson, L. Zhang, K. Ronald, P. McElhinney, and A. W. Cross. High power wideband gyrotron backward wave oscillator operating towards the terahertz region. *Physical Review Letters*, 110:165101, 2013.

[104] J. H. Booske, R. J. Dobbs, C. D. Joye, C. L. Kory, G. R. Neil, G.-S. Park, J. Park, and R. J. Temkin. Vacuum electronic high power terahertz sources. *IEEE Transactions on Terahertz Science and Technology*, 1:54–75, 2011.

[105] B. A. Knyazev, G. N. Kulipanov, and N. A. Vinokurov. Novosibirsk terahertz free electron laser: Instrumentation development and experimental achievements. *Measurement Science and Technology*, 21:054017, 2010.

[106] E. D. Courant, M. S. Livingston, and H. S. Snyder. The strong-focusing synchroton — A new high energy accelerator. *Physical Review*, 88:1190, 1952.

[107] Australian Synchrotron. How does the Australian Synchrotron work? [Online accessed: 12-Oct-2014]. URL http://www.synchrotron.org.au/index.php/about-us/our-facilities/accelerator-physics/how-does-the-australian-synchrotron-work.

[108] G. L. Carr, M. C. Martin, W. R. McKinney, K. Jordan, G. R. Neil, and G. P. Williams. High-power terahertz radiation from relativistic electrons. *Nature*, 420:153–156, 2002.

[109] G Dodel. On the history of far-infrared (FIR) gas lasers: Thirty-five years of research and application. *Infrared Physics & Technology*, 40:127–139, 1999.

[110] S. Pérez, T. González, D. Pardo, and J. Mateos. Terahertz Gunn-like oscillations in InGaAs/InAlAs planar diodes. *Journal of Applied Physics*, 103:094516, 2008.

[111] L. Ozyuzer, A. E. Koshelev, C. Kurter, N. Gopalsami, Q. Li, M. Tachiki, K. Kadowaki, T. Yamamoto, H. Minami, H. Yamaguchi, T. Tachiki, K. E. Gray, W.-K. Kwok, and U. Welp. Emission of coherent THz radiation from superconductors. *Science*, 318:1291–1293, 2007.

[112] J. Horvat and R. A. Lewis. Peeling adhesive tape emits electromagnetic radiation at terahertz frequencies. *Optics Letters*, 34:2195–2197, 2009.

[113] S. P. Mickan and X.-C. Zhang. T-ray sensing and imaging. *International Journal of High Speed Electronics & Systems*, 13:601, 2003.

[114] C. A. Burrus and W. Gordy. Millimeter and submillimeter wave spectroscopy. *Physical Review*, 101:599, 1956.

[115] V. V. Kubarev, V. K. Ovchar, and K. S. Palagin. Ultra-fast terahertz Schottky diode detector. In *International Conference on Infrared, Millimeter, and Terahertz Waves (IRMMW-THz)*, Busan, South Korea, 2009. doi: 10.1109/ICIMW.2009.5325576.

[116] Q. Wu and X.-C. Zhang. Design and characterization of traveling-wave electrooptic terahertz sensors. *IEEE Journal of Selected Topics in Quantum Electronics*, 2:693–700, 1996.

[117] D. Seliuta, I. Kašalynas, V. Tamošiŭnas, S. Balakauskas, Z. Martŭnas, S. Ašmontas, G. Valušis, A. Lisauskas, H. G. Roskos, and K. Köhler. Silicon lens-coupled bow-tie InGaAs-based broadband terahertz sensor operating at room temperature. *Electronics Letters*, 42:825–827, 2006.

[118] D. Saeedkia and S. Safavi-Naeimi. Terahertz photonics: Optoelectronic techniques for generation and detection of terahertz waves. *Journal of Lightwave Technology*, 26:2409–2423, 2008.

[119] A. J. Deninger, T. Göbel, D. Schonherr, T. Kinder, A. Roggenbuck, M. Koberle, F. Lison, T. Muller-Wirts, and P. Meissner. Precisely tunable continuous-wave terahertz source with interferometric frequency control. *Review of Scientific Instruments*, 79:044702, 2008.

[120] A. Roggenbuck, K. Thirunavukkuarasu, H. Schmitz, J. Marx, A. Deninger, I. Cámara Mayorga, R. Güsten, J. Hemberger, and M. Grüninger. Using a fiber stretcher as a fast phase modulator in a continuous wave terahertz spectrometer. *Journal of the Optical Society of America*, 29:614–620, 2012.

[121] T. Göbel, D. Schoenherr, C. Sydlo, M. Feiginov, P. Meissner, and H. L. Hartnagel. Continuous-wave single-sampling-point characterisation of optoelectronic on-chip terahertz transceiver. *Electronics Letters*, 45:23, 2009.

[122] J. Mangeney and P. Crozat. Ion-irradiated $In_{0.53}Ga_{0.47}As$ photoconductive antennas for THz generation and detection at 1.55 μm wavelength. *Comptes Rendus Physique*, 9:142–152, 2008.

[123] C. D. Ball and F. C. De Lucia. Direct measurement of rotationally inelastic cross sections at astrophysical and quantum collisional temperatures. *Physical Review Letters*, 81:305, 1998.

[124] H. Rabitz. Rotation and rotation-vibration pressure-broadened spectral lineshapes. *Annual Review of Physical Chemistry*, 25:155–177, 1974.

[125] J. C. Pearson, L. C. Oesterling, E. Herbst, and F. C. De Lucia. Pressure broadening of gas phase molecular ions at very low temperature. *Physical Review Letters*, 75: 2940, 1995.

[126] K. Rowlands, L. Dunne, S. Maddox, N. Bourne, H. L. Gomez, S. Kaviraj, S. P. Bamford, S. Brough, S. Charlot, E. da Cunha, S. P. Driver, S. A. Eales, A. M. Hopkins, L. Kelvin, R. C. Nichol, A. E. Sansom, R. Sharp, D. J. B. Smith, P. Temi, P. van der Werf, M. Baes, A. Cava, A. Cooray, S. M. Croom, A. Dariush, G. De Zotti, S. Dye, J. Fritz, R. Hopwood, E. Ibar, R. J. Ivison, J. Liske, J. Loveday, B. Madore, P. Norberg, C. C. Popescu, E. E. Rigby, A. Robotham, G. Rodighiero, M. Seibert,

and R. J. Tuffs. Herschel*-ATLAS/GAMA: Dusty early-type galaxies and passive spirals. *Monthly Notices of the Royal Astronomical Society*, 419:2545–2578, 2011.

[127] D. Bigourd, A. Cuisset, F. Hindle, S. Matton, R. Bocquet, G. Mouret, F. Cazier, D. Dewaele, and H. Nouali. Multiple component analysis of cigarette smoke using THz spectroscopy, comparison with standard chemical analytical methods. *Applied Physics B – Lasers and Optics*, 10:1007, 2006.

[128] D. Bigourd, A. Cuisset, F. Hindle, S. Matton, E. Fertein, R. Bocquet, and G. Mouret. Detection and quantification of multiple molecular species in mainstream cigarette smoke by continuous-wave terahertz spectroscopy. *Optics Letters*, 31:2356–2358, 2006.

[129] B. M. Fischer, M. Walther, and P. Uhd Jepsen. Far-infrared vibrational modes of DNA components studied by terahertz time-domain spectroscopy. *Physics in Medicine and Biology*, 47:3807, 2002.

[130] A. Markelz, S. Whitmire, J. Hillebrecht, and R. Birge. THz time domain spectroscopy of biomolecular conformational modes. *Physics in Medicine and Biology*, 47:3797, 2002.

[131] M. R. Leahy-Hoppa, M. J. Fitch, X. Zheng, L. M. Hayden, and R. Osiander. Wideband terahertz spectroscopy of explosives. *Chemical Physics Letters*, 434:227–230, 2007.

[132] E. Constable and R. A. Lewis. Optical parameters of ZnTe determined using continuous-wave terahertz radiation. *Journal of Applied Physics*, 112:063104, 2012.

[133] H. Zhong, J. Xu, X. Xie, T. Yuan, R. Reightler, E. Madaras, and X.-C. Zhang. Nondestructive defect identification with terahertz time-of-flight tomography. *IEEE Sensors Journal*, 5:203, 2005.

[134] C. A. Schmuttenmaer. Exploring dynamics in the far-infrared with terahertz spectroscopy. *Chemical Reviews*, 104:1759–1779, 2004.

[135] M. C. Beard, G. M. Turner, and C. A. Schmuttenmaer. Transient photoconductivity in GaAs as measured by time-resolved terahertz spectroscopy. *Physical Review B*, 62:15764, 2000.

[136] H. Choi, F. Borondics, D. A. Siegel, S. Y. Zhou, M. C. Martin, A. Lanzara, and R. A. Kaindl. Broadband electromagnetic response and ultrafast dynamics of few-layer epitaxial graphene. *Applied Physics Letters*, 94:172102, 2009.

[137] R. Valdés Aguilar, A. V. Stier, W. Liu, L. S. Bilbro, D. K. George, N. Bansal, L. Wu, J. Cerne, A. G. Markelz, S. Oh, and N. P. Armitage. Terahertz response and colossal Kerr rotation from the surface states of the topological insulator Bi_2Se_3. *Physical Review Letters*, 108:087403, 2012.

[138] F. Keffer and C. Kittel. Theory of antiferromagnetic resonance. *Physical Review*, 85:329–337, 1952.

[139] J. P. Jakubovics. *Magnetism and Magnetic Materials*. The Institute of Metals, London, 1987.

[140] E. W. Lee. *Magnetism*. Cox & Wyman, Ltd, London, 1963.

[141] W. Gilbert. *De Magnete*. Dover Publications, New York, 1958.

[142] P. A. M. Dirac. On the theory of quantum mechanics. *Proceedings of the Royal Society of London*, 112:762, 1926.

[143] W. Heisenberg. Mehrkörperproblem und Resonanz in der Quantenmechanik. *Zeitschrift für Physik*, 38:411–426, 1926.

[144] L. Néel. Propriétés magnétiques des ferrites; Ferrimagnétisme et antiferro-magnétisme. *Anneles des Physique*, 3:137, 1948.

[145] L. Néel. Antiferromagnetic interactions. *Anneles des Physique*, 2:261, 1967.

[146] L. Néel. Nobel prize lecture 1970. Nobelprize.org. Nobel Media AB 2014, [Online accessed: 14-Oct-2014]. URL http://www.nobelprize.org/nobel_prizes/physics/laureates/1970/.

[147] B. N. Brockhouse and C. G. Shull. Nobel prize lecture 1994. Nobelprize.org. Nobel Media AB 2014, [Online accessed: 14-Oct-2014]. URL http://www.nobelprize.org/nobel_prizes/physics/laureates/1994/.

[148] IUPAC. Compendium of chemical terminology, 2nd ed. (the "gold book"). Compiled by A. D. McNaught and A. Wilkinson. Blackwell Scientific Publications, Oxford (1997). XML on-line corrected version: http://goldbook.iupac.org (2006-) created by M. Nic, J. Jirat, B. Kosata; updates compiled by A. Jenkins. [Online accessed: 15-Oct-2014].

[149] C. N. R. Rao and B. Raveau. *Transition Metal Oxides: Structure, Properties, and Synthesis of Ceramic Oxides.* Wiley-VCH, New York, 2nd edition, 1998.

[150] H. A. Kramers. L'interaction entre les atomes magnétogènes dans un cristal paramagnétique. *Physica*, 1:182–192, 1934.

[151] P. W. Anderson. Antiferromagnetism. Theory of superexchange interaction. *Physical Review*, 79:350, 1950.

[152] J. B. Goodenough. Theory of the role of covalence in the perovskite-type manganites [La, M(II)]MnO_3. *Physical Review*, 100:564, 1955.

[153] J. B. Goodenough. An interpretation of the magnetic properties of the perovskite-type mixed crystals $La_{1-x}Sr_xCoO_{3-\lambda}$. *Journal of Physics and Chemistry of Solids*, 6:287–297, 1958.

[154] J. Kanamori. Superexchange interaction and symmetry properties of electron orbitals. *Journal of Physics and Chemistry of Solids*, 10:87–98, 1959.

[155] H. Kato, M. Yamada, H. Yamauchi, H. Hiroyoshi, H. Takei, and H. Watanabe. Metamagnetic phase transitions in $FeTiO_3$. *Journal of the Physical Society of Japan*, 51:1769–1777, 1982.

[156] J. M. D. Coey, M. Venkatesan, and C. B. Fitzgerald. Donor impurity band exchange in dilute ferromagnetic oxides. *Nature Materials*, 4:173–179, 2005.

[157] A. Loidl, H. von Loehneysen, and G. M. Kalvius. Multiferroics. *Journal of Physics: Condensed Matter*, 20:430301, 2008.

[158] N. A. Hill. Why are there so few magnetic ferroelectrics? *Journal of Physical Chemistry B*, 104:6604–6709, 2000.

[159] T. Kimura, T. Goto, H. Shintani, K. Ishizaka, T. Arima, and Y. Tokura. Magnetic control of ferroelectric polarization. *Nature*, 426:55–58, 2003.

[160] N. Hur, S. Park, P. A. Sharma, J. S. Ahn, S. Guha, and S.-W. Cheong. Electric polarization reversal and memory in a multiferroic material induced by magnetic fields. *Nature*, 429:329–395, 2004.

[161] D. Lebeugle, D. Colson, A. Forget, M. Viret, A. M. Bataille, and A. Gukasov. Electric-field-induced spin flop in $BiFeO_3$ single crystals at room temperature. *Physical Review Letters*, 100:227602, 2008.

[162] A. Pimenov, A. M. Shuvaev, A. A. Mukhin, and A. Loidl. Electromagnons in multiferroic manganites. *Journal of Physics: Condensed Matter*, 20:434209, 2008.

[163] A. Pimenov, A. A. Mukhin, V. Yu. Ivanov, V. D. Travkin, A. M. Balbashov, and A. Loidl. Possible evidence for electromagnons in multiferroic manganites. *Nature Physics*, 2:97–100, 2006.

[164] A. B. Sushkov, R. Valdés Aguilar, S. Park, S.-W. Cheong, and H. D. Drew. Electromagnons in multiferroic YMn_2O_5 and $TbMn_2O_5$. *Physical Review Letters*, 98: 027202, 2007.

[165] D. Senff, P. Link, K. Hradil, A. Hiess, L. P. Regnault, Y. Sidis, N. Aliouane, D. N. Argyriou, and M. Braden. Magnetic excitations in multiferroic $TbMnO_3$: Evidence for a hybridized soft mode. *Physical Review Letters*, 98:137206, 2007.

[166] V. G. Bhide and M. S. Multani. Mössbauer effect in ferroelectric-antiferromagnetic $BiFeO_3$. *Solid State Communications*, 3:271–274, 1965.

[167] S. Neusser and D. Grundler. Magnonics: Spin waves on the nanoscale. *Advanced Materials*, 21:2927–2932, 2009.

[168] C. Mathieu, J. Jorzick, A. Frank, S. O. Demokritov, A. N. Slavin, B. Hillebrands, B. Bartenlian, C. Chappert, D. Decanini, F. Rousseaux, and E. Cambril. Lateral quantization of spin waves in micron size magnetic wires. *Physical Review Letters*, 81:3968, 1998.

[169] J. Jorzick, S. O. Demokritov, B. Hillebrands, M. Bailleul, C. Fermon, K. Y. Gus-lienko, A. N. Slavin, D. V. Berkov, and N. L. Gorn. Spin wave wells in nonellipsoidal micrometer size magnetic elements. *Physical Review Letters*, 88:047204, 2002.

[170] J. Podbielski, F. Giesen, and D. Grundler. Spin-wave interference in microscopic rings. *Physical Review Letters*, 96:167207, 2006.

[171] M. Krawczyk and D. Grundler. Review and prospects of magnonic crystals and devices with reprogrammable band structure. *Journal of Physics: Condensed Matter*, 26:123202, 2014.

[172] M. Johnson and R. H. Silsbee. Interfacial charge-spin coupling: Injection and detection of spin magnetization in metals. *Physical Review Letters*, 55:1790, 1985.

[173] M. N. Baibich, J. M. Broto, A. Fert, F. Nguyen Van Dau, F. Petroff, P. Etienne, G. Creuzet, A. Friederich, and J. Chazelas. Giant magnetoresistance of (001)Fe/(001)Cr magnetic superlattices. *Physical Review Letters*, 61:2472, 1988.

[174] G. Binasch, P. Grünberg, F. Saurenbach, and W. Zinn. Enhanced magnetoresistance in layered magnetic structures with antiferromagnetic interlayer exchange. *Physical Review B*, 39:4828(R), 1989.

[175] A. Fert and P. Grünberg. Nobel prize lecture 2007. Nobelprize.org. Nobel Media AB 2014, [Online accessed: 16-Oct-2014]. URL http://www.nobelprize.org/nobel_prizes/physics/laureates/2007/.

[176] M. P. Walser, C. Reichl, W. Wegscheider, and G. Salis. Direct mapping of the formation of a persistent spin helix. *Nature Physics*, 8:757–762, 2012.

[177] Y. Kajiwara, K. Harii, S. Takahashi, J. Ohe, K. Uchida, M. Mizuguchi, H. Umezawa, H. Kawai, K. Ando, K. Takanashi, S. Maekawa, and E. Saitoh. Transmission of electrical signals by spin-wave interconversion in a magnetic insulator. *Nature*, 464: 262–266, 2010.

[178] M. Faraday. *Faraday's diary : Being the various philosophical notes of experimental investigation by Michael Faraday; under the editorial supervision of Thomas Martin.* Royal Institution of Great Britain, London, 1932.

[179] J. K. Furdyna. Diluted magnetic semiconductors. *Journal of Applied Physics*, 64: R29, 1988.

[180] H. A. Haus, E. P. Ippen, and K. Tamura. Additive-pulse modelocking in fiber lasers. *IEEE Journal of Quantum Electronics*, 30:200–208, 1994.

[181] I. I. Rabi. Nobel prize lecture 1944. Nobelprize.org. Nobel Media AB 2014, [Online accessed: 20-Oct-2014]. URL http://www.nobelprize.org/nobel_prizes/physics/laureates/1944/.

[182] E. D. Palik and J. K. Furdyna. Infrared and microwave magnetoplasma effects in semiconductors. *Reports on Progress in Physics*, 33:1193–1322, 1970.

[183] G. Dresselhaus, A. F. Kip, and C. Kittel. Cyclotron resoance of electrons and holes in silicon and germanium crystals. *Physical Review*, 98:368–384, 1955.

[184] C. Kittel. On the theory of ferromagnetic resoance absorption. *Physical Review*, 73: 155–161, 1948.

[185] C. Kittel. Excitation of spin waves in a ferromagnet by a uniform rf field. *Physical Review*, 110:1295–1297, 1958.

[186] C. Kittel. Theory of antiferromagnetic resonance. *Physical Review*, 82:565–565, 1951.

[187] S. Foner. High-Field antiferromagnetic resonance in MnF, using pulsed fields and millimeter wavelengths. *Physical Review*, 107:683–685, 1957.

[188] A. J. Sievers and M. Tinkham. Far infrared antiferromagnetic resonance in MnO and NiO. *Physical Review*, 129:1566–1569, 1963.

[189] A. J. Sievers and M. Tinkham. Far infrared spectra of rare-earth iron garnets. *Physical Review*, 129:1995–2004, 1963.

[190] P. L. Richards. Farinfrared magnetic resonance in CoF_2, NiF_2, $KNiF_3$, and YbIG. *Journal of Applied Physics*, 34:1237–1238, 1963.

[191] P. L. Richards. Antiferromagnetic resonance in CoF_2, NiF_2, and $MnCO_3$. *Journal of Applied Physics*, 35:850–851, 1964.

[192] P. L. Richards. Far-infrared magnetic resonance in NiF_2. *Physical Review*, 138: A1769–A1775, 1965.

[193] I. S. Jacobs, S. Roberts, and P. E. Lawrence. Antiferromagnetic resonance in $CoCl_2$ and $FeCl_2$. *Journal of Applied Physics*, 36:1197–1198, 1965.

[194] L. G. Van Uitert, R. C. Sherwood, W. A. Bonner, W. H. Grodkiewicz, L. Pictroski, and G. Zydzik. Rare earth orthoferrites for bubble domain devices. *Materials Research Bulletin*, 5:153–162, 1970.

[195] J. R. Ferraro, K. Nakamoto, and C. W. Brown. *Introductory Raman Spectroscopy.* Elsevier Science, USA, 2003.

[196] N. Koshizuka and S. Ushioda. Inelastic-light-scattering of magnon softening in $ErFeO_3$. *Physical Review B*, 22:5394–5399, 1980.

[197] R. M. White, R. J. Nemanich, and C. Herring. Light scattering from magnetic excitations in orthoferrites. *Physical Review Letters*, 25:1822–1836, 1982.

[198] S. Venugoplan, M. Dutta, A. K. Ramdas, and J. P. Remeika. Raman scattering study of magnons at the spin-reorientation transitions of $TbFeO_3$ and $TmFeO_3$. *Physical Review B*, 27:3115–3118, 1983.

[199] S. Venugopalan, M. Dutta, A. K. Ramdas, and J. P. Remeika. Magnetic and vibrational excitations in rare-earth orthoferrites: A Raman scattering study. *Physical Review B*, 31:1490–1497, 1985.

[200] N. Koshizuka and K. Hayashi. Raman scattering from magnon excitations in $RFeO_3$. *Journal of the Physical Society of Japan*, 57:4418–4428, 1988.

[201] G. Song, J. Jiang, X. Wang, Z. Jin, X. Lin, G. Ma, and S. Cao. Selective excitation of spin resonance in orthoferrite $PrFeO_3$ with impulsive polarized terahertz radiation. *Journal of Applied Physics*, 114:243104, 2013.

[202] M. Yoshikiyo, A. Namai, M. Nakajima, K. Yamaguchi T. Suemoto, and S.-i. Ohkoshi. High-frequency millimeter wave absorption of indium-substituted ϵ-Fe_2O_3 spherical nanoparticles. *Journal of Applied Physics*, 115:172613, 2014.

[203] N. Kida, Y. Ikebe, Y. Takahashi, J. P. He, Y. Kaneko, Y. Yamasaki, R. Shimano, T. Arima, N. Nagaosa, and Y. Tokura. Electrically driven spin excitation in the ferroelectric magnet $DyMnO_3$. *Physical Review B*, 78:104414, 2008.

[204] N. Kida, D. Okuyama, S. Ishiwata, Y. Taguchi, R. Shimano, K. Iwasa, T. Arima, and Y. Tokura. Electric-dipole-active magnetic resonance in the conical-spin magnet $Ba_2Mg_2Fe_{12}O_{22}$. *Physical Review B*, 80:220406(R), 2009.

[205] N. Kida, S. Kumakura, S. Ishiwata, Y. Taguchi, and Y. Tokura. Gigantic terahertz magnetochromism via electromagnons in the hexaferrite magnet $Ba_2Mg_2Fe_{12}O_{22}$. *Physical Review B*, 83:064422, 2011.

[206] N. Kida and Y. Tokura. Terahertz magnetoelectric response via electromagnons in magnetic oxides. *Journal of Magnetism and Magnetic Materials*, 324:3512–3515, 2012.

[207] A. V. Kimel, A. Kirilyuk, P. A. Usachev, R. V. Pisarev, A. M. Balbashov, and Th. Rasing. Ultrafast non-thermal control of magnetization by instantaneous photomagnetic pulses. *Nature Letters*, 435:655–657, 2005.

[208] M. Nakajima, A. Namai, S. Ohkoshi, and T. Suemoto. Ultrafast time domain demonstration of bulk magnetization precession at zero magnetic field ferromagnetic resonance induced by terahertz magnetic field. *Optics Express*, 18:18260–18268, 2010.

[209] K. Yamaguchi, M. Nakajima, and T. Suemoto. Coherent control of spin precession motion with impulsive magnetic fields of half-cycle terahertz radiation. *Physical Review Letters*, 105:237201, 2010.

[210] K. Yamaguchi, T. Kurihara, Y. Minami, M. Nakajima, and T. Suemoto. Terahertz time-domain observation of spin reorientation in orthoferrite $ErFeO_3$ through magnetic free induction decay. *Physical Review Letters*, 110:137204, 2013.

[211] L. Chaix, S. de Brion, F. Lévy-Bertrand, V. Simonet, R. Ballou, B. Canals, P. Lejay, J. B. Brubach, G. Creff, F. Willaert, P. Roy, and A. Cano. THz magnetoelectric atomic rotations in the chiral compound $Ba_3NbFe_3Si_2O_{14}$. *Physical Review Letters*, 110:157208, 2013.

[212] L. Chaix, S. de Brion, S. Petit, R. Ballou, L.-P. Regnault, J. Ollivier, J.-B. Brubach, P. Roy, J. Debray, P. Lejay, A. Cano, E. Ressouche, and V. Simonet. Magneto- to electroactive transmutation of spin waves in ErMnO₃. *Physical Review Letters*, 112: 137201, 2014.

[213] C. Toulouse, J. Liu, Y. Gallais, M.-A. Measson, A. Sacuto, M. Cazayous, L. Chaix, V. Simonet, S. de Brion, L. Pinsard-Godart, F. Willaert, J. B. Brubach, P. Roy, and S. Petit. Lattice and spin excitations in multiferroic *h*-YMnO₃. *Physical Review B*, 89:094415, 2014.

[214] R. Mendis, C. Sydlo, J. Sigmund, M. Feiginov, P. Heissner, and H. L. Hartnagel. Tunable CW-THz system with a log-periodic photoconductive emitter. *Solid-State Electronics*, 48:2041–2045, 2004.

[215] E. R. Brown, F. W. Smith, and K. A. McIntosh. Coherent milimeter-wave generation by heterodyne conversion in low-temperature-grown GaAs photoconductors. *Journal of Applied Physics*, 73:1480–1484, 1993.

[216] E. Constable. Tunable continuous-wave terahertz spectroscopy. Honours Thesis, University of Wollongong, School of Physics, 2010.

[217] Purdue University. Scanning electron microscope. [Online accessed: 23-Oct-2014]. URL http://www.purdue.edu/ehps/rem/rs/sem.htm.

[218] W. H. Bragg and W. L. Bragg. Nobel prize lecture 1915. Nobelprize.org. Nobel Media AB 2014, [Online accessed: 26-Oct-2014]. URL http://www.nobelprize.org/nobel_prizes/physics/laureates/1915/.

[219] K. Leuven. X-ray diffraction. Bruker D8 Discover 2010, [Online accessed 27-Oct-2014]. URL https://fys.kuleuven.be/iks/nvsf/experimental-facilities/x-ray-diffraction-2013-bruker-d8-discover.

[220] S. A. Danilkin, M. Yethiraj, T. Saerbeck, F. Klose, C. Ulrich, J. Fujioka, S. Miyasaka, Y. Tokura, and B. Keimer. TAIPAN: First results from the thermal triple-axis spectrometer at opal research reactor. *Journal of Physics: Conference Series*, 340: 012003, 2012.

[221] I. Dzyaloshinsky. A thermodynamic theory of "weak" ferromagnetism of antiferromagnetics. *Journal of Physics and Chemistry of Solids*, 4:241–255, 1958.

[222] T. Moriya. New mechanism of anisotropic superexchange interaction. *Physical Review Letters*, 4:228–230, 1960.

[223] F. Hindle, A. Cuisset, R. Bocquet, and G. Mouret. Continuous-wave terahertz by photomixing: Applications to gas phase pollutant detection and quantification. *Comptes Rendus Physique*, 9:262–275, 2008.

[224] M. Born and E. Wolf. *Principles of Optics*. Cambridge University Press, Cambridge, 7th (expanded) edition, 1999.

[225] A. Nahata, A. S. Weling, and T. F. Heinz. A wideband coherent terahertz spectroscopy system using optical rectification and electro-optic sampling. *Applied Physics Letters*, 69:2321–2323, 1996.

[226] C. Winnewisser, P. Uhd Jepsen, M. Schall, V. Schyja, and H. Helm. Electro-optic detection of THz radiation in $LiTaO_3$, $LiNbO_3$ and ZnTe. *Applied Physics Letters*, 70:3069–3071, 1997.

[227] Z. G. Lu, P. Campbell, and X.-C. Zhang. Free-space electro-optic sampling with a high-repetition-rate regenerative amplified laser. *Applied Physics Letters*, 71:593–595, 1997.

[228] P. Y. Han and X.-C. Zhang. Coherent, broadband midinfrared terahertz beam sensors. *Applied Physics Letters*, 73:3049, 1998.

[229] M. Sajadi, M. Wolf, and T. Kampfrath. Terahertz field enhancement via coherent superposition of the pulse sequences after a single optical-rectification crystal. *Applied Physics Letters*, 104:091118, 2014.

[230] S. Vidal, J. Degert, M. Tondusson, E. Freysz, and J. Oberlé. Optimized terahertz generation via optical rectification in ZnTe crystals. *Journal of the Optical Society of America*, 31:149–153, 2014.

[231] Z. Ollmann, J. A. Fülöp, J. Hebling, and G. Almási. Design of a high-energy ter-ahertz pulse source based on ZnTe contact grating. *Optics Communications*, 315: 159–163, 2014.

[232] M. Aven and B. Segall. Carrier mobility and shallow impurity states in ZnSe and ZnTe. *Physical Review*, 130:81–91, 1963.

[233] D. Berlincourt, H. Jaffe, and L. R. Shlozawa. Electroelastic properties of the sulfides, selenides, and tellurides of zinc and cadmium. *Physical Review*, 129:1009–1017, 1963.

[234] A. G. Fischer, J. N. Carides, and J. Dresner. Preparation and properties of n-type ZnTe. *Solid State Communications*, 2:157–159, 1964.

[235] D. T. F. Marple. Refractive index of ZnSe, ZnTe and CdTe. *Journal of Applied Physics*, 35:539–542, 1964.

[236] A. Manabe, A. Mitsuishi, and H. Yoshinaga. Infrared lattice reflection spectra of II-VI compounds. *Japanese Jounral of Applied Physics*, 6:593–600, 1967.

[237] S. S. Mitra, O. Brafman, W. B. Daniels, and R. K. Crawford. Pressure-induced phonon frequency shifts measured by Raman scattering. *Physical Review*, 186:942–944, 1969.

[238] D. L. Rode. Electron mobility in II-VI semiconductors. *Physical Review B*, 2:4036–4044, 1970.

[239] R. Beserman and M. Balkanski. Optical properties of impurities in blende type II-VI semiconductors compounds. *Journal of Physics and Chemistry of Solids*, 31: 355–361, 1970.

[240] T. Hattori, Y. Homma, and A. Mitsuishi. Indices of refraction of ZnS, ZnSe, ZnTe, CdS and CdTe in the far infrared. *Optics Communications*, 7:229–232, 1973.

[241] K. Hidaka and T. Kouno. A method for measuring electric field in space charge by means of Pockels device. *Journal of Electrostatics*, 11:195–211, 1982.

[242] D. L. Peterson, A. Petrou, W. Giriat, A. K. Ramdas, and S. Rodriguez. Raman scattering from the vibrational modes in $Zn_{1-x}Mn_xTe$. *Physical Review B*, 33:1160–1165, 1986.

[243] R. E. Ruda. Compensation and transport characteristics of n-ZnTe. *Journal of Physics D: Applied Physics*, 24:1158–1162, 1991.

[244] E. Oh, R. G. Alonso, I. Miotkowski, and A. K. Ramdas. Raman sacttering from vibrational and electonic excitations in a II-VII quaternary compound: $Cd_{1-x-y}Zn_xMn_yTe$. *Physical Review B*, 45:10934–10941, 1992.

[245] G. Gallot, J. Zhang, R. W. McGowan, T. I. Jeon, and D. Grischkowsky. Measurements of the THz absorption and dispersion of ZnTe and their relevance to the electro-optic detection of THz radiation. *Applied Physics Letters*, 74:3450–3452, 1999.

[246] M. Schall, M. Walther, and P. Uhd Jepsen. Fundamental and second-order phonon processes in CdTe and ZnTe. *Physical Review B*, 64:094301, 2001.

[247] L. J. Bignell and R. A. Lewis. Reflectance studies of candidate THz emitters. *Journal of Materials Science: Materials in Electronics*, 20:S326–S331, 2009.

[248] S. Mnasri, S. A. Nasrallah, N. Sfina, N. Bouarissa, and M. Said. Electronic, lattice vibration and mechanical properties of CdTe, ZnTe, MnTe, MgTe, HgTe and their ternary alloys. *Semiconductor Science and Technology*, 24:1–8, 2009.

[249] O. Morikawa, M. Tonouchi, and M. Hangyo. Sub-THz spectroscopic system using a multimode laser diode and photoconductive antenna. *Applied Physics Letters*, 75: 3772–3774, 1999.

[250] M. L. Johnson. Nonlinear least-squares fitting methods. *Methods in Cell Biology*, 84:781–805, 2008.

[251] M. L. Johnson. Parameter correlations while curve fitting. *Methods in Enzymology*, 321:425–446, 2000.

[252] M. L. Johnson and L. M. Faunt. Parameter estimation by least-squares methods. *Methods in Enzymology*, 210:1–37, 1992.

[253] K. Momma and F. Izumi. VESTA: A three-dimensional visualization system for electronic and structural analysis. *Journal of Applied Crystallography*, 41:653–658, 2008.

[254] B. Efron and G. Gong. A leisurely look at the bootstrap, the jacknife, and cross-validation. *The American Statistician*, 37:36–48, 1983.

[255] J. Mangeney, F. Meng, D. Gacemi, E. Peytavit, J. F. Lampin, and T. Akalin. Terahertz generation and power limits in $In_{0.53}Ga_{0.47}As$ photomixer coupled to transverse-electromagnetic-horn antenna driven at 1.55 μm wavelengths. *Applied Physics Letters*, 97:161109, 2010.

[256] S.-W. Cheong and M. Mostovoy. Multiferroics: a magnetic twist for ferroelectricity. *Nature Materials*, 6:13–20, 2007.

[257] K. F. Wang, J. M. Liua, and Z. F. Ren. Multiferroicity: The coupling between magnetic and polarization orders. *Advances in Physics*, 58:321–448, 2009.

[258] H. Katsura, A. V. Balatsky, and N. Nagaosa. Dynamical magnetoelectric coupling in helical magnets. *Physical Review Letters*, 98:027203, 2007.

[259] L. Balents. Spin liquids in frustrated magnets. *Nature*, 464:199–208, 2010.

[260] T.-H. Han, J. S. Helton, S. Chu, D. G. Nocera, J. A. Rodriguez-Rivera, C. Broholm, and Y. S. Lee. Fractionalized excitations in the spin-liquid state of a kagome-lattice antiferromagnet. *Nature*, 492:406–410, 2012.

[261] K. H. Miller, P. W. Stephens, C. Martin, E. Constable, R. A. Lewis, H. Berger, G. L. Carr, and D. B. Tanner. Infrared phonon anomaly and magnetic excitations in single-crystal $Cu_3Bi(SeO_3)_2O_2Cl$. *Physical Review B*, 174104, 2012.

[262] D. J. Arenas, L. V. Gasparov, W. Qiu, J. C. Nino, C. H. Patterson, and D. B. Tanner. Raman study of phonon modes in bismuth pyrochlores. *Physical Review B*, 82:214302, 2010.

[263] P. Millet, B. Bastide, V. Pashchenko, S. Gnatchenko, V. Gapon, Y. Ksari, and A. Stepanov. Syntheses, crystal structures and magnetic properties of francisite compounds $Cu_3Bi(SeO_3)_2O_2X$ (X=Cl, Br and I). *Journal of Materials Chemistry*, 11:1152–1157, 2001.

[264] Z. Wang, M. Schmidt, Y. Goncharov, V. Tsurkan, H.-A. Krug von Nidda, A. Loidl, and J. Deisenhofer. Terahertz spectroscopy in the pseudo-kagome system $Cu_3Bi(SeO_3)_2O_2Br$. *Physical Review B*, 86:174411, 2012.

[265] M. Pregelj, O. Zaharko, A. Günther, A. Loidl, V. Tsurkan, and S. Guerrero. Magnetic ground state and two-dimensional behavior in pseudo-kagome layered system $Cu_3Bi(SeO_3)_2O_2Br$. *Physical Review B*, 86:144409, 2012.

[266] A. Pring, B. M. Gatehouse, and W. D. Birch. Francisite, $Cu_3Bi(SeO_3)_2O_2Cl$, new mineral from Iron Monarch, South Australia: Description and crystal structure. *American Mineralogist*, 75:1421–1425, 1990.

[267] K. V. Zakharov, E. A. Zvereva, P. S. Berdonosov, E. S. Kuznetsova, V. A. Dolgikh, L. Clark, C. Black, P. Lightfoot, W. Kockelmann, Z. V. Pchelkina, S. V. Streltsov, O. S. Volkova, and A. N. Vasiliev. Thermodynamic properties, electron spin resonance, and underlying spin model in $Cu_3Y(SeO_3)_2O_2Cl$. *Physical Review B*, 90: 214417, 2014.

[268] I. Rousochatzakis, J. Richter, R. Zinke, and A. A. Tsirlin. Frustration and Dzyaloshinsky-Moriya anisotropy in the kagome francisites $Cu_3Bi(SeO_3)_2O_2X$ (x = br, cl). *Physical Review B*, 91:024416, 2015.

[269] R. Alben. Theory of magnetc-dipole exciteations in ferrous chloride. *Journal of the Physical Society of Japan*, 26:261–278, 1969.

[270] C. Kittel. On the gyromagnetic ratio and spectroscopic splitting factor of ferromagnetic substances. *Physical Review*, 76:743–748, 1949.

[271] J. Deisenhofer, R. M. Eremina, A. Pimenov, T. Gavrilova, H. Berger, M. Johnsson, P. Lemmens, H.-A. Krug von Nidda, A. Loidl, K.-S. Lee, and M.-H. Whangbo. Structural and magnetic dimers in the spin-gapped system $CuTe_2O_5$. *Physical Review B*, 74:174421, 2006.

[272] V. D. Buchel'nikov, I. V. Bychkov, and V. G. Shavrov. Coupled magnetoelastic and electromagnetic waves in uniaxial crystals having spiral magnetic structure. *Journal of Magnetism and Magnetic Materials*, 118:169–174, 1993.

[273] Y. Tokunaga, S. Iguchi, T. Arima, and Y. Tokura. Magnetic-field-induced ferroelectric state in DyFeO$_3$. *Physical Review Letters*, 101:097205, 2008.

[274] J.-H. Lee, Y. K. Jeong, J. H. Park, M.-A. Oak, H. M. Jang, J. Y. Son, and J. F. Scott. Spin-canting-induced improper ferroelectricity and spontaneous magnetization reversal in SmFeO$_3$. *Physical Review Letters*, 207:117201, 2011.

[275] Y. Tokunaga, N. Furukawa, H. Sakai, Y. Taguchi, T. Arima, and Y. Tokura. Composite domain walls in a multiferroic perovskite ferrite. *Nature Materials*, 8:558–562, 2009.

[276] R. L. White. Review of recent work on the magnetic and spectroscopic properties of the rare-earth orthoferrites. *Journal of Applied Physics*, 40:1061–1069, 1969.

[277] D. Treves. Magnetic studies of some orthoferrites. *Physical Review*, 125:1843–1853, 1962.

[278] J. R. Shane. Resonance frequencies of the orthoferrites in the spin reorientation region. *Physical Review Letters*, 20:728–732, 1968.

[279] T. Yamaguchi. Theory of spin reorientation in rare-earth orthochromites and orthoferrites. *Journal of Physics and Chemistry of Solids*, 35:479–500, 1974.

[280] S. M. Shapiro, J. D. Axe, and J. P. Remeika. Neutron-scattering studies of spin waves in rare-earth orthoferrites. *Physical Review B*, 10:2014–2020, 1974.

[281] K. B. Aring and A. J. Sievers. Role of ytterbium spins in the spin reorientation in YbFeO$_3$. *Journal of Applied Physics*, 41:1197–1198, 1970.

[282] T. Nagamiya, K. Yosida, and R. Kubo. Antiferromagnetism. *Advances in Physics*, 4:1–112, 1955.

[283] A. R. Jha. *Rare Earth Materials: Properties and Applications*. Taylor and Francis, 2014.

[284] J. P. Remeika. Growth of single crytsal rare earth orthoferrites and related compounds. *Journal of the American Chemical Society*, 78:4259–4260, 1956.

[285] S. Geller. Crystal structure of gadolinium orthoferrite, $GdFeO_3$. *Journal of Chemical Physics*, 24:1236–1239, 1956.

[286] W. C. Koehler and E. O. Wollan. Neutron diffraction study of the magnetic properties of perovskite-like compounds $LaBO_3$. *Journal of Physics and Chemistry of Solids*, 2:100–106, 1957.

[287] W. C. Koehler, E. O. Wollan, and M. K. Wilkinson. Neutron diffraction study of the magnetic properties of rare-earth-iron perovskites. *Physical Review*, 118:58–70, 1960.

[288] M. A. Gilleo. Magnetic properties of a gadolinium orthoferrite, $GdFeO_3$, crystal. *The Journal of Chemical Physics*, 24:1239–1243, 1956.

[289] R. M. Bozorth, H. J. Williams, and D. E. Walsh. Magnetic properties of some orthoferrites and cyanides at low temperatures. *Physical Review*, 103:572–578, 1956.

[290] R. M. Bozorth, V. Kramer, and J. P. Remeika. Magnetization in single crystals of some rare-earth orthoferrites. *Physical Review Letters*, 1:3–4, 1958.

[291] D. L. Wood, L. M. Holmes, and J. P. Remeika. Exchange fields and optical zeeman effect in $ErFeO_3$. *Physical Review*, 185:689–695, 1969.

[292] H. Wu, S. Cao, M. Liu, Y. Cao, B. Kang, J. Zhang, and W. Ren. Twofold spin reorientation and field-induced incomplete phase transition in single-crystal $Dy_{0.5}Pr_{0.5}FeO_3$. *Physical Review B*, 90:144425, 2014.

[293] H. Pinto, G. Shachar, and H. Shaked. Spin reorientation in $ErFeO_3$ single crystals observed by neutron diffraction. *Physical Review B*, 3:3661–3663, 1971.

[294] G. Gorodetsky, B. Sharon, and S. Shtrikman. Linear effect of the magnetic field on the magnetic susceptibility in antiferromagnetic $DyFeO_3$. *Solid State Communications*, 5:739–741, 1967.

[295] R. W. Grant and S. Geller. Mechanism of spin reorientation in $ErFeO_3$. *Solid State Communications*, 7:1291–1294, 1969.

[296] G. Gorodetsky and B. Lüthi. Sound-wave-soft-mode interaction near displacive phase transitions: Spin reorientation in $ErFeO_3$. *Physical Review B*, (9):3688–3698, 1970.

[297] H. Horner and C. M. Varma. Nature of spin-reorientation transitions. *Physical Review Letters*, 20:845–846, 1968.

[298] G. F. Herrmann. Resonance and high frequency susceptibility in canted antiferromagnetic substances. *Journal of Physics and Chemistry of Solids*, 24:597–606, 1963.

[299] R. C. LeCraw, R. Wolfe, E. M. Gyorgy, F. B. Hagedorn, J. C. Hensel, and J. P. Remeika. Resonance in canted structures. *Journal of Applied Physics*, 39:1019–1020, 1968.

[300] L. M. Levinson, M. Luban, and S. Shtrikman. Microscopic model for reorientation of the easy axis of magnetization. *Physical Review*, 187:715–722, 1969.

[301] J. O. Artman, J. C. Murphy, and S. Foner. Magntic anisotropy in antiferromagnetic corundum-type sesquioxides. *Physical Review*, 138:A912–917, 1965.

[302] R. C. Sherwood, J. P. Remeika, and H. J. Williams. Domain behavior in some transparent magnetic oxides. *Journal of Applied Physics*, 30:217–225, 1959.

[303] T. H. O'Dell. Magnetic bubble domain devices. *Reports on Progress in Physics*, 49:589–620, 1986.

[304] W. Sławiṅski, R. Przenioslo, I. Sosnowska, and E. Suard. Spin reorientation and structural changes in NdFeO$_3$. *Journal of Physics: Condensed Matter*, 17:4605–4614, 2005.

[305] M. Marezio, J. P. Remeika, and P. D. Dernier. The crystal chemistry of the rare earth orthoferrites. *Acta Crystallographica*, B26:2008–2022, 1970.

[306] D. Treves. Studies on orthoferrites at the Weizmann Institute of Science. *Journal of Applied Physics*, 36:1033–1039, 1965.

[307] E. F. Bertaut. Lattice theory of spin configuration. *Journal of Applied Physics*, 33:1138, 1962.

[308] G. F. Herrmann. Magnetic resonances and susceptibility in orthoferrites. *Physical Review*, 133:A1334–A1344, 1964.

[309] S. Yuan, Y. Wang, M. Shao, F. Chang, B. Kang, Y. Isikawa, and S. Cao. Magnetic properties of $NdFeO_3$ single crystal in the spin reorientation region. *Journal of Applied Physics*, 109:07E141, 2011.

[310] C. H. Tsang, R. L. White, and R. M. White. Spinwave damping of domain walls in $YFeO_3$. *Journal of Applied Physics*, 49:6063, 1978.

[311] E. Constable, J. Horvat, D. L. Cortie, Z. Cheng, S. Yuan, S. Cao, and R. A. Lewis. High temperature anisotropy of $NdFeO_3$ determined using time-domain THz spectroscopy. In *International Conference on Infrared, Millimeter, and Terahertz Waves (IRMMW-THz)*, Mainz, Germany, 2013. doi: 10.1109/IRMMW-THz.2013.6665932.

[312] M. Tinkham. Low-lying spectrum of rare-earth iron garnets. *Physical Review*, 124: 311–320, 1961.

[313] S. J. Yuan, W. Ren, F. Hong, Y. B. Wang, J. C. Zhang, L. Bellaiche, S. X. Cao, and G. Cao. Spin switching and magnetization reversal in single-crystal $NdFeO_3$. *Physical Review B*, 87:184405, 2013.

[314] R. Przeniosło, I. Sosnowska, and P. Fischer. Magnetic moment ordering of Nd^{3+} ions in $NdFeO_3$. *Journal of Magnetism and Magnetic Materials*, 140–144:2153–2154, 1995.

[315] R. Przeniosło, I. Sosnowska, P. Fischer, W. Marti, F. Bartolomé, J. Bartolomé, E. Palacios, and R. Sonntag. Magnetic moment ordering of Nd^{3+} and Fe^{3+} in $NdFeO_3$ at low temperature. *Journal of Magnetism and Magnetic Materials*, 160: 370–371, 1996.

[316] A. J. Sievers and M. Tinkham. Far-infrared exchange resonance in ytterbium iron garnet. *Physical Review*, 124:321, 1961.

[317] A. Pimenov, A. Shuvaev, A. Loidl, F. Schrettle, A. A. Mukhin, V. D. Travkin, V. Yu. Ivanov, and A. M. Balbashov. Magnetic and magnetoelectric excitations in $TbMnO_3$. *Physical Review Letters*, 102:107203, 2009.

[318] L. M. Helme, A. T. Boothroyd, R. Coldea, and D. Prabhakaran. Spin gaps and magnetic structure of Na_xCoO_2. *Physical Review B*, 73:054405, 2006.

[319] M. D. Lumsden, J. L. Robertson, and M. Yethiraj. UB matrix implementation for inelastic neutron scattering experiments. *Journal of Applied Crystallography*, 38: 405–411, 2005.

[320] R. Przeniosło, I. Sosnowska, and P. Fischer. Crystal field excitations of $NdFeO_3$. *Journal of Magnetism and Magnetic Materials*, 140-144:2151–2152, 1995.

[321] R. Bidaux, J. E. Bouree, and J. Hammann. Dipolar interactions in rare earth orthoferrites–I. $YFeO_3$ and $HoFeO_3$. *Journal of Physics and Chemistry of Solids*, 34:1645–1655, 1974.

[322] Ya. B. Bazaliy, L. T. Tsymbal, G. N. Kakazei, and P. E. Wigen. The role of erbium magnetization anisotropy during the magnetic reorientation transitions in $ErFeO_3$. *Journal of Applied Physics*, 95:6622–6624, 2004.

[323] M. Tachiki and T. Nagamiya. Origin of the magnetic anisotropy energy of antiferromagnetic Cr_2O_3. *Journal of the Physical Society of Japan*, 13:452–455, 1958.

[324] Z. Y. Zhao, X. Zhao, H. D. Zhou, F. B. Zhang, Q. J. Li, C. Fan, X. F. Sun, and X. G. Li. Ground state and magnetic phase transitions of orthoferrite $DyFeO_3$. *Physical Review B*, 89:224405, 2014.

[325] L. Onsager. Crystal statistics. I. A two-dimensional model with an order-disorder transition. *Physical Review*, 65:117–149, 1944.

[326] Sergio Rodriguez. Linear antiferromagnetic chain. *Physical Review*, 116:1474–1477, 1959.

[327] E Dagotto, J Riera, and D Scalapino. Superconductivity in ladders and coupled planes. *Physical Review B*, 45:5744–5747, 1992.

[328] E Dagotto. Experiments on ladders reveal a complex interplay between a spin-gapped normal state and superconductivity. *Reports on Progress in Physics*, 62: 1525–1571, 1999.

[329] J. G. Bednorz and K. A. Müller. Possible high-T_c superconductivity in the Ba-La-Cu-O system. *Zeitschrift für Physik B Condensed Matter*, 64:189–193, 1986.

[330] M. K. Wu, J. R. Ashburn, C. J. Torng, P. H. Hor, R. L. Meng, L. Gao, Z. J. Huang, Y. Q. Wang, and C. W. Chu. Superconductivity at $93\,\mathrm{K}$ in a new mixed-phase Y-Ba-Cu-O compound system at ambient pressure. *Physical Review Letters*, 58:908–910, 1987.

[331] A. Mann. High-temperature superconductivity at 25: Still in suspense. *Nature*, 475: 280–282, 2011.

[332] J. Bardeen, L. N. Cooper, and J. R. Schrieffer. Microscopic theory of superconductivity. *Physical Review*, 106:162–164, 1957.

[333] C. Gros, D. Poilblanc, T. M. Rice, and F. C. Zhang. Superconductivity in correlated wavefunctions. *Physica C*, 153-155:543–548, 1988.

[334] G. Kotliar and J. Liu. Superexchange mechanism and d-wave superconductivity. *Physical Review B*, 38:5142–5145, 1988.

[335] E. M. McCarron III, M. A. Subramanian, and J. C. Calabrese. The incommensurate structure of $(\mathrm{Sr}_{14-x}\mathrm{Ca}_x)\mathrm{Cu}_{24}\mathrm{O}_{41}$ $(0 < x \sim 8)$ a superconductor byproduct. *Materials Research Bulletin*, 23:1355–1365, 1988.

[336] R. S. Eccleston, M. Azuma, and M. Takano. Neutron-scattering and susceptibility study of spin chains and spin ladders in $(\mathrm{Sr}_{0.8}\mathrm{Ca}_{0.2})_{14}\mathrm{Cu}_{24}\mathrm{O}_{41}$. *Physical Review B*, 53:R14721–R14724, 1996.

[337] M. Braden, J. Etrillard, A. Gukasov, U. Ammerahl, and A. Revcolevschi. Neutron diffraction study of the lattice distortion related to charge ordering in $\mathrm{Sr}_{14}\mathrm{Cu}_{24}\mathrm{O}_{41}$. *Physical Review B*, 69:214426, 2004.

[338] J. Etrillard, M. Braden, A. Gukasov, U. Ammerahl, and A. Revcolevschi. Structural aspects of the spin-ladder compound $\mathrm{Sr}_{14}\mathrm{Cu}_{24}\mathrm{O}_{41}$. *Physica C: Superconductivity*, 403:290–296, 2004.

[339] M. Kato, T. Adachi, and Y. Koike. Spin gap of the one-dimensional CuO_2 chains in $\mathrm{Sr}_{14-y}\mathrm{Y}_y\mathrm{Cu}_{24}\mathrm{O}_{41-\delta}$. *Physica C: Superconductivity*, 265:107–112, 1996.

[340] N. Motoyama, T. Osafune, T. Kakeshita, H. Eisaki, and S. Uchida. Effect of Ca substitution and pressure on the transport and magnetic properties of $Sr_{14}Cu_{24}O_{41}$ with doped two-leg Cu-O ladders. *Physical Review B*, 55:R3386–R3389, 1997.

[341] H. Eisaki, N. Motoyama, K. M. Kojima, S. Uchida, N. Takeshita, and N. Mori. Electronic phase diagram of the two-leg ladder compound $Sr_{14-x}Ca_xCu_{24}O_{41}$ as investigated by the transport property measurements. *Physica C*, 341-348:363–366, 2000.

[342] J. Akimitsu, M. Uehara, T. Nagata, S. Matsumoto, Y. Kitaoka, H. Takahashi, and N. Môri. Metal-insulator transition in the S = 1/2 spin ladder system $(Sr_{0.4}Ca_{0.6})_{14}Cu_{24-x}Co_xO_{41-\delta}$. *Physica C*, 263:475–481, 1996.

[343] M. Takigawa, N. Motoyama, H. Eisaki, and S. Uchida. Spin and charge dynamics in the hole-doped one-dimensional-chain–ladder composite material $Sr_{14}Cu_{24}O_{41}$: Cu NMR/NQR studies. *Physical Review B*, 57:1124–1140, 1998.

[344] F. C. Zhang and T. M. Rice. Effective Hamiltonian for the superconducting Cu oxides. *Physical Review B*, 37:3759–3761, 1988.

[345] T. Vuletić, B. Korin-Hamzić, T. Iveka, S. Tomić, B. Gorshunov, M. Dressel, and J. Akimitsu. The spin-ladder and spin-chain system $(La,Y,Sr,Ca)_{14}Cu_{24}O_{41}$: Electronic phases, charge and spin dynamics. *Physics Reports*, 428:169–258, 2006.

[346] M. Matsuda, K. Katsumata, H. Eisaki, N. Motoyama, S. Uchida, S. Shapiro, and G. Shirane. Magnetic excitations from the singlet ground state in the S=1/2 quasi-one-dimensional system $Sr_{14-x}Y_xCu_{24}O_{41}$. *Physical Review B*, 54:12199–12206, 1996.

[347] L. P. Regnault, J. P. Boucher, H. Moudden, J. E. Lorenzo, A. Hiess, U. Ammerahl, G. Dhalenne, and A. Revcolevschi. Spin dynamics in the magnetic chain arrays of $Sr_{14}Cu_{24}O_{41}$: A neutron inelastic scattering investigation. *Physical Review B*, 59:1055–1059, 1999.

[348] R. Eccleston, M. Uehara, J. Akimitsu, H. Eisaki, N. Motoyama, and S. Uchida. Spin dynamics of the spin-ladder dimer-chain material $Sr_{14}Cu_{24}O_{41}$. *Physical Review Letters*, 81:1702–1705, 1998.

[349] M. Kato, K. Shiota, and Y. Koike. Metal-insulator transition and spin gap in the spin-1/2 ladder system $Sr_{14-x}A_xCu_{24}O_{41}$ (A = Ba and Ca). *Physica C*, 258:284–292, 1996.

[350] T. Osafune, N. Motoyama, H. Eisaki, and S. Uchida. Optical study of the $Sr_{14-x}Ca_xCu_{24}O_{41}$ system: Evidence for hole-doped Cu_2O_3 ladders. *Physical Review Letters*, 78:1980–1983, 1997.

[351] V. Kataev, K.-Y. Choi, M. Grüninger, U. Ammerahl, B. Büchner, A. Freimuth, and A. Revcolevschi. Interplay of spin and charge dynamics in $Sr_{14-x}Ca_xCu_{24}O_{41}$. *Physical Review B*, 64:104422, 2001.

[352] M. Isobe, T. Ohta, M. Onoda, F. Izumi, S. Nakano, J. Q. Li, Y. Matsui, and E. Takayama-Muromachi. Structural and electrical properties under high pressure for the superconducting spin-ladder system $Sr_{0.4}Ca_{13.6}Cu_{24}O_{41+\delta}$. *Physical Review B*, 57:613–621, 1998.

[353] A. Rusydi, A. Goos, S. Binder, A. Eich, K. Botril, P. Abbamonte, X. Yu, M. B. H. Breese, H. Eisaki, Y. Fujimaki, S. Uchida, N. Guerassimova, R. Treusch, J. Feldhaus, R. Reininger, M. V. Klein, and M. Rubhausen. Electronic screening-enhanced hole pairing in two-leg spin ladders studied by high-resolution resonant inelastic x-ray scattering at Cu *M* edges. *Physical Review Letters*, 113:067001, 2014.

[354] J.-H. Chung, T. Egami, R. J. McQueeney, M. Yethiraj, M. Arai, T. Yokoo, Y. Petrov, H. A. Mook, Y. Endoh, S. Tajima, C. Frost, and F. Dogan. In-plane anisotropy and temperature dependence of oxygen phonon modes in $YBa_2Cu_3O_{6.95}$. *Physical Review B*, 67:014517, 2003.

[355] B. Ruzicka, L. Degiorgi, U. Ammerahl, G. Dhalenne, and A. Revcolevschi. Temperature dependence of the anisotropic electrodynamics in the ladder compounds $Sr_{14-x}Ca_xCu_{24}O_{41}$. *The European Physical Journal B*, 6:301–305, 1998.

[356] T. Osafune, N. Motoyama, H. Eisaki, S. Uchida, and S. Tajima. Pseudogap and collective mode in the optical conductivity spectra of hole-doped ladders in $Sr_{14-x}Ca_xCu_{24}O_{41}$. *Physical Review Letters*, 82:1313–1316, 1999.

[357] Z. V. Popović, M. J. Konstantinović, V. A. Ivanov, O. P. Khuong, R. Gajić, A. Vietkin, and V. V. Moshchalkov. Optical properties of the spin-ladder compound $Sr_{14}Cu_{24}O_{41}$. *Physical Review B*, 62:4963–4972, 2000.

[358] D. Hüvonen, U. Nagel, T. Rõõm, P. Haas, M. Dressel, J. Hwang, T. Timusk, Y. J. Wang, and J. Akimitsu. Magneto-optic far-infrared study of $Sr_{14}Cu_{24}O_{41}$: Triplet excitations in chains. *Physical Review B*, 76:134418, 2007.

[359] Y. Gotoh, I. Yamaguchi, Y. Takahashi, J. Akimoto, M. Goto, M. Onoda, H. Fujino, T. Nagata, and J. Akimitsu. Structural modulation, hole distribution, and hole-ordered structure of the incommensurate composite crystal $(Sr_2Cu_2O_3)_{0.70}CuO_2$. *Physical Review B*, 68:224108, 2003.

[360] Z. Hiroi, S. Amelinckx, G. Van Tendeloo, and N. Kobayashi. Microscopic origin of dimerization in the CuO_2 chains in $Sr_{14}Cu_{24}O_{41}$. *Physical Review B*, 54:15849–15855, 1996.

[361] B. Ruzicka, L. Degiorgi, U. Ammerahl, G. Dhalenne, and A. Revcolevschi. Optics in the ladder compounds $Sr_{14-x}Ca_xCu_{24}O_{41}$ and $Sr_{0.73}CuO_2$. *Physica C*, 317-318: 282–285, 1999.

[362] B. Gorshunov, P. Haas, T. Rõõm, M. Dressel, T. Vuletić, B. Korin-Hamzić, S. Tomić, J. Akimitsu, and T. Nagata. Charge-density wave formation in $Sr_{14-x}Ca_xCu_{24}O_{41}$. *Physical Review B*, 66:060580(R), 2002.

[363] T. Vuletić, B. Korin-Hamzić, S. Tomić, B. Gorshunov, P. Hass, T. Rõõm, M. Dressel, J. Akimitsu, T. Sasaki, and T. Nagata. Suppression of the charge-density-wave state in $Sr_{14}Cu_{24}O_{41}$ by calcium doping. *Physical Review Letters*, 90:257002, 2003.

[364] V. Vescoli, L. Degiorgi, W. Henderson, G. Grüner, K. P. Starkey, and L. K. Montgomery. Dimensionality-driven insulator-to-metal transition in the Bechgaard salts. *Science*, 281:1181–1184, 1998.

[365] M. Matsuda, T. Yosihama, K. Kakurai, and G. Shirane. Quasi-two-dimensional hole ordering and dimerized state in the CuO_2-chain layers in $Sr_{14}Cu_{24}O_{41}$. *Physical Review B*, 59:1060–1067, 1999.

[366] G. Blumberg, P. Littlewood, A. Gozar, B. S. Dennis, N. Motoyama, H. Eisaki, and S. Uchida. Sliding density wave in $Sr_{14}Cu_{24}O_{41}$ ladder compounds. *Science*, 297: 584–587, 2002.

[367] K.-Y. Choi, M. Grove, P. Lemmens, M. Fischer, G. Güntherodt, U. Ammerahl, B. Büchner, G. Dhalenne, A. Revcolevschi, and J. Akimitsu. Charge density waves in $Sr_{14-x}Ca_xCu_{24}O_{41}$: Electron correlations versus structural effects. *Physical Review B*, 73:104428, 2006.

[368] A. Gozar, G. Blumberg, P. B. Littlewood, B. S. Dennis, N. Motoyama, H. Eisaki, and S. Uchida. Collective density-wave excitations in two-leg $Sr_{14-x}Ca_xCu_{24}O_{41}$ ladders. *Physical Review Letters*, 91:087401, 2003.

[369] M. Osada, M. Kakihana, I. Nagai, T. Noji, T. Adachi, Y. Koike, J. Bäckström, M. Käll, and L. Börjesson. Raman-active phonons and their doping dependence in spin-ladder $Sr_{14}Cu_{24}O_{41}$. *Physica C*, 338:161–165, 2000.

[370] S. Sugai and M. Suzuki. Raman studies of spin and charge excitations in two-leg ladder $Sr_{14-x-y}Ca_xY_yCu_{24}O_{41}$. *Journal of Physics and Chemistry of Solids*, 62: 119–124, 2001.

[371] M. V. Abrashev, A. P. Litvinchuk, C. Thomsen, and V. N. Popov. Optical phonons in the orthorhombic double-chain $Sr_{1-x}Ca_xCuO_2$ ($x=0$, 0.5). *Physical Review B*, 55: 9136–9141, 1997.

[372] M. V. Abrashev, C. Thomsen, and M. Surtchev. Doping effects in the $Sr_{14}Cu_{24}O_{41}$-type structure: A Raman scattering study. *Physica C*, 280:297–303, 1997.

[373] E. T. Heyen, R. Liu, C. Thomsen, R. Kremer, and M. Cardona. Optical phonons in $YBa_2Cu_4O_8$ and $Y_2Ba_4Cu_7O_{15-\delta}$. *Physical Review B*, 41:11058, 1990.

[374] G. Kliche and Z. V. Popović. Far-infrared spectroscopic investigations on CuO. *Physical Review B*, 42:10060–10066, 1990.

[375] Z. V. Popović, S. D. Dević, V. N. Popov, G. Dhalenne, and A. Revcolevschi. Phonons in $CuGeO_3$ studied using polarized far-infrared and Raman-scattering spectroscopies. *Physical Review B*, 52:4185–4190, 1995.

[376] A. Sacuto, C. Julien, V. A. Shchukin, C. Perrin, and M. Mokhtari. Charge transfer in YBa$_2$Cu$_3$O$_6$ doped with fluorine: Infrared refectance and Raman scattering studies. *Physical Review B*, 52:7619–7628, 1995.

[377] M. Grüningera, D. van der Mare, H. P. Geserichb, Th. Wolf, A. Erb, and T. Kopp. Infrared spectroscopy on Y$_{1-x}$RE$_x$Ba$_2$Cu$_{3-y}$Zn$_y$0$_6$ (RE = Pr, Gd, $x = 0$ and 0.8; $y = 0$ and $\simeq 0.15$). *Physica B: Condensed Matter*, 244:60–65, 1998.

[378] C. C. Homes and J. E. Eldridge. Lattice-mode coupling to the charge-density wave in (TMTSF)$_2$ReO$_4$ (where TMTSF is bis-tetramethyltetraselenafulvalene). *Physical Review B*, 40:6138–6143, 1989.

[379] J. E. Eldridge, C. C. Homes, F. E. Bates, and G. S. Bates. Far-infrared powder absorption measurements of some tetramethyltetraselenafulvalene salts [(TMTSF)$_2$X]. *Physical Review B*, 32:5156–5162, 1985.

[380] X. K. Chen, J. C Irwin, and J. P. Franck. Evidence for a strong spin-phonon interaction in cupric oxide. *Physical Review B*, 52:13130–13133, 1995.

[381] B. Gorshunov, E. Zhukova, V. I. Torgashev, L. S. Kadyrov, E. A. Motovilova, F. Fischgrabe, V. Moshnyaga, T. Zhang, R. Kremer, U. Pracht, S. Zapf, and M. Dressel. Boson peak in overdoped manganites La$_{1-x}$Ca$_x$MnO$_3$. *Physical Review B*, 87:245124, 2013.

[382] A. Damascelli, D. van der Marel, G. Dhalenne, and A. Revcolevschi. Optical spectroscopy of pure and doped CuGeO$_3$. *Physical Review B*, 61:12063–12074, 2000.

[383] T. Bauer and C. Falter. Microscopic modeling of phonon dynamics and charge response in NdCuO. *Physical Review B*, 77:144503, 2008.

[384] M. d'Astuto, A. Mirone, P. Giura, D. Colson, A. Forget, and M. Krisch. Phonon dispersion in the one-layer cuprate HgBa$_2$CuO$_{4+\delta}$. *Journal of Physics: Condensed Matter*, 15:8827–8836, 2003.

[385] G. Theodorou and T. M. Rice. Statics and dynamics of incommensurate lattices. *Physical Review B*, 18:2840–2856, 1978.

[386] J. D. Axe and P. Bak. Long-wavelength excitations in incommensurate intergrowth compounds with application to $Hg_{3-\delta}AsF_6$. *Physical Review B*, 26:4963–4973, 1982.

[387] G. Theodorou. Energy gap in the phonon spectrum of incommensurate lattices: The role of Coulomb forces. *Solid State Communications*, 33:561–563, 1980.

[388] M. Ortolani, P. Calvani, S. Lupi, U. Schade, A. Perla, M. Fujita, and K. Yamada. Effects of superconductivity and charge order on the subterahertz reflectivity of $La_{1.875}Ba_{0.125-y}Sr_yCuO_4$. *Physical Review B*, 73:184508, 2006.

[389] R. Fukaya, Y. Okimoto, M. Kunitomo, T. Ishikawa, K. Onda, S. Koshihara, A. Isayama, and T. Sasagawa. Unconventional photonic change of charge-density-wave phase in two-leg ladder cuprate $Sr_{14}Cu_{24}O_{41}$. *Journal of the Physical Society of Japan*, 82:083707, 2013.

[390] J. E. Lorenzo, L. P. Regnault, C. Boullier, N. Martin, A. H. Moudden, S. Vanishri, C. Marin, and A. Revcolevschi. Macroscopic quantum coherence of the spin triplet in the Spin-Ladder compound $Sr_{14}Cu_{24}O_{41}$. *Physical Review Letters*, 105:097202, 2010.

[391] G. Coslovich, B. Huber, W.-S. Lee, Y.-D. Chuang, Y. Zhu, T. Sasagawa, Z. Hussain, H. A. Bechtel, M. C. Martin, Z.-X. Shen, R. W. Schoenlein, and R. A. Kaindl. Ultrafast charge localization in a stripe-phase nickelate. *Nature Communications*, 4: 2643, 2013.

[392] K. Naruse, T. Kawamata, M. Ohno, Y. Matsuoka, K. Kumagai, and Y. Koike. Thermal conductivity due to magnons in high-quality single crystals of the two-leg spin-ladder system $(Ca,Sr,La)_{14}Cu_{24}O_{41}$. *Solid State Communications*, 154:60–63, 2013.

[393] T. Rõõm, U. Nagel, E. Lippmaa, H. Kageyama, K. Onizuka, and Y. Ueda. Far-infrared study of the two-dimensional dimer spin system $SrCu_2(BO_3)_2$. *Physical Review B*, 61:14342–14345, 2000.

[394] T. Rõõm, D. Hüvonen, U. Nagel, J. Hwang, T. Timusk, and H. Kageyama. Far-infrared spectroscopy of spin excitations and Dzyaloshinskii-Moriya interactions in

the Shastry-Sutherland compound $SrCu_2(BO_3)_2$. *Physical Review B*, 70:144417, 2004.

[395] T. Rõõm, D. Hüvonen, U. Nagel, Y. J. Wang, and R. K. Kremer. Low-energy excitations and dynamic Dzyaloshinskii-Moriya interaction in α'-NaV_2O_5 studied by far-infrared spectroscopy. *Physical Review B*, 69:144410, 2004.

[396] M. Matsuda and K. Katsumata. Observation of a dimerized state in the S = 1/2 quasi-one-dimensional antiferromagnet $Sr_{14}Cu_{24}O_{41}$. *Physical Review B*, 53:12201–12205, 1996.

[397] R. W. G. Wyckoff. *Crystal Structures*, volume 1. Interscience Publishers, New York, 2nd edition, 1963.

[398] V. A. Streltsov and N. Ishizawa. Synchrotron x-ray study of the electron density in $RFeO_3$ (R = Nd, Dy). *Acta Crystallographica*, B55:1–7, 1999.